Hydrogen-selective porous carbon-based membranes for catalytic steam reforming of bio-ethanol

Von der Naturwissenschaftlichen Fakultät der

Gottfried Wilhelm Leibniz Universität Hannover

zur Erlangung des Grades

Doktor der Naturwissenschaften (Dr. rer. nat.)

genehmigte Dissertation

von

Alexander Wollbrink, geb. Schulz, M. Sc.

2021

Citation

„Jeder Irrtum ist ein Schritt zur Wahrheit. Die Wissenschaft besteht nur aus Irrtümern. Aber diese muss man begehen. Es sind die Schritte zur Wahrheit."—Jules Verne

Preface

The results of my dissertation display a summary of selected works carried out at the Institute of Physical Chemistry and Electrochemistry at the Gottfried Wilhelm Leibniz Universität Hannover. My research dealt with the synthesis, development and characterisation of porous membranes for the selective extraction of hydrogen from multi-component gas mixtures under the supervision of Prof. Dr. rer. nat. Jürgen Caro. The work was embedded in the project "Hydrogen production from bio-ethane and bio-ethanol in catalytic membrane reactors", which was financed by the Deutsche Forschungsgemeinschaft (Ca 147/19-1) and the National Natural Science Foundation of China (NSFC 21322603) under the guidance of Prof. Dr. rer. nat. Jürgen Caro and Prof. Dr. rer. nat. Armin Feldhoff.

The dissertation contains a selection of seven research articles which includes five research articles as corresponding author (1th author) and two research articles as co-author (2nd author). In addition to this, i was further involved into six research articles as co-author, which are not included in the dissertation. My contributions to the selected research articles included in my dissertation are described in the following.

The one research article and two manuscripts included in Chapter 3.1. "Microporous carbon membranes" were written by me. The synthesis of the amorphous and crystalline carbon membrane were done by myself whereas the turbostratic carbon membrane was provided by Dr. H. Richter and S. Kämnitz at the Frauenhofer Institute of Ceramic Technologies and Systems (IKTS) in Hermsdorf. SEM and HRTEM analyses were carried out by me with the help of Prof. Dr. Armin Feldhoff and F. Steinbach. XPS analyses were measured by J. Koch and Prof. Dr. C. Tegenkamp at the Institute of Solid State Physics, Leibniz Universität Hannover and were fitted and evaluated by me with the help of Dr. K. Volgmann. Contact angle measurements were conducted by Prof. Dr. Y. Li of the Dalian Institute of Chemical Physics in Dalian (China) and evaluated by me. Analyses and evaluation of micro-focused Raman spectroscopy as well as permeation experiments were carried out by me.

In the case of the research article of "Multiple polymerisation – formation of hybrid materials consisting of two or more polymers from one monomer" was written by Dr. T. Ebert of the Institute of Chemistry, Professorchip of Polymer Chemistry at TU Chemnitz. For this research article, the demanding sample preparation and also characterisation by HAADF-STEM micrograph were carried out by me. The corresponding manuscript on "Separation performance of a composite Carbon Molecular Sieve (cCMS/SiO$_2$) membrane from a hybrid

material by twin polymerization" was written by me. The synthesis of the hybrid material and subsequent carbonisation was carried out by Dr. T. Ebert of the Institute of Chemistry, Professorchip of Polymer Chemistry at TU Chemnitz in agreement with me. The characterisation and corresponding evaluation of the membrane by means of XRPD, HAADF-STEM micrographs, permeation experiments, TG/DTA analyses and hydrophobic treatment as well as the sample preparation for TEM analysis was executed by me. XPS analyses were measured by J. Koch and Prof. Dr. C. Tegenkamp at the Institute of Solid State Physics, Leibniz Universität Hannover and were fitted and evaluated by me.

In the case of the research article "Metal-organic frameworks" the research article on "A novel CAU-10-H MOF membrane for hydrogen separation under hydrothermal conditions" was written by Dr. H. Jin and Prof. Dr. Y. Li at the Institute of Chemical Physics in Dalian (China). Analyses of the MOF membrane by means of XRPD, SEM micrographs and element mapping by EDXS analyses were carried out by me. The permeation experiments were executed by me and were assisted by Dr. H. Jin under close supervision of me.

The two research articles of Chapter 3.2 "Porous graphite Membranes" were completely written by me. The research article on "Pressed graphite crystals as gas separation membrane for steam reforming of ethanol" was written with the help of Prof. Dr. J. Caro, since it was the first of my publications included to this dissertation. Here, SEM and HRTEM analyses were carried out by me still with the help of F. Steinbach. Further, permeation experiments as well as XRPD analyses were executed by me. For the research article on "Improved hydrogen selectivity of Surface Modified Graphite (SMG) membranes: Permeation experiments and characterisation by micro-Raman spectroscopy and XPS" was written by me. XPS analyses were measured by J. Koch and Prof. Dr. C. Tegenkamp at the Institute of Solid State Physics, Leibniz Universität Hannover and were fitted and evaluated by me. The permeation experiments as well as micro.-focused Raman spectroscopy measurements were carried out by me. The shown Raman sepctra were evaluated with the help of Prof. Dr. C.H. Rüscher from the Institute of Mineralogy at the Leibniz Universität Hannover.

Acknowledgement

At first, I have to express my deepest thanks to Prof. Dr. Jürgen Caro, who gave me the opportunity to issue my dissertation in his research group at the Institute of Physical Chemistry and Electrochemistry at the Leibniz University of Hannover. Especially, i thank Prof. Dr. Jürgen Caro who allows me to participate at several advanced training courses, e.g.: Bronkhorst High-Tech Product Training in Ruurlo (NL), the DMG/DGK Ph.D. student course for basic principles and applications for Rietveld refinements at Max-Planck Institute (MPI) Stuttgart and the International School on Ab initio Modelling of Solids at the University of Regensburg and Turino 2014 for "CRYSTAL14" calculations.

I thank Prof. Dr. Armin Feldhoff and F. Steinbach for their instructions in sample preparation, operation and data evaluation of the field-emissions "scanning electron microscope" as well as the "transmission electron microscope".

The fine mechanical workshop represented by W. Becker, P. Mühr and M. Köhler and also J. Kuckuck deserves my thanks because of their willingness to help for the construction of new components and the fast repair of a high number of broken components.

Furthermore, I thank Y. Gabbey-Uebbe, K. Battermann, K. Janze and M. Schlüter for their great help at all organizing from ordering chemicals or gases to manage bureaucratic hurdles.

Supplementary I want to thank all research colleagues from our project and cooperation partners for their great help during my dissertation like Prof. Dr. Y. Li and Dr. H. Jin from the Dalian Institute of Chemical Physics in China; Dr. T. Ebert and Prof. Dr. S. Spange from the Institute of Chemistry, Professorchip of Polymer Chemistry of the TU Chemnitz; Dr. K. Kanthasamy, J. Koch and Prof. Dr. C. Tegenkamp from the Institute of Solid State Physics at the Leibniz University of Hannover; Dr. H. Richter und Dr. S. Kämnitz from the Frauenhofer Institute of Ceramic Technologies and Systems (IKTS) in Hermsdorf; Prof. Dr. C.H. Rüscher and Prof. Dr. J.-Ch. Buhl from the Institute of Mineralogy at the Leibniz University of Hannover.

I also have to thank all the helping colleagues at the Institute of Physical Chemistry and Electrochemistry, which were always open for ideas and critical discussion: Dr. K. Volgmann, N. Bösebeck, Dr. V. Nair, Dr. A. Düvel, Dr. J. Xue, Dr. W. Fang, W. Liang, Dr. F. Liang, Dr. N. Wang, Dr. Y. Liu, Dr. K. Partovi, Dr. O. Wittich. In addition to this, i expecially want to thank the students who passed their practical course like M. Schulze and A. Duong as well as A. Breuksch who passed his Bachelor Thesis under supervision of me.

Acknowledgement

Finally, i still want to thank my family for giving me the appropriate support for writing this dissertation. Especially i have to thank my grandmother (deceased in 2013) who always believed and supported me, my wife Miriam who always supported me over the last 7 years that I finally found the power to finish my dissertation. In addition, my biggest thanks is to my wife and my daughter Mathilda who supported me in my greatest despair and always encouraged me to finish this dissertation.

Abstract

Today's demand from science and research on the usage of sustainable and renewable energy sources arises mainly from the embargo of oil shipments to the Western nations by the arab members of the "Organization of the Petroleum Exporting Countries" (OPEC) in 1973-1974 until today. But the global production of pure hydrogen still originates primarily from fossil fuels and is dominated by industry, i.e. mainly by petroleum refining and ammonia production. Numerous disadvantages are described for the commercial production of hydrogen by catalytic steam reforming (CSR) of hydrocarbons (e.g. use of non-renewable resources, high energy requirement, the release of high amounts of CO etc.). Nevertheless, the huge advantage of the established procedure is related to its cost-effective manufacture of hydrogen due to high hydrogen-selectivity and full conversion. The use of suitable porous carbon-based membranes and of renewable resources (e.g. bio-ethanol) at relative low temperatures (below 400 °C) can overcome most of the related problems in classic CSR technique.

In this context, a new concept of different porous and hydrogen-selective carbon-based membranes were investigated as suitable candidates for the purpose of the production of so-called "green hydrogen" by means of catalytic membrane reactor (CMR) for bio-ethanol steam reforming (b-ESR). The carbon-based membranes under study were investigated by means of classic gas separation experiments. Temperature- and pressure-dependent single and mixed-gas permeation experiments were applied in laboratory scale, closely adapted to industrial conditions. From the carbon-based membranes under study, it could be shown that two kinds of membranes, i.e. the metal-organic framework (CAU-10-H) membrane and the group of surface-modified graphite membranes (SMG), comparatively showed the most promising results. The mixed gas separation factors of the CAU-10-H and SMG graphite (e.g. ETMS-modified) membrane could reached for α (H_2/CO_2) of 11.1 or 8.0 and for α (H_2/H_2O) of 5.7 and 10.2, respectively. Additionally, the SMG and the CAU-10-H membrane types show beneficial separation performances of hydrogen in the presence of large quantities of water steam (up to 18 Vol.-% H_2O) and have a good hydrothermal stability in classical gas separation experiments.

Keywords: Hydrogen separation, Gas separation, Mixed-gas separation, Carbon-based membrane, Graphite membrane, surface modified graphite, steam reforming, micro-Raman spectroscopy, G1/D1 peak relationship, XPS, CAU-10-H membrane, metal-organic frameworks

Kurzzusammenfassung

Die heutige Nachfrage aus Wissenschaft und Forschung nach der Nutzung nachhaltiger und erneuerbarer Energiequellen ergibt sich hauptsächlich aus dem Embargo für Öllieferungen in die westlichen Länder durch die arabischen Mitglieder der „Organisation der erdölexportierenden Länder" (OPEC) in den Jahren 1973-1974 bis heute. Die weltweite Produktion von reinem Wasserstoff stammt jedoch immer noch hauptsächlich aus fossilen Brennstoffen und wird von der Industrie dominiert, d.h. hauptsächlich von der Erdölraffination und der Ammoniakproduktion. Für die kommerzielle Herstellung von Wasserstoff durch katalytische Dampfreformierung (CSR) von Kohlenwasserstoffen werden zahlreiche Nachteile beschrieben (z.B. Verwendung nicht erneuerbarer Ressourcen, hoher Energiebedarf, Freisetzung hoher Mengen an CO etc.). Der große Vorteil des etablierten Verfahrens hängt jedoch mit seiner kostengünstigen Herstellung von Wasserstoff aufgrund der hohen Wasserstoffselektivität und der vollständigen Umwandlung zusammen. Die Verwendung geeigneter poröser Membranen auf Kohlenstoffbasis und erneuerbarer Ressourcen (z. B. Bioethanol) bei relativ niedrigen Temperaturen (unter 400 °C) kann die meisten damit verbundenen Probleme bei der klassischen CSR-Technik überwinden.

In diesem Zusammenhang wurde ein neues Konzept verschiedener poröser und wasserstoffselektiver Membranen auf Kohlenstoffbasis als geeignete Kandidaten für die Herstellung von sogenanntem „grünem Wasserstoff" mittels eines katalytischen Membranreaktors (CMR) zur Bioethanol-Dampfreformierung (b-ESR) untersucht. Die untersuchten Membranen auf Kohlenstoffbasis wurden mittels klassischer Gastrennungs-experimente untersucht. Temperatur- und druckabhängige Einzel- und Mischgaspermeations experimente wurden im Labormaßstab durchgeführt, eng an die industriellen Bedingungen angepasst. Aus den untersuchten Membranen auf Kohlenstoffbasis konnte gezeigt werden, dass zwei Arten von Membranen, nämlich die metallorganische Gerüstmembran (CAU-10-H) und die Gruppe der oberflächenmodifizierten Graphit-membranen (SMG) zeigten vergleichsweise die vielversprechendsten Ergebnisse. Die Mischgastrennfaktoren der CAU-10-H und SMG-Graphitmembran (z.B. ETMS-modifizierte Membran) konnten für α (H_2/CO_2) von 11,1 oder 8,0 und für α (H_2/H_2O) von 5,7 bzw. 10,2 erreicht werden. Zusätzlich zeigen die SMG- und die CAU-10-H-Membrantypen vorteilhafte Trennleistungen von Wasserstoff in Gegenwart großer Mengen Wasserdampf (bis zu 18 Vol.-% H_2O) und besitzen eine gute hydrothermale Stabilität bei klassischen Gastrennungsexperimenten.

Kurzzusammenfassung

Schlagwörter: Wasserstofftrennung, Gastrennung, Mischgastrennung, kohlenstoffbasierte Membran, Graphit Membran, modifizierte Graphitoberflächen, Dampfreformierung, mikrofokussierte Ramanspektroskopie, G1/D1 Peak-Beziehung, XPS, CAU-10-H Membran, Metall-organische Gerüstverbindungen

Content

Content

1. Introduction

In consideration of the numerous national and international conferences and dialogues (Kyoto 1997 and Paris 2015) in terms of preventing the climate change by CO_2 emissions, it is almost surprising that the leading industrial and upcoming industrial nations still cover their energy needs mainly from fossil energy sources [1–5]. The usage of renewable or fossil energy sources has always been a question of the local availability, production costs, the progress of technology and related environmental pollution of water or air. From European history, several examples for the change of energy sources or carriers can be found for the use of renewable or fossil energy sources [6]. Examples include the transition from medieval societies, dominated by renewable energy source like wind- and watermills as well as biomass, to industrial nations, dominated at first by coal powered steam engines and followed by internal combustion engines using liquid fuels. These developments have been promoted by the rapid progress in upcoming technologies and the growing needs of the rapid population growth. Nevertheless, at the beginning of the 20th century, pioneering works for the development of sustainable engines for mobility powered from renewable energy carriers by R. Diesel, who presented its peanut oil powered engines at the Exhibition in Paris 1900, and the development of electric vehicles became less attractive by the faster technological progress of gasoline powered engines [7,8].

Today's demand from science and research on the usage of sustainable and renewable energy sources arises mainly from the embargo of oil shipments to the Western nations by the arab members of the "Organization of the Petroleum Exporting Countries" (OPEC) in 1973-1974 [6]. The subsequently drawn supply shortage of fuels caused a dramatic increase of the oil export prices, followed by a global recession and revitalised the search and development of alternative and renewable energy sources and fuels.

In the progress of technology of the last 40 years, it might appears as the irony of history that latest renewable energy sources almost based on the medieval energy sources (wind, water, biomass) and solar energy [9]. The disadvantage of wind, water, biomass and solar power as primary energy source is their location and time dependency in the availability of wind power, solar radiation, the limited number of rivers with sufficient gradients or suitable feedstocks for biomass production. To become independent from the disadvantages mentioned before, hydrogen is primarily discussed as clean and sustainable carbon-free energy carrier to store the energy generated by sustainable primary power plants [10,11]. In

the next step, the stored hydrogen can be freely applied in end-use technologies such as fuel cells, engines, turbines or boilers [11]. To produce electric energy by fuel cells, hydrogen only produced water as by-product and is a suitable approach as carbon-free key technology for preventing global warming by CO_2 emission. Currently, in contradiction to hydrogen as clean energy carrier, most of the world hydrogen production is conducted by steam reforming of natural gas [12], see Equation 1, taken from [13].

Eq. 1
$$C_mH_n + mH_2O = mCO + \left(m + \frac{1}{2}n\right)H_2$$
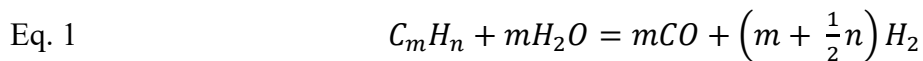
In industry, steam reforming of hydrocarbons is the most preferred process for the production of hydrogen. The process required low process temperatures and generate the highest H_2/CO ratio. The produced CO is convertible to CO_2 by a low temperature water gas shift reaction (WGSR). Here, the most serious problems are the dependence on fossil fuels and the production of high amounts of CO_2, which increase the greenhouse effect.

A new strategy is the clean and sustainable hydrogen production from biomass by pyrolysis, gasification or biologic fermentation of organic matter from energy crops and organic wastes from agriculture, forestry or municipality. The process also produce H_2 and CO_2 as by-product, but biomass also consume CO_2 from atmosphere during its growth, so that it is described as carbon neutral resource [13,14]. The disadvantages of the direct production of hydrogen from biomass are the numerous liquid (tar and oils) and solid (char and carbon) co-products and residuals, which need further processing steps or deposition. Furthermore, unsolved problems for the riskless storage and release of gaseous or chemical bonded hydrogen remain, here.

A cleaner, more riskless and cheaper technical solution is the production of so-called "green hydrogen" by catalytic steam reforming (CSR) of bio-ethanol [11,13,15–17]. This process offers several advantages as compared to the direct production of hydrogen from biomass: bio-ethanol is also a clean renewable energy carrier with an closed carbon cycle, since it is produced by fermentation of biomass using ethanolgenic microorganisms [18–20]; with a molar ethanol/water ratio of about 1:13, bio-ethanol is a riskless and stable chemical for storage or transportation; steam reforming of bio-ethanol is a clean process, only gaseous products are generated and the process is already established in recent industrial application, as mentioned before. Ethanol steam reforming (ESR) is an endothermic reaction and benefits thermodynamically from higher temperatures. Therefore, classic ESR is conducted at high temperatures of between 400 °C and 1000 °C because of the full ethanol conversion and high

Introduction

hydrogen selectivity. Essential for this process is the choice of a suitable catalyst, which directly decides on ethanol conversion, numerous and complex reaction pathways and hydrogen selectivity dependent on ethanol/steam ratio and process temperature. The huge disadvantage of catalytic steam reforming of bio-ethanol at high temperature is the production of high amounts of CO, beside several other side-reactions. Since carbon monoxide is a toxic gas and deactivates the anodic catalyst in fuel cells (poison effect), it has to be removed from the reaction mixture by further process steps like low temperature WGSR, pressure swing adsorption or a hydrogen-selective Membrane (ceramics or noble metals), which makes the reaction handling further complicated and cost intensive [11,13]. The formation of CO and other side-products is suppressed by CESR at low temperatures (< 400 °C), but the process suffers from a low ethanol conversion, low hydrogen selectivity, low catalyst stability by the formation of coke and benefits the formation of methane, beside several other side-reactions [21–23].

The introduction of a membrane-supported low temperature CESR process for the *in situ* extraction of hydrogen could minimise most of the disadvantages described before. Further, the removal of hydrogen from the product-side of the CESR process using a so-called "catalytic membrane reactor" (CMR), as commonly described in *Eq. 1*, should improve the ethanol conversion, hydrogen selectivity of the reaction, prevent undesired hydrogen consuming side-reaction like methanation, $CO_2 + 4H_2 \leftrightarrows CH_4 + 2H_2O$, or hydrogenolysis of ethanol to methane, $C_2H_5OH + 2H_2 \leftrightarrows 2CH_4 + H_2O$, and improves drastically the purity of produced hydrogen. For the application of the bio-ethanol steam reforming (b-ESR) process in a catalytic membrane reactor (CMR), a suitable membrane that meets various requirements has to be found. Firstly, the membrane has to separate preferentially hydrogen in the excess of water (steam) that require a sufficient high mixed gas selectivity of α (H_2/H_2O) to prevent that too much steam is extracted from the reaction, which would decrease the reaction efficiency. Secondly, a sufficient high mixed gas selectivity of α (H_2/CO_2) is required for a high purity of the produced hydrogen, which reduces further purification processes. Finally, the suitable membrane requires a thermal stability up to 400 °C in the presence of huge amounts of steam, CO_2 and traces of other undesired by-products.

For this purpose, the focus of my dissertation was on the synthesis, development and characterisation of microporous carbon membranes and their further developments built on the findings obtained. Furthermore, we investigated a selected metal-organic framework (MOF) membrane for the challenging separation process. Thus, the dissertation is structured

in the following by the theoretical and experimental basics, followed by the two topic areas as follows: microporous carbon membranes and porous graphite membranes, the Conclusions and a brief outlook.

2. Theoretical and experimental basics

2.1. Permeation in porous membranes

2.1.1. Membranes as porous solids

A porous solid is generally described by the presence of cavities, channels or interstices in the solid, which proportions are deeper than their width [24]. Irregularities on a material with proportions less deep than their width are defined as surface roughness. The pores of a solid are commonly classified by their shape (cylindrical, ink-bottle, funnel or slit shaped), their accessibility to an external fluid (open, closed, blind or dead-end pores) and size (pore diameter or width). The pore size defines the smallest possible distance between two opposite pore walls, which limits the pore entrance. Usually, porous materials are classified into three domains by their pore sizes: micropores are smaller than 2 nm, mesopores are inbetween of 2 nm and 50 nm, and macropores are larger than 50 nm. Materials with pore sizes in the order of 1 nm to 100 nm are commonly summerised under the term of nanoporous materials [25,26]. Due to the huge importance in versatile applications in porous membranes or catalysts, e.g. for a size-selective separation mechanism (see molecular sieving), the pore size of porous materials need to be determined precisely. Nevertheless, the precise determination of the "pore size" or "pore width" is a still complex question by the presence of different pore shapes, their connectivity or the distribution of pore sizes in the same material.

2.1.2. Mass transport in membranes

In the terminology of membranes and membrane processes, a membrane is simply defined as a structure through which a mass transfer can occur due to numerous driving forces with a lateral dimension much greater than thick [27]. The mass transfer is generally described as the flux (J_i) by the number of moles, volume or mass of a component i passing the membrane per time and surface area normal to the membrane thickness. The driving force of physical as well as chemical processes thermodynamically based on the dissipation of energy, which is described by the Entropie S [28]. The direction of a process (mass transfer) or reaction is defined by the change of the free Enthalpy (ΔG) as a function of the variation of the inner Energy (ΔU) or Enthalpy (ΔH) and Entropie (ΔS) of a system under study, see Eq. 2:

Eq. 2
$$\Delta G_{T,p} = \Delta H_{T,p} - T \Delta S_{T,p}$$

Theoretical and experimental basics: Permeation in porous membranes

In general, a physical or chemical process spontaneously occurs at constant pressure and temperature by the decrease of free Enthalpy ($\Delta G < 0$) of a system. Without a change of the free Enthalpy ($\Delta G = 0$), the observed system or process is in equilibrium and no driving force is present. As example, from Eq. 2 it follows that, in an isolated system a spontaneous physical change of state or process only occurs by the increase of Entropy S at constant pressure (p) and temperature (T).

The diffusive mass transport of a component i through a medium is defined by Fick's first law of diffusion, which commonly describes the flux as a function of a transport or diffusion coefficient and a gradient in concentration (*grad c*). The local change of concentration is mathematically formulated as the first derivation of concentration with respect to the place [28]. Fick's first law of diffusion is written in terms of solids or porous solids with very narrow pores (micropores) by

Eq. 3
$$J_i = -D_i \frac{\partial c_i}{\partial x}, \quad \text{with a gradient of concentration,}$$

in terms of an ideal solution by

Eq. 4
$$J_i = -C\,D_i \frac{\partial y_i}{\partial x}, \text{with a gradient of mole fraction,}$$

or in terms of an ideal gas by

Eq. 5
$$J_i = -\frac{D_i}{RT} \frac{\partial p_i}{\partial x}, \text{with a gradient of partial pressure,}$$

which partly contain related thermodynamic correction factors [29]. In all cases, the driving force of diffusive mass transport is independently described, from the state of the aggregate, by the gradient of chemical potential (*grad μ*), see refs. [25,28]. This thermodynamically means, that in a system in equilibrium, no diffusive mass transport occurs since no gradient of chemical potential exist. In accordance with the discussion of Eq. 2, for pure substances the chemical potential μ is only a synonym for the free Enthalpy (G). Further, the maximum of non-volume work (dw) that a system can perform is in accordance to the change of free Enthalpy (ΔG) at constant pressure (p) and temperature (T). Thus, the performed work of a system for diffusive mass transport corresponds to the change of chemical potential or free Enthalpy ($dw=d\mu=\Delta G$) with respect to the place, which is described by Eq. 6.

Eq. 6
$$dw = d\mu = \left(\frac{\partial \mu_i}{\partial x}\right)_{p,T} dx$$

In general, the work required in a system to move a particle by a distance dx against a counterforce F is defined by Eq. 7.

Eq. 7
$$dw = -F\,dx$$

In comparison of Eq. 6 and 7, it follows that the gradient of the chemical potential (*grad μ*) is commonly described as the driving force of diffusive mass transport, see Eq. 8.

Eq. 8
$$F_{Th} = - \left(\frac{\partial \mu}{\partial x} \right)_{p,T}$$

Due to the spontaneous tendency of particle movement, the driving force of diffusive mass transport is described as thermodynamic force F_{Th} (as function of pressure and temperature), rather than as real force [28].

2.1.3. Experimental Approach

In general, membrane permeation experiments under quasi-steady-state conditions are the most commonly used method for the determination of mass transfer through a porous membrane or catalyst [30,31]. One side (feed or upstream) of the porous membrane is constantly kept under a defined pressure and the pressure on the other membrane side (permeate or downstream) subsequently increases due to the amount of permeated gas through the membrane with the time or is also kept constant, see Fig. 1.

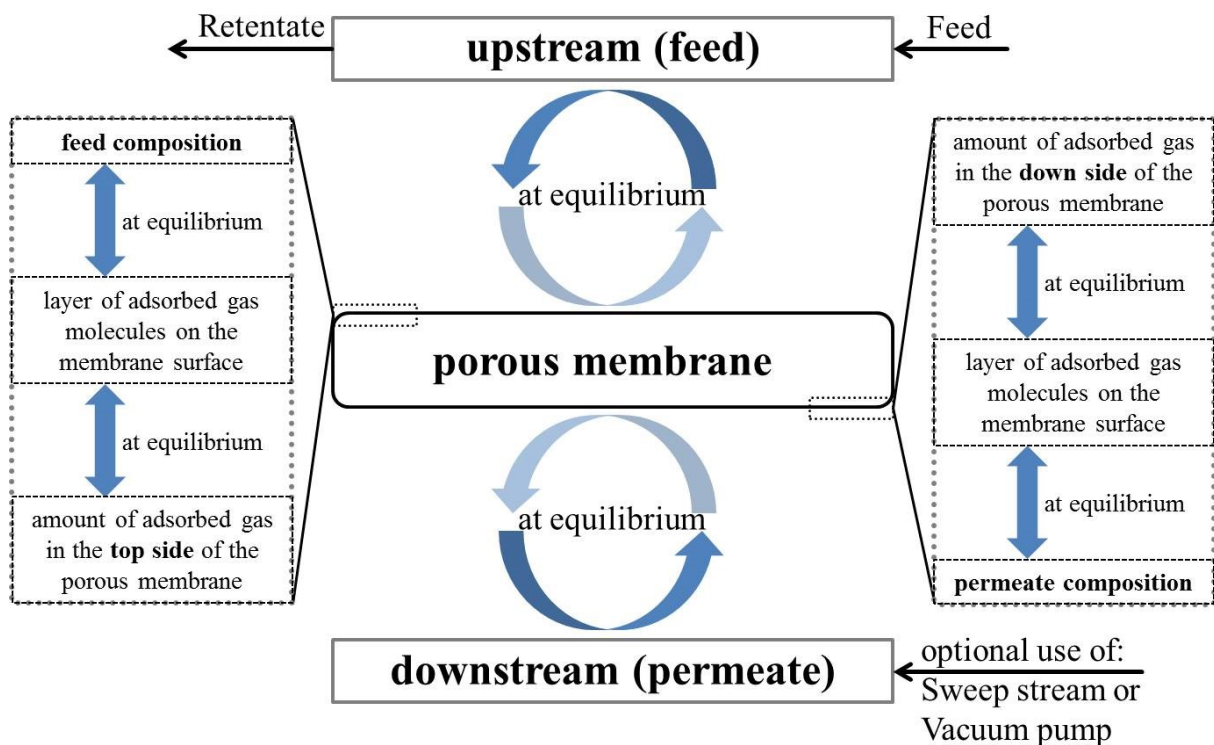**Figure 1:** Schematic illustration of the different phase boundaries of permeation experiments under quasi-steady-state conditions at equilibrium.

The advantage of this concept is the simple experimental setup and application of this method. Furthermore, it allows the easy description of the flux J_i of a component *i* through a porous membrane, which is proportional to the permeability *(B)* and the quotient of the

pressure difference (Δp_i), between the feed and permeate side of the membrane, and the membrane thickness L, see Eq. 9 and Fig. 1.

Eq. 9 $$J_i = B_i \frac{\Delta p_i}{L}$$

For single gases, the permeability (B_i) is simply described as the flux (J_i) normalised by the known pressure difference (Δp_i) between feed and permeate side of the membrane and the membrane thickness (L), see Eq. 10. For gas mixtures, the known pressure difference (Δp_i) is defined by the partial pressure.

Eq. 10 $$B_i = J_i \frac{L}{\Delta p_i}$$

This uniform description of the flux J_i of a component i through a membrane by Eq. 10, is essential for the comparison of different membranes with unequal shapes, thicknesses and were measured at varying conditions. In literature, the flux J_i is commonly discussed by the permeance P due to description of single membrane permeation experiments. The permeance P is defined as the flux J_i of a component i normalised by the known pressure difference (Δp_i) between feed and permeate side of the membrane [27]. In this work, membrane permeation experiments were performed under quasi-steady-state conditions as mentioned before and in a modified Wicke-Kallenbach setup for the characterisation of the porous membranes under study [31,32]. For the latter method, the feed side of the membrane was also constantly kept at a defined pressure, but the permeate side was swept with a pure carrier gas stream, see Fig. 1. Further, a vacuum pump was partially used to generate a pressure of about 1×10^3 Pa (~ 10 mbar) on the permeate side of the membrane, which was analysed by an online coupled gas chromatograph. The full miscibility of the used gas mixtures was achieved by high gas velocities of about 50-100 mL/ min on the feed and optional 5-50 mL/min on the sweep side of the porous membrane.

The disadvantage of membrane permeation experiments under quasi-steady-state conditions is the interpretation of the quite complex interactions of different mass transport regimes, phase boundaries and driving forces, which are in thermodynamic equilibrium to each other. As illustrated in Fig. 1, four phase boundaries need to be considered for membrane permeation experiments. The first phase boundary is between the free gas molecules of the feed and the layer of adsorbed gas molecules on the surface of the porous membrane. The diffusive mass transport of the feed mixture, described by the gradient of partial pressure p_i (see Eq. 5), as well as the process of physical adsorption on the membrane surface based on the gradient of chemical potential μ_i. The amount of surface adsorbed molecules on the membrane surface is

commonly defined as the degree of coverage (Θ), which describes the dynamic equilibrium between the number of occupied and available adsorption sites on the porous membrane surface. The degree of coverage (Θ) of a surface is generally characterised by i) various adsorption isotherms, e.g. Langmuir and Freundlich isotherm are to mention, as a function of pressure (p) for single gases or partial pressure (p_i) for gas mixtures and ii) by the van't Hoff or Clausius-Clapeyron equation as a function of temperature (T) [28,33]. The second phase boundary is between the layer of physically adsorbed gas molecules on the membrane surface and the amount or concentration of adsorbed molecules within the porous membrane. In porous membranes, the diffusive mass transport generally occurs by various transport mechanisms in dependence on the characteristic properties of the pores and the diffusing gas molecules, which passes through the porous membrane [33,34]. Thus, the diffusive mass transport based on the gradient of concentration (*grad c*) or partial pressure (*grad p_i*) of a component *i* within the membrane surface on the feed (2nd phase boundary) and permeate (3rd phase boundary) side of the porous membrane, see Eq. 3 and 5. Consequently, the membrane surface on the permeate side of the membrane (4th phase boundary) is also in a thermodynamic equilibrium with the permeate composition.

2.1.4.   Transport mechanisms

In porous membranes, the most relevant transport mechanisms are molecular sieving, selective surface diffusion, Knudsen diffusion, and viscous flow or molecular diffusion. Which of these mechanisms dominates of the porous membrane under study is mainly determined by two sensible ratios of the effective pore size (d_{eff}) to i) the mean free path length (λ) and to ii) the kinetic diameter (σ) of diffusing molecules. Additionally, permeation experiments may selectively be affected by adsorption of the diffusing gas species on the surrounding pore surface by dispersion interactions. The mean free path length (λ) describes the distance travelled between two molecule collisions of a single molecule species as a function of temperature (T), Boltzmann constant (k), pressure (p) and the collision cross-section (A_i) of a molecule species (*i*), see Eq. 11 [28].

Eq. 11
$$\lambda_i = \frac{k \cdot T}{\sqrt{2} \cdot A_i \cdot p}$$

The kinetic diameter (σ) of a molecule is defined as the intermolecular distance of the closest approach of two molecules, which collides with an initial kinetic energy of zero [33,35,36]. Dependent on the shape and polarity of a molecule, the molecular dimension is calculated for i) spherical and nonpolar molecules by the Lennard-Jones potential (ϕ), ii) diatomic, long and

more complex molecules, e.g. hydrocarbons or n-paraffins, by the minimum of the cross-sectional molecular diameter and iii) polar molecules by the Stockmayer potential. Exemplary values of the kinetic diameter (σ) for H_2, CO_2, H_2O and ethanol (C_2H_5OH) in accordance with their rising diameter are given as follows:

$$\sigma_{H_2O}\,(2.65\,\text{Å}) > \sigma_{H_2}\,(2.89\,\text{Å}) > \sigma_{CO_2}\,(3.30\,\text{Å}) > \sigma_{C_2H_5OH}\,(4.50\,\text{Å})$$

Due to the complex architecture of porous membrane related to the pore shape, pore size distribution, connectivity, surface roughness and so on, the following discussion of occurring diffusion mechanisms is limited to the simple description of mass transfer through a single pore with the shape of a straight cylindrical pore. The diffusive mass transport in a porous membrane with a pore size larger than the mean free path length ($d_{Pore} > \lambda_{Molecule}$), is dominated by molecule-molecule collisions rather than by molecule collisions with the pore wall and similarly occurs to those conditions described in an ideal gas, see Eq. 5. Thus, the flux through a porous membrane is described by the Hagen-Poiseuille law (see Eq. 12), which is commonly called as non-selective viscous flow or Poiseuille flow [34,37,38].

Eq. 12 $$\dot{V} = \frac{dV}{dt} = \frac{\pi \cdot r^4}{8 \cdot \eta}\frac{\Delta p}{l}$$

For single gases and gas mixtures, the volume flux ($\dot{V}$) through a straight cylindrical tube simply depends on the pressure difference (Δp) between the two openings of a tube with a length (l), a radius (r) and the gas viscosity (η). The gas viscosity generally results from the direction-dependent moment transfer of between the diffusively reflected molecules from the pore walls and the free gas molecules passing through the pore as a function of the molecular weight (M_i), the mean free path length (λ_i), the mean velocity ($\bar{c}_i$) and the concentration [A_i], see Eq. 13 [28].

Eq. 13 $$\eta_i = \frac{1}{3} M_i \lambda_i \bar{c}_i [A_i]$$

For pore sizes equal to or smaller than the mean free path length ($d_{Pore} \leq \lambda_{Molecule}$), the diffusive mass transport in porous membranes is increasingly determined by molecule-wall collisions with the decrease of the pore size. Thus, the molecular transport is dominated by the properties of the pore in size, shape and the interaction of the diffusing gas molecules with the pore wall by adsorption due to dispersions or polar interactions [26]. In this case, the diffusive mass transport (permeance) of two different gas species (J_A, J_B) through a porous membrane is equivalent to the square root of their molar mass ratio, see Eq. 14 [34,37–40].

Eq. 14 $$\frac{J_A}{J_B} = \sqrt{\frac{M_B}{M_A}}$$

For porous membranes with very narrow pores, the diffusive mass transport is generally dominated by two size-selective transport mechanisms: i) molecular sieving and ii) selective surface diffusion. Size-selective molecular sieving occurs in very narrow pores related to the dimension of the kinetic diameter (σ) of diffusing molecules. Here, the diffusive mass transport is limited by steric hindrance, so that only these molecules can pass through such pores with a suitable kinetic diameter (σ) equal to or smaller than the effective pore size (d_{eff}) of the porous membrane. In pores with an effective pore size (d_{eff}) equal to or greater than the kinetic diameter (σ) of diffusing molecules, selective surface diffusion may occur due to preferential adsorption and permeation of the larger molecule species. Thus, the smaller molecules of a gas mixture are sterically hindered to enter the pores by the presence of the larger molecules in the pore but the smaller molecules cannot completely be excluded from the permeation process. Nevertheless, the assumption of a constant value of the kinetic diameter (σ) of molecules or pore size (d) is at least questionable by the dependence of bond length and vibration modes on temperature (T) and pressure (p) conditions. With regard to molecular sieving, the size-selective separation mechanism sensible dependence on the binding conditions of the limiting atoms of a pore. In the case of zeolite membranes, the temperature effect on the effective pore size (aperture) ranges between 0.1 Å or 0.2 Å, which can strongly affect the separation performance of a porous membrane [33]. Therefore, the effective pore size (d_{eff}) is experimentally determined by systematic permeation studies under required conditions.

2.1.5. Systematic permeation studies

The characterisation of a porous membrane by temperature- and pressure-dependent permeation experiments under steady-state condition (see Eq. 9) allows to draw conclusions of the specific transport mechanisms and related separation properties of the porous membrane under study with regard to Fick's first law of diffusion (see Eqs. 3-5). In all cases, the specific performance of a porous membrane based on the velocity determining step by the contributions of the diffusivity (D_i) and amount of adsorbed molecules (*grad i*) of a component (*i*) between the feed and permeate side of the membrane. Therefore, an increase as well as a decrease of the single gas permeance (P_i) of a component (*i*) through a porous membrane is generally observed in temperature-dependent permeation measurements. An increase of the mixed gas permeance of a single gas component with rising temperature probably results from an activated diffusion process as described for a molecular sieving or

surface diffusion mechanism [34]. The hopping rate (ϑ_i) of a molecule (i) from an occupied site to a vacancy with a distance (δ) on the pore surface may require a certain activation energy (E_A), at a temperature (T) and the universal gas constant (R) is described by an arrhenius-like equation, see Eq. 15.

Eq. 15
$$D_i = \vartheta_i \delta_i^2 \cdot e^{\left(-\frac{E_A}{RT}\right)}$$

A decrease of the single gas permeance (P_i) of a component (i) through a porous membrane with rising temperature generally results from two effects: i) the increase of mixed gas viscosity (η) for a pore size larger than the mean free path length ($d_{Pore} > \lambda_{Molecule}$), see Eq. 12 and 13, or ii) the decrease of adsorbed gas molecule on the porous membrane for pore sizes equal to or smaller than the mean free path length ($d_{Pore} \leq \lambda_{Molecule}$). The decrease of adsorption with rising temperature is due to the exothermic nature of adsorption. Since physical adsorption is a voluntary process and only occurs in the case of a reduction of the free Enthalpy (ΔG), see Eq. 2. As a consequence of adsorption, the value of Entropie (ΔS) is negative by the reduction of the degree of freedom in molecular vibrations for the adsorbed species. Therefore, the need of a negative value of the free Enthalpy (ΔG) is only achieved by the reduction of the inner Energy (ΔU) or Enthalphy (ΔH) of the molecule, which defines the process of adsorption as an exothermic reaction. For multi-component gas mixtures, both effects of diffusion and also adsorption as velocity determining step can separately as well as together dominate the gas permeation of a single membrane. This means, that for a binary or multi-component gas mixture, all gases or some of the gas species can follow a diffusion or adsorption dominated permeation behavior within a single porous membrane as a function of the nature of diffusing gas molecules (kinetic diameter, mean free path length), pores (effective pore size or distribution, adsorption properties, diffusion mechanisms), pressure and temperature.

For pressure-dependent permeation experiments at constant temperature (T), the flux (J_i) of a component (i) through a porous membrane ideally increases proportional to the applied pressure difference (Δp) between the feed and permeate side of the membranes, assumed for an ideal adsorption behavior (Henry's law). In this case, the mixed gas permeance (P_i) of a component (i) is invariant with increasing pressure difference, since the permeance is defined as the flux normalsied by the known pressure difference (Δp_i), as mentioned above. A deviation from this behaviour indicates a change of the dominating transport mechanism or adsorption behavior.

2.2.　　　　Carbon-based materials

Nowadays, carbon-based materials are used in a countless number of industrial and technological applications, e.g. in lubricants; brake manufacturing; refractories for steelworks, foundries or others; carbon brushes; pencils; graphite anodes in the processes of fused-salt electrolysis for the production of aluminium or alkali metals; as well as energy sector as part of batteries, or fossil carbon energy resources (coal or hydrogen) etc. [12,13,41,42]. The use of carbon-based materials in all of these applications is closely linked to the specific properties of carbon-based materials as a function of their large range of structural chemistry. Consequently, there is the same countless body of quotable literature that in the following chapter only a selected number of references are present to show the most important key points in the structural and chemical evolution of carbon-base materials, from amorphous or disordered materials to carbon in the crystalline state as graphite, for this dissertation.

The formation of carbon-based materials from any starting material (e.g. organic matter or synthetic organic polymers) is accompanied by a number of quite complex processes, i.e. carbonization and subsequent graphitization, **see Fig. 2**. In general, the processes of primary
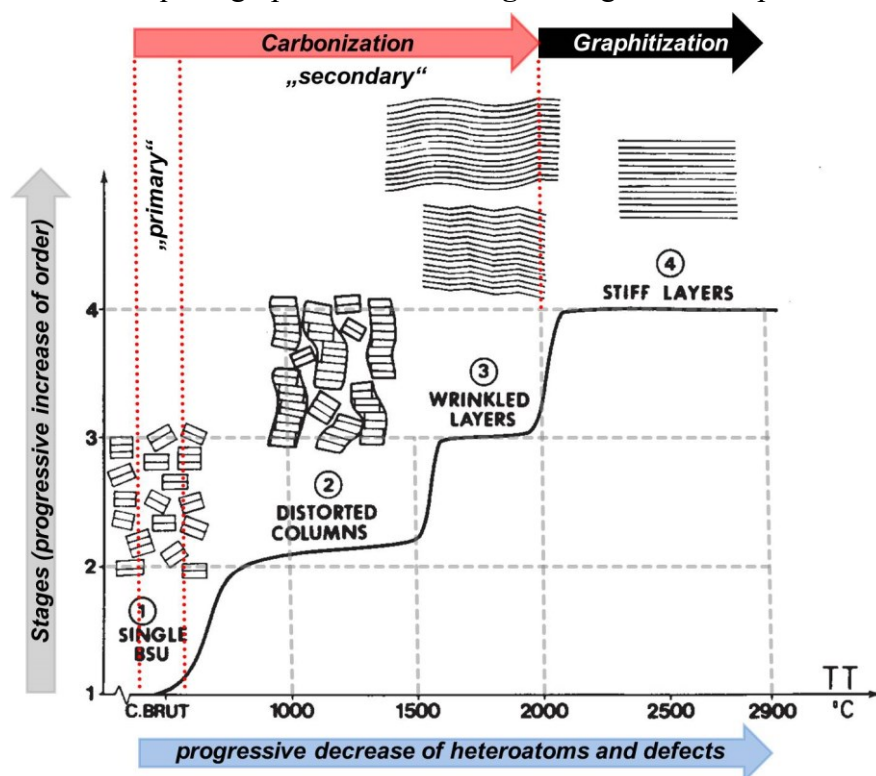

Figure 2: Schematic illustration of the structural evolution for a "graphitizing" carbonaceous material (e.g. anthracene-based precursor) passing "4 Stages" of order through high temperature treatment (HTT), adapted from Rouzaud et. al. (1989) [43], with permission. The added classifications of "Carbonization" and "Graphitization" and others being in accordance with Oberlin et. al (2012) [44].

and secondary Carbonization can be described by the progressively increase of structural order through 4 Stages accompanied by the chemical conversion of the used starting organic material (precursor) forming carbonaceous materials and finally carbon-rich materials ("pristine carbon") [44,43,45,46], **see Fig. 3a**. Here, only the nomenclature separates the processes of thermal conversion of a carbonaceous material in two keywords like "Coalification", accompanied by a progressive increase of pressure due to long-term metamorphism, and short-term "Carbonization" at ambient pressure due to laboratory or industrial conditions. Consequently, the same processes independently occurs until the final process of graphitization in the case of "Coalification" at much lower temperatures, approximately between 200°C and 700°C, than in the case of "Carbonization" with the need of "high temperature treatment" (HTT) up to 3000°C (**cf. Fig. 2 and 3b**). In the following chapter, it is shown that the formation of a specific microtexture in carbon-based materials (independent from the ability to be graphitizing or nongraphitizing) during "Carbonization" by HTT is primarily determined by the choice of starting materials (precursors), its related chemistry in terms of the quantity and kind of heteroatoms, and formation conditions.
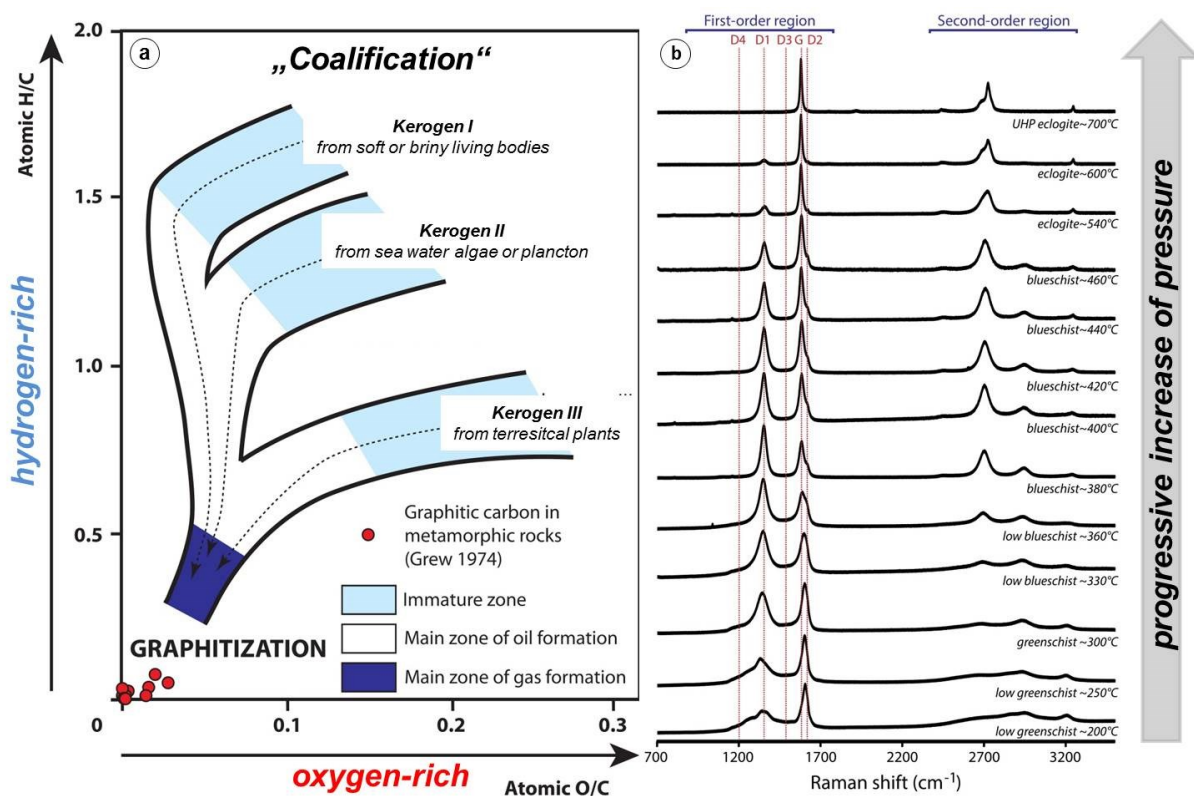

Figure 3: Chemical evolution from hydrogen-rich to oxygen-rich carbonaceous rocks (kerogen types I to III) shown in a "van Krevelen diagram" during processes from Coalification to Graphitization in (a), and Raman spectra of carbonaceous materials in metamorphic rocks with related "metamorphic facies" in (b). Indicated peaks in the first order region are marked in red, adapted from [46], with permission. General details of facies related pressures are taken from [47].

The general process of "Carbonization" can be intrinsically divided into the range of "primary Carbonization" by the formation of a carbonaceous material with a specific microtexture associated with the thermal conversion of an organic precursor (**see Fig. 4a**), and "secondary Carbonization" by the progressive development of the already formed microtexture of the carbonaceous material during primary Carbonization, **see Fig. 2**. The primary Carbonization is generally accompanied by "Softening" and "Solidification" of an organic precursor. The secondary Carbonization can be additionally subdivided into 3 Stages associated with different ordering processes which occurs in graphitizing as well as nongraphitizing carbon materials with the related difference in the size of the formed coherent microtexture [43]. For graphitizing carbon materials, further HTT up to 3000°C results into a fourth Stage which is commonly described by "Graphitization". Here, the process also occurs only for graphitizing materials which are able to form three-dimensional periodic structures (crystals), i.e. that of graphite, as shown in **Fig. 4b-d**.

2.2.1.   Primary Carbonization

As mentioned above, primary Carbonization corresponds with an increase of the carbon content and extends beyond the phase of "Softening" of an organic precursor (**see Fig. 4a**). The Softening occurs with the thermally induced release of condensable hydrocarbons and is mainly dominated by the quantity and kind of heteroatoms [44]. For a graphitizing organic precursor hydrogen (H) is the most important heteroatom. Here, the organic precursor breaks into smaller molecules with its maximum formation rate at the initial stages of primary carbonization and is related to a maximum of aliphatic C-H groups. Consequently, primary Carbonization ends with the absence of condensable hydrocarbons to be released accompanied with the "Solidification" of the evolved carbonaceous material between 460°C and 550°C. Therefore, primary Carbonization takes place only in a small temperature range between approximately 400°C and 600°C. Other heteroatoms commonly present in natural as well as synthetic organic precursors like e.g. oxygen (O), sulfur (S), nitrogen (N) or chlorine (Cl) have much higher thermal stability and disappear only at HTT of approximately 1400°C or higher, **see Table 1**. In comparison with the process of Coalification, the primary Carbonization covers the so-called "oil window" (white area) which corresponds to the main zone of oil formation in the "van Krevelen plot", **see Fig. 3a**. Consequently, the most important heteroatom of graphitizing carbons is hydrogen (H), whereas oxygen (O) and sulfur (S) are described as the most critical heteroatoms since both elements are described as strong
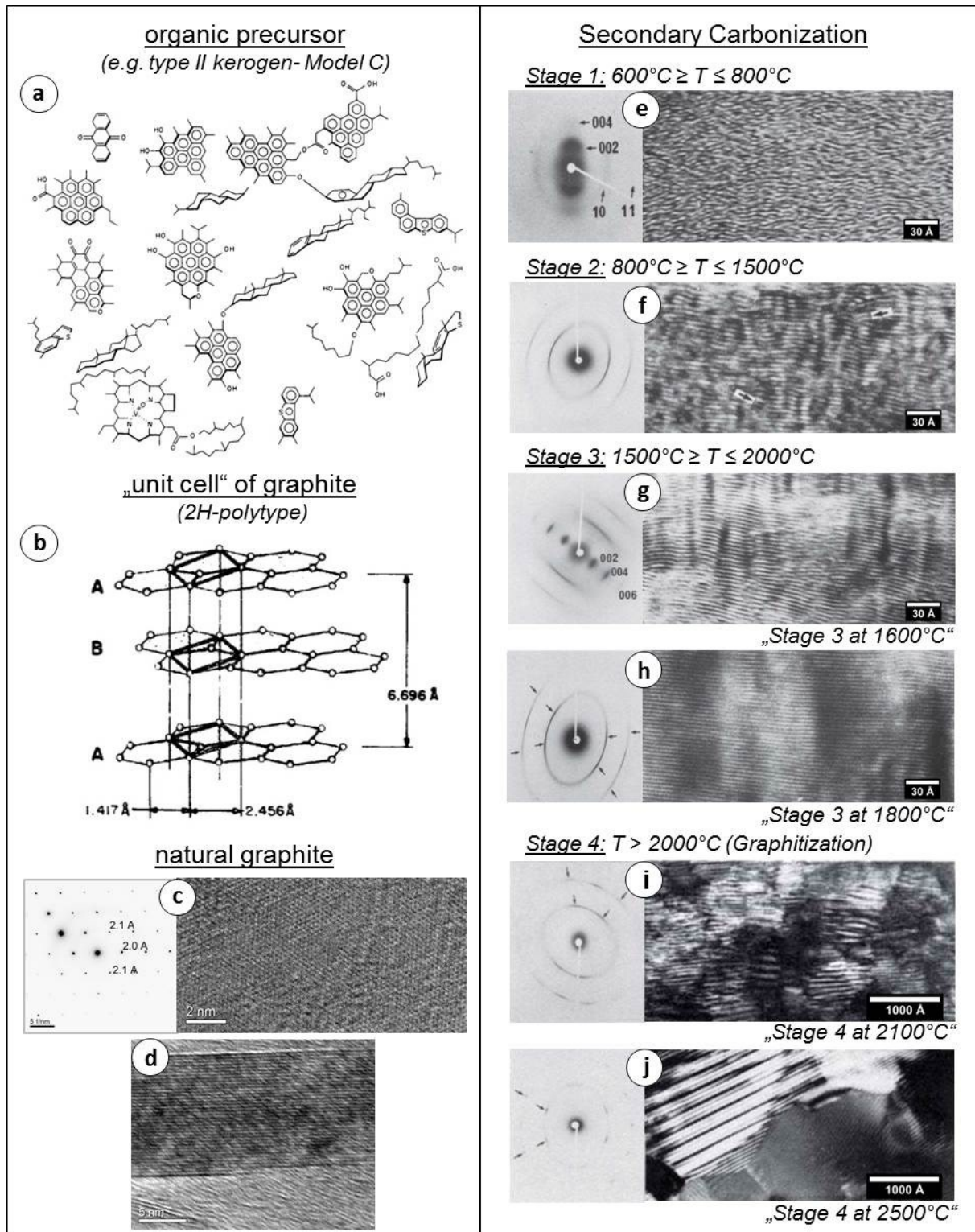
Figure 4: Overview of the most important aspects in the microtextural development for a graphitizing carbon-based material (e.g. anthracene-based precursor): an example of an organic precursor is demonstrated in (a), adapted from [48], with permission; the unit cell of 2H-polytpye of graphite is displayed in (b), adapted from [49], with permission; experimental data of a natural graphite crystal are displayed by "scanning transmission-electron microcopy" (STEM) micrograph (right) combined with related "selected area electron diffraction pattern" (SAED) micrograph (left) parallel to c_0 in (c), and parallel to a_0 in (d), measured in this work. Additional SAED and STEM micrographs are shown for ordering processes during secondary Carbonization in (e) to (j), adapted from [43], with permission.

Table 1: List of usually occurring heteroatoms (Elements) in starting materials (precursors) of carbon-based materials and its known thermal stability for several "heat treatment temperatures" (HTT) from literature [44].

Elements	starting materials (precursor)	HTT stability of heteroatoms	Ref.
H	aliphatic/aromatic compounds (e.g. anthracene)	600 to 1500°C	[43,44]
O	coals, coal-derived cokes, saccharose cokes, industrial resin-based products	$\geq$ 1500°C	[43,44,50]
S	coals, pitches	$\geq$ 1700°C	[51,52]
N	PAN-based carbon fibers	$\leq$ 1400°C	[53]
Cl	PVC- or PVDC-derived carbons	= 2000°C	[44]

"cross-linkers" [43,44]. As a consequence of high quantities of strong cross-linkers (e.g. O or S), the point of solidification can be shifted to lower temperature or even the phase of softening does not occur. The absence of material softening is an important characteristic of nongraphitizing precursors or carbonaceous materials accompanied by the formation of noncondensable gases that corresponds to the latter stage of solidification but with much higher heteroatom content before and afterwards of primary carbonization. For a graphitizing (anthracene-based) and nongraphitizing (saccharose-based) carbonaceous material, the development of atomic ratios for (H/C) and (O/C) during the release of heteroatoms through HTT is exemplarily shown in **Fig. 5**. Here, the progressive release of hydrogen until its minimum of (H/C: 0.03) for the graphitizing precursor at relative low HTT (< 1000°C) in comparison with the high variable change for the nongraphitizing precursor until its minimum of (H/C: 0.01) at high HTT (~ 1500°C) illustrates the difference of these precursors at best, **see Fig. 5a**. Furthermore, for the nongraphitizing precursor, the hydrogen release seems to be related with the release of the much higher content of oxygen, **see Fig. 5b**. This relation can be described by the quantity and kind of heteroatoms in the microtexture of carbonaceous materials or carbon-based materials.
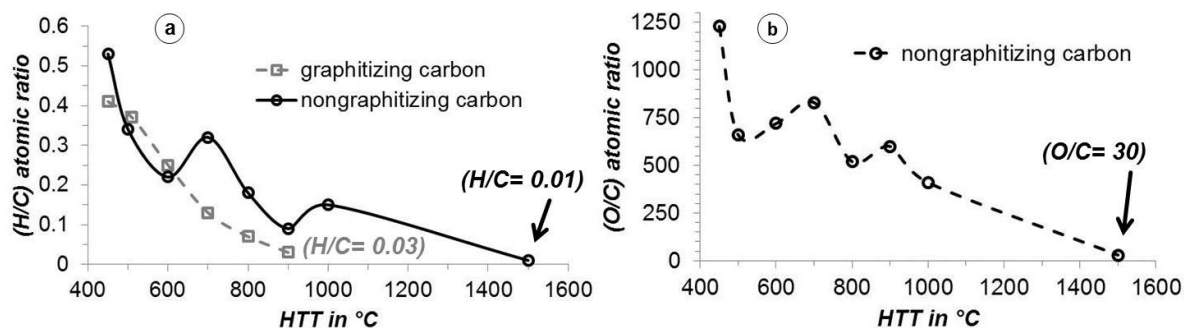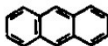
Figure 5: Development of atomic ratios for (H/C) in (a) and (O/C) in (b) during the release of heteroatoms (i.e. oxygen, hydrogen) for a graphitizing (anthracene-based) and a nongraphitizing (saccharose-based) carbonaceous material through high temperature treatment (HTT) up to 1500 °C in argon. Data are taken from [43].

During primary Carbonization, the formation of a specific "microtexture" from an organic precursor also begins with the softening. During the release of condensable hydrocarbons a viscous suspension can be formed in which heavier molecular fragments (e.g. aromatic hydrocarbons) are dispersed in a medium of smaller molecular fragments (i.e. condensable hydrocarbons). Here, the heavy molecular fragments are described as the so-called "basic structural units" or "BSUs" from which the specific microtexture of carbon-based materials is generally built (**cf. Fig. 4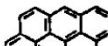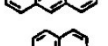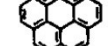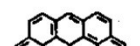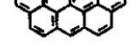a and Table 2**). The basic structural units are formed, e.g. at the expense of aromatic molecules already present in the organic precursor, with a random distribution in the carbonaceous material. Molecular mechanics calculations for various geometric arrangements and combination of polynuclear aromatic hydrocarbons in pitches (**see Table 2**) could show that the most probable arrangement in carbonaceous materials is the formation of coronene- (Ø: 9.2 Å) or ovalene-like (dimension: 9.2 x 11.6 Å) BSUs saturated at most by hydrogen [44,54]. For homologous as well as heterogeneous polynuclear aromatic hydrocarbons (BSUs), the association preferentially occurs "face to face" in a parallel shifted stack arrangement of 2 to 3 BSUs with a general displacement of 4.7 Å (**see Table 3**). The addition of a third or fourth BSU to an already formed stack leads to its orientation "perpendicular" (with its face to the edges) to the previous one. Furthermore, methyl groups seem to encourage the interaction between dissimilar polynuclear aromatic hydrocarbons (BSUs) by its preferential orientation inside the stacks.

Table 2: Single molecules of polynuclear aromatic hydrocarbons with different size and structure used in „Molecular mechanics calculations [54], shown in Table 2. With permission from Elsevier.

Structure	Name and molecular formula	Mol. wt. (g/mol)	Wt. % carbon	Wt. % hydrogen
	Benzene C_6H_s	78.11	92.26	7.74
	Anthracene $C_{14}H_{10}$	178.23	94.34	5.66
	Dibenzochrysene $C_{22}H_{12}$	276.35	95.62	4.38
	Coronene $C_{24}H_{12}$	300.37	95.97	4.03
	Ovalene $C_{32}H_{14}$	398.46	96.46	3.54
	Tetrabenzoovalene $C_{42}H_{16}$	546.64	96.68	3.32
	Dodecabenzocoronene $C_{54}H_{18}$	666.74	97.28	2.72

Table 3: Calculated energies for 4 configurations of homogeneous aromatic hydrocarbon dimers relative to the molecules at infinite separation, described in Table 1 [54]. With permission from Elsevier.

Hydrocarbon	Face-to-face	Shifted stack	Perpendicular	Edge-to-edge
Benzene	−0.6	−2.9	−3.0	−0.4
Anthracene	−3.5	−8.2	−7.9	−0.7
Dibenzochrysene	−7.8	−11.4	−8.4	−0.5
Coronene	−9.2	−11.2	−6.1	−0.2
Ovalene	−14.2	−16.8	−8.7	−0.3
Tetrabenzoovalene	−21.8	−26.2	−12.5	−0.5
Dodecabenzocoronene	−29.8	−33.0	−8.9	−0.1

Experimental analyses by different techniques revealed and therefore verifies for carbonaceous materials with relative low carbon content (~65 to 86 wt.-%) the occurrence of single BSUs randomly oriented in the materials (e.g. immature kerogens, coals, oil derivatives, saccharose- or resin-based chars etc.) in accordance with the previously described theoretical data. Small-angle neutron scattering of asphaltenes could show aromatic molecules of the size between 0.7 and 1.5 nm and molecule stacks of 1 nm or less in diameter [55,56]. Transmission electron microscopy (TEM) studies of thin amorphous and crystalline carbon films show the occurrence of BSUs (as described above) by small localized coherent domains with an general diameter of 1 nm or less [44,57]. Independent from the used diffraction technique (e.g. wide-angle x-ray diffraction-WAXRD, small-angle electron diffraction-SAED), all data show a more or less bright halo at about 0.2 Å^{-1} (4.6Å) [57–61]. Here, the halo position varies in the reciprocal space from 0.22 Å^{-1} related to a distance of 4.6 Å (for carbonaceous materials with a very low carbon content at about 65 wt.-%) to 0.24 Å^{-1} related to a distance of 4.1 Å (for carbonaceous materials with a very low carbon content of less than 86 wt.-%) [44]. Nevertheless, analyses of the carbonaceous materials by spectroscopic methods (e.g. UV, VIS, IR, ESR, TPD-MS, HRTEM, or neutron diffraction technique) at that stage show that heteroatoms like H, O, N, S, or Cl are grafted at the edges of BSUs by various kinds of possible functional groups in relative large amounts, see subsection of "Functional groups"[44,62–74]. Here, the thermal stability of functional groups located at the edges of BSUs prevents a further association of BSUs into larger coherent scattering domains which corresponds to a rather low carbon content of about 65 to 86 wt.-%.

The limit of BSUs with a random orientation within the carbonaceous material is described by the sudden occurrence of BSUs organized in areas of "local molecular orientation" (LMOs) due to the further release of heteroatoms [44]. It occurs shortly before solidification at the point of the minimal release of condensable hydrocarbons and maximum of aromatic ones. Here, the carbon content reaches values higher than 86 wt.-%. At first, the coronene- or

ovalene-like BSUs are mainly organized in stacks of 2 to 3 layers. These stacks suddenly start to cluster by self-organization into areas of BSUs almost in preferred parallel orientation (LMOs). The BSUs already have a misorientation by tilting and twisting of the layer in the range of 20 to 40 degrees. This process is observed in TEM micrograph by clustering of the bright scattering domains (BSU with random orientation) into areas of roughly isometrical shape only limited by digitized contours (LMOs) of various diameter from 50 Å (detection limit here) up to several micrometers (> 2000 Å). The BSUs form a columnar texture with a limited number of fringes (BSUs). Here, the content of critical heteroatoms like strong cross-linkers (O or S) plays also an essential role which can hinder the BSUs with a random orientation to be self-organized into LMOs as function of its heteroatom content **see Fig. 6a**. The critical atomic ratio of residual heteroatoms (O+S)/H of carbonaceous materials seems to be at about 0.1, **see Fig. 6b**. For atomic ratio below 0.1, the size drastically increase with the decrease of cross-linking heteroatoms, whereas for an atomic ratio above 0.1 leads to the formation of very small LMOs or is related to their absence. This is in complete accordance with the data present in **Fig. 3** observed in natural systems.

Furthermore, the sudden occurrence of BSUs within areas of LMOs is accompanied by the sudden formation of a well-defined 002 reflection at about 0.28 Å^{-1} (3.6 Å) in diffraction experiments without the appearance of hkl reflections. Here, only broad relfections (haloes) in the reciprocal space at 0.5 Å^{-1} (2.13 Å) and 0.8 Å^{-1} (1.23 Å) related with hk0 reflections are observed for carbonaceous materials at the end of primary Carbonization (HTT ≤ 600°C), **see Fig 7a** [75,44,43]. Theoretical data numerically calculated by Debye radial distribution functions of randomly oriented aromatic molecules could show that the occurrence of two
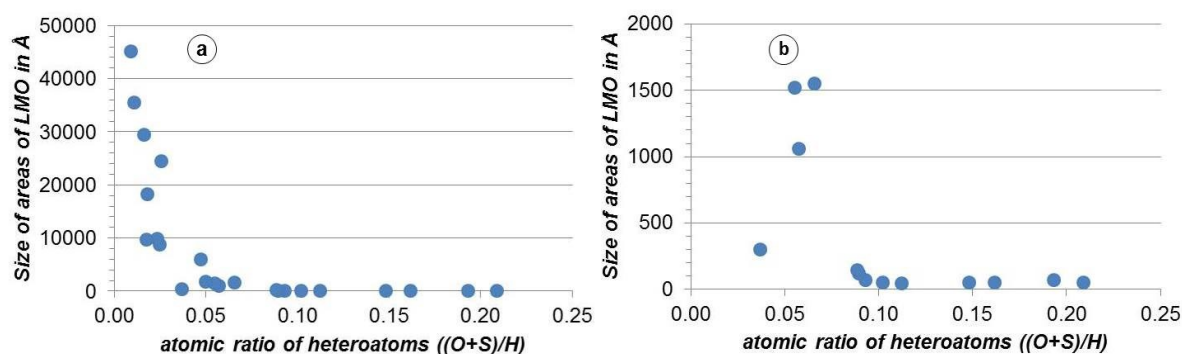
Figure 6: Comparison of the size of "local molecular orientation" (LMOs) as a function of the residual heteroatom content plotted as atomic ratio ((O+S)/H) in (a) for the full data set and in (b) for the first data points at relative high atomic ratio of heteroatoms, determined at their occurrence at about 1000°C. Shown data are from [44] which based on [76,77].
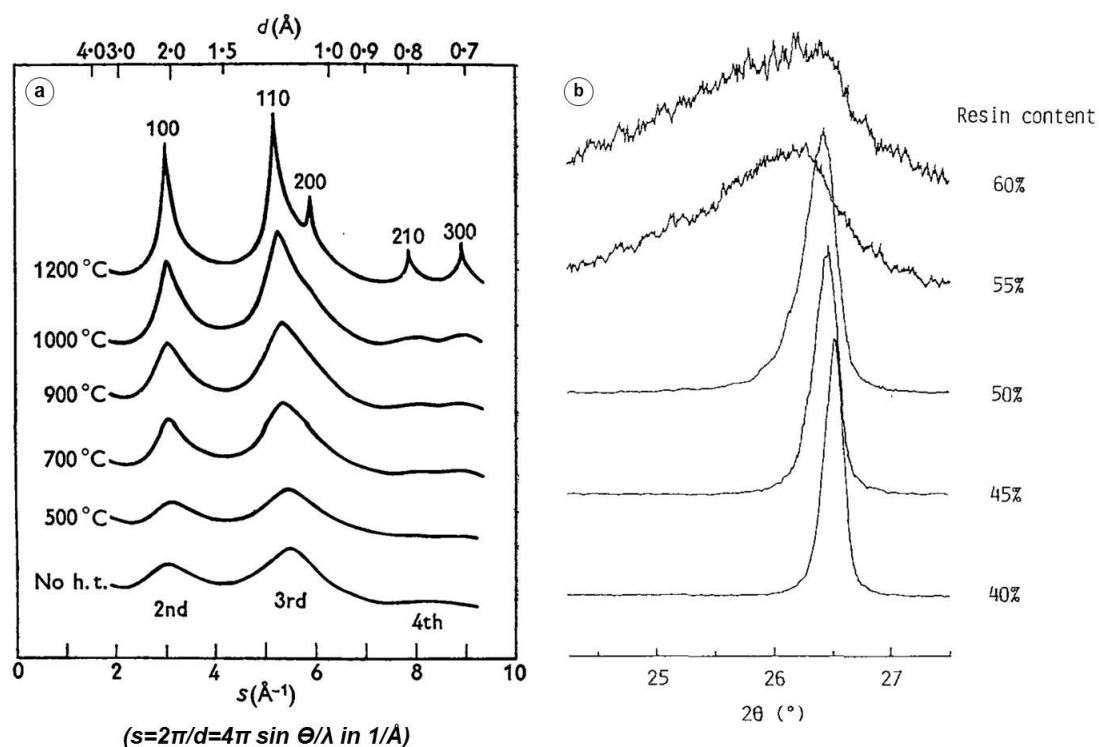
Figure 7: Experimental X-ray diffraction data of evaporated carbon films deposited at room temperature and high temperature treated (HTT) from as-deposited state to about 1200°C (Adapted from [75,78], with permission) in (a), and X-ray diffraction profiles of 002 line of graphitizing and nongraphitizing precursor mixtures after HTT at 3000°C (Adapted from [79], with permission) in (b).
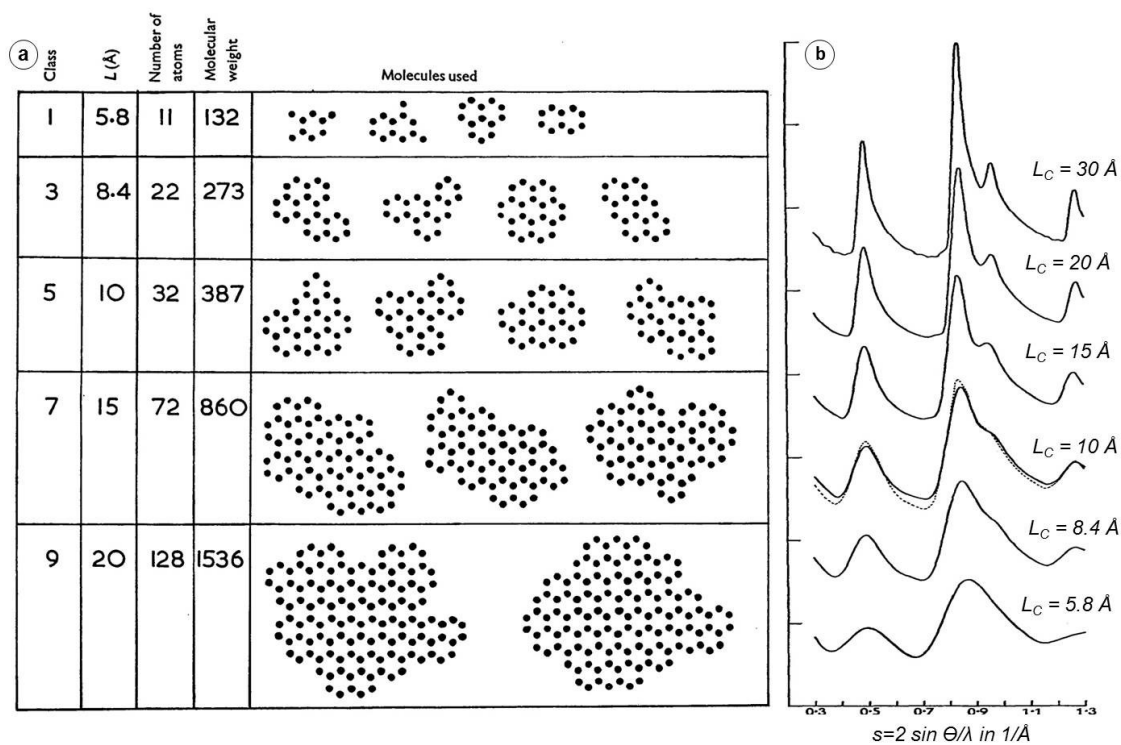
Figure 8: Theoretical approach of single molecules of aromatic hydrocarbons with different lateral dimensions (sizes) from 5.8 Å to 30 Å are displayed in (a), and diffraction patterns calculated from theoretical data of related single molecules in (b). (Adapted from [60], with permission)

additional broad reflection bands results from the two-dimensionality of aromatic molecules (BSUs) as a function of various size in lateral dimensions, **see Fig. 8a** [60,61]. The calculated data for x-ray diffraction of randomly oriented single aromatic molecules (BSUs) of increasing size between 5.8 Å and 20 Å results in the formation of hk0 peaks related to intralayer distances known from graphite, **see Fig. 8b and Table 4**. Here, only broad halos near the 10 and 11 are present whereas 00l or hkl related to three-dimensional-order in graphite as well as for the 002 reflections at 0.298 Å^{-1} (3.35 Å) are systematical not visible between incident beam and 0.469 Å^{-1}. The data show for lower aromatic molecule sizes that the number of peaks is reduced, **cf. Table 4 and Fig. 8b**. For example, an aromatic molecule with a lateral dimension of 20 Å can generate hk0 relfections related to 10, 11, 20 and 30 are observed whereas for an smaller aromatic molecule (coronene-like) with an lateral dimension of about 10 Å only hk0 reflections related to 10 and 11 are present with a low intensity.

Comparable to that observations, for different carbonaceous materials the occurrence of LMOs is generally located in the temperature range of 460 to 475 °C for a carbon content of about 85.5 5 to 88.7 wt.-%. Between the sudden occurrence of BSUs in area of LMO and solidification of carbonaceous materials the described LMOs grow by coalescence until maximum of anisotropy is reached. The temperature of LMO occurrence decreases with the increasing content of cross-linking heteroatoms to 430 °C or the absence of LMO formation [44]. The absence of LMO formation is simultaneously related with the solidification of such a material. These circumstances reveal the biggest difference of graphitizing and

Table 4: Experimental data of Interference Function I(s) of single aromatic molecules (e.g. "BSUs") of increasing size compared with calculated data of graphite. Reciprocal data of distances are shown for s= 2 sin Θ/λ in 1/Å. Data are taken from [44] which based on [60].

Peak number	s in Å^{-1}			calculated data of graphite		
	single Coronene layer of 24 C atoms	single Ovalene layer of 32 C atoms	aromatic layer of 288 C atoms	s in Å^{-1}	hkl	d_{hkl} in Å
1	-	-	-	0.298	002	3.35
2	**0.48**	**0.489**	**0.488**	**0.469**	**100**	**2.13**
3	-	-	-	0.596	004	1.68
4	**0.85**	**0.848**	**0.838**	**0.813**	**110**	**1.23**
5	-	0.93	0.963	0.939	200	1.06
6	-	> 1.30	1.275	1.422	300	0.70
7	-	-	-	1.626	220	0.62

nongraphitizing carbon materials, as mentioned in the first sentences to primary carbonization, with the related difference in the size of the formed coherent microtexture. Here, x-ray powder diffraction (XRPD) data of defined mixtures of a graphitizing (benzene-soluble pitch) and nongraphitizing (phenolic resin) precursor displays at best, the serious effect of the presence of strong cross-linking heteroatoms shown by the evolution of the 002 diffraction peak after HTT at 3000 °C, **see Fig 7b**. For a resin content (nongraphitizing precursor) from 40 to 50 % the 002 reflection modulates to lower diffraction angles (so to higher d values) and transforms its discrete shape into a broad reflection band at 55%.

Additionally, in the case of hydrogen-rich precursor (e.g. typically found in pitches), the arrangement of LMOs into larger areas can take place by its organization into the so-called "Mesophase" which is described as "columnar liquid crystals" [44,80–82]. The Mesophase is classified by its lateral dimensions. The so-called Mesophase A consist of spheres in the range of 5 to 10 µm with an spherical arrangement of the BSUs, also with an columnar texture with fringe sizes of ≤ 1 nm. Intermediate forms Mesophase A with LMOs are described as Mesophase B with the dimensions of about 350 nm to 1 µm or Mesophase C with the dimensions of about 200 to 350 nm with a more ellipsoidal shape. In the case of Mesophase, the BSUs are still associated face to face in long distorted columns without any lateral coherence as present for other carbonaceous materials only at HTT at about 1500 °C (secondary Carbonization), **see Fig. 4f**. In the mesophase the BSUs are still associated face to face in long distorted columns without any lateral coherence.

The process of primary Carbonization finally ends with the "Solidification" of the formed carbonaceous material. For a graphitizing carbonaceous material, solidification generally occurs in the temperature range between 460°C to 600 °C related to a carbon content of about 92 to 95 wt.-%, atomic ratio of H/C of about 0.5 for the most graphitizing materials, and is related to infinite microhardness [44,58,76,82]. For a nongraphitizing carbonaceous material, solidification can occur at much lower temperatures, as mentioned above. In Coalification, the state of solidification is reached by the end of the release of condensable hydrocarbons, the formation of noncondensable gases begins by the release of residual heteroatoms (begin of main zone of gas formation), and atomic ratios of H/C ≤ 0.5 and O/C < 0.1, **see Fig. 3**. During the Solidification, the areas of LMO of BSUs still growth into domains of medium to fine mosaics wheres merging of the Mesophase spheres (growth) occurs by coalescence of LMOs into larger domains with a random orientation in the bulk "mosaic texture" which introduces defects. This defects are described as "disclinations which implies the occurence of discotic

molecules which are free in rotation and tilting, as described for "liquid crystals" [44,83,84]. Disclinations are described as "three-dimensional dislocations" able to break the local structure or lattice before removing or adding a line of C atoms that makes the carbonaceous material very flexible or plastic which explains the possibility of folded layers in the absence of carbon pentagons or heptagons as known from fullerenes during "secondary carbonization" [85,86]. Solidification is an important step at the end of primary Carbonization since it precedes the occurrence of the "turbostratic order".

2.2.2.   Secondary Carbonization

In nature, secondary carbonization does not occur by the impact of high pressure or stress so that a graphitizing carbonaceous material directly starts to graphitize after Coalification, **see Fig. 3b**. In the absence of high pressure or stress, the process of secondary Carbonization is characterized by the progressively release of residual heteroatoms mainly as volatiles associated with the progressively increase in carbon content of the carbonaceous material from about 92-96 wt.-% up to 100 wt.-%. The increase of HTT and the progressive release of heteroatoms are strongly related to the presence of ordering processes in the range of 600°C to 2000°C before graphitization occurs, **see Fig. 2**. For oxygen-rich precursors, functional groups containing e.g. "ether groups" seem to maintain its oxygen-based functional groups even to high HTT, **see Table 1**. The release of heteroatoms (e.g. O, S, or Cl) is related with the formation of "dangling bonds", i.e. the concentration of free unpaired electrons increases, detectable by "Electron Spin resonance" (ESR) and depends on the quantity and kind of functional groups still present in the carbonaceous material [44,58,87]. The maximum of free electron concentration generally occurs at the end of solidification and decreases during secondary Carbonization. The decrease of formed "dangling bonds" is related with the recombination of free bonds between neighboring BSUs during the increase of carbon content. The progressive recombination of free electrons can result in a decrease of the size and concentration of already formed columns in areas with LMO. However, all processes which are described in the following section are progressive and does not occur at a sharp or precise point as a function of HTT, residual heteroatoms (functional groups) and microtexture already formed at the end of primary Carbonization. During secondary Carbonization, the "turbostratic order" is formed by the expense of the described areas of LMO, as described in primary Carbonization, through the further alignment of BSUs to each other [44,45,81,88,89].

Theoretical and experimental basics: Carbon-based materials

During primary Carbonization the formed stacks consists of BSUs with a general misorientation in the range of 20 to 40 degree, as mentioned above. By the formation of the turbostratic order, the misorientation of BSUs is reduced to very small rotational displacement of about 1 degree or less. Each turbostratic stack can be aligned in azimuthal disorder to each other. In diffraction patterns, this process is accompanied by the progressive development of the previously described broad halos at about 0.5 Å^{-1} (10 band) and 0.8 Å^{-1} (11 band) into discrete hk0 reflections related with the occurrence of the 00l or hkl reflections (e.g. 002) similar to graphite, **cf. Figs. 4e and 7a**. The turbostratic order is mainly associated with a carbon content of higher than 94 wt.-%. The maximum diameter of turbostratic stacks does not exceed more than 95 Å [43,44,90], and finally disappears at the end of secondary Carbonization. The occurrence of the turbostratic order is directly related to the occurence of the hk0 reflections in diffraction data which results in the formation of discrete nodes of graphite (graphitization), **cf. Figs. 4e-j with 4c**.

In the following, the microtextural evolution during secondary Carbonization is mainly described by the examples of the thermal conversion of a graphitizing anthracene-based (C$_{14}$H$_{10}$) carbonaceous materials but also occurs in other dimensions for a nongraphitizing saccharose-based (C$_{12}$H$_{22}$O$_{11}$) one, **see Fig. 2 and Fig 4e-j** [43]. Here, the results of TEM studies for the microtextural evolution during secondary Carbonization is displayed by STEM micrographs and related SAED patterns. The microtextural evolution passes through three Stages whereas the first stage is already initiated in the range of primary Carbonization by the formation of BSUs with an random orientation as well as their formation into area of LMO, **see Fig. 2**.

For the graphitizing anthracene-based precursor, **Stage 1** is related with the heteroatom release of aromatic CH groups, oxygen or other heteroaotms for the graphitizing or nongraphitizing carbonaceous materials, and extends the temperature range of about 500°C to 800 °C (low HTT), **cf. Figs. 2, 4e and 5**. TEM micrographs show the BSUs are isometric in shape with a diameter of less than 1 nm and thickness. The BSUs are arranged into stacks with a number of fringes (*N*) up to three (BSUs) with an average misorientation (*β*) of the observable fringes (BSUs) of about 21 degree at the beginning of Stage 1 (LMO formation) or be randomly oriented as single BSUs, **see Fig. 9a-b**. At the end of Stage 1, the average misorientation (*β*) of BSUs in a stack is reduced to 13 degrees accompanied with a strong decrease in their interlayer distances (*d$_{002}$*) so-called here as "interfringe spacing spreading
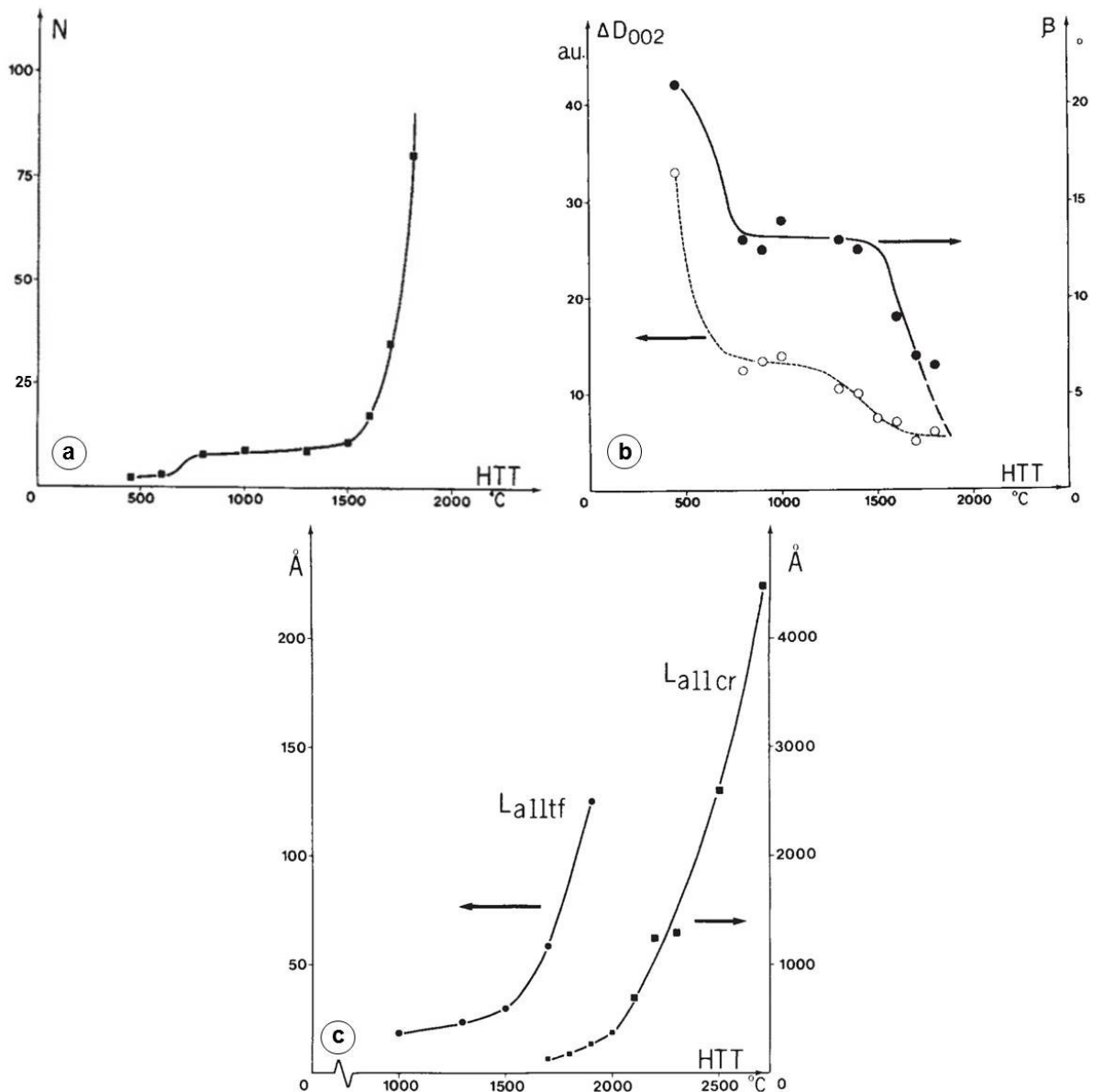
Figure 9: Experimental data of the microtextural evolution of a graphitizing carbonaceous precursor (anthracene-based) during secondary Carbonization of the number of fringes (N) related to the BSUs within a stack in (a), the average of interfringe (interlayer) spacing spreading (ΔD_{002}) and average misorientation of the fringes (BSUs) in (b), and the length of fringes related to the turbostratic order (L_{a11tf}) and coherent domains with homogenous fringes related to a hexagonal symmetry (L_{a11Cr}), adapted from [43], with permission.

(ΔD_{002})", **see Fig. 9b**. **Stage 2** is related with the release of interlayer defects between superimposed BSUs and extends the temperature range of about 800°C to 1500°C. At the beginning of Stage 2, BSUs coalesce in a "face to face" arrangement which results in the formation of distorted columns, **cf. Figs. 2 and 4f**. The coalescence of BSUs results in a rapid increase of number of fringes (N) from three up to 8 or 10, **see Fig. 9a**. The lateral growth of the distorted columns is inhibited by the presence of misoriented BSUs as shown in **Fig. 4f**, marked by arrows or observed in the area above the scale bar. Single BSUs are trapped

between the small distorted columns related to the imperfect arrangement between adjacent layers. Consequently, the average misorientation (β) of BSUs remains stable, **see Fig. 9b**. Therefore, the lateral dimension of the distorted columns (L_a) remains almost stable and equal to the size of the initially formed BSUs, **cf. Stage 1 and Fig. 9c**. In the progress of **Stage 2** with increasing HTT, the number of misoriented single BSUs and the interfringe spacing spreading (ΔD_{002}) slowly decreases. Here, the end of Stage 2 is characterized by the disappearance of misoriented BSUs. Stage 3 is related with the release of in-plane defects by the lateral coalescence of distorted columns in a "edge to edge" arrangement and extends the temperature range of about 1500°C to 2000°C, **cf. Figs. 2 and 4g**. At the beginning of **Stage 3**, the distorted columns are still arranged as in the initial Stage of their formation. During the further progress of HTT, the thickness of columns considerable increases by the disappearance of misoriented single BSUs which results in a fast increase in the number of fringes (N), **see Fig. 9a**. The average misorientation (β) of BSUs and their interfringe spacing spreading (ΔD_{002}) decrease to its observed minimum, **see Fig. 9b**. Here, the considerable decrease of distortions of the BSUs is responsible for the high decline of the average misorientation (β) of BSUs in a column. Additonally, adjacent columns are able to coalesce with a strong increase in its lateral dimension of the distorted columns (L_a) but their distortions remain in the size or diameter of BSUs, **see Figs. 9c**. Here, the length of fringes related to the turbostratic order (L_{a11tf}) moderately increase. In the same Stage coherent domains with homogenous fringes related to a hexagonal symmetry (L_{a11Cr}) starts to occur which display the transition from the turbostratic order, **see Fig. 9c.** At the end of Stage 3, the column distortions are progressively annealed related to the occurrence of increasing 00l order, **cf. Figs. 9c and 4h**. The lateral coalescence of the distorted columns results into the formation of distorted continuous layer stacks. Here, very weak modulations of the 10 and 11 relfections starts to appear at 1900°C related with the occurrence of coherent scattering domains localized in space becomes visible in 11 DF images, not shown here. It is important to notice that until the end of secondary Carbonization which is equal to the end of Stage 3 no graphitization occurs in the thermal conversion of carbonaceous materials until 2000°C. The occurrence of the described Stages related to ordering processes depends on the type of defects present.

In the case of the nongraphitizing saccharose-based carbonaceous material, the microtextural evolution during secondary Carbonization also occurs by the same three stages described previously. Here, the only difference is due to the size of formed BSUs and their organization

into LMOs of about several nanometers (e.g.: < 10 nm) until their absence related to large amounts of strong-crosslinkers (heteroatoms) at the end of primary Carbonization. The final diameter of the formed stacks is limited by the initial extensions of formed LMO, **see Fig. 10**. The previously described Stages and order processes occur only inside the formed areas of BSUs in LMO. During the release of heteroatoms also at high HTT the diameter of LMO remains constant whereas approximately their thickness is reduced by the decrease of the average misorientation (β) of BSUs as well as interfringe spacing spreading (ΔD_{002}). Consequently, through the release of heteroatoms a characteristic porosity can be formed related with the missing coalescence and orientation of BSUs into a dense material, generally described by a "crumbled sheet of paper" model, **see Fig. 10a**. Here, the pores in Carbon-based materials can have an irregular entangled shape due to the microtexture which is commonly described as "slit-shaped" [66,91,92].
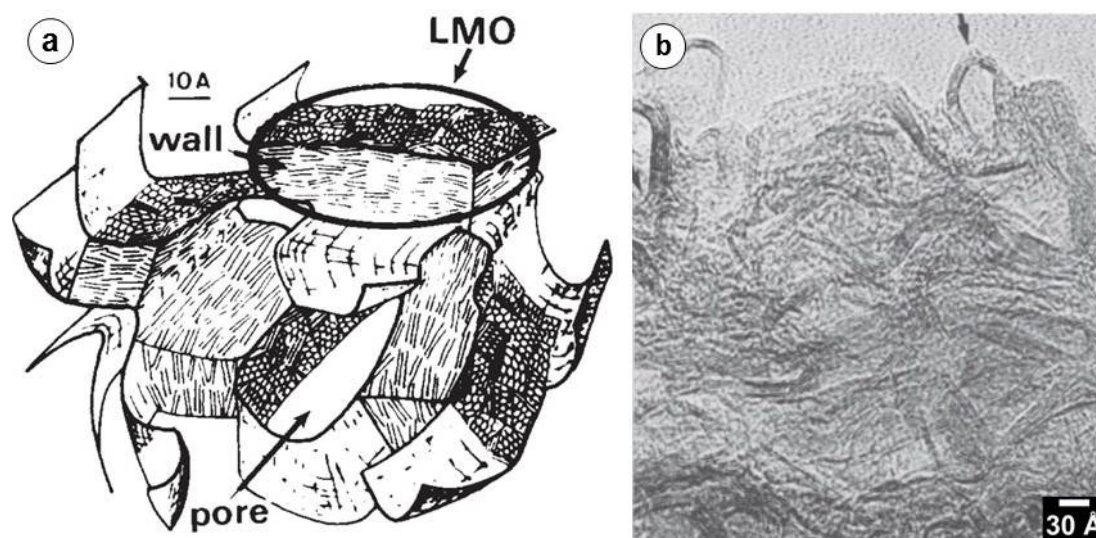
Figure 10: Schematic illustration of the microtexture of nongraphitizing carbons with sketched LMOs (marked region) in (a) and STEM micrograph of a nongraphitizing carbon (e.g. saccharose-based precursor) after a high temperature treatment (HTT) at ~3000°C in (b), adapted from [43], with permission.

2.2.3. Graphitization

The thermal induced process of Graphitization only begins for graphitizing materials slightly above 2000°C by the progressive development of a three-dimensional periodic order, **see Fig. 2** [44]. Here, the general described process of Graphitization is in accordance with the Stage 4 which subsequently extends the temperature range of about 2000°C to 3000°C [43]. At this Stage, the formed layers are stiff and perfect due to the successively disappearance of heteroatoms, interlayer and in-plane defects, **see Fig. 4c-d**. The average

misorientation (β) of BSUs and their interfringe spacing spreading (ΔD_{002}) are decreased to zero, **see Fig. 9b**. **Stage 4** (Graphitization) is related to the occurrence of crystal growth by the expense of the turbostratic order, **cf. Figs. 9c and 4i**. The diameter of coherent scattering with a hexagonal symmetry of graphite strongly increases accompanied with the modulation or sharpening of hk lines into hkl reflections, **cf. Figs. 4i-j and 4c**. At the end of Graphitization, the size and dimensions of the formed graphite crystals is almost the same of the areas with LMO after solidification. The degree of graphitization is described by numerical values of P_1 which is only obtained by the continuous evolution or modulation of the 11 (hk0) reciprocal line in diffraction patterns, **cf. Figs. 4i-j and 4c** [44,89,93–96]. Both hk bands generally observed with the occurrence of the turbostratic order of 10 and 11 modulate up to discrete nodes near the final position of hkl reflections near 101 or 112 of graphite, respectively. For calculations of P_1, only the 11 band is taken into account since the 10 band is described to be sensitive to stacking faults. Other parameters like the interlayer spacing (d_{002}), thickness of a bright domain (L_C) or length (La), or number of fringes in a stack of BSU (N), as described by TEM studies for the previous stages in secondary Carbonization, are not sufficient enough because their variations occur in the same manner and earlier for nongraphitizing materials. For example, the relation between the interlayer spaces (d_{002}) as a function of P_1 can show a sufficient correlation to distinguish between materials between a P_1 of 0.1 and 0.8 but loses its significance between a P_1 value of 0.3 and 0.8 by a minimal change in d_{002} of 3.38 Å to 3.36 Å. Therefore, the degree of graphitization described by P_1 is related with the probability of layer pair with a stacking sequence of graphite, e.g. the 2H-polytype (AB), with an interlayer spacing (d_{002}) of 3.35 Å. Here, P_1 can variate for thermal induced graphitization from 0.10 with a related interlayer spacing of 3.43 Å (e.g. saccharose-based nongraphitizing precursor) to 0.75 (max. 0.8) with a related interlayer spacing of 3.36 Å (e.g. polyvinyl chloride-based graphitizing material). The value of P_1= 1.0 is defined for natural graphite formed by long-term metamorphism. Here, experimental data show for e.g. polyvinyl chloride-based materials that a value of **P1** equal to 1.0, as described for natural graphite, is not reached by the HTT stability of heteroatoms such as oxygen (O) and chlorine (Cl), **see Table 1** [44,97]. Nongraphitizing materials are in the range of 0.0 to 0.1 that is not a significant value. So the data from literature show that the extent and development of graphitization is mainly limited by the quantity and kind of heteroatoms (i.e. strong cross-linkers) stable up to HTT at 3000°C, as already described for
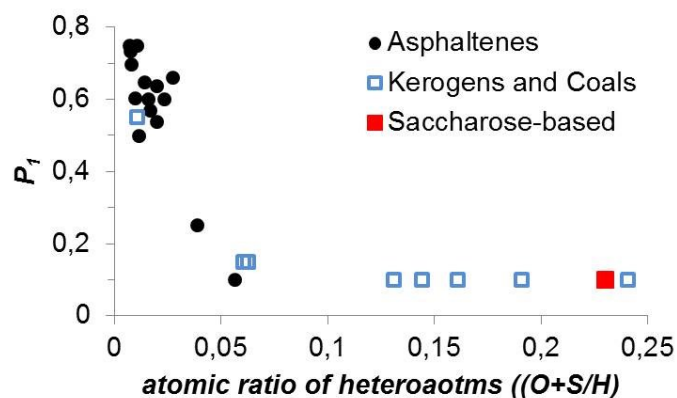
Figure 11: Comparison of the P_1 (degree of graphitization) as a function of the residual heteroatom content plotted as atomic ratio ((O+S)/H). Shown data are from [44] which based on [98,99].

the initial steps of primary Carbonization, **cf. Figs. 6a and 11.** In the case of the nongraphitizing saccharose-based carbonaceous material, the microtextural evolution during Graphitization also forms stiff and perfect layers within the areas of LMO, as described for secondary Carbonization. The thermal induced changes during HTT up to 3000°C results in the formation of stable grain boundaries of small coherent domains beside distortion that cannot be annealed further [43]. Here, the graphitization is also limited to the areas of LMO so that the process individually occurs in each LMO. As a result of this localized graphitization, the pores previously formed, during the release of heteroatoms become polyhedral (*Polygonization*), **see Fig. 10b** [43–45,81].

2.2.4. Functional groups

As mentioned above, the quantity and kind of functional groups present in a carbonaceous material mainly depends on its precursor and can be subsequently modified by various aftertreatments (physical or chemical activation) using diverse oxidizing media (gaseous media: H_2O, CO_2, O_2, or other media: acids, alkaline solutions, or zinc chloride etc.) as described for the huge class of "activated carbons" [64–66,100].

Carbon-based materials are mainly dominated by heteroatoms of hydrogen- and oxygen-containing functional groups which are commonly located at the edges of BSUs, **see Fig. 12**. The functional groups can be classified into "chemically active" and "chemically inactive" functional groups. Here, the "chemically inactive" groups are commonly assigned to terminal carbon or hydrogen in polynuclear aromatic hydrocarbons (BSUs). The "chemically active" functional groups are assigned to oxygen-containing functional groups with characteristics of

a solid acid or base in terms of the Brønstedt "acid-base concept", **see Fig. 13**. In this concept, mainly high reactive carboxyl- and anhydride, moderately reactive lactone and other ether groups, and weak reactive phenolic and carbonyl groups are described with an acidic
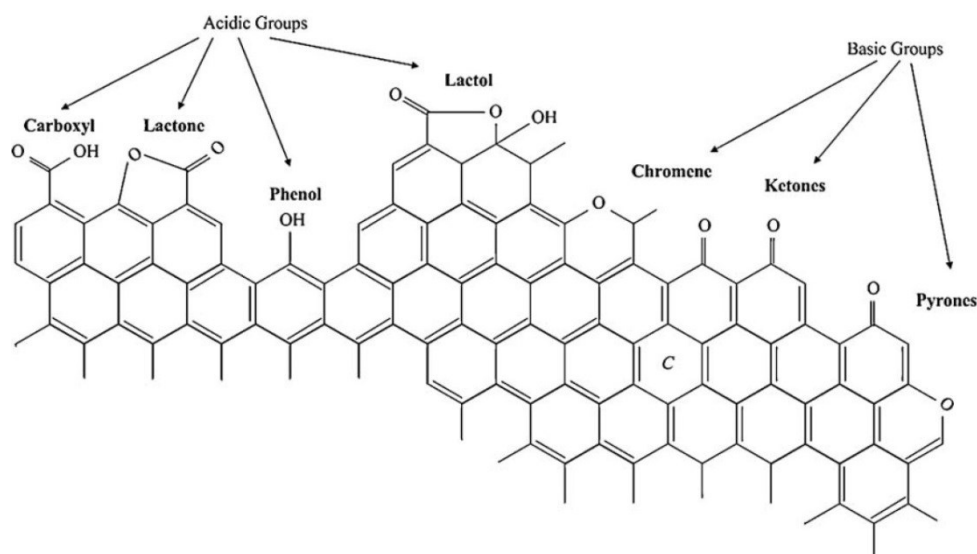

Figure 12: Schematic illustration of some examples for oxygen-containing functional groups located at the edges of BSUs generally classified into groups with acidic and basic functions, adapted from [68], with permission.

character whereas quinoidic and pyrone (superquinoidic) structure are assigned to a high reactive basic character. Their thermal stability is inversely related to their reactivity, this means that the e.g. carboxylic- and acid anhydride groups with a high reactivity have a low thermal stability up 500°C to 700°C whereas phenolic and carbonyl groups of weak reactivity are stable above 900°C [65,67,70]. Finally, only a small number of heteroatoms or functional groups are chemically accessible for reactions of acid-base character or substitution. Here, surface functional groups at primary Carbon particles can result in significant aggregation phenomena of Carbon that can form a large number of meso- and macro-pore volumina related with many application properties [65]. In all of these publications mentioned here, the functional groups are generally described and analyzed in terms of "surface functional groups" present or synthetically generated for further characterization. As previously described (see "primary Carbonization"), graphitizing and nongraphitizing carbonaceous materials mainly differs in their quantity and kind of strong cross-linking heteroatoms (e.g. oxygen). The ability of the formation of cross-links during the initial stage of primary Carbonization is of essential importance for the development of a certain microtexture related to the physical and chemical properties of carbon-based materials (e.g. conductivity, adsorption behavior, porosity etc.). From the discussion of experimental of TPD-MS data, it can be concluded that the formation of cross-links, especially of oxygen-containing functional

groups, originates from secondary reactions of functional groups during low HTT in the temperature range between 50°C and 300°C (initial stage of primary Carbonization) [67,70]. The cross-link formation is related to the reaction of neighboring functional groups and is accompanied by the release of water (dehydration), e.g. a carboxylic acid and a phenol group form a lactone group, or two phenol groups form an ether group. Consequently, these secondary reactions (among others) can occur within one and/or between several BSUs or their initial fragments before, present in the precursor. To illustrate the complex interplay of interlayer crosslinks between BSUs, as mentioned above, the microtexture of two Pyrocarbon (PyC) is exemplarily described in the following, **see Fig. 13** [69,89,101,102]. The Snapshots of enlarged atomistic models for a high-textured "rough laminar" (RL) and high textured "regenerative laminar" (ReL) Pyrocarbon (e.g. comparable with soot) show the atomic arrangement present as synthesized at 1050°C [69]. The two Pyrocarbons (PyCs) are synthesized by the conversion of aliphatic hydrocarbons deposited on a substrate using propane (for ReL) or a methane/propane mixture (for RL) as precursor. For RL and ReL PyCs, the only heteroatom is hydrogen present at about 0.7 at.-% or 2.5 at.-%, a size of BSU of about 5 nm or 2.7 nm, and a interlayer distance (d_{002}) of 0.345 nm or 0.346 nm,
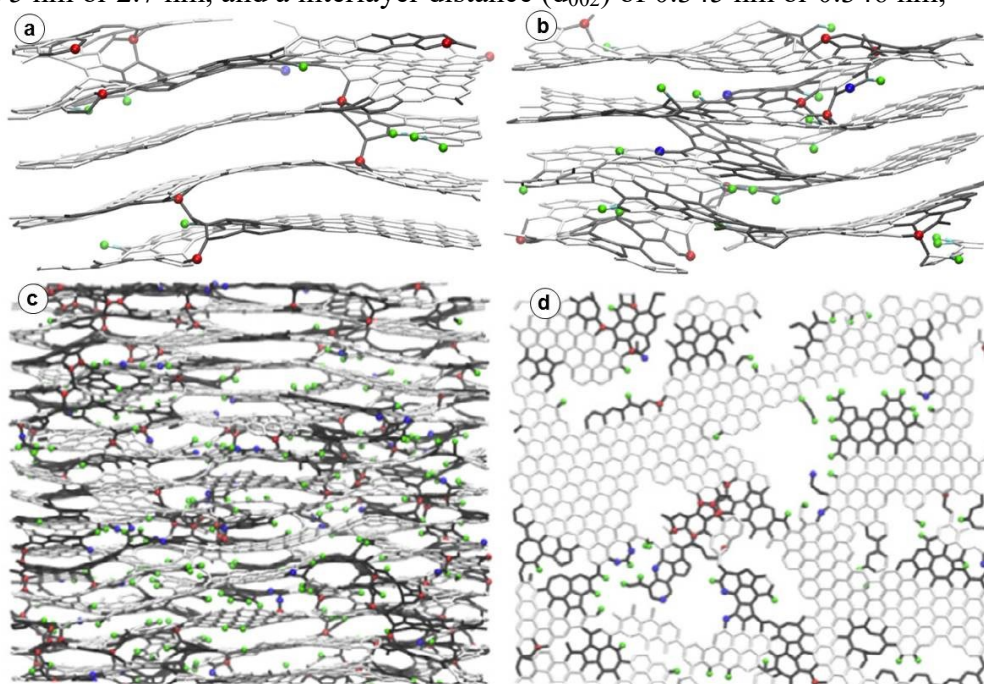
Figure 13: Snapshots of atomistic models of two well-known Pyrocarbons (PyCs), a high-textured "rough laminar" (RL) in (a) and high-textured "regenerative laminar" (ReL) in (b) in a view parallel with the lateral dimensions of BSUs as synthesized at 1050°C. The described color scheme shows bonds in pure hexagonal fragments (white), other bond types (black), twofold carbons (blue), fourfold carbons (red), and hydrogen (green spheres). A larger Snapshot of about 25.000 atoms for the high-textured regenerative laminar (ReL) pyrocarbon is shown in a view parallel in (c) and perpendicular in (d) with the lateral dimensions of BSUs, adapted from [69], with permission.

respectively. Here, atomistic models using HR-TEM and neutron diffraction data show that 97-99 at.-% of the present hydrogen (H) is located at the aromatic edges of BSUs bond to mainly trivalent Carbon atoms. The edges are described as related with "grain boundaries" present, rather rare interlayer cross-links occurs by fourfold Carbon atoms, and the most edges of BSUs only consist of three or less hydrogen atoms.

Additionally, only references are made to nitrogen-containing functional groups [68,71,72] as well as to sulfur-containing functional groups [73,74].

2.2.5. Metal-organic frameworks (MOFs)

Metal-organic frameworks (MOFs) are described as of an enormous interest by their high crystallinity, exceptional porosity, and high functionality due to the numerous combinations of SBUs and organic linkers resulting in much more than 20.000 MOF structures during the past two decades [103].

The structure of metal-organic frameworks (MOFs) is generally built from i) clusters of inorganic metals (e.g. Cu, Zn, Al, Ga etc.), which are described as "secondary building blocks" (SBUs), and ii) organic linkers (e.g. organic acids as carboxylic acid, terephtalic acid etc.) [104,105]. The secondary building blocks (SBUs) are described for MOFs as analogue units commonly used in the description of complex zeolite frameworks (e.g. polyeder and SBUs). In terms of MOFs, SBUs are defined as aggregated metal ions connected with functional groups, e.g. carboxylates, forming clusters. The SBUs (metal clusters) have the function of rigid vertices in a framework like "rigid organic struts" for the organic linkers [103]. Therefore, the formation of a MOF mainly depends on the choice of both, the SBUs and organic linkers. Here, the connectivity of SBUs to form a letter MOF structure is important for the arrangement of organic linkers. The connectivity of SBUs, so the number of possible bonds formed between a SBU and others through organic linkers is described by the so-called "point of extension" in MOF chemistry. The connectivity of SBUs starting from 3 up to 24 as well as to infinite are exemplarily illustrated **in Fig. 14**. As example, the $Zn_4O(-COO)_6$ cluster (or SBU) consists of 6 carboxylate carbons which results in a connectivity of 6 forming an octahedral-shaped building block. In addition to the effect of the connectivity of SBUs, the choice of the organic linker directly results in a complete new arrangement of the SBUs in another MOF structure, **see Fig. 15**. As example, starting from the same SBU of a metal cluster consisting of two copper metal ions containing four carboxylate groups [$Cu_2(-$

COO)$_4$], the addition of two different organic linkers i) adamantine-1,3,5,7-tetracarboxylic acid (H$_4$ATC) and ii) benzene-1,3,5-tricarboxylic acid (H$_3$BTC) results in the formation of two different MOFs as MOF-11 or HKUST-1, respectively. Here, the kind and number of functional groups of the organic linkers as well as free metal size of the SBUs are the most important feature for the enormous interest of MOFs, e.g. for the application as porous material, adsorption medium, or catalysis reactions [103]. In comparison the previously described topic of "Carbon-based materials", the organic linkers present in a MOF with its various functional groups can be described as small "BSU fragments" in terms of a maximum of heteroatoms or functional groups located at their edges.
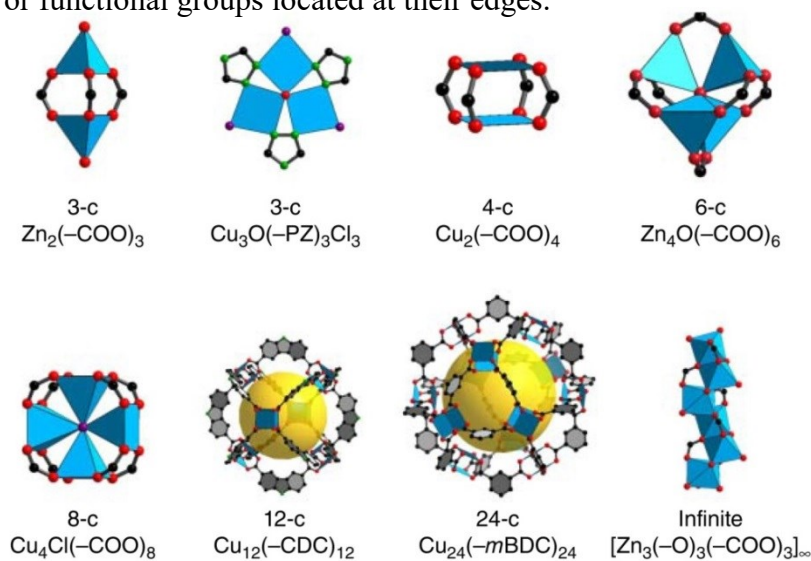
Figure 14: Selected number of "secondary building block" (SBUs) described in MOF chemistry consisting of metal or metaloxide clusters with organic compounds (groups of: -COO: carboxylate PZ: pyrazolate, AD: adeninate, CDC: 9H-carbazole-3,6-dicarboxylate, mBDC: 1,3-benzenedicarboxylate). N-c is related with the connecitivity of SBUs, adapted from [103], with permission. (Color code, Carbon (black spheres), oxygen (red spheres), nitrogen (green spheres), Chlorine (purple spheres), metals are located in the blue polyhedrons)
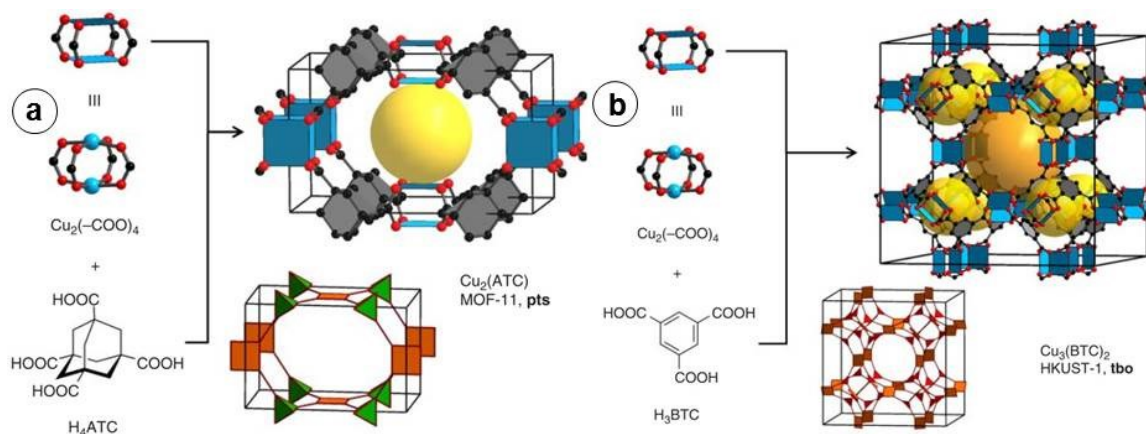
Figure 15: MOF structures of MOF-11 (guest free form) in (a) and HKUST-1 in (b). For MOF-11, the Cu-paddle wheels show open metal sites in the direction of the pore. The yellow ball displays the empty porespace in the framework, adapted from [103], with permission. (Color code, Carbon (black spheres), oxygen (red spheres), Cu is located in blue polyhedrons)

3. Results and Discussion

As discussed in the introduction (see section 1.), the application of a catalytic membrane reactor (CMR) for catalytic steam reforming of bio-ethanol at low temperatures (< 400°C) can be a cleaner and more riskless technical solution for the production of so-called "green hydrogen" as a sustainable energy carrier using a closed carbon circle. For this purpose a suitable membrane with the right characteristics, i.e. a sufficient high mixed gas hydrogen-selectivity (i.e. high purity level), and long-term hydrothermal stability up to 400°C (in high excess of water steam), has to be found, in addition to the right choice of catalyst.

3.1. Microporous carbon membranes

The following chapter deals with permeation and separation behavior of four different kinds of microporous carbon membranes in terms of their hydrogen-selectivity under dry and hydrothermal conditions. The membranes under study are described as amorphous, turbostratic, composite Carbon Molecular Sieve ($cCMS/SiO_2$), and a CAU-10-H metal-organic framework membrane. In addition to the amorphous and turbostratic carbon membrane, a graphite membrane is comparatively described. The investigations of the membranes summarized in this chapter are related with 3 accepted publications and 2 publications still in progress.

For the described application of CMR for bio-ethanol steam reforming (b-ESR), the microporous carbon membranes are studied under i.) dry conditions, i.e. using an equimolar binary feed gas mixture of (H_2/CO_2), and ii) under hydrothermal conditions, i.e. using a ternary feed mixture of 41 vol.-% H_2/ 41 vol.-% CO_2/ 18 vol.-% H_2O. Here, the membranes under study are primarily investigated in the feed pressure range between 1×10^5 Pa (1 bar) and 6×10^5 Pa (6 bar) and in the temperature range of room temperature under dry conditions or 100°C (hydrothermal conditions) and 300°C. The permeate side of the membranes under study primarily remains at ambient pressure at 1×10^5 Pa (1bar).

Publications to "Microporous carbon membranes"

3.1.1. Amorphous, turbostratic and crystalline carbon membranes with hydrogen selectivity

Authors: **A. Wollbrink**, K. Volgmann, J. Koch, K. Kanthasamy, C. Tegenkamp, Y. Li, H. Richter, S. Kämnitz, F. Steinbach, A. Feldhoff, J. Caro

Contents lists available at ScienceDirect

Carbon

journal homepage: www.elsevier.com/locate/carbon

Amorphous, turbostratic and crystalline carbon membranes with hydrogen selectivity

A. Wollbrink [a, b, *], K. Volgmann [a, b], J. Koch [c], K. Kanthasamy [c], C. Tegenkamp [c], Y. Li [d], H. Richter [e], S. Kämnitz [e], F. Steinbach [a, b], A. Feldhoff [a, b], J. Caro [a, b]

[a] Institute of Physical Chemistry and Electrochemistry, Leibniz University Hannover, Callinstr. 3A, D-30167, Hannover, Germany
[b] ZFM — Center for Solid State Chemistry and New Materials, Leibniz University Hannover, Callinstr. 3 — 3A, D-30167, Hannover, Germany
[c] Institute of Solid State Physics, Leibniz University Hannover, Appelstr. 2, D-30167, Hannover, Germany
[d] State Key Laboratory of Catalysis, Dalian Institute of Chemical Physics, Chinese Academy of Sciences, CN-116023, Dalian, China
[e] Fraunhofer Institute of Ceramic Technologies and Systems IKTS, Michael-Faraday-Str. 1, D-07629, Hermsdorf, Germany

ARTICLE INFO

ABSTRACT

Hydrogen production by catalytic steam reforming of renewable hydrocarbons like bio-methane or bio-ethanol has become an attractive goal of sustainable chemistry. Side reactions as in ethanol steam reforming decrease the hydrogen selectivity. A low-temperature catalytic membrane reactor with a hydrogen-selective membrane is expected to solve this problem. Three different carbon membranes are investigated with respect to their performance to extract hydrogen selectively from the binary and ternary reaction mixtures (H_2/CO_2), ($H_2/CO_2/H_2O$), and (H_2/ethanol) as model systems for bio-ethanol steam reforming. The three carbon membranes under study are (i) an amorphous carbon layer prepared by physical vapour deposition (PVD) of carbon on a porous alumina support using a carbon fibre yarn, (ii) a turbostratic carbon layer obtained by pyrolysis of a supported organic polymer blend as precursor, and (iii) a crystalline carbon prepared by pressing of graphite flakes into a self-supporting disc. For the equimolar binary feed mixture (H_2/CO_2) all carbon membranes were found to be hydrogen selective. For the ternary feed mixture (41vol.-% H_2/41vol.-% CO_2/18vol.-% H_2O), in the case of the amorphous and crystalline carbon membrane, the hydrogen selectivity remains also in the presence of steam. The turbostratic carbon membrane separates preferentially steam (H_2O) from the ternary feed mixture ($H_2/CO_2/H_2O$).

© 2016 Elsevier Ltd. All rights reserved.

1. Introduction

In reforming reactions, steam is reacted with hydrocarbons such as methane (natural gas or bio-gas) or (bio-) ethanol to give hydrogen and carbon dioxide according to $CH_4 + 2H_2O \leftrightarrows 4H_2 + CO_2$ or $C_2H_5OH + 3H_2O \leftrightarrows 6H_2 + 2\,CO_2$. Due to the endothermic character of reforming, the reactions takes place at high temperatures. Moreover, carbon monoxide is also formed, which reacts with steam in the exothermic water gas shift reaction at lower temperatures to hydrogen and carbon dioxide [1—6]. If the reforming reaction of methane or ethanol is conducted at lower temperatures, the

formation of by-products is suppressed, but the conversion is low [7—11]. However, when the produced hydrogen is extracted from the reactor through a hydrogen-selective membrane, the reaction mixture can be pushed towards complete conversion.

For the hydrogen extraction from a catalytic membrane reactor, a membrane has to be found that transports selectively hydrogen in the presence of steam, carbon dioxide and hydrocarbons (methane, ethanol). Current state of the art technique is reported by the application of Pd alloys as hydrogen-selective membrane (100% H_2 selectivity) for methane and also for ethanol reforming [12—17]. However, Pd is expensive and not long-time stable in the presence of hydrocarbons at temperatures above 400 °C [18—20]. Molecular sieve membranes (zeolite, metal-organic framework) separate according to the kinetic diameter of a molecule. This means, such membranes separate preferentially the smaller water molecule (2.6 Å) rather than the slightly larger hydrogen molecule (2.9 Å) and also carbon dioxide (3.3 Å) [21]. The other reaction components are

* Corresponding author. Leibniz University of Hannover, Institute of Physical Chemistry and Electrochemistry, Callinstr. 3A, 30167, Hannover, Lower Saxony, Germany
E-mail address: alexander.wollbrink@pci.uni-hannover.de (A. Wollbrink).

less critical because of their much larger kinetic diameters (CO: 3.8 Å, CH_4: 3.8 Å, C_2H_5OH: 4.5 Å).

In this context, the selective separation of hydrogen faces also different challenges by the strong adsorption of water or steam in highly polar membranes like aluminosilicate zeolites. In the case of metal-organic frameworks (MOFs) this effect of blocking water is probably reduced, but steam containing atmospheres in combination with high temperatures (up to 400 °C) are unfavorable for the stability of these materials.

Carbon-based materials offer some suitable properties like chemical and thermal stability, hydrogen selectivity and hydrophobic character in general. Thus, we decided to evaluate different carbon-based membranes in terms of hydrogen-selectivity for the mixture H_2/CO_2 in the presence of steam. Three different carbon membranes were prepared and tested. Among them, a new type of carbon membrane was prepared by physical vapour deposition (PVD) using the sublimation of carbon through resistance heating and subsequent deposition of amorphous carbon layers on a porous alumina support as demonstrated in Ref. [22]. A further carbon membrane was obtained by controlled pyrolysis of an organic polymer blend layer on a porous alumina support as it has been proposed in literature especially for air separation [23–25]. This procedure results in a turbostratic arrangement of carbon layers. A third carbon membrane was obtained by pressing of commercial graphite flakes into self-supporting disc, we name it crystalline carbon in this study. In a previous paper on such pressed graphite membranes, we found a hydrogen selectivity for binary (H_2/CO_2) and ternary ($H_2/CO_2/H_2O$) mixtures independent of temperature [26].

The aim of this work is to compare the separation behaviour of these three differently structured carbon membranes. As model systems for the ethanol steam reforming process, the binary equimolar mixtures H_2/CO_2 and $H_2/EtOH$ as well as the ternary gas mixture (41 vol.-% H_2/41 vol.-% CO_2/18 vol.-% H_2O) were selected.

2. Experimental

2.1. Preparation of carbon membranes

2.1.1. Supported *amorphous carbon membrane* by sublimation and deposition of carbon using resistance heating

Porous α-Al_2O_3 discs (Fraunhofer Institute for Ceramic Technologies and Systems IKTS, prior HITK/Inocermic, Hermsdorf, Germany) with a diameter of 18 mm, a thickness of 1.0 mm, and a pore size in the top layer of around 70 nm, were used as supports for carbon deposition. These supports were coated with amorphous carbon in a high vacuum sputter coater (Leica EM SCD500) using a carbon fibre yarn (Leica: 16LZ02308VN) with a static arrangement of the support. Before sublimation the chamber was rinsed with argon for several times. The carbon fibre yarn was resistively heated in vacuum at approximated 10^{-4} mbar. To produce a carbon layer of a sufficient thickness, two supports were placed directly under the carbon yarn with a short distance between yarn and support. Because of the very low mass of the carbon fibre yarn, a double carbon fibre yarn was applied and the carbon deposition had to be repeated several times with new carbon yarns. Finally, the deposition of 13 double carbon yarns lead to a crack-free carbon layer.

2.1.2. Supported *turbostratic carbon membrane* by pyrolysis of an organic polymer blend

A precursor solution was prepared by reaction of a diol with an unsaturated carboxylic acid to give an unsaturated polyester under subsequent addition of an olefin. In this specific case, propane diol was mixed with maleic anhydride and phthalic anhydride to give the unsaturated polyester, before finally styrene was added. The

same porous alumina discs as described above were dip-coated with the polymer blend followed by drying and pyrolysis (Appendix A: Supplementary materials). During the pyrolysis under different gas atmospheres, a software-controlled heating sequence was applied up to a final temperature of 500 °C. The hydrogen-rich precursors formed polyaromatic layers which arranged into layered agglomerates in two steps known from literature (carbonization + graphitization) [27,28]. The degree of graphitization depends on used precursor, temperature and pressure.

2.1.3. Self-supporting *crystalline carbon membrane* by pressing of graphite flakes

A self-supporting graphite membrane was prepared by pressing (392 MPa) a certain amount of commercial graphite flakes (single crystals) to a disc with a diameter of 18 mm and a thickness of around 1 mm. For feed pressures $\geq 3 \times 10^5$ Pa, porous alumina discs as described above were used additionally for a mechanical stabilisation, for further details see Ref. [26].

2.2. Characterisation

2.2.1. Sample preparation for scanning electron microscopy (SEM) and transmission electron microscopy (TEM)

For SEM analysis, the different carbon membranes were broken and glued with a conductive carbon tab for top view and cross-section micrographs. For high-resolution TEM (HRTEM) analysis, the turbostratic and crystalline carbon membranes were epoxy-glued between two silicon wafers. Thereafter they were cut and sliced to a thickness of 10 μm. Supported by a copper slot grid, the samples were 1–3 kV argon-ion sputtered until electron transparency. The amorphous carbon was carefully scratched from the alumina support and put on a holey carbon film supported by a copper grid (i.e. TEM grid). Investigations took place at locations were the specimen was placed over holes in the supporting film.

2.2.2. Methods

SEM micrographs were taken in secondary electron contrast with a JEOL JSM-6700F instrument using a cold-field emission gun with an acceleration voltage between 2 and 5 kV and an emission current of 10 μA. For *TEM investigations*, a JEOL JEM-2100F UHR with a Schottky field-emitter (ZrO_2/W (100)) was used at an acceleration voltage of 200 kV. A Gatan Imaging Filter (GIF 2001) with a 1k-charge-coupled device (CCD) camera was applied for imaging and spectral recording. HRTEMs were acquired at a point resolution of 0.19 nm, and the Digital Micrograph software was used to calculate from these two-dimensional fast Fourier transforms (FFTs). Each FFT was rotated around its center to give simulated intensity circles in the reciprocal space. Then, radial intensity distribution profiles were extracted to display the intensity over reciprocal distances [29]. For *electron energy-loss spectroscopy (EELS)*, with a dispersion of 0.5 eV/channel, the instrument was operated as a scanning transmission electron microscope (STEM) with an annular dark-field (ADF) detector. Raman spectra were taken with a Bruker Senterra for *micro-focused Raman spectroscopy* with a spatial resolution of around 1 μm^2 using a green laser with a wavelength of 532 nm (depolarized beam) and a 50 × 1000 μm objective lens. The membranes were measured with a laser power of 10 mW for the amorphous carbon membrane, 2 mW for the turbostratic carbon membrane and 5 mW for the crystalline carbon membrane. An integration time of 1s and 5 co-additions were always used. *X-ray photoelectron spectroscopy (XPS)* measurements were carried out in an ultra-high vacuum chamber at room temperature. A non-monochromatic X-ray source with an Al-K_α line (SPECS XR-50), an acceleration voltage of 12 kV and emission current of 8.3 mA

under an incident angle of 45° were used. The kinetic energies of the photoelectrons were measured with a hemispherical analyser (SPECS-PHOIBOS 225, Detector: 100 MCD) with 30 scans and a pass energy of 20 eV. All XPS spectra are shown as a function of binding energy with respect to the Fermi level. The quantitative XPS spectra are analysed with "XPS peak fit" software [30]. The photoelectron peak areas are calculated after background corrections using the Shirley algorithm described in Ref. [31]. *Contact angle measurements* were carried out with an automatic tensiometer (K100/DSA 100: Co. Krüss, Hamburg, Germany) at room temperature. The probing liquid was distilled water. For *permeation studies* the membranes were sealed with black O-rings (Perlast G75B-FFKM, Co. C. Otto Gehrckens) with an inner diameter of 14 mm and a cord diameter of 2 mm, in a module which was developed by TU Delft (F. Kapteijn, J. Gascon). For mixed gas permeation experiments, the absolute feed pressure of any mixture was varied from 1 up to 5×10^5 Pa while the permeate pressure was always at 1×10^5 Pa (atmospheric pressure). The composition of the permeate was analysed by a calibrated gas chromatograph (Agilent 7890B) using a steam-stable column for the analysis with high amounts of steam (RT$^®$-Q-Bond, Co. Restek) and a HP-Molsieve column (Co. Agilent Technologies). The feed gases were controlled by calibrated mass flow controllers (MFC's, Co. Bronkhorst) using an analogue input/output signal. The total fluxes were determined by a simple soap bubble counter with a total volume of 4 ml $\pm$ 0.02 ml. A Controlled-Evaporator-Mixer-System (type: W102A, Co. Bronkhorst- Nord GmbH) coupled with a digital mass flow meter/controller (mini-CORI-FLOW: M–12P) was used to saturate the gas flow with selected liquids (H$_2$O, C$_2$H$_5$OH). The different pressures were regulated and measured by modified back-pressure regulator (type: KBP1F0D4D5A20000, Co. Swagelok) and universal manometer made of steel with security glas (type: PGI-63B, Co. Swagelok) for a stable performance using medium temperatures between 100 and 160 °C at different pressures. The precision of measurements for the manometers ranges between $\pm$ 0.05 and $\pm$ 0.1 $\times 10^5$ Pa (accuracy $\pm$ 1.5%) depending on the used manometer. The permeation module as well as the 3 mm stainless steel pipes were constantly heated using heating bands (Co.Horst) controlled by K-type thermocouples (type: LTR 4200, Co. Juchheim Solingen).

2.3. Evaluation of mixed gas permeation and mixed gas separation

Membrane permeation is a stationary method under non-equilibrium conditions for testing the membrane performance in the view of a desired separation system. In our case we used the following gas mixtures as model system. The feed consists of an equimolar mixture of H$_2$ and CO$_2$ and also water (as steam) was added in the composition of 41 vol.-% H$_2$/41 vol.-% CO$_2$/18 vol.-% H$_2$O. We limit the steam content of the ternary gas mixture (H$_2$/CO$_2$/H$_2$O) to 18 vol.-% H$_2$O in order to prevent the pressure regulating system from undesired and uncontrollable pressure jumps due to spontaneous condensation of small water drops and to reach a constant feed pressure.

According to the IUPAC classification [32], the molar flux (J) of a fluid component i through a membrane can be described as the number of moles of component i passing the membrane per time and surface area. The permeance (P) is the pressure-normalised molar flux J, *e.g.* the flux per transmembrane pressure as driving force. In the case of mixture permeation, it is the difference in the partial pressure Δp of the individual gases of the feed (higher partial pressure) and permeate (lower partial pressure) side of the membrane. The permeability (P') is the thickness-normalised permeance P, i.e. the product of permeance and membrane thickness L.

The composition of the permeate results from the interplay of diffusion and adsorption of the mixture components for the

membrane. In porous solids, transport mechanisms can be molecular sieving, selective surface diffusion, Knudsen diffusion, or viscous flow diffusion. These mechanisms depend on the critical ratio of the kinetic molecule diameter to the effective pore size together with the specific adsorption properties of the respective membrane under study.

The mixed gas separation factors α (i,j) of the binary (H$_2$/CO$_2$, H$_2$/H$_2$O) and α (i,j,k) of the ternary (H$_2$/CO$_2$/H$_2$O) mixtures are determined as the ratio of the individual mixed gas permeances P (pressure-normalised fluxes) to the sum of the permeances of the other components i, j or k analysed by an online coupled gas chromatograph.

2.4. Error calculations

For all measurements the stochastic errors for the permeances were calculated and plotted in each related figure following the equations for error propagation after Gauss [33]. Therefore, the stochastic standard deviations of the gas chromatographic concentrations and of the total flow measurements were used. Other errors are also shown for temperatures and pressures in the related figure.

3. Results and discussion

3.1. Membrane characterisation

3.1.1. Macroscopic description (SEM)

The three carbon membranes differ in thickness and shape as a result of their different procedures in synthesis and preparation described in detail in Section 2.1. The **amorphous carbon** membrane was generated by physical vapour deposition which results in a crack-free carbon layer of about 300 nm on a porous α-Al$_2$O$_3$ disc (see Fig. 1a). The synthesis of the **turbostratic carbon** membrane also gave a crack-free carbon layer of about 8 μm on a porous α-Al$_2$O$_3$ disc (see Fig. 1b) and the **crystalline carbon** membrane was made by pressing graphite crystals and generate a 1 mm thick self-supporting carbon body (see Fig. 1c).

3.1.2. Microscopic description (HRTEM)

The different carbon membranes were characterised by HRTEM micrographs (Fig. 2a–c). For the **amorphous carbon** membrane a layered arrangement of carbon was observed (Fig. 2a) with obviously higher amounts of disordered areas compared to the **turbostratic carbon** membrane (Fig. 2b). From Fig. 2b, the turbostratic shape of the polyaromatic layers of the organic precursor, which arranged into layered agglomerates with short range-order is clearly seen. The HRTEM micrograph of the oriented graphite crystals, embedded in epoxy resin and aligned perpendicular to their c$_0$-axis, shows the stacked layers of the C$_6$-rings known from literature, see Fig. 2c [27,28].

Rotational averaged profiles of the related FFTs of the HRTEM micrographs from Fig. 2a,b were calculated to classify the pore system of the respective membrane under study. The distances from radial electron intensity distribution profiles show similar unimodal distributions of the inter-atomic array for the **amorphous** and **turbostratic carbon** membrane (see Fig. 2d, Table 1). The distances of the **amorphous carbon** layers vary between 0.24 and 0.73 nm with a maximum at 0.38 nm and also for the **turbostratic carbon** between 0.29 and 1.11 nm with a maximum at 0.43 nm. The effective pore diameter for the **amorphous** and **turbostratic carbon** membrane is calculated from the distances of the radial electron intensity distribution profiles (Table 1) minus twice of the covalent radius of a single bonded carbon atom of 0.154 nm (see Table 2), taken from literature [34].
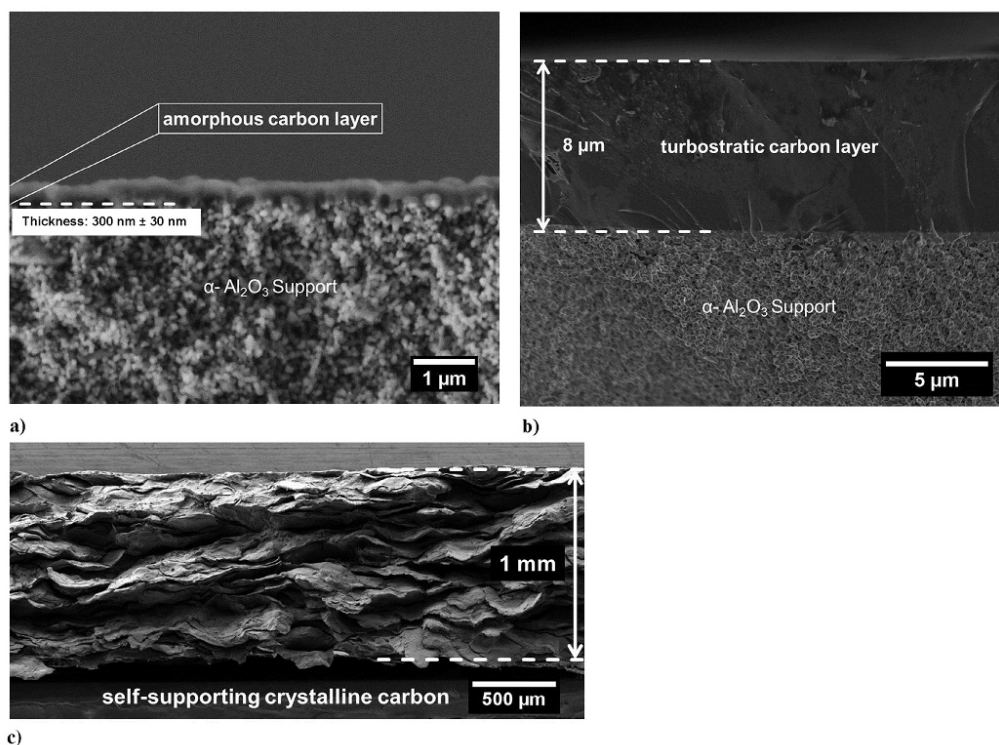
Fig. 1. SEM cross-sections of the broken carbon membranes: amorphous **a**), turbostratic **b**), and crystalline carbon **c**).

From these data, it follows that the **amorphous** and **turbostratic carbon** membranes belong to the microporous solids, according to the IUPAC classification [35], which defines porous solids with a pore diameter smaller than 2 nm as microporous. In microporous materials, the pore size is of the order of molecule diameters (H_2: 0.29 and CO_2: 0.33 nm) and the molecules cannot escape from the force field of the pore walls. For the **amorphous** and **turbostratic carbon** membrane, surface diffusion or molecular sieving is expected to be the dominant transport mechanism. The molar flux (J) of a component i through a microporous membrane is described by Fick's first law [36,37]:

$$J = -D \ grad \ c \qquad (1)$$

where D is the diffusion coefficient of component i, grad c is the concentration gradient of a component i over the membrane between the individual component adsorbed in the pores between feed and permeate side. The challenge in the evaluation of membrane permeation data is the distinction of the influence of diffusion and adsorption, as discussed in pioneering publications by Krishna et al. [38,39]. The diffusion coefficient D of a component i increases with increasing temperature, in accordance to the Arrhenius law, while the amounts of adsorbed gases decrease with increasing temperature, in accordance to the van't Hoff law. Systematic temperature-dependent permeation measurements of a membrane will give a hint, what effects finally dominates the

individual permeation performance.

For the view of structural comparison we aligned the graphite crystals of the **crystalline carbon** membrane perpendicular to c_0-axis (see Fig. 2c). The observed stacked layers of the C_6-rings with a distance of 3.5 Å are identical with the interlayer distance in graphite ($d_{002} = c_0/2$) [40]. It is obvious that the diffusion of the gases only occurs along the calculated pore sizes larger or equal than the smallest kinetic diameter of 2.6 Å with respect to the water molecule (see Table 2, Fig. 2d). The pore system of the **crystalline carbon** membrane is the result of the extra-crystalline voids between the dense graphite crystals and cannot be estimated from TEM data. From permeation experiments, we can classify the size of the extra-crystalline voids indirectly.

3.1.3. Spectroscopic description (Raman, XPS-EELS)

3.1.3.1. Raman. The three carbon membranes under study are classified into **amorphous** (i), **turbostratic** (ii), and **crystalline** (iii) **carbon** by micro-focused Raman measurements (see Fig. 3, Table 3). The Raman-active vibrations of the **amorphous carbon** membrane are very broad and dominated by defect vibrations which results in a plateau between 1300 and 1700 cm^{-1} (G + D1 + D3 + D4) [41–43]. The Raman spectrum of the **turbostratic carbon** membrane shows also broad vibration bands but two vibrations can be distinguished. The Raman-active vibration at 1597.5 cm^{-1} (G) corresponds to a highly ordered graphite-like structure related to an E_{2g}-symmetry, known as G-

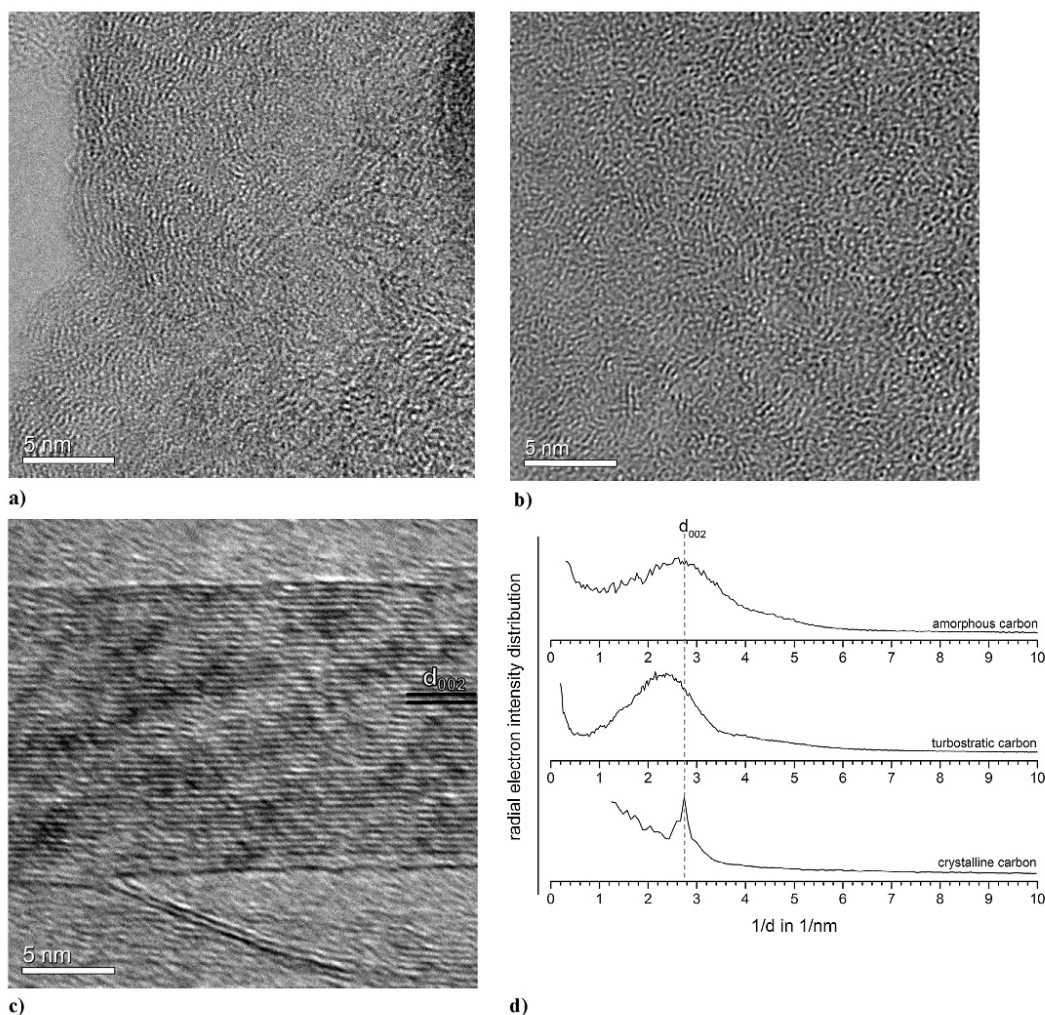# Results and Discussion: Microporous carbon membranes

Fig. 2. HRTEM micrographs of the amorphous **a)**, turbostratic **b)**, and crystalline **c)** carbon membrane. The crystalline carbon membrane is embedded in epoxy resin and aligned perpendicular to c_0-axis. Radial electron intensity distribution profiles of the related fast Fourier transforms (FFTs) of the shown micrographs are given in **d)** (see Table 1).

Table 1
Calculated distances of the radial electron intensity distribution profiles (see Fig. 2d) of the inter-atomic array for the amorphous and turbostratic carbon membrane.

Membrane	Maximum of internal distance distribution (d) in nm	Range of internal distance distribution (d) in nm
Amorphous carbon	0.38	$0.24 \leq r \leq 0.73$
Turbostratic carbon	0.43	$0.29 \leq r \leq 1.11$

band (C—C stretching vibration). The vibration at 1338.9 cm^{-1} (D1) is related to a disordered graphitic structure with an A_{1g}-symmetry, known as D1-band ("defects"). In addition to these two signals, a vibration at around 2834.9 cm^{-1} (2·D1) is observed. In the range from 50 to 2000 cm^{-1}, all vibrations are described as first order vibration modes. All vibrations higher than 2000 cm^{-1} belong either to second order vibrations, representing the multiple wavenumber of their first order vibration (see Table 3).

The spectrum of the **turbostratic carbon** is similar to those of different types of soot described in literature [41,43]. These soot

Table 2

Effective pore diameter from calculated distances of the radial electron intensity distribution profiles minus twice of the covalent radius of a single bonded carbon atom (see Fig. 2d, Table 1).

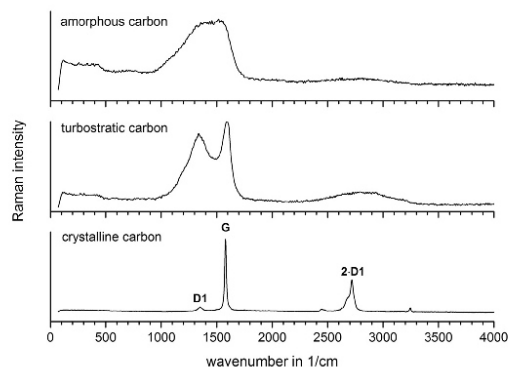| Membrane	Maximum of pore diameter distribution (d′) in nm	Range of pore diameter distribution (d′) in nm
Amorphous carbon	0.23	$0.09 \leq d \leq 0.58$
Turbostratic carbon	0.28	$0.14 \leq d \leq 0.96$

Fig. 3. Micro-focused Raman spectra of the three carbon membranes under study (see Table 3).

carbons consist of more than 80% of carbon and are composed of 10–30 nm agglomerated parts with amorphous and graphite-like domains with average distances (pores) of 3–4 Å, in accordance to the distances from HRTEM measurements (see Tables 1 and 2). The Raman spectra of soot are similar to the Raman spectra of the **amorphous** and **turbostratic carbon** membrane. The differently structured domains are strongly controlled by carbonization conditions like temperature and atmosphere as well as by the choice of the polymer precursor [27,28]. In addition, the broad vibration bands are the result of two defect vibrations, known from literature, at ~1500 cm^{-1} (D3) and ~1200 cm^{-1} (D4) which are invisible because of the other dominating vibrations of the sample. This shows a higher amount of defect-vibrations of the **amorphous carbon** membrane which form the observed plateau as mentioned above as a result of overlaying defect-signals.

For the **crystalline carbon** membrane, the Raman spectrum shows well defined vibrations corresponding to the highly ordered graphite structure at 1580.2 cm^{-1}, as expected. But also small amounts (with low intensity) of the defect vibration at 1347.6 cm^{-1} (D1) are observed. The **crystalline carbon** shows here all typical vibration modes for graphite known from literature [42,43].

3.1.3.2. XPS and EELS analysis. The surface analysis by means of X-ray photoelectron spectroscopy of all three carbon membranes is shown in Fig. 4 and given in detail in Table 4. For all carbon membranes we can distinguish between two main signals (Signals:

I, II) with a relative binding energy distance of around 1.0 eV (± 0.1 eV) between their maxima. In accordance with literature, these two C 1s signals are associated with different hybridisation states. The C 1s signal at lower binding energy (I) corresponds to the sp^2-hybridisation and the signal (II) with an energy shift of around 1 eV (to higher energy) is related to the sp^3-hybridisation state of carbon [44]. The content of sp^2 and sp^3 hybridised carbon was estimated by their signal areas ratio. The contributions show for the **amorphous carbon** membrane a sp^2/sp^3 ratio of 1:2. For the **turbostratic** and **crystalline carbon** membrane the opposite sp^2/sp^3 ratio of 2:1 was determined (see Table 4).

These results are qualitatively in agreement with those obtained from Raman measurements (see Fig. 3). According to literature, the hybridisation state of the carbon membranes can be deduced also from our Raman spectra (see Section 3.1.3.1) [45–47]. We know that amorphous carbon consists of a mixture of sp^2- and sp^3-hybridised states [45]. Therefore, the evolution of the G-band position and the intensity ratio of D1-band/G-band can be used to estimate the sp^2/sp^3 ratio in a sample with visible Raman scattering. However, the most striking problems are the opposite contributions to the G-band position or D1/G ratio by bond disorder, clustering, domain size or content of sp^3 hybridised carbon which make a quantitative evaluation of the sp^2/sp^3 ratio difficult [45]. The apparent high content of sp^3-hybridised material on the surface of the graphite crystals is not found in volume-sensitive methods as checked with X-ray powder diffraction (see Fig. S1, supplementary materials).

Furthermore, a third signal (III) is observed for all three carbon membranes at around 288 eV. Electron energy-loss spectra of the **amorphous** and **turbostratic carbon** showed no other elements beside carbon (see Fig. S2, supplementary materials). Therefore, we attributed signal (III) as residual C–O contamination from air [44].

In addition to the described signals (I,II,III), for the **amorphous carbon** membrane a weak signal (IV) with a relative high shift of binding energy of 8.1 eV related to signal (I) and for the **crystalline carbon** membrane a signal (V) with a relative shift of 6.1 eV related to signal (I) could be observed. Because of the relative large shift in binding energy and the absence of oxygen, proven by EELS [48], we attribute signal (IV) to fluorine by some contact contamination of the **amorphous carbon** membrane with the black O-rings (F source) as a result of the long-time permeation experiments at temperatures up to 250 °C [49,50]. The relative shift in binding energy of signal (V) is attributed to some carboxyl groups on the graphite surface of the **crystalline carbon** membrane [51].

3.1.4. Contact angle measurements

To verify our assumption, mentioned in the introduction, that carbon-based materials offer some suitable properties as their

Table 3

Raman-Shift of the three carbon membranes under study from 0 to 4000 cm^{-1} (see Fig. 3). Data from literature [43] in brackets.

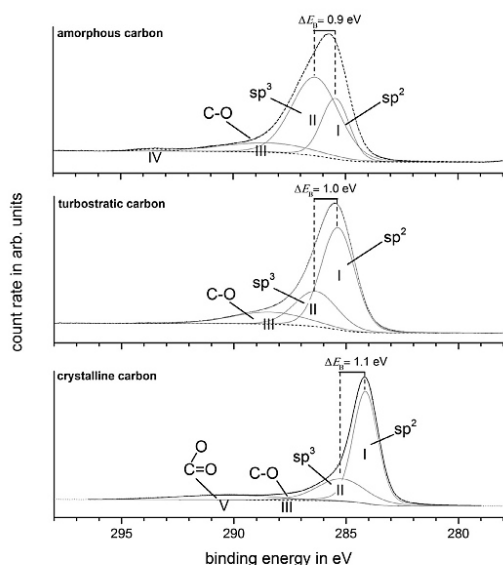| Vibration bands [cm^{-1}]	1st order	1st order	1st order	2nd order	2nd order	2nd order
Abbreviations	G	D1	D3	2·D4	2·D1	2·D2
Amorphous carbon	1532.7	1387.3	~1500	–	2738.4	–
Turbostratic carbon	1597.5	1338.9	~1500	–	2834.9	–
Crystalline carbon	1580.2 (1580)	1347.6 (1350)	–(1500)	2443.1 (2450)	2717.9 (2720)	3245.9 (3240)

Fig. 4. Surface analysis by means of XPS spectra of the surface of the three carbon membranes under study (see Table 4).

hydrophobic character, we measured the contact angle of water on the different carbon membranes at room temperature. As expected, all membranes under study show contact angles which are typical for hydrophobic materials. The **amorphous carbon** membrane shows mean contact angles of around $80° \pm 1°$ and the **turbostratic carbon** membrane around $77° \pm 1°$. In the case of the **crystalline carbon** membrane the measured contact angle were around $82° \pm 2°$ (see Table S1, supplementary materials).

3.2. Membrane permeation and separation

The permeation properties of the three different carbon membranes were evaluated by binary and ternary mixed gas experiments. In general, the molar flux and separation behaviour of mixed gases by porous membranes depend on pore size, pore surface properties and the interactions between surfaces and molecules. We start the discussion with the influence of different feed pressures on the permeation of an equimolar binary feed mixture H_2/CO_2 on the **amorphous**, **turbostratic** and **crystalline carbon** membranes. The mixed gas permeances and separation factors for this mixture were determined as a function of feed pressure ($2-5 \times 10^5$ Pa) with a constant permeate pressure of 1×10^5 Pa and for selected temperatures ($25-250$ °C). Permeation experiments for the ternary mixture 41 vol.-% H_2/41 vol.-% CO_2/18 vol.-% H_2O (steam) were performed and compared to the results of the binary feed mixture. Finally, permeation measurements for the H_2/ethanol separation are given as short outlook towards the application of the carbon membranes for bio-ethanol steam reforming.

3.2.1. Effect of varying feed pressure on permeation of the binary feed mixture (H_2/CO_2)

The **amorphous carbon** membrane showed very high and pressure-independent permeances (10^{-7} mol/m^2 s Pa) from 1.5 to 3.0×10^5 Pa feed pressure (see Fig. 5a). For the **turbostratic carbon** membrane, constant permeances (10^{-9} mol/m^2 s Pa) between 2.0 and 4.0×10^5 Pa feed pressure are also found (see Fig. 5b). Only in the case of the **crystalline carbon** membrane, a significant increase of both the H_2 and CO_2 permeances as a function of the feed pressure was observed between 2.0 and 5.0×10^5 Pa (see Fig. 5c). If we compare the mixed gas separation factor α (H_2/CO_2) for the three carbon membranes under study, stable but low mixed gas separation factors were found for both the **amorphous carbon** (α (H_2/CO_2) $\approx$ 2.5) and the **turbostratic carbon** (α (H_2/CO_2) $\approx$ 1.9) membrane, see Fig. 5d.

The pressure-independent permeances and separation factors for the **amorphous** and **turbostratic** carbon membrane show that the molar flux of H_2 and CO_2 is proportional to the feed pressure at a given temperature (see Eq. (1)). This finding indicates a linear adsorption isotherm with increasing pressure related to the concentration gradient of Fick's first law. Deviations from that linearity at low feed pressure for the **amorphous carbon** membrane (1.25×10^5 Pa) (see Fig. 5a) and at high feed pressure for the **turbostratic carbon** membrane (5.00×10^5 Pa) (see Fig. 5b), may result from a complicated interplay of mixed gas H_2/CO_2 adsorption and diffusion.

The **crystalline carbon** membrane differs from the two other carbon membranes by a strong pressure-dependent mixed gas separation factor which results from a stronger increase of the CO_2 permeance compared to H_2 in the examined pressure range. At a feed pressure of 2×10^5 Pa the mixed gas separation factor is α (H_2/CO_2) $\approx$ 5.0 and decreases gradually with increasing feed pressure to $\approx$ 2.1 at 5×10^5 Pa. The mixed gas separation of about 5 shows a

Table 4

Surface analysis by means of X-ray photoelectron spectroscopy (XPS) of the three carbon membranes under study. With E_B: binding energy, FWHM: full width at half maximum, Area: related area to the described signals, conent of sp^2 and sp^3 hybridisation is calculated from the total area of peak I and II of the respective membrane (see Fig. 4).

| Carbon membrane	Peak	C 1s			Content of sp^2 and sp^3 hybridisation in %
		E_B in eV	FWHM	Area	
Amorphous	I (sp^2)	285.44	1.46	1060.53	31.3
	II (sp^3)	286.34	2.48	2324.82	68.7
	III	288.44	4.87	539.00	–
	IV	293.50	1.62	40.72	–
Turbostratic	I (sp^2)	285.36	1.77	2464.40	69.6
	II (sp^3)	286.35	2.24	1076.10	30.4
	III	288.41	3.83	636.96	–
Crystalline	I (sp^2)	284.14	1.29	1832.90	71.3
	II (sp^3)	285.21	2.56	737.27	28.7
	III	287.75	1.48	31.37	–
	V	290.24	5.00	304.66	–
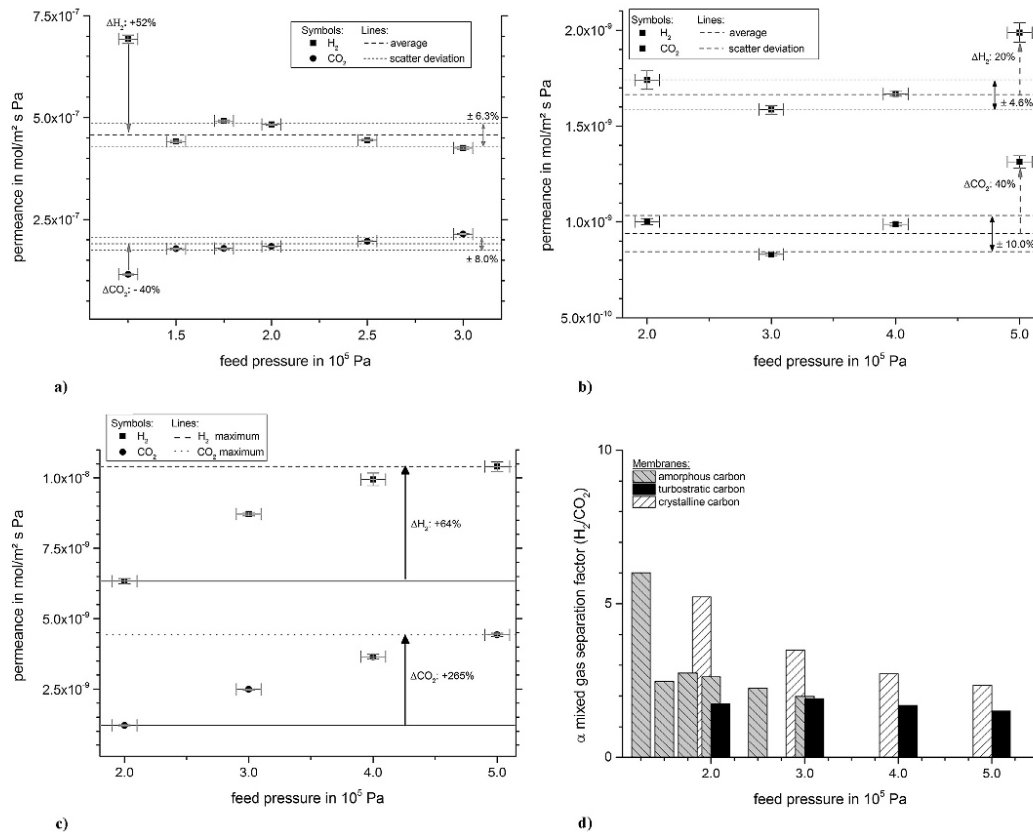
Fig. 5. Pressure-dependent H_2 and CO_2 mixed gas permeances of the three carbon membranes under study: amorphous carbon **a)**, turbostratic carbon **b)**, crystalline carbon **c)** as a function of the feed pressure at room temperature (23 °C). The permeate was at a pressure of 1×10^5 Pa. Mixed gas separation factors α (H_2/CO_2) derived from the permeances given in **a)** to **c)** of the three carbon membranes are given in **d)**. An equimolar mixture of H_2 and CO_2 (binary system) was used. Arrows indicate the increase/decrease of permeances between the used feed pressures.

Knudsen separation mechanism at feed pressures of $\leq 2 \times 10^5$ Pa. Therefore, we can classify the size of the extra-crystalline voids of the **crystalline carbon** membrane in the range of meso- or macroporous materials. Knudsen diffusion dominates if the mean free path length λ of the probe molecules is larger than the effective pore diameter and results from a momentum transfer of inelastic and elastic collisions between molecules and the pore wall [52,53]. The Knudsen diffusivity D_K only depends on the pore size r (radius of the pore) and molecular weight M, varies only weakly with temperature T and is independent from pressure p [37,52,53]. If a strong pressure-dependence is found, the dominating mechanism appears by molecule (free gas) and molecule (reflected off the pore wall) collisions and therefore the separation is a function of the mean free path length λ and occurs in the case of the **crystalline carbon** membrane in the extra-crystalline voids between the pressed graphite crystals (see Fig. 1c). If we calculate the mean free path length λ of H_2 and CO_2 as a function of pressure – according to the Knudsen model - at room temperature, we can estimate from the critical value of λ the medium or main size of extra-crystalline voids as an indirect method (see Eq. (2), Table 5).

$$\lambda = \frac{kT}{\sqrt{2}\sigma p} \qquad (2)$$

where λ is the mean free path length, k: the Boltzmann constant, T: the absolute temperature, p: the used pressure, and σ: the collision cross-section [54]. The decrease in the selectivity with increasing pressure – as found for the **crystalline carbon** membrane – results therefore from a gradual change of the Knudsen regime into the unselective viscous flow regime, where the molar flux is described by the Hagen–Poisseuille law [52].

For the **crystalline carbon** membrane (see Table 5), the critical mean free path length $\lambda(p)$, as a function of pressure, is around 50 nm for H_2 and 40 nm for CO_2 at 2×10^5 Pa, which corresponds to the mixed gas separation factor α (H_2/CO_2) $\approx$ 5.0 assuming a Knudsen separation mechanism. At the highest feed pressure of 5×10^5 Pa the contributions of Knudsen separation and non-selective viscous flow for H_2/CO_2 are 30% and 70%, respectively, and result in α (H_2/CO_2) $\approx$ 2.1. The related mean free path length $\lambda(p)$ of around 22 nm for H_2 and 17 nm for CO_2 represent the

Table 5
Calculated mean free path length λ for the used probe gases as a function of pressure and temperature.

Mean free path length $\lambda(p)$ in nm			Mean free path length $\lambda(T)$ in nm			
Pressure in 10^5 Pa, at 25 °C	Binary feed mixture		Temperature in °C, at 3×10^5 Pa	Ternary feed mixture		
	H_2	CO_2		H_2	CO_2	H_2O
1	110.0	85	25	36.7	28.3	45.6
2	55.0	42.5	50	39.8	30.7	49.4
3	36.7	28.3	100	45.9	35.5	57.1
4	27.5	21.3	150	52.1	40.2	64.7
5	22.0	17.0	200	58.2	44.9	72.4
			250	64.4	49.7	80.1

contribution of the smallest distances of the **crystalline carbon** membrane to the mixed gas permeation. These calculations show a rough estimate for the distribution of the extra-crystalline voids in the **crystalline carbon** membrane in the range of mesoporous materials [35]. In mesoporous materials, the diffusive mass transport is always a combination of several processes as Knudsen diffusion, molecular diffusion or viscous flow.

The large difference in the absolute values of the permeances between the three carbon membranes under study cannot be explained as a result of different thicknesses (see Table 6). The permeability (P'), i.e. the product of permeance and the membrane thickness, differs also by around two orders of magnitude. Therefore, the different permeabilities result from different separation mechanisms related to the respective pore system as mentioned above.

3.2.2. Effect of varying temperature on permeation of the binary feed mixture (H_2/CO_2)

As mentioned in Section 3.1.2 (HRTEM analysis), the biggest challenge in the evaluation of membrane permeation data is the distinction of two contributions: diffusivity and adsorption. The dominant process can be revealed from systematic temperature-dependent measurements. The diffusivity D of a gas component normally increases with increasing temperature and therefore it can be described by the Arrhenius equation. On the contrary, the permeation of a gas component i through a membrane may be lowered with increasing temperature causing a stronger desorption which results in a smaller concentration gradient.

The permeation experiments as a function of temperature revealed two different trends. With increasing temperature, the permeances of the two gases, H_2 and CO_2, decrease for the **amorphous** and **crystalline carbon** membrane, but increase for the **turbostratic** one in the temperature range between 100 and 250 °C (see Fig. 6).

For the **amorphous carbon** membrane, the permeances of H_2 and CO_2 drop equally with increasing temperature by around 60%, and the mixed gas separation factor α (H_2/CO_2) remains almost constant at ≈ 2.8 (see Fig. 6a). This temperature-effect is explained similar to the pressure-dependent measurements with the proportional decrease of adsorbed H_2 or CO_2 which lead to a lowered contribution of the *grad c* term of Eq. (1) which turns out to be the

Table 6
Mixed gas permeabilities P' and corresponding mixed gas separation factor α (H_2/CO_2) for the three carbon membranes using an equimolar feed mixture at room temperature. Feed pressure 2.0×10^5 Pa, permeate pressure of 1.0×10^5 Pa.

Membrane	$P'(H_2)$	$P'(CO_2)$	α
	[mol m/m² s Pa]	[mol m/m² s Pa]	H_2/CO_2
Amorphous carbon	1.4×10^{-13}	5.5×10^{-14}	2.6
Turbostratic carbon	1.4×10^{-14}	8.2×10^{-15}	1.7
Crystalline carbon	6.3×10^{-12}	1.2×10^{-12}	5.2

dominant parameter here.

The **turbostratic carbon** membrane showed an opposite permeation behaviour by the disproportional rise of permeances and the mixed gas separation factor with increasing temperature (see Fig. 6b). At 250 °C, the permeance of hydrogen increased from 2.0×10^{-9} to 8.8×10^{-9} mol/m² s Pa (+335%) and the permeance of carbon dioxide increased from 8.9×10^{-10} to 1.5×10^{-9} mol/m² s Pa (+60%) related to the values at room temperature. Therefore, the mixed gas separation factor α (H_2/CO_2) rises from 1.9 at room temperature to 6.0 at 250 °C. The increase in permeance and separation is typical for a thermally activated process which we assign to a selective surface diffusion mechanism [37]. The hopping of the adsorbed molecules through the **turbostratic carbon** membrane along its pore surface requires a certain activation energy described by an Arrhenius-like equation (see Eq. (3)) for the diffusivity of a component i, related to the Fickian law as given by Eq. (1):

$$D_i = \nu_i \delta_i^2 e^{-(E_A)_i/RT} \tag{3}$$

where for a component i, ν is jump rate, δ is jump distance between two adsorption sites, E_A is the necessary activation energy for the jump, R is the universal gas constant, and T is the absolute temperature. The apparent activation energy, calculated from the slope of hydrogen and carbon dioxide permeances in an Arrhenius plot, are 8.7 kJ/mol (0.09 eV) for H_2 and 2.9 kJ/mol (0.03 eV) for CO_2 (see Fig. S3). Therefore, hydrogen is stronger physically adsorbed than carbon dioxide which partly prevents CO_2 to pass the pores (see Table 2). The higher activation energy for H_2 than for CO_2 shows rather the selective surface mechanism as diffusivity controlled process than affected by the concentration gradient related to Eq. (1). The entirely different behaviour of the **turbostratic carbon** membrane compared to the **amorphous carbon** membrane is caused rather to the opposite hybridisation states than to the pore size distribution (see Fig. 4, Table 4).

The **crystalline carbon** membrane shows a similar temperature-dependent behaviour as the **amorphous** one, where the permeance of the two gases, H_2 and CO_2, also decreases with increasing temperature by approximately 60% (see Fig. 6c). From the pressure-dependent measurements discussed above we know, that the separation mechanism of the **crystalline carbon** membrane mainly depends on molecule-wall and molecule–molecule interactions. The decrease of permeances is rather explained by the increase of viscosity with increasing temperature than by lower amounts of adsorbed molecules in the extra-crystalline voids. The viscosity η_i of an individual component i is proportional to its mean free path length λ_i, the average velocity c_i, and the molecular weight M_i [54].

The mixed gas separation factor α (H_2/CO_2) increases from 3.5 to 4.6 which is related to the temperature-dependent change of the mean free path length $\lambda(T)$ (see Table 5). With increasing temperature the mean free path length $\lambda(T)$ increases to values comparable to the related path length at room temperature at 2×10^5 Pa. The

Results and Discussion: Microporous carbon membranes
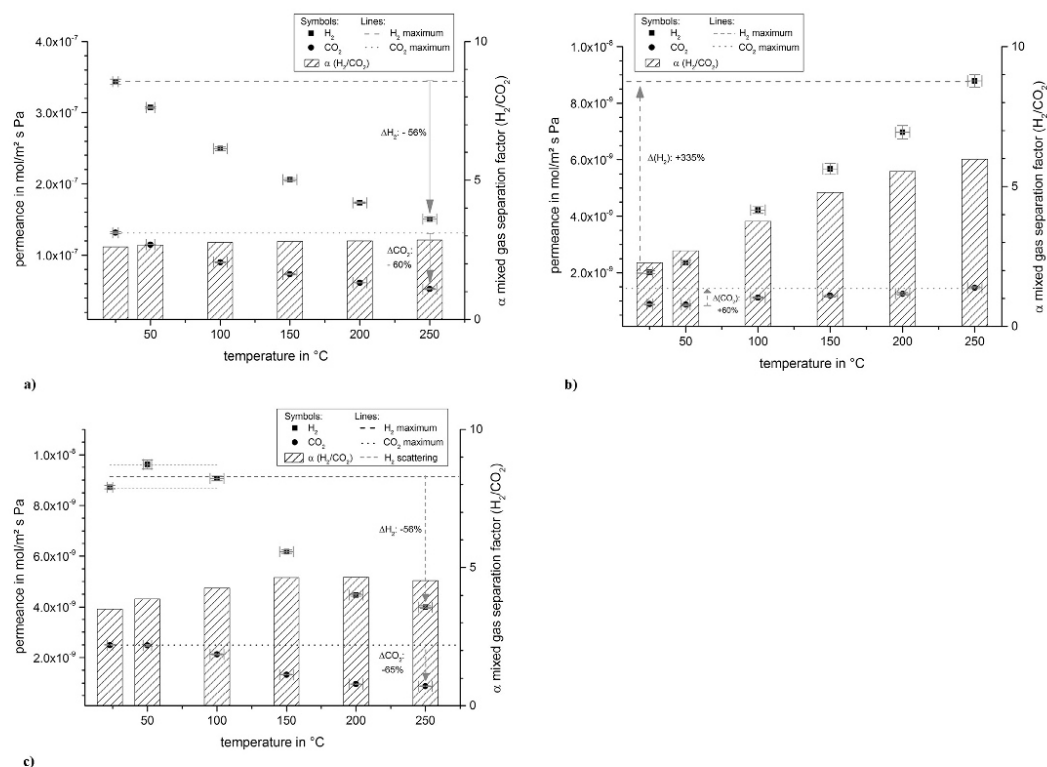
Fig. 6. Temperature-dependent H_2 and CO_2 mixed gas permeances and related mixed gas separation factors for α (H_2/CO_2) of the three carbon membranes: amorphous carbon (feed pressure of 2×10^5 Pa) **a)**, turbostratic carbon (feed pressure 3×10^5 Pa) **b)**, crystalline carbon (feed pressure of 3×10^5 Pa) **c)**. An equimolar mixture of H_2 and CO_2 (binary system) was used. The permeate side was kept at 1×10^5 Pa. Arrows indicate the increase/decrease of permeances between room temperature and 250 °C in percentage [%].

critical temperature is here about 150 °C.

3.2.3. Effect of varying temperature on permeation of the ternary feed mixture (41 vol.-% H_2/41 vol.-% CO_2/18 vol.-% H_2O)

From practical aspects of bio-ethanol or bio-methane steam reforming it is interesting to study the separation behaviour of the ternary system $H_2/CO_2/H_2O$ (steam). Assuming that all ethanol or methane is reacted to hydrogen and carbon dioxide in the excess of steam, we have studied the permeation of the ternary gas mixture of 41 vol.-% H_2/41 vol.-% CO_2/18 vol.-% H_2O (steam) in the range of 100–250 °C, as mentioned in Section 2.3 (see Fig. 7). Results from contact angle measurements point towards a hydrophobic behaviour (see Section 3.1.4.).

All three carbon membranes showed reduced permeances of H_2 and CO_2 if steam is present in the feed mixture compared to the binary feed mixture without steam. The **amorphous** and **crystalline carbon** membranes were less affected than the **turbostratic** one. For the **amorphous carbon** membrane, the permeances of H_2 and CO_2 are decreased by around 50% (see Fig. 7a) in the presence of steam. The mixed gas separation factor α^{*1} (H_2/CO_2) for the **amorphous carbon** membrane is slightly increased from around

---

[1] The asterisk denotes the mixed gas separation factor α (H_2/CO_2) for the ternary feed mixture with (41 vol.-% H_2/41 vol.-% CO_2/18 vol.-% H_2O).
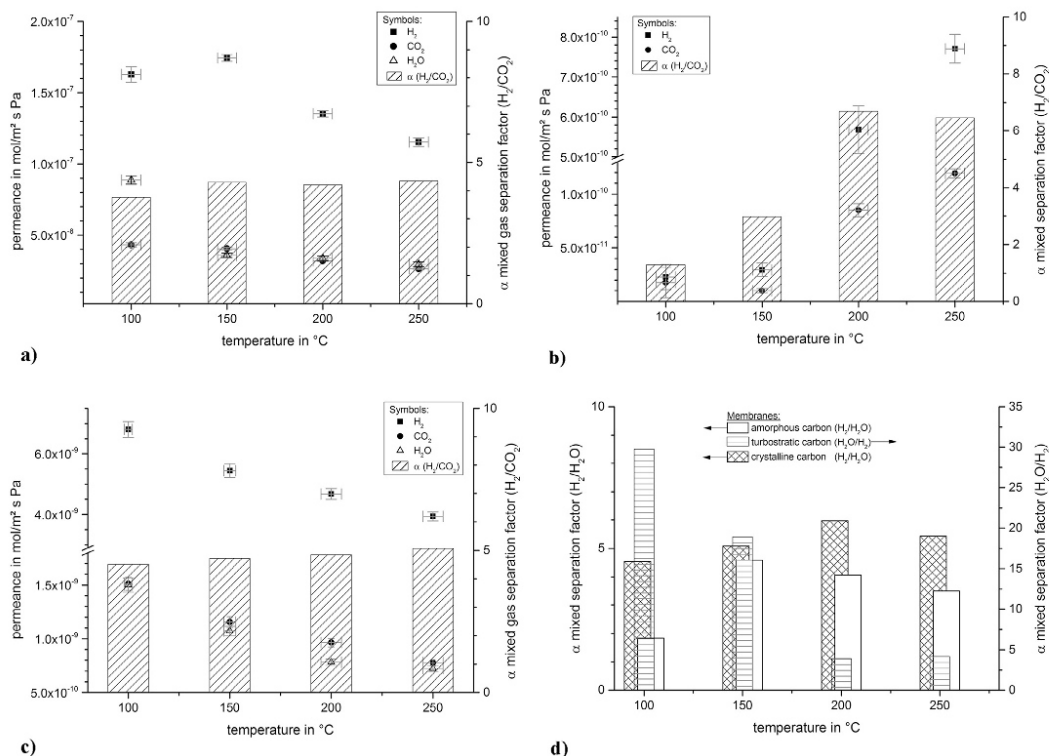
2.8 (without steam) to around 4 in the presence of steam (see Figs. 6a and 7a). The permeance of steam ranges in the order of the CO_2 permeance and results in a similar mixed gas separation factor α (H_2/H_2O) of around 4.5, but decreases with increasing temperature to α (H_2/H_2O) $\approx$ 3 at 250 °C (see Fig. 7d). The lower permeance of steam compared to H_2 may results most likely from the different adsorption behaviour of the different gaseous species and is obviously related to the difference of hybridisation states (see section 3.1.3.2 XPS and EELS analysis). The **crystalline carbon** membrane shows, similar to the **amorphous carbon** membrane, 30% lower permeances of H_2 and CO_2 (see Fig. 7c) compared to the binary feed mixture (H_2/CO_2) without steam (see Fig. 6c). The mixed gas separation factor α^{*1} (H_2/CO_2) remains at around 4.8. Also the permeance of steam ranges in the order of the CO_2 permeance and results in a similar mixed gas separation factor α (H_2/H_2O) of around 5. So it represents a 60% higher separation than calculated for ideal Knudsen separation. This effect of higher separation results from its strong dependency from the mean free path length λ_i and the higher deviation in the viscosity of the individual components (see Table 5, Eq. (2)) [26]. This interpretation is in accordance to the pressure- and temperature-dependent measurements of the **crystalline carbon** membrane in the binary feed gas system.

For the **turbostratic carbon** membrane, almost steam is present in the permeate at temperatures $\leq$ 200 °C. The permeances of H_2 and CO_2 drop by around 2 orders of magnitude related to the binary

Fig. 7. Temperature-dependent H_2, CO_2 and H_2O mixed gas permeances and related mixed gas separation factors α (H_2/CO_2) of the three carbon membranes under study: amorphous carbon (feed pressure 2×10^5 Pa) **a)**, turbostratic carbon (feed pressure 3×10^5 Pa) **b)**, and crystalline carbon (feed pressure 3×10^5 Pa) **c)**. The ternary feed composition was 41 vol.-% H_2, 41 vol.-% CO_2 and 18 vol.-% H_2O (steam). The permeate side was always at 1×10^5 Pa in contact with the permeated gas. The mixed separation factors α (H_2/H_2O) derived from **a)** and **c)** are given in **d)**. Values of α (H_2O/H_2) derived from **b)** are calculated from the different mole fractions between feed and permeate side.

feed mixture if steam is present (see Figs. 7b and 8a). In accordance to the blocking effect, the mixed gas separation factor α^{*1} (H_2/CO_2) decreased from 3.8 (without steam) to 1.3 at 100 °C (with steam). At 150 °C the effect is slightly reduced and α^{*1} (H_2/CO_2) increases to 3. At temperatures $\geq$ 200 °C, the permeate remains steam-dominated but the permeances of H_2 and CO_2 increase and remain one order of magnitude lower compared to the data in Fig. 6b (without steam). At temperatures $\geq$ 200 °C, the mixed gas separation factor α^{*1} (H_2/CO_2) in the presence of steam is similar to α (H_2/CO_2) without steam (see Figs. 7b and 8a). The observed blocking effect corresponds to the same effect of selective surface diffusion mentioned for the binary system, where H_2 was preferentially adsorbed instead of CO_2 resulting in a higher activation energy (see Fig. 6b). In the presence of steam, a highly polar molecule is inserted to the **turbostratic carbon** membrane which is stronger adsorbed than hydrogen. Consequently, this blocking effect should be diminished with increasing temperature since the adsorption of steam is reduced at a constant steam partial pressure (see Fig. 7b,d). The **turbostratic carbon** membrane shows selectivities with a mixed gas separation factor α (H_2/H_2O)< 1. So the effect of selective surface diffusion by the dipolar nature of the water molecule results in a hydrophilic separation behaviour and the mixed gas separation factor α (H_2O/H_2) amounts 30 at 100 °C and decreases to 8 at 250 °C, calculated from its mole fractions (see Fig. 7d).

The differences in the permeation performance of the **turbostratic carbon** membrane compared to the **amorphous carbon** membrane result from the different adsorption properties of these membranes rather described by their different hybridisation states, as seen from XPS and Raman measurements, than by their slightly different pore sizes (see sections *3.1.2* HRTEM analysis, *3.1.3.2*., XPS and EELS analysis). Fig. 8 illustrates the permeate concentration in vol.-% over a testing period of several hours for the **turbostratic carbon** membrane at different temperatures (100–250 °C) for the ternary feed mixture (41 vol.-% H_2/41 vol.-% CO_2/18 vol.-% H_2O). On the permeate side of the **turbostratic carbon** membrane almost pure steam (99 vol.-%) was found at 100 °C. The steam content of permeate decreased with increasing temperature to around 60 vol.-% at 250 °C (Fig. 8a). At low temperatures, mainly water could pass the membrane and very low permeances of H_2 and CO_2 were detected, calculated following Eq. S1 (supplementary materials).

Different to the previous permeations studies, where the permeate side of the membranes were always found to be in contact with permeate, we used in a test experiment N_2 as sweep gas in order to reduce the steam partial pressure to approximately zero. The blocking effect induced by strongly adsorbed water is diminished by either high temperature or low steam partial pressure (Table 7, Fig. 8a,b). The permeance of all three gases H_2, CO_2, and H_2O increase immediately if a sweep gas was used and reached a
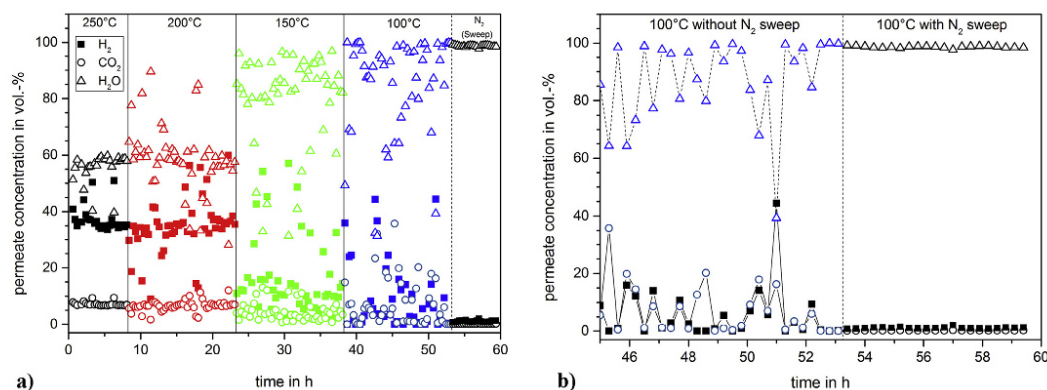
Fig. 8. a) Composition of the permeate by gas chromatographic analysis [vol.-%] of the **turbostratic carbon** membrane with the ternary feed mixture $H_2/CO_2/H_2O$ for different temperatures without sweep gas. Additionally, only at 100 °C, sweep gas was used. In addition at 100 °C the permeate side was swept with 1 ml/min N_2 at 1×10^5 Pa, see **b)**. The shown concentrations at 100 °C with N_2 sweep exclude the nitrogen content for comparison. (A colour version of this figure can be viewed online.)

constant value (Fig. 8b). If the sweep gas was used, a high mixed gas separation factor α (H_2O/H_2) = 270 was found and α^* (H_2/CO_2) increases from 1 (without sweep gas) to 6.1 (with sweep gas). This experiment shows the influence of membrane permeation conditions for the stationary method under non-equilibrium conditions for testing the membrane performance in the view of desired separation system.

3.3. Outlook towards the binary system ($H_2/EtOH$)

Finally, in the focus of bio-ethanol (EtOH) steam reforming for an intended catalytic membrane reactor, the mixed gas separation factor α ($H_2/EtOH$) was studied. In Table 8 the separation behaviour of hydrogen and ethanol (EtOH) is summarized for the three different carbon membranes under study at 150 °C. The **amorphous** and **crystalline carbon** membranes show a low selectivity α ($H_2/EtOH$) of around 2.7 whereas the **turbostratic carbon** membrane showed the highest selectivity of 20. In accordance with the permeation data of pressure- and temperature-dependent permeation results shown above, the rather low separation factor of the **amorphous carbon** membrane results from a higher adsorption of ethanol compared to the **turbostratic carbon** membrane as a function of hybridisation as mentioned before. In this context, the relative high selectivity of the **turbostratic carbon** membrane is rather explained by a lower adsorption of ethanol compared to hydrogen than in terms of molecular sieving. In the case of the **crystalline carbon** membrane the separation is lower than the calculated ideal Knudsen separation factor of α ($H_2/EtOH$) = 4.8 which results from the very small mean free path length λ of ethanol of around 21.6 nm in complete accordance to the pressure-dependent permeation data (see Section 3.2.1). It is calculated for a feed pressure of 3×10^5 Pa, a temperature of 150 °C, and with a molecule diameter of 4.5 Å [55].

Table 7

Mixed gas permeances P and corresponding mixed gas separation factors α for the **turbostratic carbon** membrane with nitrogen (N_2) as sweep gas (Feed side: 3.0×10^5 Pa, Sweep side: 1.0×10^5 Pa) at 100 °C, as shown in Fig. 8.

P (H_2)	P (CO_2)	P (H_2O)	α	α	α
[mol/m^2 s Pa]	[mol/m^2 s Pa]	[mol/m^2 s Pa]	H_2/CO_2	H_2O/H_2	H_2O/CO_2
9.3×10^{-11}	1.5×10^{-11}	2.5×10^{-08}	6.1	270	1645

Table 8

Mixed gas permeances P and corresponding mixed gas separation factors α ($H_2/EtOH$) using an equimolar feed ($H_2/EtOH$) mixture at 150 °C related to the binary feed conditions and a permeate pressure of 1.0×10^5 Pa.

Membrane	P (H_2)	P (EtOH)	α
	[mol/m^2 s Pa]	[mol/m^2 s Pa]	$H_2/EtOH$
Amorphous carbon	8.4×10^{-08}	3.0×10^{-08}	2.8
Turbostratic carbon	1.5×10^{-09}	7.4×10^{-11}	20.0
Crystalline carbon	3.6×10^{-09}	1.4×10^{-09}	2.6

4. Conclusions

Three different carbon membranes were investigated for the *in-situ* separation of hydrogen from the reaction mixture of bio-ethanol steam reforming for an intended catalytic membrane reactor operating at low temperatures ($\leq$ 400 °C). **Amorphous carbon** made by physical vapour deposition (PVD) of sublimated carbon from a glowing carbon fibre yarn on a porous alumina support, **turbostratic carbon** generated by pyrolysis of a supported polymer precursor film on a porous alumina support, and **crystalline carbon** from pressed graphite crystal flakes as self-supporting disc, were prepared and evaluated for binary H_2/CO_2, H_2/H_2O and also ternary $H_2/CO_2/H_2O$ gas mixture separation as a function of feed pressure and temperature.

Evaluating the separation features of the three carbon membranes under study for the equimolar binary feed mixture (H_2/CO_2), all carbon membranes were found to be hydrogen-selective in the range from 1.25 to 5.00×10^5 Pa feed pressure and from room temperature to 250 °C. In the case of the ternary feed mixture with 41 vol.-% H_2/41 vol.-% CO_2/18 vol.-% H_2O, between 100 and 250 °C, only for the **amorphous** and **crystalline carbon** membrane turned out to be hydrogen-selective. This preference for hydrogen (and not for steam) transport is in accordance with their hydrophobic character which follows from the contact angles. The **turbostratic carbon** membrane separates preferentially steam (H_2O) from the ternary feed mixture. Here, water is transported by selective surface diffusion which is in accordance to another sp^2/sp^3 ratio of hybridised carbon in comparison to the **amorphous carbon** membrane. For all three carbon membranes, the mixed gas separation factor α (H_2/H_2O) shows a stronger temperature-dependence than α (H_2/CO_2).

Results and Discussion: Microporous carbon membranes

The use of a **crystalline carbon** membrane coated with **amorphous carbon** should result in a probable mixed gas separation factor up to 10. Adding the **turbostratic carbon** layer, an *in-situ* extraction of hydrogen in ethanol steam reforming in a catalytic membrane reactor should give a separation factor up to $\alpha \, (H_2/CO_2) \approx 20$.

Acknowledgements

Appendix A. Supplementary data

Supplementary data related to this article can be found at http://dx.doi.org/10.1016/j.carbon.2016.04.062.

References

[1] M. Ni, D.Y.C. Leung, M.K.H. Leung, A review on reforming bio-ethanol for hydrogen production, Int. J. Hydrogen Energy 32 (2007) 3238–3247.
[2] Y. Men, G. Kolb, R. Zapf, V. Hessel, H. Löwe, Ethanol steam reforming in a microchannel reactor, IChemE 85 (2007) 413–418.
[3] A. Therdthianwong, T. Sakulkoakiet, S. Therdthianwong, Hydrogen production by catalytic ethanol steam reforming, ScienceAsia 27 (2001) 193–198.
[4] S. Cavallaro, Ethanol steam reforming on Rh/Al$_2$O$_3$ catalysts, Energy & Fuels 14 (2000) 1195–1199.
[5] M.D. Lazar, M. Dan, M. Mihet, G. Borodi, V. Almasan, Hydrogen production by ethanol steam reforming on Ni/oxide catalysts, AIP Conf. Proc. 1425 (2012) 131–134.
[6] V.V. Galvita, G.L. Semin, V.D. Belyaev, V.A. Semikolenov, P. Tsiakaras, V.A. Sobyanin, Synthesis gas production by steam reforming of ethanol, Appl. Catal. A General 220 (2001) 123–127.
[7] H.-S. Roh, A. Platon, Y. Wang, D.L. King, Catalyst deactivation and regeneration in low temperature ethanol steam reforming with Rh/CeO$_2$–ZrO$_2$ catalysts, Catal. Lett. 110 (2006) 1–6.
[8] H.-S. Roh, Y. Wang, D.L. King, A. Platon, Y.-H. Chin, Low temperature and H$_2$ selective catalysts for ethanol steam reforming, Catal. Lett. 108 (2006) 15–19.
[9] P. Ciambelli, V. Palma, A. Ruggiero, Low temperature catalytic steam reforming of ethanol. 1. The effect of the support on the activity and stability of Pt catalysts, Appl. Catal. B Environ. 96 (2010) 18–27.
[10] P. Ciambelli, V. Palma, A. Ruggiero, Low temperature catalytic steam reforming of ethanol. 2. Preliminary kinetic investigation of Pt/CeO$_2$ catalysts, Appl. Catal. B Environ. 96 (2010) 190–197.
[11] V. Palma, E. Palo, F. Castaldo, P. Ciambelli, G. Iaquaniello, Catalytic activity of CeO$_2$ supported Pt-Ni and Pt-Co catalysts in the low temperature bio-ethanol steam reforming, Chem. Engin. Trans. 25 (2011) 947–952.
[12] F. Gallucci, A. Basile, S. Tosti, A. Iulianelli, E. Drioli, Methanol and ethanol steam reforming in membrane reactors: an experimental study, Int. J. Hydrogen Energy 32 (2007) 1201–1210.
[13] S. Tosti, A. Basile, F. Borgognoni, V. Capaldo, S. Cordiner, S. Di Cave, F. Gallucci, C. Rizzello, A. Santucci, E. Traversa, Low temperature ethanol steam reforming in a Pd-Ag membrane reactor Part 1: Ru-based catalyst, J. Membr. Sci. 308 (2008) 250–257.
[14] G. Manzolini, S. Tosti, Hydrogen production from ethanol steam reforming: energy efficiency analysis of traditional and membrane processes, Int. J. Hydrogen Energy 33 (2008) 5571–5582.
[15] W.H. Lin, C.S. Hsiao, H.F. Chang, Effect of oxygen addition on the hydrogen production from ethanol steam reforming in a Pd-Ag membrane reactor, J. Membr. Sci. 322 (2008) 360–367.
[16] S. Tosti, A. Basile, L. Bettinali, F. Borgognoni, F. Gallucci, C. Rizzello, Design and process study of Pd membrane reactors, Int. J. Hydrogen Energy 33 (2008) 5098–5105.
[17] S. Tosti, Overview of Pd-based membranes for producing pure hydrogen and state of art at ENEA laboratories, Int. J. Hydrogen Energy 35 (2010) 12650–12659.
[18] S.H. Jung, K. Kusakabe, S. Morooka, S.D. Kim, Effects of co-exisiting hydrocarbons on hydrogen permeation through a palladium membrane, J. Membr. Sci. 170 (2000) 53–60.
[19] Y.S. Cheng, M.A. Peña, J.L. Fierro, D.C.W. Hui, K.L. Yeung, Performance of alumina, zeolite, palladium, Pd-Ag alloy membranes for hydrogen separation from towngas mixture, J. Membr. Sci. 204 (2002) 329–340.
[20] S. Uemiya, Brief review of steam reforming using a metal membrane reactor, T. Catal. 29 (2004) 79–84.
[21] D.W. Breck, Zeolite Molecular Sieves, John Wiley & Sons Inc., 1974.
[22] H.S. Kim, M. Shioya, A. Takaku, Sublimation and deposition of carbon during internal resistance heating of carbon fibres, J. Mat. Sci. 34 (1999) 4613–4622.
[23] P.S. Rao, M.Y. Wey, H.H. Tseng, I.A. Kumar, T.H. Wenig, A comparison of carbon/nanotube molecular sieve membranes with polymer blend carbon molecular sieve membranes for the gas permeation application, Micropor. Mesopor. Mater. 113 (2008) 499–510.
[24] A.F. Ismail, L.I.B. David, A review on the latest development of carbon membranes for gas separation, J. Membr. Sci. 193 (2001) 1–18.
[25] H.B. Park, I.Y. Suh, Y.M. Lee, Novel pyrolytic carbon membranes containing silica: preparation and characterization, Chem. Mater. 14 (2002) 3034–3046.
[26] A. Schulz, F. Steinbach, J. Caro, Pressed graphite crystals as gas separation membrane for steam reforming of ethanol, J. Membr. Sci. 469 (2014) 284–291.
[27] O. Beyssac, D. Ruble, Graphitic carbon: a ubiquitous, diverse, and useful geomaterial, Elements 10 (No. 6) (2014) 415–420.
[28] P.R. Buseck, O. Beyssac, From organic matter to graphite: graphitization, Elements 10 (2014) 421–426.
[29] D.R.G. Mitchell, B. Schaffer, Scripting-customised microscopy tools for Digital Micrograph^{TM}, Ultramicroscopy 103 (2005) 319–332.
[30] R. Kwok, Software for the Analysis of XPS Spectra, http://xpspeak.software.informer.com/4.1/.
[31] D.A. Shirley, High-Resolution X-Ray Photoemission Spectrum of the Valence Bands of Gold, Phys. Rev. B 5 (No. 12) (1972) 4709–4714.
[32] W.J. Koros, Y.H. Ma, T. Shimidzu, Terminology for membranes and membrane processes, Pure Appl. Chem. 68 (1996) 1479–1489.
[33] C.-D. Schönwiese, Gebrüder Borntraeger, Practical Statistic for Metereologists and Geoscienctists, third ed., 2000. Stuttgart.
[34] A.F. Hollemann, E. Wiberg, N. Wiberg, Textbook of Inorganic Chemistry 102, Walter de Gruyter & Co, 2007.
[35] J. Rouquerol, D. Avnir, D.H. Everett, C. Fairbridge, M. Haynes, N. Pernicone, J.D.F. Ramsay, K.S.W. Sing, K.K. Unger, Guidelines for the characterization of porous solids, Stud. Surf. Sci. Catal. 87 (1994) 1–9.
[36] H.W. Haynes, A note on diffusive mass transport, Chem. Eng. Ed. 20 (1986) 22–27.
[37] J. Kärger, D.M. Ruthven, D.N. Theodorou, Diffusion in Nanoporous Materials, vol. 1, Wiley-VCH, 2012.
[38] R. Krishna, J.M. van Baten, Investigating the relative influences of molecular dimensions and binding energies on diffusivities of guest species inside nanoporous crystalline materials, J. Phys. Chem. 116 (2012) 23556–23568.
[39] R. Krishna, Describing the diffusion of guest molecules inside porous structures, J. Phys. Chem. C 113 (2009) 19756–19781.
[40] L. Bragg, G.F. Claringbull, Crystal Structures of Minerals, vol. 4, G. Bell and Sons, LTD, London, 1965, pp. 32–34.
[41] K.H. Homann, Fullerenes and soot formation: new pathways to large particles in flames, Angew. Chem. Int. Ed. 37 (1998) 2434–2451.
[42] F. Tuinstra, J.L. Koenig, Raman spectrum of graphite, J. Chem. Phys. 53 (No. 3) (1969) 1126–1130.
[43] A. Sadezky, H. Muckenhuber, H. Grothe, R. Niessner, U. Pöschl, Raman microscopy of soot and related carbonaceous materials: spectral analysis and structural information, Carbon 43 (2005) 1731–1742.
[44] P. Mérel, M. Tabbal, M. Chaker, S. Moisa, J. Margot, Direct evaluation of sp^3 content in diamond-like-carbon films by XPS, Appl. Surf. Sci. 136 (1998) 105–110.
[45] A.C. Ferrari, J. Robertson, Interpretation of Raman spectra of disordered and amorphous carbon, Phys. Rev. B 20 (2000) 14095–14107.
[46] A.C. Ferrari, J. Robertson, Raman spectroscopy of amorphous, nanostructured, diamond-like carbon, and nano diamond, Phil. Trans. R. Soc. Lond. A 362 (2004) 2477–2512.
[47] C. Casiraghi, A.C. Ferrari, J. Robertson, Raman spectroscopy of hydrogenated amorphous carbons, Phys. Rev. B 72 (2005), 085401–1(-14).
[48] J.L. Mansot, V. Golabkan, L. Romana, T. Césaire, Chemical and physical characterization by EELS of strontium hexanoate reverse micelles and strontium carbonate nanophase produced during tribological experiments, J. Microsc. 210 (2003) 110–118.
[49] C. Nordling, ESCA: Electron spectroscopy for chemical analysis, Angew. Chem. Intern. Ed. 11 (1972) 83–92.
[50] U. Gellius, P.F. Hedén, B.J. Lindberg, R. Manne, R. Nordberg, C. Nordling, K. Siegbahn, Molecular spectroscopy by means of ESCA, Phys. Scr. 2 (1970) 70–80.
[51] G.P. Lopéz, D.G. Castner, B.D. Ratner, XPS O 1s binding energies for polymers containing hydroxyl, ether, ketone and ester groups, Surf. Interface Anal. 17 (1991) 267–272.
[52] J. Caro, Fluid Flow, in: F. Schüth, K.S.W. Sing, J. Weitkamp (Eds.), Handbook of Porous Solids, vol. 1, Wiley-VCH, Weinheim, 2002, pp. 352–370.
[53] M. Mulder, Handbook of Membrane Technology, Kluwer Academic Publisher, Dordrecht, 1996, pp. 226–227.
[54] P.W. Atkins, J. de Paula, in: Textbook of Physical Chemistry, vol. 4, Wiley-VCH, Weinheim, 2006.
[55] T. Borjigin, F. Sun, J. Zhang, K. Cai, H. Ren, G. Zhu, A microporous metal-organic framework with high stability for GC separation of alcohols from water, Chem. Commun. 48 (2012) 7613–7615.

3.1.2. Manuscript:"Effect of steam containing gas mixtures on the separation performance of amorphous, turbostratic and crystalline carbon membranes"

Authors: **A. Wollbrink**, K. Volgmann, J. Koch, K. Kanthasamy, C. Tegenkamp, Y. Li, H. Richter, S. Kämnitz, J. Caro

(Not published results)

Effects of steam containing gas mixtures on the separation performance of amorphous, turbostratic and crystalline carbon membranes

A. Wollbrink[a,b*], K. Volgmann[a,b], J. Koch[c], K. Kanthasamy[c], C. Tegenkamp[c], Y. Li[d], H. Richter[e], S. Kämnitz[e], J. Caro[a,b]

[a] *Institute of Physical Chemistry and Electrochemistry, Leibniz University Hannover, Callinstr. 3A, D-30167 Hannover, Germany*

[b] *ZFM – Center for Solid State Chemistry and New Materials, Leibniz University Hannover, Callinstr. 3 – 3A, D-30167 Hannover, Germany*

[c] *Institute of Solid State Physics, Leibniz University Hannover, Appelstr. 2, D-30167 Hannover, Germany*

[d] *State Key Laboratory of Catalysis, Dalian Institute of Chemical Physics, Chinese Academy of Sciences, CN-116023 Dalian, China*

[e] *Fraunhofer Institute of Ceramic Technologies and Systems IKTS, Michael-Faraday-Str. 1, D-07629 Hermsdorf, Germany*

Abstract:

For three carbon membranes: (i) an amorphous, (ii) a turbostratic and (iii) a crystalline carbon membrane, the effects of steam containing gas mixtures on their H_2/CO_2 separation performance were studied. Permeation experiments of the three carbon membranes were carried out with a steam content of 18 vol.-% in the feed for at least 72 hours up to 250 °C. Measuring the permeation of an equimolar binary feed mixture (H_2/CO_2) showed dramatic changes in the separation performance between the as-synthesised and steam-exposed carbon membranes. In accordance with these data, X-ray photoelectron spectroscopy analysis revealed chemical changes on the surfaces of all carbon membranes which differently change their separation mechanism due to steam exposure. For the amorphous and turbostratic carbon membranes, the transmembrane flow was reduced up to 73 % whereas the flow through the crystalline one remained unchanged. The corresponding mixed gas separation factor α (H_2/CO_2) was halved for the amorphous carbon from 3 to 1.6, was improved for the turbostratic carbon from 6 to 8 and was unchanged with a selectivity of 4.7 for the crystalline carbon. These data revealed the importance of comparative studies for the degradation behaviour of different kinds of carbons.

Keywords: Carbon membranes; permeation induced alteration; Gas separation; Hydrogen separation; XPS/ESCA.

* Corresponding author. phone: (+49)51176214427. E-mail: alexander.wollbrink@pci.uni-hannover.de (Alexander Wollbrink)

2

1. Introduction

Steam reforming of e.g. bio-ethanol or bio-methane, is performed at high temperatures in terms of full conversion [1]. When steam reforming is executed at temperature below 400 °C, the formation of by-products, e.g. carbon monoxide, is reduced while the conversion tends to be rather low [2,3]. Therefore, the selective removal of hydrogen from the product-side of a steam reformer becomes attractive to enhance the reaction to full conversion by the use of a hydrogen-selective membrane (-reactor). In this context, we evaluated three carbon membranes which were classified as an amorphous, a turbostratic and a crystalline carbon membrane by micro-focused Raman spectroscopy [4].

Structural analyses of the three carbon membranes under study allow to classify the amorphous and turbostratic carbon membrane as microporous whereas the extra-crystalline voids of the crystalline carbon membrane are in the mesoporous dimension, in accordance with the IUPAC classification [4,5]. Temperature-dependent permeation experiments up to 250 °C showed decreasing mixed gas permeances of H_2 and CO_2 of about 60% with an almost constant mixed gas separation factor α (H_2/CO_2) of 2.8 for the amorphous and of 4.6 for the crystalline carbon membrane [4]. Contrary to that, the turbostratic carbon membrane showed increasing mixed gas permeances preferable of H_2 compared with CO_2 which results in an increased hydrogen selectivity from 1.9 to 6.0 with rising temperature.

In principle, carbon-based materials offer some suitable properties such as chemical and thermal stability, hydrogen selectivity and hydrophobicity at certain conditions. In this study, we show the effects of steam containing gas mixtures on the separation performance of amorphous, turbostratic and crystalline carbon membranes. Therefore, an equimolar binary feed mixture (H_2/CO_2) is selected as probe mixture for permeation studies between 100 and 250 °C. The reported analyses show very well the surface-property relationships of the effects arising from steam containing gas mixtures on three different carbon membranes by the use of X-ray photoelectron spectroscopy (XPS) in the context of the identified separation mechanisms, as described in ref. [4]. Furthermore, the analyses of the underlying bulk materials are given by transmembrane permeation experiments.

3

2. Experimental

The amorphous carbon membrane was generated by sublimation and deposition of a carbon fibre yarn on a porous alumina support which formed a crack-free carbon layer of 300 nm thickness. The turbostratic carbon membrane was made by controlled pyrolysis of a polyester precursor layer on a porous alumina support at 500 °C in Argon atmosphere and formed a crack-free carbon layer with a thickness of 8 µm. The used porous alumina supports had a diameter of 18 mm and a thickness of 1 mm. The crystalline carbon membrane was prepared by pressing graphite flakes to 1 mm thick discs. All synthesis parameters are described in detail, see ref. [4].

For the evaluation of mixed gas permeation and mixed gas separation we used an equimolar binary feed mixture of (H_2/CO_2). The steam containing permeation experiments were carried out in a permeation unit using a steam content of about 18 vol.-% for at least 72 h. Here, the membranes were stepwise heated from 100 to 250 °C and dried for several hours in the binary feed mixture of (H_2/CO_2) at 250 °C. The mixed gas permeances and separation factors were determined as a function of temperature. The mixed gas separation factor α *(i,j)* of the binary (H_2/CO_2) mixture was given by the ratio of the individual mixed gas permeances P (pressure-normalised flux) with respect to the sum of the permeances of the components *i* or *j* analysed by an online coupled gas chromatograph. The description of the experimental methods and our setup can be found in detail in ref. [4].

Regarding the XPS experiments, the analysis were performed with a non-monochromatic X-ray source using an Al-K_α emission (SPECS XR-50, 100W, 54° incident angle, excited area of about 1 cm^2). The kinetic energies of the photoelectrons were measured with a hemispherical analyser (SPECS-PHOIBOS 100, Detector: MCD-5) with 30 scans and a pass energy of 20 eV. All XPS spectra are shown as a function of binding energy with respect to the Fermi level. The photoelectron peak areas are calculated after background corrections using the Shirley algorithm described in ref. [6].

In the shown measurements the stochastic error of mixed gas permeances and related separation factors are plotted following the equations for error propagation after Gauss [7]. The stochastic standard deviations of the permeate composition and the total flow measurements are included to the shown errors.

4

3. Results and discussion

3.1 Surface analysis by X-ray photoelectron spectroscopy (XPS)

Surface analysis of the *as-synthesised* membranes show for the **amorphous carbon** membrane two main C 1s signals with a binding energy at 285.5 eV ± 0.1 eV (I) and at 286.5 eV ± 0.1 eV (II), see **Fig. 1a**. In accordance with literature, these two C 1s signals are assigned to different hybridisation states [8]. Signal I corresponds with the sp^2-hybridisation state of carbon while signal II is related to the sp^3-configuration of carbon. The ratio of sp^2/sp^3 hybridised carbon was calculated from their integral signal intensities of about 1:2 (see **Table 1, Scheme 1**). Other signals are observed at 289.5 eV ± 0.1 eV (V) which are attributed to some carboxyl groups and also some CF_x groups at 293.5 eV ± 0.1 eV (VII) [9,10]. Here, the attributed fluorine signal VII (CF_3 groups) originates from some contamination of the used O-ring (F source) which is used for the gas-tight sealing of the disc membranes in the permeation unit. After long-term permeation experiments at temperatures up to 250 °C some sealing material can remain on the membrane surface after it was detached. Comparative surface analysis of the **amorphous carbon** membrane shows, *after the exposure with a steam containing gas mixture,* a reversed sp^2/sp^3 ratio of about 2:1 compared with the ratio of the as-synthesised one of 1:2 (see **Fig. 1a**, **Table 1**). The observed carboxyl groups at 289.3 eV ± 0.1 eV (V) are slightly reduced from 7.3 % to 5.5 %.

For the **turbostratic carbon** membrane, also two signals at 285.4 ± 0.1 eV (I) and at 286.4 eV ± 0.1 eV (II) are observed, see **Fig. 2a**. These two signals are also identified as differently hybridised carbons but with a sp^2/sp^3 ratio of about 2:1 (see **Table 2**). Furthermore, two additional signals with lower intensity are found at 288.4 eV ± 0.1 eV (IV) which is attributed to carbonyl groups (C=O) and also some carboxyl groups at 289.4 eV ± 0.1 eV (V) (see **Table 2, Scheme 1**). Surface analysis of the **turbostratic carbon** membrane shows, *after the exposure with steam*, that the integral intenisties of signals I and II were reduced to 34.6 % of the intensity of the former C 1s spectrum while an additional signal becomes visible at 286.9 eV ± 0.1 eV (III) and displays with 57.7 % the main signal intensity. In accordance with literature, signal III corresponds to hydroxyl groups (C-OH), see **Fig. 2a. Table 2** [9].
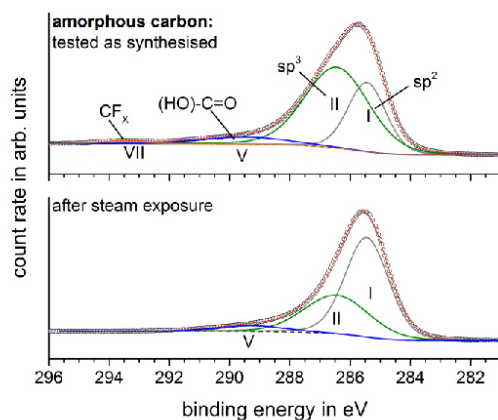
5

Fig. 1a: Amorphous carbon membrane characterised by means of XPS surface analysis.
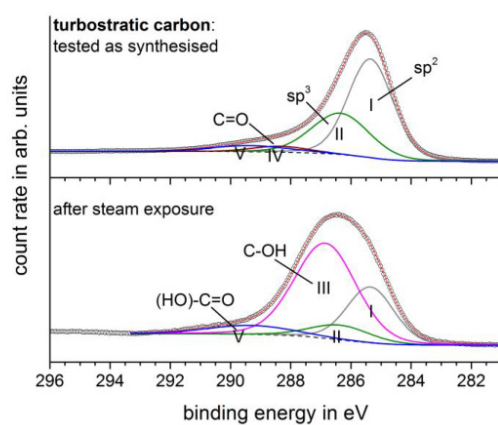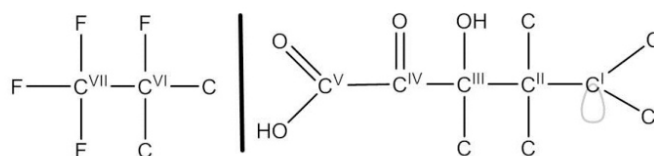

Fig. 2a: Turbostratic carbon membrane characterised by means of XPS surface analysis.

Scheme 1: Overview of all identified signals of the three carbon membranes under study observed in the XPS C 1s spectra as given in **Tables 1-3**.

6

Table 1: X-ray photoelectron spectroscopy (XPS) of the **amorphous carbon** membrane surface for the cases: (**i**) as-synthesised and (**ii**) after steam exposure. With E_B: binding energy, FWHM: full width at half maximum, Area: signal areas in percentage for each spectrum (see **Figs. 1a**).

| carbon membrane | peak | C 1s | | | signal classification after refs. [8,9,11,12,10] |
		E_B in eV	FWHM in eV	Area in %	
amorphous (as-synthesised)	I	285.5	1.5	30.8	sp^2
	II	286.5	2.5	60.6	sp^3
	V	289.5	3.4	7.3	O=C-OH
	VII	293.5	1.8	1.2	CF_X
(after steam exposure)	I	285.5	1.7	60.0	sp^2
	II	286.5	2.5	34.6	sp^3
	V	289.3	2.6	5.5	O=C-OH

Table 2: X-ray photoelectron spectroscopy (XPS) of the **turbostratic carbon** membrane surface for the cases: (**i**) as-synthesised and (**ii**) after steam exposure. With E_B: binding energy, FWHM: full width at half maximum, Area: signal areas in percentage for each spectrum (see **Figs. 2a**).

| carbon membrane | peak | C 1s | | | signal classification after refs. [8,9,11,12,10] |
		E_B in eV	FWHM in eV	Area in %	
turbostratic (as-synthesised)	I	285.4	1.8	58.1	sp^2
	II	286.4	2.3	31.2	sp^3
	IV	288.4	2.2	4.3	C=O
	V	289.4	3.1	6.3	O=C-OH
(after steam exposure)	I	285.4	1.8	25.9	sp^2
	II	286.4	2.4	8.7	sp^3
	III	286.9	2.4	57.7	C-OH
	V	289.4	3.4	7.6	O=C-OH

7

XPS analysis of the **crystalline carbon** membrane also reveals, in comparison with the amorphous or turbostratic carbon membrane, two dominant signals at 284.1 ± 0.1 eV (I) and at 285.1 eV ± 0.1 eV (II) which we attribute to differently hybdridised carbons with an sp^2/sp^3 ratio of about 2.5 (see **Fig. 3a**, **Table 3**). Other signals are attributed to some carbonyl groups at 287.1 eV ± 0.1 eV (IV), carboxyl groups at 288.1 eV ± 0.1 eV (V) and also flourine groups at 290.7 eV ± 0.1 eV (VI) and at 294.0 eV ± 0.1 eV (VII) [11,12]. Analysis of the crystalline carbon surface, *after the exposure with steam*, revealed a decrease of about 10 % of signal I (sp^2-hybridised carbon) whereas the intensity of signal II (sp^3-hybridised carbon) is increased of about 10 %, see **Fig. 3a**, **Table 3**. Furthermore, the signal intensity of carboxyl groups at 290.5 eV ± 0.1 eV (V) is increased by a factor of 3, but the other signals, described before, are strongly decreased in their integral intensity.
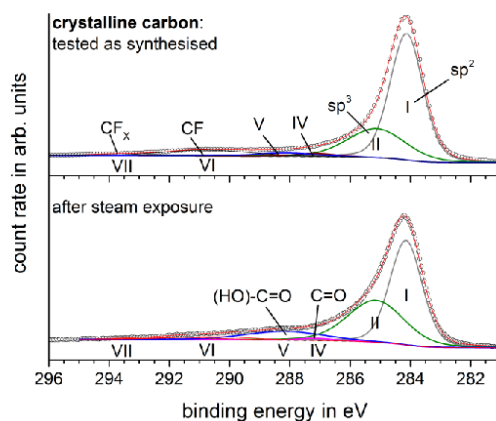
Fig. 3a: Crystalline carbon membrane characterised by means of XPS surface analysis.

8

Table 3: X-ray photoelectron spectroscopy (XPS) of the **crystalline carbon** membrane surface for the cases: (**i**) as-synthesised and (**ii**) after steam exposure. With E_B: binding energy, FWHM: full width at half maximum, Area: signal areas in percentage for each spectrum (see **Figs. 3a**).

carbon membrane	peak	C 1s			signal classification after refs. [8,9,11,12,10]
		E_B in eV	FWHM in eV	Area in %	
crystalline (as-synthesised)	I	284.1	1.3	61.6	sp^2
	II	285.1	2.3	24.9	sp^3
	IV	287.1	1.5	1.8	C=O
	V	288.1	2.4	3.1	O=C-OH
	VI	290.7	3.5	7.9	CF
	VII	294.0	1.7	0.8	CFx
(after steam exposure)	I	284.2	1.3	49.1	sp^2
	II	285.2	2.2	34.6	sp^3
	IV	287.2	1.4	1.1	C=O
	V	288.2	3.0	10.0	O=C-OH
	VI	290.5	3.1	3.2	CF
	VII	291.5	3.2	2.1	CFx

9

3.2 Membrane permeation and separation

In temperature-dependent permeation experiments, two different trends are commonly found for the three carbon membranes under study, described in full detail in ref. [4]. The **amorphous** and **crystalline carbon** membranes show a similar decrease of the mixed gas permeances of H_2 and CO_2 between 100 and 250 °C of about 60% with an almost constant mixed gas separation factor α (H_2/CO_2) of 2.8 for the amorphous and of 4.6 for the crystalline carbon membrane (see **Figs. 1b-c**, **3b-c**). Contrary to that, for the **turbostratic carbon** membrane the mixed gas permeances of H_2 increased more than compared with CO_2 which results in a temperature-dependent hydrogen selectivity from 1.9 to 6.0 with rising temperature (see **Figs. 2b-c**).

Permeation experiments, *after the exposure with steam*, reveal for the **amorphous carbon** membrane decreased mixed gas permeances of H_2 (-46 %) and CO_2 (-13 %) between 100 and 200 °C (see **Fig. 1b**). The related mixed gas separation factor α (H_2/CO_2) of the steam-exposed **amorphous carbon** membrane drops from 2.8 (as-synthesised) to a halved separation factor of about 1.7 (see **Fig. 1c**).
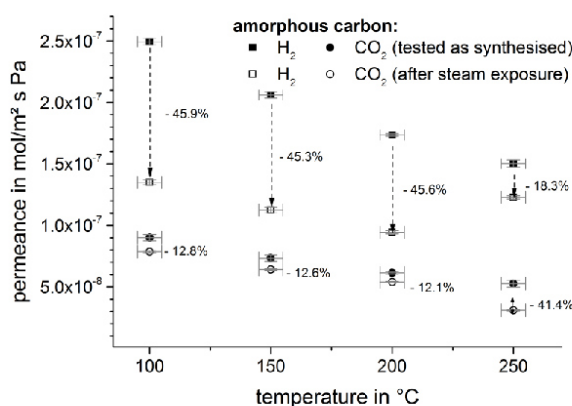
Fig. 1b: Temperature-dependent permeation experiments for the evaluation of mixed gas permeances of the amorphous carbon membrane.

10
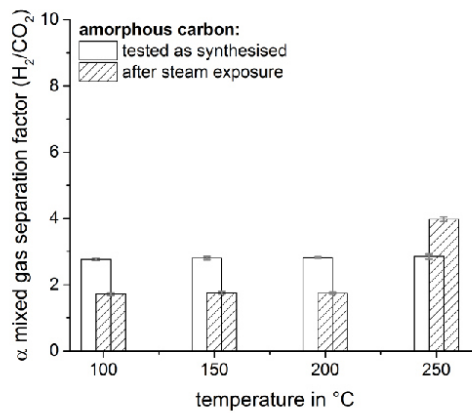
Fig. 1c: Corresponding mixed gas separation factor α (H_2/CO_2) of Fig. 1b.

This effect changes only at 250 °C where α (H_2/CO_2) rises from 1.7 to 4. Permeation experiments, after the exposure with steam, show for the **turbostratic carbon** membrane an almost systematic decrease of the mixed gas permeances of H_2 (-60 %) and CO_2 (-70 %) between 100 and 250 °C (see **Fig. 2b**). Since this decrease is smaller for H_2 in comparison with CO_2, α (H_2/CO_2) increases from 3.8 to 4.2 (+10%) at 100 °C and 6.0 to 8.0 (+33%) at 250 °C (see **Fig. 2c**).
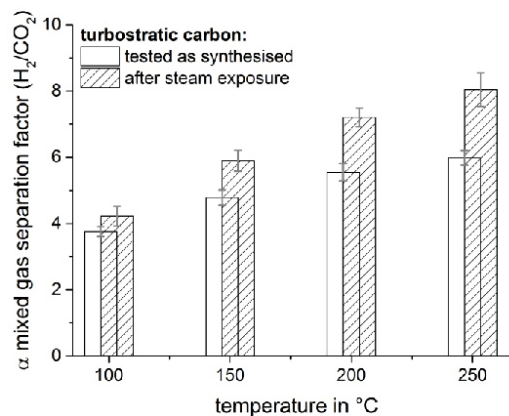
Fig. 2b: Temperature-dependent permeation experiments for the evaluation of mixed gas permeances of the turbostratic carbon membrane.

11
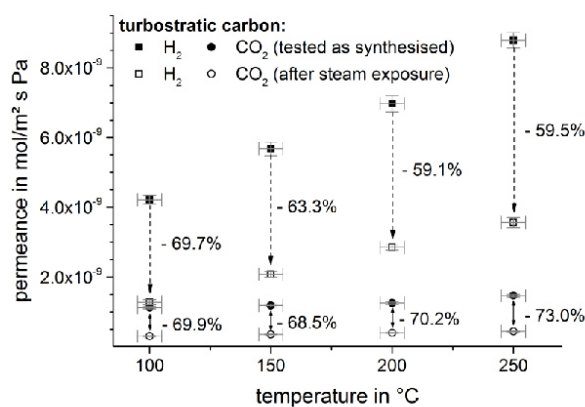
Fig. 2c: Corresponding mixed gas separation factor α (H_2/CO_2) of Fig. 2b.

Comparative permeation experiments between the **crystalline carbon** membrane for the as-prepared and steam-exposed samples showed no relative changes of the mixed gas permeances of H_2 and CO_2 between 100 and 250 °C which is confirmed by the almost stable hydrogen selectivity of about 4.5 (see **Figs. 3b-c**).
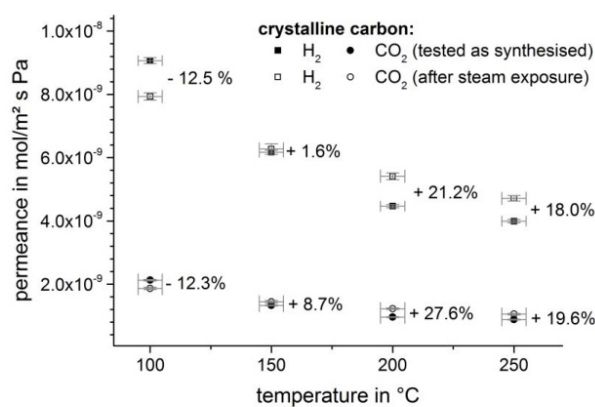
Fig. 3b: Temperature-dependent permeation experiments for the evaluation of mixed gas permeances of the crystalline carbon membrane.
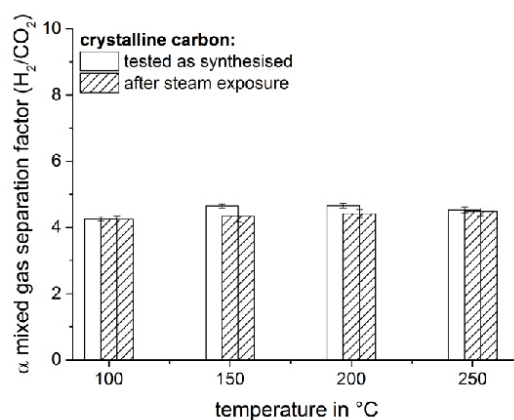
Fig. 3c: Corresponding mixed gas separation factor α (H_2/CO_2) of Fig. 3b.

All permeation experiments showed that the general behaviour of the **amorphous**, **turbostratic** and **crystalline carbon** membrane remained unchanged after the exposure with a steam containing gas mixture. The **amorphous** and **turbostratic carbon** membrane showed opposite permeation and separation performances although both membranes were classified as microporous with comparable effective pore diameter distributions between 0.10 and 1.06 nm with a maximum at 0.29 nm [4,5]. The effective pore size in microporous materials is in the order of the molecule diameters (H_2O: 0.26 nm H_2: 0.29 nm and CO_2: 0.33 nm) [13]. The selectivity of microporous membranes is closely related to the interplay of diffusion selectivity as well as adsorption selectivity. Their different effects are discussed in literature [14,15]. Therefore, the difference between the **amorphous** and **turbostratic carbon** membrane is their chemical composition, or in this case, their hybridisation states of carbon plus the presence of different functional groups, as carbonyl, carboxyl groups or others [16]. These chemical differences have directly or indirectly huge effects on the interactions between the permeating gases passing the pore walls in microporous solids [17].

In this context, the decreased separation performance of the **amorphous carbon** surface, after the exposure with steam between 100 and 250 °C, is displayed by the change from a sp^3- to a sp^2-hybridised carbon dominated surface as well as pore surface (see **Fig. 1a**). The presence of C-H bonds can not to be distinguished from sp^2-hybridised carbon in XPS, but can be excluded from the discussion here by the lack of additional hydroxyl groups (C-OH) as

13

expected for an partial dissociative adsorption of water on the carbon surface and is also not reported for carbon materials made by PVD methods, see **Scheme 1** [16,18]. The decreased mixed gas permeances and hydrogen selectivity support the compositional changes observed by XPS analysis (see **Figs. 1a-c**). The decrease of sp^3-hybridised carbon (aliphatic) can be interpreted as a loss of the carbon connectivity which should be followed by a loss of hydrogen selectivity, as observed from permeation data. In this case, the relative transmembrane flow should be increased, which is obviously not the case (see **Fig. 1b**). However, if the formation of sp^2-hybridised carbon (aromatic) results in C_6-rings, which are impermeable for (H_2, CO_2), the transmembrane flow should decrease. Furthermore, the mixed gas permeance of H_2 is probably stronger reduced by these changes than the permeance of CO_2 since the smallest pores should be much more affected here than the bigger ones, as observed in mixed gas permeances (see **Fig. 1c**).

In the case of the **turbostratic carbon** membrane an additional signal at 286.9 eV ± 0.1 eV (III) attributed to hydroxyl groups (C-OH) is observed after steam exposure at the expense of sp^2/sp^3 hybridised carbon (see **Fig. 2a**). The presence of hydroxyl groups on the membrane surface as well as pore surface in the case of the **turbostratic carbon** membrane may result from the low carbonisation temperature of 500 °C which can be related to a metastable state of carbon from the pyrolysed polyester precursor [4]. An indication may be here the occurrence of signal IV at 288.4 eV ± 0.1 eV which is only present for the as-synthesised **turbostratic carbon** membrane. Nevertheless, the **turbostratic carbon** membrane shows the highest changes of its separation performance displayed by the change of a pure carbon to a C-OH dominated surface or pore surfaces. Consequently, the increase of the mixed gas separation factor α (H_2/CO_2) results from two possible effects: (**a**) from the change of the surface composition which affects its adsorption behaviour or (**b**) from steric hindrance, since the micropores were effectively narrowed by the formation of hydroxyl groups. An increase of the permeances is characteristic of thermally activated processes which is the case for a selective surface diffusion transport mechanism [4]. In this case, steric hindrance should be the main reason for the increased mixed gas separation performance. Therefore, the reduced permeances are also related to the increased apparent activation energies for H_2 and CO_2 permeation from about 8 kJ/mol to 11.0 kJ/mol and from about 2.8 kJ/mol to 4.0 kJ/mol respectively (see **Fig. 4**, **Table 4**). These data are in accordance with values reported in literature where the activation energy (E_A) of H_2 varies typically between 2 and 35 kJ/mol for microporous membranes [19]. The higher activation energy of the H_2 permeation compared

14

with the permeation of CO_2 is commonly observed in microporous membranes related to the selective surface mechanism [20,21].

Although changes of the crystalline carbon surface are observed (see **Fig. 3a**), the separation performance of H_2 and CO_2 remains almost not affected (see **Figs. 3b-c**) due to its separation mechanism which is based on the momentum transfer of molecule-wall collisions [4].
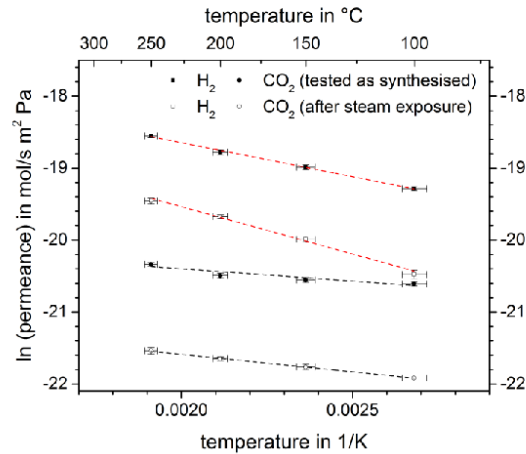

Fig. 4: Arrhenius plot for the hydrogen and carbon dioxide mixed gas permeances of the (i) as-synthesised (dashed line, red) and (ii) after steam exposure (dashed line, black) **turbostratic carbon** membrane as a function of the reciprocal temperature (see **Table 4**).

Table 4: Data collection of the apparent activation energies, calculated from the slope of hydrogen and carbon dioxide permeances of the **turbostratic carbon** membrane: (**i**) as-synthesised and (**ii**) after steam exposure, shown in **Fig. 4**.

gases	function	E_A in kJ/mol
H_2 (as-synthesised)	$f(1/T) = -945.89 \left(\dfrac{1}{T}\right) - 16.75, R^2 = 0.99$	7.87
H_2 (steam modified)	$f(1/T) = -1317.17 \left(\dfrac{1}{T}\right) - 16.90, R^2 = 0.99$	10.95
CO_2 (as-synthesised)	$f(1/T) = -337.35 \left(\dfrac{1}{T}\right) - 19.73, R^2 = 0.90$	2.81
CO_2 (steam modified)	$f(1/T) = -486.00 \left(\dfrac{1}{T}\right) - 20.62, R^2 = 0.99$	4.04

15

4. Conclusions

The effects arising from steam containing gas mixtures on carbon-based membranes were analysed by mixed gas permeation and X-ray photoelectron spectroscopy studies. Therefore, an amorphous, a turbostratic and a crystalline carbon membrane were investigated for two different cases: (i) as-synthesised and (ii) steam-exposed samples. For the microporous carbon membranes, the transmembrane flow was reduced up to 73 %. Permeation experiments of the steam-exposed carbon membranes showed for the amorphous carbon membrane a halved mixed gas separation factor α (H_2/CO_2) from 3 to 1.6, for the turbostratic carbon membrane an improved selectivity from 6 to 8 (+33%). In accordance with these data, XPS analyses revealed a shift in its hybridisation ratio (sp^2: aromatic-C/sp^3: aliphatic-C) for the amorphous carbon membrane and the formation of hydroxyl groups for the turbostratic carbon membrane after the exposure in steam at temperature up to 250 °C. For the crystalline carbon membrane, the relative mixed gas permeances of H_2 and CO_2 remained unchanged with a hydrogen-selectivity of about 4.7, independent from the observed chemical changes of the surfaces.

16

References

---

[1] M. Ni, D.Y.C. Leung, M.K.H. Leung, A review on reforming bio-ethanol for hydrogen production, Int. J. Hydrogen Energy 32 (2007) 3238-3247.

[2] V. Palma, E. Palo, F. Castaldo, P. Ciambelli, G. Iaquaniello, Catalytic activity of CeO_2 supported Pt-Ni and Pt-Co catalysts in the low temperature bio-ethanol steam reforming, Chem. Engin. Trans. 25 (2011) 947-952.

[3] V. Palma, E. Palo, F. Castaldo, P. Ciambelli, G. Iaquaniello, Catalytic activity of CeO_2 supported Pt-Ni and Pt-Co catalysts in the low temperature bio-ethanol steam reforming, Chem. Engin. Trans. 25 (2011) 947-952.

[4] A. Wollbrink, K. Volgmann, J. Koch, K. Kanthasamy, C. Tegenkamp, Y. Li, H. Richter, S. Kämnitz, F. Steinbach, A. Feldhoff, J. Caro, Amorphous, turbostratic and crystalline carbon membranes with hydrogen selectivity, Carbon 106 (2016) 93-105.

[5] J. Rouquerol, D. Avnir, D. H. Everett, C. Fairbridge, M. Haynes, N. Pernicone, J. D. F. Ramsay, K.S.W. Sing, and K.K. Unger, Guidelines for the characterization of porous solids, Studies in Surface Science and Catalysis, Vol. 87 (1994) 1-9.

[6] D.A. Shirley, High-resolution x-ray photoemission spectrum of the valence bands of gold, Phys. Rev. B, 5, No. 12 (1972) 4709-4714.

[7] C.-D. Schönwiese, Gebrüder Borntraeger, Textbook of practical statistic for metereologists and geosciencists. 3rd Edition, Stuttgart; 2000.

[8] P. Mérel, M. Tabbal, M. Chaker, S. Moisa, J. Margot, Direct evaluation of sp³ content in diamond-like-carbon films by XPS, Appl. Surf. Sci. 136 (1998) 105-110.

[9] G. Nguila Inari, M. Petrissans, J. Lambert, J.J. Ehrhardt and P. Gérardin, XPS characterization of wood chemical composition after heat-treatment, Surf. Interface Anal. 38 (2006) 1336-1342.

[10] W.-K. Lee, I. Losito, and J.A. Gardella, Jr., Synthesis and Surface properties of fluorocarbon end-capped biodegradable polyester, Macromolecules 34 (2001) 3000-3006.

[11] C. Nordling, ESCA: Electron spectroscopy for chemical analysis, Angew. Chem. Internat. Edit. 11 (1972) 83-92.

[12] U. Gellius, P.F. Hedén, B.J. Lindberg, R. Manne, R. Nordberg, C. Nordling and K. Siegbahn, Molecular spectroscopy by means of ESCA, Physica Scripta 2 (1970) 70-80.

[13] D.W. Breck, John Wiley & Sons Inc., Zeolite molecular sieves. 1974.

17

[14] R. Krishna, J.M. van Baten, Investigating the relative influences of molecular dimensions and binding energies on diffusivities of guest species inside nanoporous crystalline materials, J. Phys. Chem. 116 (2012) 23556-23568.

[15] R. Krishna, Describing the diffusion of guest molecules inside porous structures, J. Phys. Chem. C 113 (2009) 19756-19781.

[16] F. Rodríguez-Reinoso, Speciality Carbons, in: F. Schüth, K.S. Sing and J. Weitkamp: Hanbook of porous solids, Vol. 3, Wiley-VCH, Weinheim, 2002, pp. 1799-1801.

[17] J. Kärger, D.M. Ruthven, D.N. Theodorou, Diffusion in Nanoporous Materials, Vol. 1, Wiley-VCH, Weinheim, 2012, 85-109.

[18] P. Cabrera-Sanfelix and G.R. Darling, Dissociative adsorption of water at vacancy defects in graphite, J. Phys. Chem. 111 (2007) 18258-18263.

[19] H. Jin, A. Wollbrink, R.Yao, Y. Li, J. Caro, W. Yang, A novel CAU-10-H MOF membrane for hydrogen separation under hydrothermal conditions, J. Membr. Sci. 513 (2016) 40-46.

[20] De Lange, R. S. A., K. Keizer, and A. J. Burggraaf, Analysis and theory of gas transport in microporous sol-gel derived ceramic membranes, J. Membr. Sci. 104 (1995) 81-100.

[21] Koutsonikolas, D., S. Kaldis, and G. P. Sakellaropoulos, A low-temperature CVI method for pore modification of sol–gel silica membranes, J. Membr. Sci. 342 (2009) 131-137.

18

3.1.3. Manuscript: "Separation performance of a composite Carbon Molecular Sieve (cCMS/SiO₂) membrane from a hybrid material by twin polymerization"

Authors: **A. Wollbrink**, T. Ebert, J. Koch, C. Tegenkamp, S. Spange, J. Caro

(Not published results)

Separation performance of a composite Carbon Molecular Sieve (cCMS/SiO$_2$) membrane obtained from a hybrid material synthesised by twin polymerisation

A. Wollbrink[a,b*], T. Ebert [c], J. Koch[d], C. Tegenkamp[d], S. Spange [c], J. Caro[a,b]

[a] *Institute of Physical Chemistry and Electrochemistry, Leibniz University Hannover, Callinstr. 3A, D-30167 Hannover, Germany*

[b] *ZFM – Center for Solid State Chemistry and New Materials, Leibniz University Hannover, Callinstr. 3, D-30167 Hannover, Germany*

[c] *Institute of Chemistry, Professorship Polymer Chemistry, Straße der Nationen 62, D-09111 Chemnitz, Germany*

[d] *Institute of Solid State Physics, Leibniz University Hannover, Appelstr. 2, D-30167 Hannover, Germany*

1

Abstract:

A composite Carbon Molecular Sieve (cCMS/SiO$_2$) membrane was evaluated by permeation experiments for being a suitable membrane for a catalytic membrane reactor in bio-ethanol steam reforming below 400 °C. The cCMS/SiO$_2$ membrane was obtained by carbonisation of a hybrid material, synthesised by the thermally induced twin polymerisation of 2,2′-spirobi[4H-1,3,2-benzodioxasiline]. The concept of nanostructured hybrid materials as membranes is a suitable approach since it allows the synthesis of materials with tailored properties, e.g. the domain sizes are adjustable by the choice of monomers. X-ray diffraction data of the cCMS/SiO$_2$ membrane revealed an effective pore diameter distribution between 1.0 and 4.3 Å for the carbon matrix and HAADF-STEM micrographs a silica domain size of about 2.0 nm. Permeation experiments of binary (H$_2$/CO$_2$) and also ternary (41 vol.-% H$_2$/ 41 vol.-% CO$_2$/ 18 vol.-% H$_2$O) feed gas mixtures displayed a diffusion dominated permeation behaviour for H$_2$, CO$_2$ and an adsorption dominated behaviour for H$_2$O. Therefore, a steam selectivity α (H$_2$O/H$_2$) up to 23 and a hydrogen selectivity α (H$_2$/CO$_2$) of 2.5 was observed. Hydrophobic treatment of the cCMS/SiO$_2$ membrane surface with 1,1,1,3,3,3-hexamethyldisilazane (HMDS) enhanced its steam selectivity α (H$_2$O/H$_2$) from 23 to 32 (+39%) by steric hindrance of H$_2$ and CO$_2$ permeation.

* Corresponding author. phone: (+49)51176214427. E-mail: alexander.wollbrink@pci.uni-hannover.de (Alexander Wollbrink)

1. Introduction

Bio-ethanol steam reforming $C_2H_5OH + 3H_2O \leftrightarrows 6\ H_2 + 2\ CO_2$ is an important tool in terms of renewable energies [1,2,3]. The reaction suffers from a low conversion and selectivity at temperatures below 400 °C. Therefore, the *in situ* removal of the generated hydrogen in a hydrogen-selective catalytic membrane reactor can push the reaction equilibrium to much higher conversion. In this work, we developed and tested a composite Carbon Molecular Sieve (cCMS/SiO₂) membrane obtained from a hybrid material (phenolic resin/SiO₂) made by twin polymerisation which promises extremely narrow pore sizes for an efficient hydrogen-selective separation performance.

Twin polymerisation is a recently established synthesis method for hybrid materials starting from only one monomer. The organic-inorganic hybrid materials are obtained using at most one catalyst in only one reaction step [4,5]. This procedure allows the synthesis of nanostructured organic-inorganic hybrid materials with single phase domains in the range of 0.5 to 3.0 nm [6]. Silicon is commonly used as central atom in the monomer, but it can also be replaced by other metals or metalloids [5]. The organic parts of these hybrid materials can be phenolic resin or poly(furfuryl alcohol), which are well established carbon precursors [7]. In general, the removal of the silica component by HF leaching from the cCMS/SiO₂ membrane results in a nanoporous carbon matrix with specific surface areas of about 1000 m²/g [6]. The size of the organic as well as inorganic phase domains can be tailored by the monomer reactivity, by the choice of the monomers (organic component) and also by the use of two or more twin monomers in simultaneous twin polymerisation [8,9,10,11]. The ideal twin monomer 2,2′-spirobi[4*H*-1,3,2-benzodioxasiline] can be polymerised by an acid or base catalyst and also thermally induced resulting in a hybrid material with similar nanostructured domains [6,12,13]. Such nanostructured hybrid materials are easily converted into carbon/silica nanocomposites with micropores much smaller than 2 nm [14]. Therefore, carbon membranes converted from resins or hybrid materials are commonly described as Carbon Molecular Sieves [15,16,17].

In this work we evaluate a composite Carbon Molecular Sieve (cCMS/SiO₂) membrane, obtained from the thermally induced twin polymerisation of 2,2′-spirobi[4*H*-1,3,2-benzodioxasiline] for its potential application in a hydrogen-selective catalytic membrane reactor for steam reforming below 400 °C. Therefore, the cCMS/SiO₂ membrane was investigated by permeation of an equimolar binary (H₂/CO₂) and a ternary (41 vol.-% H₂/ 41 vol.-% CO₂/ 18 vol.-% H₂O) feed composition as model feed mixture, see ref. [18]. As

3

novelty, the cCMS/SiO$_2$ membrane is characterised by X-ray diffraction, X-ray photoelectron spectroscopy and mixed gas permeation experiments. Furthermore, we describe the contribution of the carbon matrix and the silica component to the separation performance as well as the influence of the hydrophobic treatment of the cCMS/SiO$_2$ membrane surface with 1,1,1,3,3,3-hexamethyldisilazane (HMDS).

2. Experimental

2.1 Preparation of the cCMS/SiO$_2$ and of the carbon matrix membrane

For the cCMS/SiO$_2$ membrane, the used monomer 2,2'-spirobi[4H-1,3,2-benzodioxasiline] has been synthesised and polymerised as reported in literature [6,13]. The thermally induced twin polymerisation was applied in a cylindrical polytetrafluoroethylene (PTFE) reaction vessel with 0.448 g of the described monomer at 220 °C for three hours. The obtained monolithic hybrid material was carbonised under argon atmosphere (80 mL/min) at 800 °C for three hours in a quartz tube furnace (Carbolite AGD 12/4), using a heating rate of 4.3 K /min. The resulting disc was about 0.67 mm thick with a diameter of about 18 mm. The carbon matrix membrane was prepared by HF leaching of the cCMS/SiO$_2$ membrane with concentrated hydrofluoric acid (HF) in a polyethylene (PE) vessel for 72 h at room temperature to remove the silica component. Afterwards, the resulting microporous carbon membrane was intensively washed, with distilled water and ethanol, and dried at 1×10^3 Pa at 110 °C for several days. The hydrophobic treatment of the cCMS/SiO$_2$ and carbon matrix membrane was carried out in a laboratory glass-bottle (Duran) using 10 mL toluene (Roth, 7346.2), 2 mL 1,1,1,3,3,3-Hexamethyldisilazane (HMDS, Acros: 120581000) which was heated to 110 °C, for two hours under reflux in an argon atmosphere. Finally, the modified membranes were washed with toluene and dried overnight at 80 °C in air.

2.2 Methods

The X-ray powder diffraction (XRPD) was carried out with a D8 Advance diffractometer (Bruker AXS GmbH) using a Bragg–Brentano geometry with Cu (K$\alpha_{1,2}$) radiation, secondary Ni-filter and a 1-dimensional LynxEye detector (silicon strip). The XRPD measurements were performed between 10 ° and 100 ° (2θ), step size of 0.01 ° (2θ), time per step of 0.60 s, a total number of 9000 steps, at room temperature. For Scanning Transmission Electron Microscopy

4

(STEM) investigations, a JEOL JEM-2100F UHR with a Schottky field-emitter (ZrO_2/W(100)) was used at an acceleration voltage of 200 kV. The instrument was operated with a high angle annular darkfield (HAADF) detector. For TEM analysis, the hybrid material and the cCMS(SiO_2) membrane was epoxy-glued between two silicon wafers. Thereafter, the prepared samples were cut and sliced to a thickness of 10 µm. Supported by a copper slot grid, the samples were argon-ion sputtered (1-3 kV) until an electron transparency was achieved. The size of the silica domains were analysed with the software ImageJ using HAADF-STEM micrographs [19]. X-ray photoelectron spectroscopy (XPS) analyses were performed with a non-monochromatic X-ray source using an Al-K_α emission (SPECS XR-50, 100W, 54° incident angle, excited area of about 1 cm^2). The kinetic energies of the photoelectrons were measured with a hemispherical analyser (SPECS-PHOIBOS 100, Detector: MCD-5) with a pass energy of 20 eV. All XPS spectra are shown as a function of binding energy with respect to the Fermi level. The photoelectron peak areas are calculated after background corrections using the Shirley algorithm, described in ref. [20]. Thermogravimetric Analyses (TGA) were carried out with a Setsys-Evolution device (Co. Setaram) with a heating rate of 10 K/ min from 25 °C to 1000 °C and a dwell time of three hours. Thus, about 10 mg sample (powdered) was added in an alumina crucible and swept with 20 mL/ min synthetic air (N_2: 80%, O_2: 20%). The used alumina crucible was pretreated blank under the same condition mentioned before. For permeation studies the membranes were sealed with black O-rings (Perlast G75B-FFKM, Co. C. Otto Gehrckens) with an inner cord diameter of 14 mm and a cord thickness of 2 mm, placed in a module which was developed by TU Delft (F. Kapteijn, J. Gascon). For mixed gas permeation experiments, the absolute feed pressure of any mixture could be varied from 1 up to 5×10^5 Pa while the permeate pressure was swept with 5 mL/ min N_2 at 1×10^5 Pa (atmospheric pressure). The composition of the permeate was analysed by a calibrated gas chromatograph (Agilent 7890B) using a steam-stable column for analyses with high amounts of steam (RT®-Q-Bond, Co. Restek) and a HP-Molsieve column (Co. Agilent Technologies). The feed gases were controlled by calibrated mass flow controllers (MFC's, Co. Bronkhorst). The total fluxes were determined by a simple soap bubble counter with a total volume of 4 ml ± 0.02 ml. A Controlled-Evaporator-Mixer-System (type: W102A, Co. Bronkhorst- Nord GmbH) coupled with a digital mass flow meter/controller (mini-CORI-FLOW: M-12P) was used to saturate the gas flow with steam, as described in detail see ref. [18]. In the shown measurements the stochastic error of mixed gas permeances and corresponding mixed gas separation factors is plotted following the equations for error propagation after Gauss [21]. The stochastic standard

5

deviations of the permeate composition and the total flow measurements are included to the shown errors.

2.3 Evaluation of mixed gas permeation and mixed gas separation

Membrane permeation is a quasi-stationary method under non-equilibrium conditions for testing the membrane performance in the view of a desired separation system. For this purpose, an equimolar binary feed mixture of (H_2/CO_2) and a ternary feed mixture of 41 vol.-% H_2/ 41 vol.-% CO_2/ 18 vol.-% H_2O was used, see ref. [18]. The permeate side was swept with 5 mL/ min N_2 at 1×10^5 Pa.

According with the IUPAC classification [22], the molar flux (*J*) of a fluid through a membrane is described as the number of moles of a component passing the membrane per time and surface area. The permeance (*P*) is the calculated pressure-normalised molar flux *J*, i.e. the flux per transmembrane pressure as driving force. In the case of mixture permeation, it is the difference in the partial pressures Δp of the individual gases between the feed and permeate side of the membrane. The permeability (*P'*) is the thickness-normalised transmembrane pressure, i.e. the product of permeance *P* and membrane thickness *L*.

The composition of the permeate results from the interplay between diffusion and adsorption properties of the mixture components for the membrane under study [23]. In porous solids, relevant transport mechanisms are molecular sieving, selective surface diffusion, Knudsen diffusion, and viscous flow. These transport mechanisms depend on the critical ratio of the kinetic molecular diameter to the effective pore size together with the specific adsorption properties of the membrane under study.

The mixed gas separation factor α *(i,j,k)* of the binary as well as ternary gas mixtures was determined from the ratio of the individual mixed gas permeances *P* (pressure-normalised fluxes) of a component *i, j* or *k* compared with the permeance of another component *i, j* or *k* analysed by an online coupled gas chromatograph.

6

3. Results and discussion

3.1 X-ray Powder Diffraction (XRPD) and Scanning Transmission Electron Microscopy (STEM)

The XRPD pattern of the hybrid material (phenolic resin/SiO_2) shows only a broad diffraction peak at 19.6 ° (2θ), which corresponds to an internal distance of 4.5 Å and ranges between 6.7 Å and 2.7 Å, see **Fig**. **1a** and **Table 1**. The shape and position of the diffraction peak of the hybrid material (phenolic resin/SiO_2) is characteristic for materials of medium range order [24,25]. The HAADF-STEM micrograph of the hybrid material reveals the typical composite domain structure of a phenolic resin/SiO_2 material with organic-inorganic domain sizes of about 3 nm, see **Fig. 1b** [5,6]. In contrast to that, the XRPD pattern of the cCMS/SiO_2 membrane, reveals a sharper diffraction peak at 23.8 ° (2θ), as observed for the hybrid material, which corresponds to an internal distance of 3.7 Å and ranges between 5.9 Å and 2.6 Å, see **Fig. 1a** and **Table 1**. Furthermore, two additional diffraction peaks are visible at 43.9 ° and 79.7 ° (2θ), which are related to internal distances of about 2.1 Å and 1.2 Å, respectively. These two diffraction peaks correspond to the first diffraction peak of 2nd and 4th order, in accordance with the Bragg equation [26]. Therefore, the cCMS/SiO_2 membrane shows a long range order in contrast to the hybrid material. The HAADF-STEM micrograph of the cCMS/SiO_2 membrane reveals well separated and distributed silica domains in the carbon matrix with a domain size of about 2 nm, see **Fig. 1c**.

For the cCMS/SiO_2 membrane, the XRPD data show a quite ordered material due to the carbonisation of the hybrid material (phenolic resin/SiO_2) [27,28]. The effective pore diameter distribution of the cCMS/SiO_2 membrane is calculated from the internal distance distribution, from XRPD data, minus twice of the covalent radius of a single bonded carbon atom which is 1.54 Å [29]. Therefore, the effective pore diameter distribution was estimated to be in the range of 1.1 Å to 4.3 Å with a mean pore size of 2.2 Å, see **Table 2**. For the evaluation of the shown permeation results above, only these pores are involved in the permeation, which have a diameter in the size equal or bigger than the kinetic molecular diameter of H_2O (2.6 Å), H_2 (2.9 Å) or CO_2 (3.3 Å) [30]. Additionally, comparative XRPD measurements between the cCMS/SiO_2 and the carbon matrix membrane show no differences between the observed diffraction pattern, see **Fig. 1a**. This result reveals that the origin of the diffraction peak results mainly from the carbon matrix and not from the silica domains.
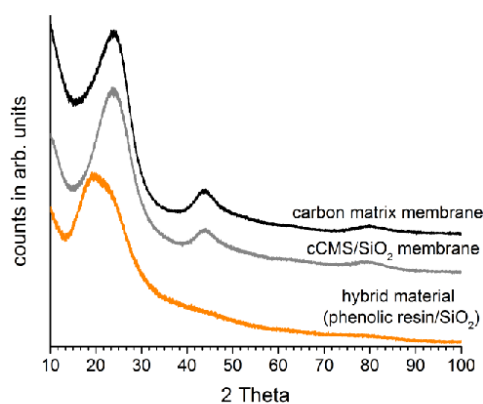
7

Fig. 1a: X-ray diffraction patterns of the hybrid material (phenolic resin/SiO_2), the cCMS/SiO_2 and carbon matrix membrane in (a), see **Table 1**.

Table 1: Analysis of XRPD patterns of the hybrid material (phenolic resin/SiO_2) and the cCMS/SiO_2 membrane, see **Fig. 1**.

sample	maximum of internal distance distribution d		range of internal distance distribution d	
	in Å	in 2 Theta	in Å	in 2 Theta
hybrid material (phenolic resin/SiO_2)	4.5	19.6	$6.7 \leq d \leq 2.7$	$13.3 \leq d \leq 32.9$
cCMS/SiO_2	3.7	23.8	$5.9 \leq d \leq 2.6$	$15.1 \leq d \leq 34.6$

Table 2: Effective pore diameter distribution of the cCMS/SiO_2 membrane calculated from X-ray diffraction patterns minus twice of the covalent radius of a single bonded carbon atom, see **Table 1**.

median of the pore diameter distribution d*	range of the pore diameter distribution d*
2.2 Å	$1.1 \text{ Å} \leq d^* \leq 4.3 \text{ Å}$

8
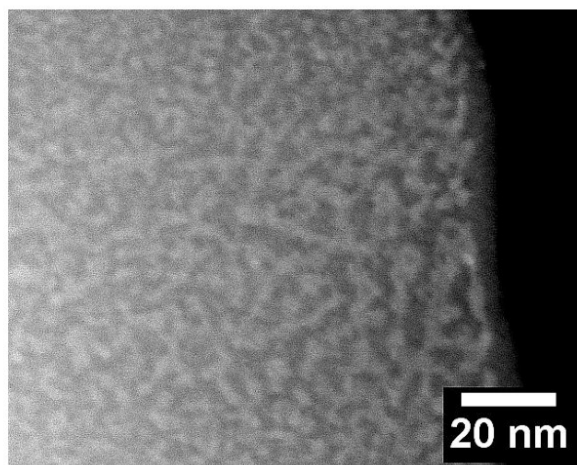
Fig. 1b: HAADF-STEM micrograph of the hybrid material (phenolic resin/SiO_2). The organic or carbon domains are shown as dark/grey areas whereas the inorganic (silica) domains are shown as white areas.
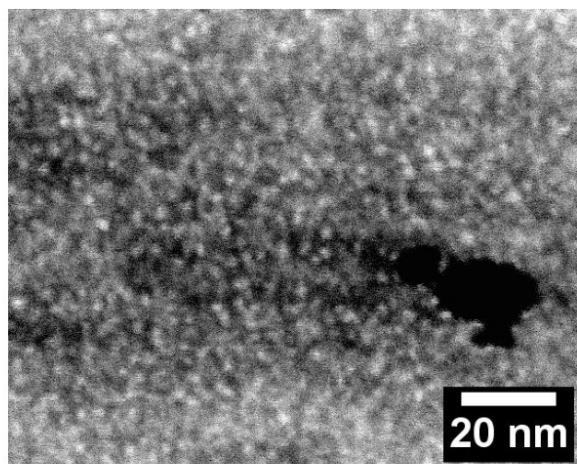
Fig. 1c: HAADF-STEM micrograph of the cCMS/SiO_2 membrane. The organic or carbon domains are shown as dark/grey areas whereas the inorganic (silica) domains are shown as white areas.

9

3.2 Surface Analysis by X-ray Photoemission Spectroscopy (XPS) and Thermogravimetric Analysis (TGA)

XPS analysis of the cCMS/SiO$_2$ membrane surface reveals two main C 1s signals with a binding energy at 284.4 eV $\pm$ 0.1 eV (I) and at 285.9 eV $\pm$ 0.1 eV (II), see **Fig. 2a** and **Table 3**. Signal I is assigned to sp^2 hybridised carbon whereas signal II is related to C-O bonds, in accordance with literature [31,32]. Thus, the cCMS/SiO$_2$ membrane surface reveals a carbon (sp^2)/ C-O signal ratio of about 0.82. Furthermore, two other signals are present on the cCMS/SiO$_2$ membrane surface with low signal intensities at 288.2 eV $\pm$ 0.1 eV (III) and at 289.9 eV $\pm$ 0.1 eV (IV), which are attributed to carboxyl groups (5%) and CF$_x$ groups (2%), respectively, [33,34]. The Si 2p spectrum of the cCMS/SiO$_2$ membrane shows only a single peak structure at 103.3 eV $\pm$ 0.1 eV (I) of silica [35,36], which originates from the silica domains shown by STEM micrographs, see **Fig. 1c** and **Table 4**. From these data, a silica/carbon ratio is estimated for the cCMS/SiO$_2$ membrane surface of about 1 : 12, calculated from C 1s and Si 2p spectra, see **Fig. 2a** and **Tables 3-4**, by using the relative sensitivity factors (RSF) 1.0 (C 1s) and 0.85 (Si 2p) from ref. [37]. Data from Thermogravimetric analyses of the cCMS/SiO$_2$ membrane show a combustion residue of silica of about 27.8 wt.-% for the bulk material. Therefore, the carbon matrix is estimated to be of about 72.2 wt.-% for the cCMS/SiO$_2$ membrane with an unknown carbon/oxygen ratio for the bulk material.
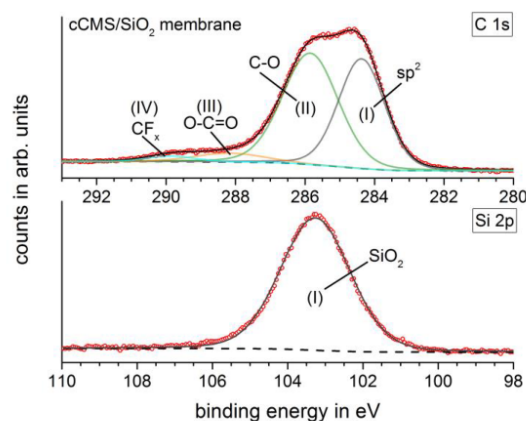
Fig. 2a: C 1s and Si 2p spectra of the cCMS/SiO$_2$ membrane, see **Table 3**.

10
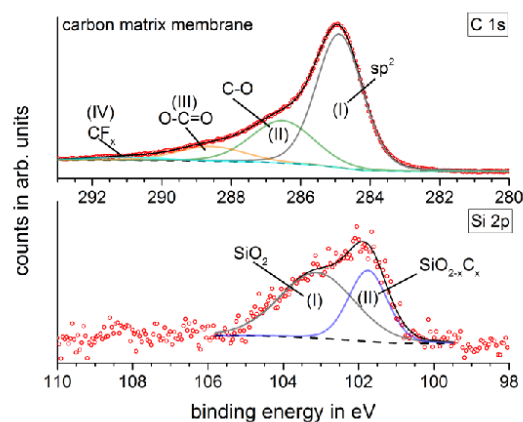
Fig. 2b: C 1s and Si 2p spectra of the carbon matrix membrane, see **Table 3**.
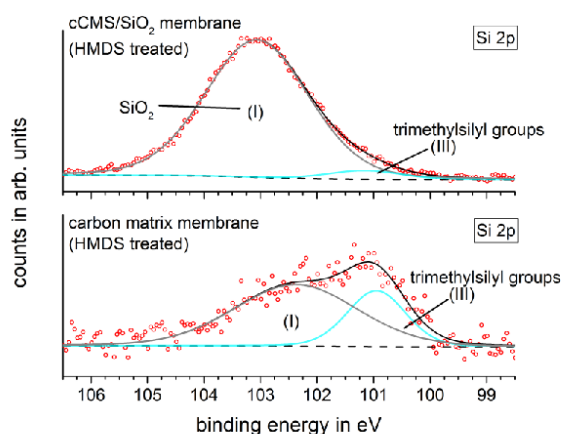
Fig. 2b: Si 2p spectra of the HMDS treated cCMS/SiO₂ and carbon matrix membrane, see **Table 4**.

XPS analyses of the carbon matrix membrane surface show in comparison to the cCMS/SiO$_2$ membrane, an increase of the sp^2 hybridised carbon signal (I) from 41.8 % to 61.6 % of the C 1s signal in total, see **Fig. 2b** and **Table 3**. Consequently, signal II (C-O bonds) decreases from 51.1 % to 26.4 % in the C 1s spectrum. In accordance with the membrane preparation, the carbon matrix displays only traces of residual silica in the Si 2p spectrum, see **Table 4**.

11

Therefore, the silica/carbon ratio of the carbon matrix surface is still only of about $1:313$. Additionally, traces of a $SiO_{2-x}C_x$ signal at 101.8 eV (II) are observed in the Si 2p spectrum [35,36]. The bulk material of the carbon matrix membrane completely burnt off without any residue within the detection limit of thermogravimetric analysis which is in accordance with the detected traces of silica by XPS, see **Figs. 2b**.

The hydrophobic treatment was carried out by the reaction of the hydroxyl groups of the membrane surface with HMDS which generates trimethylsilyl groups linked by an oxygen bridge to the membrane surface under the release of ammonia (NH_3). XPS analyses show qualitatively the successful functionalisation of the $cCMS/SiO_2$ and the carbon matrix membrane surfaces by the hydrophobic treatment with HMDS by the appearance of the new signal at 101.1 ± 0.1 eV (III) in the Si 2p spectra, see **Fig. 2c** and **Table 4**. The observed signal (III) in the Si 2p spectra, which can be assigned to the trimethylsilyl groups [36]. From C 1s and Si 2p spectra, quantitative estimations reveal a trimethylsilyl/carbon ratio of about $1:235$ for the $cCMS/SiO_2$ and of $1:440$ for the carbon matrix membrane surface, see **Tables 3-4** and **Fig. 2c**.

Table 3: Surface analysis by XPS of the $cCMS/SiO_2$ and carbon matrix membrane, see **Figs. 2a-b**. With E_B: binding energy, FWHM: full width at half maximum and signal area: as measured and in percentag terms of the C 1s spectra for the respective membrane under study.

membrane	peak	C 1s				signal classification [31,32,33,34]
		E_B in eV	FWHM in eV	area abs.	area in %	
cCMS/SiO₂	I	284.4	1.6	1339.8	41.8	sp²
	II	285.9	1.9	1637.6	51.1	C-O
	III	288.2	2.4	161.0	5.0	O-C=OH
	IV	289.9	1.6	67.2	2.1	CFₓ
carbon matrix (by HF leaching)	I	284.9	1.6	1972.3	61.6	sp²
	II	286.5	2.1	846.3	26.4	C-O
	III	288.6	2.4	318.3	9.9	O-C=OH
	IV	291.0	2.4	67.4	2.1	CFₓ

12

Table 4: Si 2p spectra of the cCMS/SiO$_2$ and the carbon matrix membrane, see **Figs. 2a-c**. With E$_B$: binding energy, FWHM: full width at half maximum and signal area: as measured and in percentag terms of the C 1s spectra for the respective membrane under study.

membrane	peak	Si 2p			signal classification [35,36]
		E$_B$ in eV	FWHM in eV	area abs.	
cCMS/SiO$_2$	I	103.3	2.2	223.9	SiO$_2$
HMDS treated	I	103.1	2.2	261.0	SiO$_2$
	III	101.2	1.5	11.6	SiOC$_3$
carbon matrix (by HF leaching)	I	103.1	2.3	8.7	SiO$_2$
	II	101.8	1.2	4.9	SiO$_{2-x}$C$_x$
HMDS treated	I	102.4	2.6	14.6	SiO$_2$
	III	101.0	1.2	6.2	SiOC$_3$

13

3.3 Mixed gas permeances and separation

As shown by XRPD analysis, the cCMS/SiO$_2$ membrane belongs to the microporous solids in which the mixed gas permeation occurs mainly by transport mechanisms like surface diffusion or molecular sieving, see section 2.3 [18]. Membrane permeation in microporous solids depends on the critical ratio of effective pore diameter and the kinetic diameter of molecules as well as the interplay of diffusion and adsorption properties (dispersion interactions) [38,39]. Thus, the molar flux (*J*) of a molecule through a microporous membrane is described by Fick's first law. In accordance with the Arrhenius law, a diffusion-dominated transport mechanism is displayed by an increase of the permeance with rising temperature. In contrast to that, an adsorption-dominated transport mechanism leads to a decrease of the permeance with rising temperature, in accordance with the van't Hoff law.

The cCMS/SiO$_2$ membrane has been evaluated in temperature- and also pressure-dependent permeation experiments between 25-250 °C and 1-4×10^5 Pa to characterise its dominant transport mechanism. Furthermore, we investigated the different contributions of the carbon matrix and silica domains to the membrane separation performance by removing the silica component, as described in section 2.1. In addition to that, we analysed the effect of the hydrophobic treatment with HMDS on the cCMS/SiO$_2$ and carbon matrix membrane performance to generate a hydrophobic surface by the introduction of non-polar trimethylsilyl groups.

3.3.1 Permeation experiments of the cCMS/SiO$_2$ membrane

Temperature-dependent mixed gas permeances of the cCMS/SiO$_2$ membrane using the equimolar binary feed mixture (H$_2$/CO$_2$) are shown in **Fig. 3**. The cCMS/SiO$_2$ membrane was tested (as synthesised) from room temperature to 250 °C. At first, the mixed gas permeance of H$_2$ decreases from 2.9×10^{-12} mol/ s m^2 Pa to 1.6×10^{-12} mol/ s m^2 Pa between room temperature and 50 °C, see **Fig. 3a**. After that, the mixed gas permeance of H$_2$ increases with increasing temperature to 3.7×10^{-12} mol/ s m^2 Pa at 250 °C. A second measurement at room temperature after the cCMS/SiO$_2$ membrane was tested at 250 °C reveals a strong reduction of the mixed gas permeance of about 83% for H$_2$ to 4.8×10^{-13} mol/ s m^2 Pa. However, such a drop of hydrogen permeance is huge but in the systematic increase of the shown permeances between 100 °C and 250 °C. For CO$_2$, the mixed gas permeance also increases with increasing temperature from 3.5×10^{-13} mol/ s m^2 Pa to 1.5×10^{-12} mol/ s m^2 Pa between room
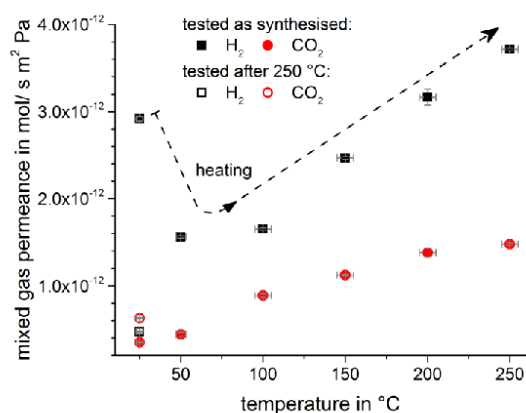
14

Fig. 3a: Temperature-dependent mixed gas permeances of the cCMS/SiO$_2$ using an equimolar binary feed mixture of (H$_2$, CO$_2$) between room temperature and 250 °C.
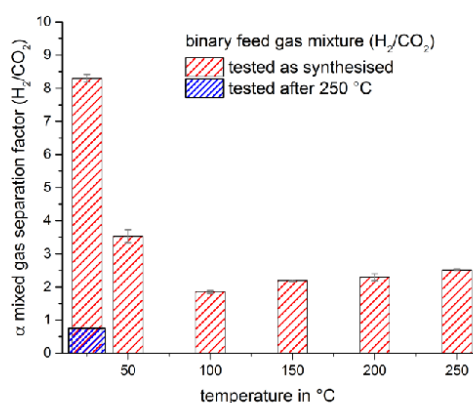

Fig. 3b: Corresponding mixed gas separation factor α (H$_2$/CO$_2$) of Fig. 3a.

temperature and 250 °C. Here, the second measurement of CO$_2$ permeance displays an opposite trend compared to H$_2$, but remains also in the systematic increase of the related mixed gas permeances of CO$_2$ between 100 °C and 250 °C. Consequently, the corresponding mixed gas separation factor α (H$_2$/CO$_2$) of 8.3 decreases to 1.9 at 100 °C and slowly increases to 2.5 with increasing temperature, see **Fig. 3b**. For the second measurement at room temperature, α (H$_2$/CO$_2$) of 0.8 is observed, which indicates a change of α (H$_2$/CO$_2$) from 0.8

15

to 2.5 between room temperature and 250 °C. The observed difference of the mixed gas permeances and the corresponding separation factor α (H_2/CO_2) between room temperature and 50 °C is described by an artificial effect since the analysed membranes were stored under open atmosphere (humidity). This hydration effect is removed by a thermal activation process at 100 °C, see **Figs. 3a-b**.

Comparative permeation studies between the use of an equimolar binary and a ternary feed mixture for the cCMS/SiO$_2$ membrane are shown in **Fig. 4**. The mixed gas permeances of H_2 and CO_2 show a temperature-dependent increase with rising temperature for the ternary feed mixture as observed also for the equimolar binary feed mixture with almost identical values, see **Fig. 4a**. A systematic decrease for both permeances H_2 and CO_2 by about 36% is found at 100 °C, which becomes negligible with increasing temperature. Therefore, the corresponding mixed gas separation factor for a ternary feed mixture shows the same slow increase of α (H_2/CO_2) from 1.8 to 2.3 from 100 °C to 250 °C, as observed for the binary feed mixture, see **Fig. 4b**.
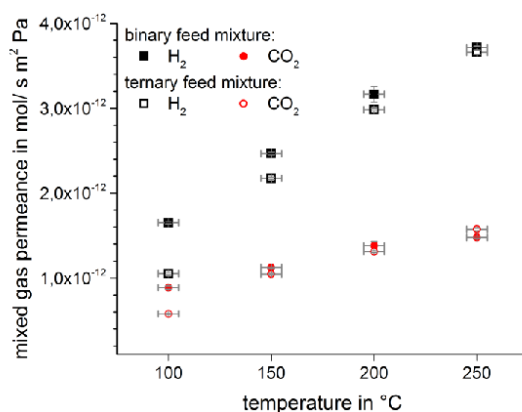
Fig. 4a: Comparison of temperature-dependent mixed gas permeances of the cCMS/SiO$_2$ membrane between an equimolar binary (H_2/CO_2) and the ternary (41 vol.-% H_2/ 41 vol.-% CO_2/ 18 vol.-% H_2O) feed mixture between 100 °C and 250 °C.

In contrast to the permeation behaviour of H_2 and CO_2, the temperature-dependent permeation experiments reveal an one order of magnitude higher mixed gas permeance of H_2O (steam), as observed for H_2, which decreases with increasing temperature from 100 °C to 250 °C, see **Fig. 5**.

16
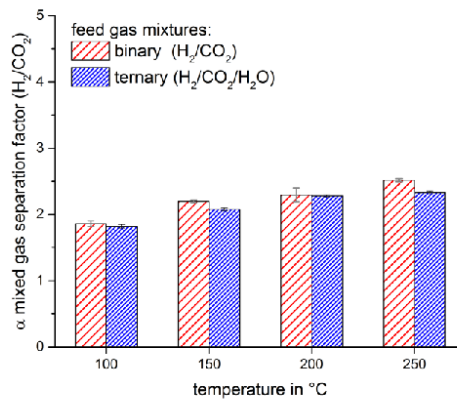
Fig. 4b: Corresponding mixed gas separation factors α (H$_2$/CO$_2$) of Fig. 4a.

The mixed gas permeance of H$_2$O (steam) decreases from 2.4×10^{-11} mol/ s m^2 Pa at 100 °C to 6.3×10^{-12} mol/ s m^2 Pa at 250 °C which displays a decrease of about 74%. In accordance with that, the cCMS/SiO$_2$ membrane shows a steam-selective separation behaviour α (H$_2$O/H$_2$) which decreases from 23 at 100 °C to 1.7 at 250 °C.
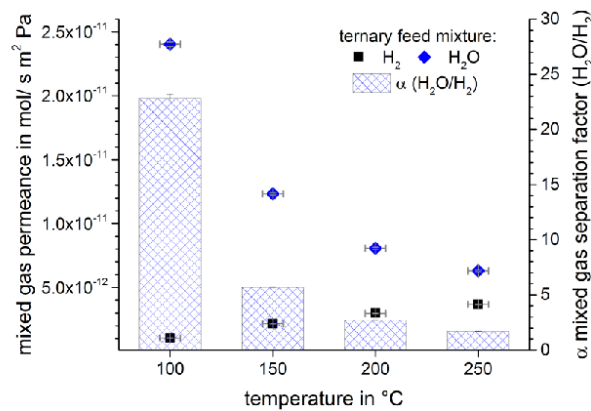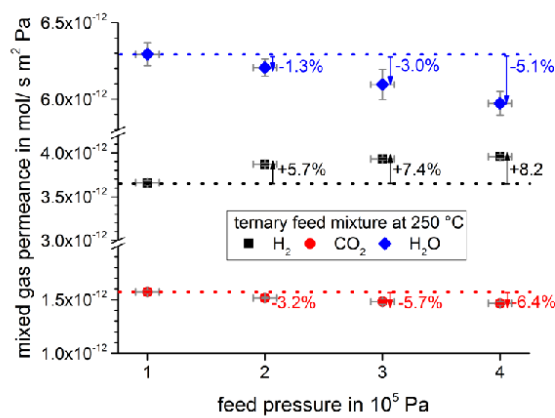

Fig. 5: Temperature-dependent mixed gas permeances of the cCMS/SiO$_2$ membrane of H$_2$ and H$_2$O for the ternary feed mixture (41 vol.-% H$_2$/ 41 vol.-% CO$_2$/ 18 vol.-% H$_2$O) between 100 °C and 250 °C and corresponding mixed gas separation factors α (H$_2$O/H$_2$).

17

The cCMS/SiO$_2$ membrane shows comparable separation properties to other microporous carbon membranes, e.g. a turbostratic carbon membrane obtained by the carbonisation of a polyester blend at 500 °C under protective gas, see ref. [18].

Here, XPS analysis showed that the carbonisation results in an almost pure carbon surface which consists mainly of sp^2 and sp^3 hybridised carbon with a low percentage of oxygen. The effective pore size distribution of the turbostratic carbon membrane lies between 2.9 Å and 11.1 Å, which is more than twice as large as the pore of the cCMS/SiO$_2$ membrane, see **Table 5**. For the comparison of the cCMS/SiO$_2$ with the turbostratic carbon membrane, the permeation results are shown by the membrane mixed gas permeability, which is described above, see section 2.3. For an equimolar binary feed mixture (H$_2$/CO$_2$), the turbostratic carbon membrane shows also a diffusion-dominated transport mechanism since its mixed gas permeances of H$_2$, CO$_2$ and H$_2$O also increase from 100 °C to 250 °C. The mixed gas permeance of H$_2$ increases more than that of CO$_2$, which results in a hydrogen selectivity α (H$_2$/CO$_2$) of 1.9 at 100 °C and increases to 6.0 at 250 °C. This effect is explained by a thermally activated surface diffusion transport mechanism, as described in detail in ref. [18]. Permeation experiments with a ternary feed mixture showed that the mixed gas permeances of H$_2$ and CO$_2$ drop three orders of magnitude and the membrane became non-selective at temperatures equal or below 150 °C since the turbostratic carbon membrane was blocked by steam. This blocking effect of H$_2$ and CO$_2$ by water slowly disappeared for temperatures above 150 °C or by the continuous extraction of steam from the permeate membrane side with sweep gas [18].

Table 5: Comparison of temperature-dependent mixed gas permeability and corresponding separation factors of a turbostratic carbon membrane, obtained from polyester precursor as reported in ref. [18], and the cCMS/SiO$_2$ membrane (this study) for a ternary feed mixture (41 vol.-% H$_2$/ 41 vol.-% CO$_2$/ 18 vol.-% H$_2$O) at 100 °C (left value) and 250 °C (right value).

membrane type	effective pore distribution d* in Å	mixed gas permeability (P') in 10^{-16} mol m/ s m^2 Pa at 100 °C/ 250 °C			selectivity α (H$_2$/CO$_2$) at 100 °C/ 250 °C	selectivity α (H$_2$O/H$_2$) at 100 °C/ 250 °C
		H$_2$	**CO$_2$**	**H$_2$O**		
turbostratic carbon	2.9≤ 4.3 ≤ 11.1	1.9/63.0	1.5/9.8	57.0/260.0	1.3/6.4	38.0/4.1
cCMS/SiO$_2$	1.1 ≤ 2.2 ≤ 4.3	7.0/24.0	3.8/10.0	160.0/42.0	1.8/2.4	22.9/1.8

18

Using N_2 as sweep gas at 100 °C showed again a hydrogen selectivity α (H_2/CO_2) of 6.1 but the steam selectivity α (H_2O/H_2) rises from 38 (no sweep gas) to 270 (with sweep gas). Further investigations revealed that the observed blockage effect resulted from a dramatic change by surface oxidation of the turbostratic carbon membrane, see ref. [40].

This problem is not observed for the cCMS/SiO_2 membrane and also the permeation of steam is reduced by a factor of 1.7 at 100 °C and 2.3 at 250 °C, see **Table 5**. Moreover, the cCMS/SiO_2 membrane displays a complete hydrothermal stability, see **Fig. 4a**. This hydrothermal stability originates from the already oxidised carbon matrix despite of the carbonisation process under argon, see **Fig. 2a** and **Table 3**. Therefore, pressure-dependent permeation experiments could also be conducted at the highest testing temperature of 250 °C using the ternary feed mixture (41 vol.-% H_2/ 41 vol.-% CO_2/ 18 vol.-% H_2O), see **Fig. 6**. The mixed gas permeances of the cCMS/SiO_2 membrane show in the feed pressure range from 1- 4×10^5 Pa a stable performance, see **Fig. 6a**. For H_2, a slight increase of 8.2% is observed whereas CO_2 and H_2O decrease slightly by 6% and 5%, respectively. Therefore, the corresponding mixed gas separation factor of α (H_2/CO_2) increases slightly with rising pressure from 2.3 to 2.7 and α (H_2O/H_2) decreases slightly from 1.6 to 1.5, see **Fig. 6b**.

Fig. 6a: Pressure-dependent mixed gas permeances of the cCMS/SiO_2 membrane of H_2, CO_2 and H_2O for the ternary feed mixture (41 vol.-% H_2/ 41 vol.-% CO_2/ 18 vol.-% H_2O) at 250 °C.

19
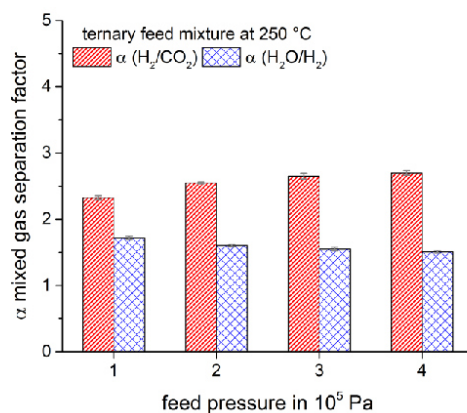
Fig. 6b: Corresponding mixed gas separation factors α (H_2/CO_2) and α (H_2O/H_2) of Fig. 6a.

3.3.2 Permeation experiments for the carbon matrix membrane

The carbon matrix membrane was generated by the removal of the silica domains from the $cCMS/SiO_2$ membrane with concentrated hydrofluoric acid, see section 2.1. This procedure, causes an additional porosity in the size of the silica domains of 2 nm to the already existing micropores of between 1.1 and 4.3 Å, see sections 3.1-3.2. XPS analysis revealed the existence of residual traces of silica on the membrane surface confirmed by TG analysis, see section 3.2.

Now, the mixed gas permeances of H_2 and CO_2 display for the carbon matrix membrane a reversed temperature-dependent behavior, as observed for the $cCMS/SiO_2$ membrane, see **Fig. 7**. The carbon matrix membrane shows an increased mixed gas permeance of H_2 by a factor of 169 to 1.8×10^{-10} mol/ s m^2 Pa at 100 °C, which decreases with rising temperature to 1.1×10^{-10} mol/ s m^2 Pa at 250 °C, see **Fig. 7a**. For CO_2, the mixed gas permeance increases also but by a larger factor of 270 to 1.6×10^{-10} mol/ s m^2 Pa at 100 °C, which also decreases to 4.6×10^{-11} mol/ s m^2 Pa at 250 °C, see **Fig. 7b**. In the case of H_2O (steam), the adsorption dominated permeation behavior remains unchanged, , see **Fig. 7c**. The mixed gas permeance is increased also but by a one order of magnitude smaller factor of 13 to 3.3×10^{-10} mol/ s m^2 Pa at 100 °C, which decreases with increasing temperature to 9.7×10^{-11} mol/ s m^2 Pa at 250 °C. As a result of these differences in mixed gas permeances of H_2, CO_2 and H_2O, the
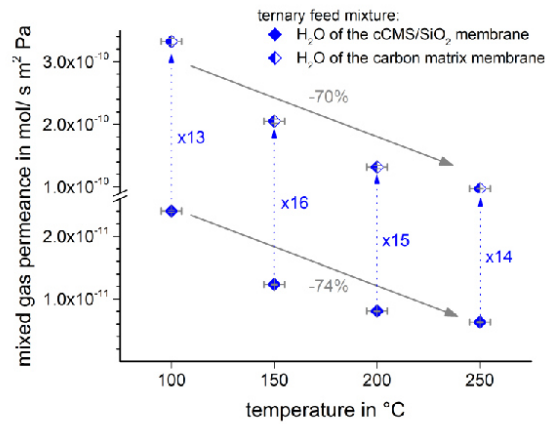
20
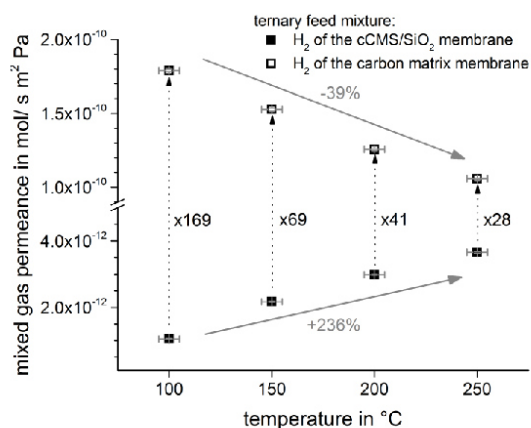
Fig. 7a: Comparison of temperature-dependent mixed gas permeances between the cCMS/SiO$_2$ and carbon matrix membrane of H$_2$ for the ternary feed mixture (41 vol.-% H$_2$/ 41 vol.-% CO$_2$/ 18 vol.-% H$_2$O) between 100 °C and 250 °C.
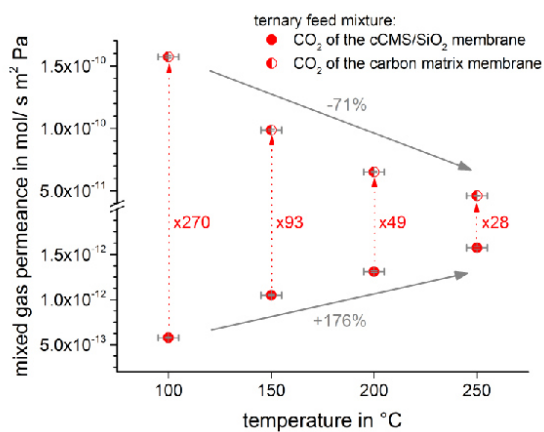
Fig. 7b: Comparison of temperature-dependent mixed gas permeances between the cCMS/SiO$_2$ and carbon matrix membrane of CO$_2$ for the ternary feed mixture (41 vol.-% H$_2$/ 41 vol.-% CO$_2$/ 18 vol.-% H$_2$O) between 100 °C and 250 °C.

21

Fig. 7c: Comparison of temperature-dependent mixed gas permeances between the cCMS/SiO$_2$ and carbon matrix membrane of H$_2$O for the ternary feed mixture (41 vol.-% H$_2$/ 41 vol.-% CO$_2$/ 18 vol.-% H$_2$O) between 100 °C and 250 °C.

corresponding mixed gas separation factors are changed, see **Fig. 8**. The hydrogen selectivity of α (H$_2$/CO$_2$) is reduced to 1.1 (non-selective) at 100 °C but α (H$_2$/CO$_2$) increases with increasing temperature to 2.3 again, which is in accordance with the value observed for the cCMS/SiO$_2$ membrane, see **Fig. 8a**.
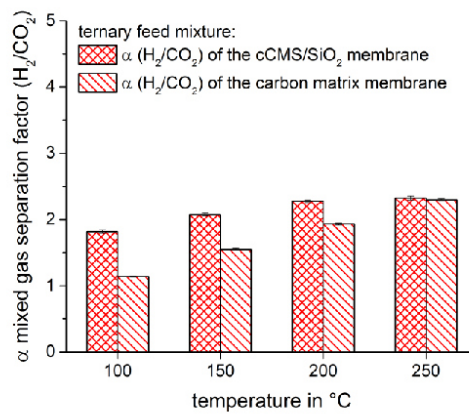
Fig. 8a: Corresponding mixed gas separation factors α (H$_2$/CO$_2$) of **Fig. 7a-b**.

22

In the case of the steam selectivity, α (H_2O/H_2) is strongly reduced from 23, shown for the cCMS/SiO_2 membrane, to 1.9 at 100 °C and decreases to 0.9 (non-selective) at 250 °C for the carbon matrix membrane, see **Fig. 8b**.
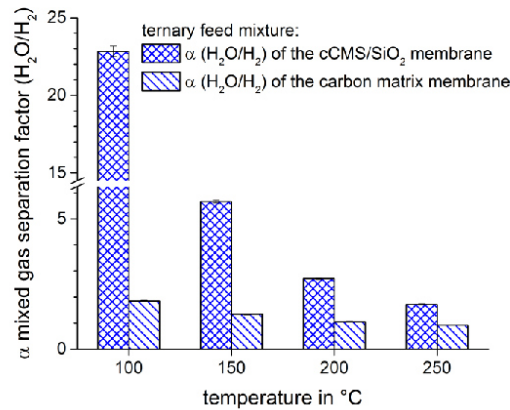
Fig. 8b: Corresponding mixed gas separation factors α (H_2/CO_2) of **Fig. 7a,c**.

From these data, it follows that for the cCMS/SiO_2 membrane, the mixed gas permeances of H_2 and CO_2 can be described by a diffusion dominated transport mechanism, whereas the mixed gas permeance of H_2O (steam) seems to be dominated by adsorption. The mixed gas permeances of H_2 and CO_2 turn into an adsorption dominated transport mechanism due to the removal of the embedded silica domains from the carbon matrix, which results in larger pores. Furthermore, for the carbon matrix membrane, the mixed gas permeance of H_2O is much less increased (by a factor of 13) as compared to the permeances of CO_2 (by a factor of 270) or H_2 (by a factor of 169) at 100 °C. Therefore, the permeation selectivity can be distinguished between the carbon matrix and the cCMS/SiO_2 membrane with respect to their different porosity as follows: (i) the carbon matrix membrane with its bimodal porosity shows a slight temperature-dependent hydrogen selectivity α (H_2/CO_2) of about 2.3 and no steam selectivity at 250 °C, (ii) the silica domains of the cCMS/SiO_2 membrane do not directly affect the hydrogen selectivity α (H_2/CO_2) whereas the steam selectivity α (H_2O/H_2) seems to be affected. Consequently, the removal of the silica component shows that the accessible pore size distribution of the silica domains have to be mainly of the order of H_2O (steam) and partly of H_2 with a kinetic molecular diameter of 2.6 Å and 2.9 Å, respectively [30].

23

3.3.3 Hydrophobic treatment of cCMS/SiO$_2$ and carbon matrix membrane

In this section, the effect of the hydrophobic treatment of the cCMS/SiO$_2$ and of the carbon matrix membrane with HMDS on their permeation performance is discussed, see **Fig. 9**. The successful modification of the different membrane surfaces by the attachment of the non-polar trimethylsilyl groups was shown by XPS analysis (see **Fig. 2c** and **Table 4**).

For the cCMS/SiO$_2$ membrane, the hydrophobic treatment with HMDS results in a systematic reduction of the mixed gas permeances of about 30 % to 16 % for H$_2$ and CO$_2$ depending on temperature, see **Figs. 9a-b**. Contrary to that, the mixed gas permeance of H$_2$O (steam) shows almost no effects at 100 °C, which changes into an increased H$_2$O permeance up to 17.7 % at 250 °C, see **Fig. 9c**. Therefore, the corresponding mixed gas permeances, show no effect for α (H$_2$/CO$_2$), see **Fig. 10a**, whereas the steam selectivity α (H$_2$O/H$_2$) increased from 23 (untreated) to 32 (HMDS treated) at 100 °C, see **Fig. 10b**. The increased steam selectivity α (H$_2$O/H$_2$) decreases also with rising temperature to 2.6 at 250 °C, similar to the untreated cCMS/SiO$_2$ membrane. The value of α (H$_2$O/H$_2$) for the HMDS treated cCMS/SiO$_2$ membrane remains always slightly higher than that observed for the untreated membrane. In the case of the HMDS treated carbon matrix membrane, no changes in its permeation selectivity could be observed, as shown in **Fig. 8**.
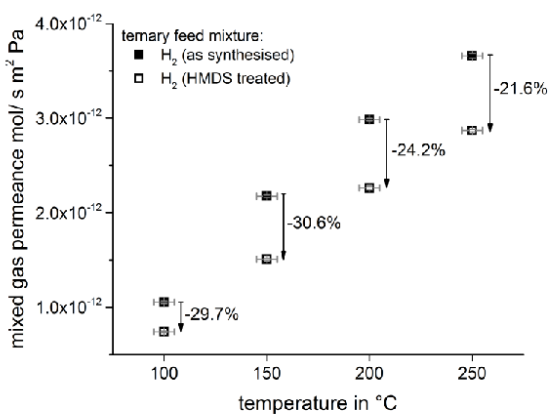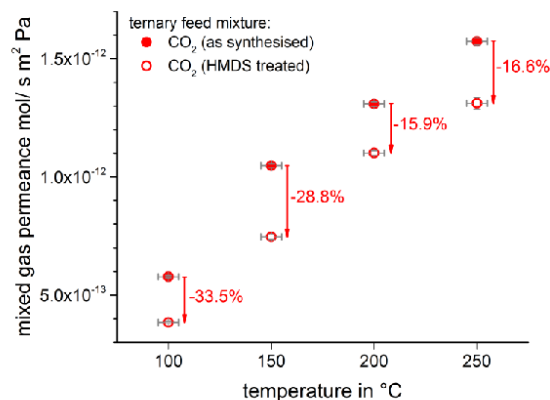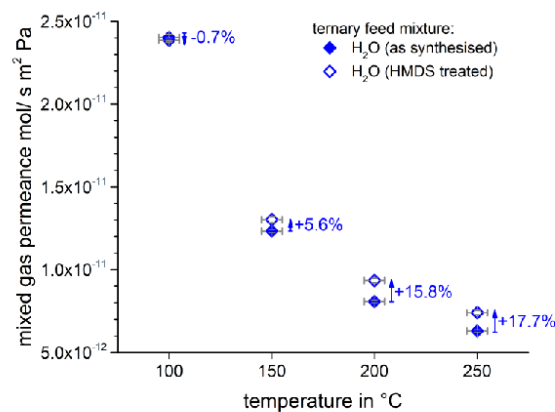

Fig. 9a: Comparison of the mixed gas permeances between the cCMS/SiO$_2$ (as synthesised) and cCMS/SiO$_2$ (HMDS treated) membrane for H$_2$ using a ternary feed mixture (41 vol.-% H$_2$/ 41 vol.-% CO$_2$/ 18 vol.-% H$_2$O) between 100 °C and 250 °C.
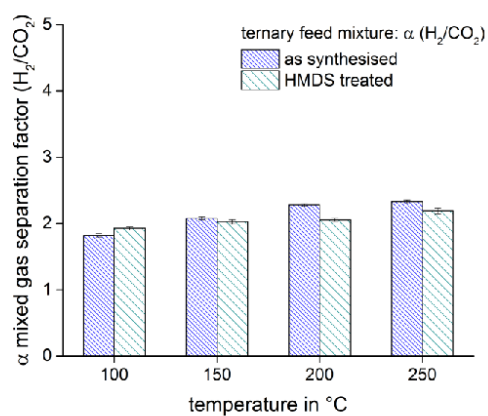
24

Fig. 9b: Comparison of the mixed gas permeances between the cCMS/SiO$_2$ (as synthesised) and cCMS/SiO$_2$ (HMDS treated) membrane for CO$_2$ using a ternary feed mixture (41 vol.-% H$_2$/ 41 vol.-% CO$_2$/ 18 vol.-% H$_2$O) between 100 °C and 250 °C.

Fig. 9c: Comparison of the mixed gas permeances between the cCMS/SiO$_2$ (as synthesised) and cCMS/SiO$_2$ (HMDS treated) membrane for H$_2$O using a ternary feed mixture (41 vol.-% H$_2$/ 41 vol.-% CO$_2$/ 18 vol.-% H$_2$O) between 100 °C and 250 °C.

25

Fig. 10a: Comparison of the separation performance between the cCMS/SiO$_2$ (as synthesised) and cCMS/SiO$_2$ (HMDS treated) membrane for α (H$_2$/CO$_2$). All data are shown for the ternary feed mixture (41 vol.-% H$_2$/ 41 vol.-% CO$_2$/ 18 vol.-% H$_2$O) between 100 °C and 250 °C. The corresponding mixed gas permeances are shown in **Figs. 4-5**, **9** for the cCMS/SiO$_2$ membrane.
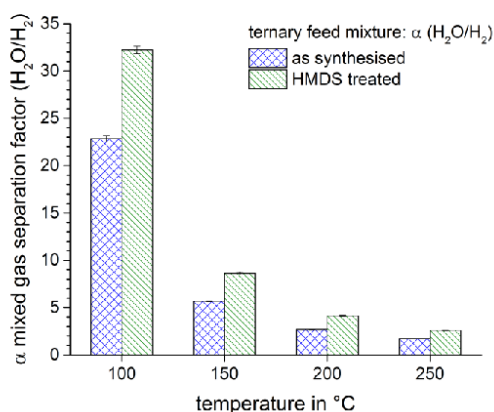
Fig. 10b: Comparison of the separation performance between the cCMS/SiO$_2$ (as synthesised) and cCMS/SiO$_2$ (HMDS treated) membrane for α (H$_2$O/H$_2$). All data are shown for the ternary feed mixture (41 vol.-% H$_2$/ 41 vol.-% CO$_2$/ 18 vol.-% H$_2$O) between 100 °C and 250 °C. The corresponding mixed gas permeances are shown in **Figs. 4-5**, **9** for the cCMS/SiO$_2$ membrane.

26

The hydrophobic treatment of the cCMS/SiO$_2$ membrane revealed that the reduced interaction of the polar H$_2$O molecules with the cCMS/SiO$_2$ membrane surface by the introduction of non-polar trimethylsilyl groups causes an increased H$_2$O permeance with increasing temperature. Furthermore, the systematic reduction of the mixed gas permeance of H$_2$, CO$_2$ indicate that this effect originates from steric hindrance caused by the non-polar trimethylsilyl groups, which limit the pore entrance more for such molecules with a kinetic molecular diameter of 2.9 Å (H$_2$) and 3.3 Å (CO$_2$) rather than for the smaller H$_2$O (2.6 Å), see ref. [30].

4. Conclusions

A composite carbon molecular sieve (cCMS/SiO$_2$) membrane, obtained by the carbonisation of the hybrid material (phenolic resin/SiO$_2$) from thermally induced twin polymerisation of 2,2′-spirobi[4*H*-1,3,2-benzodioxasiline], was tested with an equimolar binary (H$_2$/CO$_2$) and a ternary (41 vol.-% H$_2$/ 41 vol.-% CO$_2$/ 18 vol.-% H$_2$O) feed mixture. Pressure- and temperature-dependent permeation experiments revealed a high steam stability up to 250 °C and 4×10^5 Pa. Furthermore, a strong temperature-dependent separation performance with a hydrogen selectivity of α (H$_2$/CO$_2$) up to 2.3 and a steam selectivity α (H$_2$O/H$_2$) of up to 23 was observed. These results show that the narrow pore size distribution, as determined from XRPD, of the carbon matrix between 4.3 Å and 1.1 Å allows molecular sieving, which leads to a preferred permeation of H$_2$O, as the molecule with the smallest kinetic molecular diameter of 2.6 Å compared with the bigger molecules H$_2$: 2.9 Å or CO$_2$: 3.3 Å. Comparing the permeation experiments of the cCMS/SiO$_2$ membrane with the carbon matrix membrane, it was shown that the steam selectivity of the cCMS/SiO$_2$ membrane corresponds to the silica domains of the composite material. Surface modification of the cCMS/SiO$_2$ membrane with non-polar trimethylsilyl groups confirmed this finding since the hydrophobic treatment results in a systematic reduction of the H$_2$ and CO$_2$ permeances rather than that of H$_2$O. This effect is explained by steric hindrance of the bigger molecules (H$_2$: 2.9 Å and CO$_2$: 3.3 Å) compared to the small H$_2$O molecule (2.6 Å). Further investigations should show if the choice of the hybrid material precursor or the carbonisation temperature are the critical parameters for a higher hydrogen selectivity to prevent H$_2$O and CO$_2$ from passing the membrane. Additionally, no estimations could be done for the effect of hybrid materials with smaller domain sizes than 3 nm.

27

References

——————————————

[1] M. Ni, D.Y.C. Leung, M.K.H. Leung, A review on reforming bio-ethanol for hydrogen production, Int. J. Hydrogen Energy 32 (2007) 3238-3247.

[2] V. Palma, E. Palo, F. Castaldo, P. Ciambelli, G. Iaquaniello, Catalytic activity of CeO_2 supported Pt-Ni and Pt-Co catalysts in the low temperature bio-ethanol steam reforming, Chem. Engin. Trans. 25 (2011) 947-952.

[3] V. Palma, E. Palo, F. Castaldo, P. Ciambelli, G. Iaquaniello, Catalytic activity of CeO_2 supported Pt-Ni and Pt-Co catalysts in the low temperature bio-ethanol steam reforming, Chem. Engin. Trans. 25 (2011) 947-952.

[4] S. Grund, P. Kempe, G. Baumann, A. Seifert, S. Spange, Nanocomposite prepared by twin polymerization of a single-source monomer, Angew. Chem. Int. Ed. 46 (2007) 628–632.

[5] T. Ebert, A. Seifert, S. Spange, Twin polymerization - a new principle for hybrid material synthesis, Macromol. Rapid Commun. 36 (2015) 1623–1639.

[6] S. Spange, P. Kempe, A. Seifert, A.A. Auer, P. Ecorchard, H. Lang, M. Falke, M. Hietschold, A. Pohlers, W. Hoyer, G. Cox, E. Kockrick und S. Kaskel, Nanocomposites with structure domains of 0.5 to 3 nm by polymerization of silicon spiro compounds, Angew. Chem. Int. Ed. 48 (2009) 8254–8258.

[7] E. Fitzer, W. Schaefer, S. Yamada, The formation of glasslike carbon by pyrolysis of polyfurfuryl alcohol and phenolic resin, Carbon 7 (1969) 643–648.

[8] T. Löschner, A. Seifert, R. Lungwitz, G. Cox, A. Lange, H.-J. Hähnle, S. Spange, Simultaneous twin polymerisation – controlling the nanostructure formation of hybrid materials Macromol. Rapid Commun. 32 (2011) F60–F61.

[9] T. Löschner, A. Mehner, S. Grund, A. Seifert, A. Pohlers, A. Lange, G. Cox, H.-J. Hähnle, S. Spange, A modular approach for the synthesis of nanostructured hybrid materials with tailored properties: the simultaneous twin polymerization, Angew. Chem. Int. Ed. 51 (2012) 3258–3261.

[10] T. Löschner, Synthese nanostrukturierter, organisch-anorganischer Hybridmaterialien über Zwillingspolymerisation, Germany, TU Chemnitz, Ph.D. thesis, **2013**.

[11] P. Kitschke, A.A. Auer, T. Löschner, A. Seifert, S. Spange, T. Rüffer, H. Lang, M. Mehring, microporous carbon and mesoporous silica by use of twin polymerization: an integrated experimental and theoretical approach to precursor reactivity, ChemPlusChem 79 (2014) 1009–1023.

29

[12] T. Ebert, G. Cox, E. Sheremet, O. Gordan, D.R.T. Zahn, F. Simon, S. Spange, Carbon/carbon nanocomposites fabricated by base catalysed twin polymerization of a Si-spiro compounds on graphite sheets, Chem. Commun. 48 (2012) 9867-9869.

[13] P. Kempe, T. Löschner, A.A. Auer, A. Seifert, G. Cox, S. Spange, Thermally induced twin polymerization of 4*H*-1,3,2-Benzodioxasilines, Chem. Eur. J. 20 (2014) 8040–8053.

[14] J. Rouquerol, D. Avnir, D.H. Everett, C. Fairbridge, M. Haynes, N. Pernicone, J.D.F. Ramsay, K.S.W. Sing, and K.K. Unger, Guidelines for the characterization of porous solids, Studies in Surface Science and Catalysis, Vol. 87 (1994) 1-9.

[15] T.A. Centeno, A.B. Fuertes, Carbon molecular sieve membranes derived from a phenolic resin supported on porous ceramic tubes, Sep. Purif. Technol. 25 (2001) 379-384.

[16] T.A. Centeno, A.B. Fuertes, Supported carbon molecular sieve membranes based on a phenolic resin, J. Membr. Sci. 160 (1999) 201-211.

[17] D.Q. Vu, W.J. Koros, S.J. Miller, Mixed matrix membranes using carbon molecular sievs I. Preparation and experimental results, J. Membr. Sci. 211 (2003) 311-334.

[18] A. Wollbrink, K. Volgmann, J. Koch, K. Kanthasamy, C. Tegenkamp, Y. Li, H. Richter, S. Kämnitz, F. Steinbach, A. Feldhoff, J. Caro, Amorphous, turbostratic and crystalline carbon membranes with hydrogen selectivity, Carbon 106 (2016) 93-105.

[19] Software for analysis of the silica domain size: https://imagej.net

[20] D.A. Shirley, High-resolution X-ray photoemission spectrum of the valence bands of gold, Phys. Rev. B, 12 (1972) 4709-4714.

[21] C.-D. Schönwiese, Gebrüder Borntraeger, Textbook of practical statistic for metereologists and geoscienctists. 3rd Edition, Stuttgart; 2000.

[22] W. J. Koros, Y.H. Ma and T. Shimidzu, Terminology for membranes and membrane processes, Pure & Appl. Chem. 68 (1996) 1479-1489.

[23] J. Kärger, D.M. Ruthven, D.N. Theodorou, Diffusion in Nanoporous Materials, vol. 1, Wiley-VCH, 2012, pp. 85-109.

[24] J. Göttlicher and H.J. Pentinghaus, Compositional influence on shape and position of the first sharp diffraction peak (FSDP) in silicate and germanate glasses, Phys. Chem. 100 (1996) 1563-1568.

[25] S.R. Elliott, The origin of the first sharp diffraction peak in the structure factor of covalent glasses and liquids, J. Phys. Condens. Matter 4 (1992) 7661-7678.

[26] W.L. Bragg, The structure of some crystals as indicated by their diffraction of X-rays, Proc. R. Soc. London, Ser. A, 89, No. 610 (1913) 248-281.

30

[27] O. Beyssac, D. Ruble, Graphitic carbon: a ubiquitous, diverse, and useful geomaterial, Elements, 10, No. 6 (2014) 415-420.

[28] P. R. Buseck, O. Beyssac, From organic matter to graphite: graphitization, Elements, 10, No. 6 (2014) 421-426.

[29] A.F. Holleman, E. Wiberg, N. Wiberg, Textbook of inorganic chemistry, vol. 102, Walter de Gruyter & Co., 2007, p. 2006.

[30] D.W. Breck, Zeolite molecular sieves, John Wiley & Sons Inc., 1974.

[31] P. Mérel, M. Tabbal, M. Chaker, S. Moisa, J. Margot, Direct evaluation of sp^3 content in diamond-like-carbon films by XPS, Appl. Surf. Sci. 136 (1998) 105-110.

[32] G. Nguila Inari, M. Petrissans, J. Lambert, J.J. Ehrhardt and P. Gérardin, XPS characterization of wood chemical composition after heat-treatment, Surf. Interface Anal. 38 (2006) 1336-1342.

[33] I.P. Asanov, V. M. Paasonen, L.N. Mazalov and A.S. Nazarov, X-Ray photoelectron study of fluorinated graphite intercalation compounds, J. Struct. Chem. 39 (1998) 928-932.

[34] W.-K. Lee, I. Losito, J.A. Gardella, Jr. and W.L. Hicks, Jr., Synthesis and surface properties of fluorocarbon end-capped biodegradable polyesters, Macromolecules 34 (2001) 3000-3006.

[35] C. Önneby and C.G. Pantano, Silicon oxycarbide formation on SiC surfaces and at the SiC/SiO_2 interface, J. Vac. Sci. Technol. A 15 (1997) 1597-1602.

[36] M. Ouyang, C. Yuan, R.J. Mulsener, A. Boulares, and J.T. Koberstein, Conversion of some siloxane polymers to silicon oxide by UV/Ozone photochemical processes, Chem. Mater. 12 (2000) 1591-1596.

[37] Private communication from Co. SPECS GmbH.

[38] J. Kärger, D.M. Ruthven, D.N. Theodorou, Diffusion in Nanoporous Materials, vol. 1, Wiley-VCH, 2012, pp. 85-109.

[39] H.W. Haynes, A note on diffusive mass transport, Chem. Eng. Ed. 20 (1986) 22-27.

[40] A. Wollbrink, K. Volgmann, J. Koch, K. Kanthasamy, C. Tegenkamp, Y. Li, H. Richter, S. Kämnitz, J. Caro, Effects of steam containing gas mixtures on the separation performance of amorphous, turbostratic and crystalline carbon membranes, submitted to Sep. Purif. Technol.

31

3.1.4. Multiple polymerisation – formation of hybrid materials consisting of two or more polymers from one monomer

Authors: T. Ebert, **A. Wollbrink**, A. Seifert, R. John, S. Spange

CrossMark
click for updates

Multiple polymerization – formation of hybrid materials consisting of two or more polymers from one monomer†

T. Ebert,[a] A. Wollbrink,[b] A. Seifert,[a] R. John[a] and S. Spange*[a]

Hybrid materials consisting of three different components were synthesized by the polymerization of one heterotrifunctional monomer in just one reaction step using, at the most, one catalyst. The polymerization of 2-furfuyloxy-2-methyl-4H-1,3,2-benzodioxasiline leading to a hybrid material consisting of phenolic resin, poly(furfuryl alcohol), and polymethylsilsesquioxane is, to the best of our knowledge, the first polymerization of this kind. The influence of different catalysts on the polymerization behavior and thus on the structure of the hybrid material was investigated. In accordance with the term "twin polymerization", which is used for the polymerization of one monomer yielding two separate polymers, this type of polymerization could be called "triple polymerization". The term "multiple polymerization" is introduced as a general term for the underlying concept of the synthesis of multiple polymers starting from one monomer in one process step.

Introduction

The importance of nanostructured materials has been reported for a variety of applications, such as the support of catalysts, energy storage, and conversion or separation processes.[1–4] For this purpose the combination of more than two components and a precise structuring in the nanometer range are often required.[5] Template-assisted polymerization and sol–gel chemistry are suitable procedures for this scope. However, most of the established synthetic methods require a work up procedure afterwards.

In recent years, the synthetic concept of twin polymerization has been established as a strategy for hybrid material synthesis.[6–8] During the twin polymerization process two different polymers are formed from just one monomer in a mechanistically coupled process. This concept differs from other established synthetic strategies for the synthesis of hybrid materials.[9] Nanostructured hybrid materials can directly be synthesized by polymerizing a monomer melt, partly even without the need of a catalyst.[10] For the synthesis of hybrid materials of multiple components and the tuning of the domain size the simultaneous twin polymerization has

been developed.[11–13] This concept describes the polymerization of two different twin monomers in one process step, and yields a hybrid material consisting of up to four homopolymers. If two twin monomers with one identical structural element are polymerized, either three homopolymers, or one homopolymer and one copolymer are obtained. A nanostructured hybrid material consisting of poly(furfuryl alcohol), phenolic resin and silicon dioxide has been synthesized by a simultaneous twin polymerization of 2,2′-spirobi[benzo-4H-1,3,2-dioxasiline] (Spiro) and tetrafurfuryloxysilane (TFOS).[11]

We herein demonstrate that a hybrid material consisting of three different polymers can also be synthesized by polymerizing only one monomer. Thus, the concept of twin polymerization is only an example of a more general procedure – the formation of several polymers within just one synthetic step, starting from only one monomer. When this concept is compared with other well-known polymerization procedures, it can be regarded as the opposite of a copolymerization where, starting from more than one monomer one copolymer is formed. In accordance with the term "twin polymerization", the general term of multiple polymerization is suggested (Fig. 1).

Homopolymerization and copolymerization are defined by IUPAC.[14] The simultaneous polymerization is described in the literature[11] and the related term "simultaneous interpenetrating polymer network" is also defined by IUPAC.[15] So far, the twin polymerization is, to the best of our knowledge, the only example of a multiple polymerization. The concept is useful for the synthesis of nanostructured hybrid materials, and consequently also for nanoporous materials, which are accessible

[a]Polymer Chemistry, Technische Universität Chemnitz, 09107 Chemnitz, Germany.
E-mail: stefan.spange@chemie.tu-chemnitz.de
[b]Institute of Physical Chemistry and Electrochemistry, Leibniz University Hannover,
Callinstrasse 3A, D-30167 Hannover, Germany
†Electronic supplementary information (ESI) available: Experimental details, monomer characterization and supporting figures. See DOI: 10.1039/c6py01619g
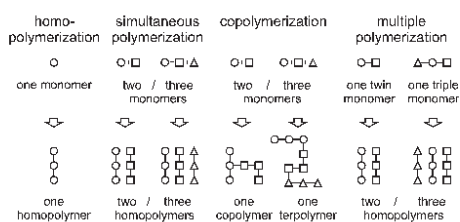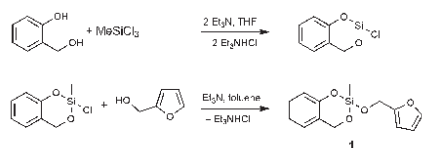
Fig. 1 Comparison of multiple polymerization with the well-established polymerization concepts of homopolymerization, simultaneous polymerization and copolymerization.

Scheme 1 Synthesis of the heterotrifunctional monomer 2-furfuryl-oxy-2-methyl-4H-1,3,2-benzodioxasiline (**1**).

by the annealing and removing of one of the components of the hybrid material.[9] For the formation of nanostructured phase domains it is crucial that two or more polymers are formed in the vicinity at the same time, so that the viscosity is increased fast and phase separation is reduced. Monomers for multiple polymerization can be constructed to yield more than two different polymers. Furthermore, as for twin polymerization, it is also possible to construct the monomers in such a way that functional polymers are obtained.[9]

To prove the concept, we synthesized and investigated the polymerization behavior of the heterotrifunctional monomer 2-furfuryloxy-2-methyl-4H-1,3,2-benzodioxasiline (**1**, see Scheme 1). To be consistent with the terminology of twin polymerization and twin monomers, this monomer could be regarded as a "triple monomer", and the polymerization to three polymers could be called a "triple polymerization". However, the term "heterotrifunctional monomer" should be used, as this expression is independent of its polymerization behavior during the differently catalyzed polymerizations.

Results and discussion

Preliminary synthetic work showed that monomer **1** cannot easily be obtained in a transesterification reaction using tri-alkoxysilanes, salicyl alcohol and furfuryl alcohol. However, a stepwise approach was developed, which depends on the synthesis of the key intermediate 2-chloro-2-methyl-4H-1,3,2-ben-zodioxasiline, which is obtained by a reaction of trichloro-methylsilane with one equivalent of salicyl alcohol (see Scheme 1). It can be purified by distillation, and the chlorine

atom can readily be substituted with different polymerizable groups. Therefore, 2-chloro-2-methyl-4H-1,3,2-benzodioxasiline can act as a precursor for many heteromultifunctional monomers. In this publication, we report on the reaction with furfuryl alcohol to yield the final heterotrifunctional monomer 2-furfuryloxy-2-methyl-4H-1,3,2-benzodioxasiline (**1**), which can easily be synthesized in a multigram scale. In all reaction steps water has to be excluded to prevent hydrolysis. 2-Chloro-2-methyl-4H-1,3,2-bezodioxasiline can react with moisture, leading to the formation of hydrochloric acid, which catalyzes its polymerization.

The polymerization behavior of monomer **1** was studied with differential scanning calorimetry (DSC). The two related and already described twin monomers 2,2′-spirobi[benzo-4H-1,3,2-dioxasiline] (**Spiro**) and tetrafurfuryloxysilane (**TFOS**) differ in their polymerization behavior. **Spiro** can be polymerized by simple thermal annealing,[10] or catalyzed by acids[8] and bases.[16] **TFOS** can only be polymerized under acidic conditions.[6] An annealing of this monomer does not lead to an exothermic peak in the thermogram of the differential scanning calorimetry (see Fig. S1, ESI†). Thus, no polymerization occurs (also not in the presence of a base) below a temperature of 350 °C.

When both the respective organic moieties, the furfuryl alcohol and the salicyl alcohol, are combined in one monomer (monomer **1**), it is expected that, by the choice of the catalyst, the number of ongoing polymerization reactions can be controlled. An acid catalyst should be able to trigger the polymer formation of poly(furfuryl alcohol), phenolic resin, and poly-methylsilsesquioxane, whereas a base catalyzed reaction is expected to lead to phenolic resin, and poly(methyl-furfuryloxysiloxane), a so-called twin prepolymer. This is shown in Scheme 2 together with a schematic description, where X symbolizes the inorganic fragment and Y, and Z the two different organic moieties of the heterotrifunctional monomer. W mirrors the water released during the polymerization of the furfuryloxy fragment Z.

In the course of the cationic multiple polymerization a copolymerization between the poly(furfuryl alcohol) and the
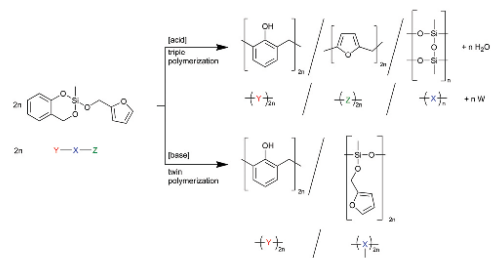
Scheme 2 Schematic description and reaction equation of the expected polymerization scenarios of the heterotrifunctional monomer 2-furfuryloxy-2-methyl-4H-1,3,2-benzodioxasiline (**1**) either leading to three different polymers or one polymer and one twin prepolymer.
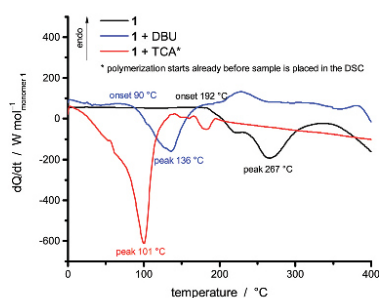
Fig. 2 Differential scanning calorimetry measurements of the monomer 2-(furfuryloxy)-2-methyl-4H-1,3,2-benzodioxasiline (**1**) solely (black line) and together with 1,8-diazabicycloundec-7-ene (DBU, blue line) and trichloroacetic acid (TCA, red line) catalysts.

phenolic resin cannot be excluded but is unlikely. Zhang and Solomon investigated the curing behavior of novolac/furfuryl alcohol resins and described their reaction with each other of minor importance. However, methylene linkages could be observed when hexamethylenetetramine was used for further crosslinking.[17] Pizzi et al. and Abdalla et al. investigated the reaction of mimosa tannin extract and furfuryl alcohol and identified reaction products using MALDI-TOF. Besides the products of the reaction of fisetinidin flavonoid units with furfuryl alcohol, they always found oligomers derived from the self-condensation of furfuryl alcohol.[18,19] As fisetinidin flavonoid units are much more reactive than phenol in Friedel–Crafts reactions, this shows that the self-condensation of furfuryl alcohol should be favored over the reaction with phenol. When comparing the π-nucleophilicity parameters according to Mayr,[20] the value of furan ($N = 1.33$, $s_N = 1.29$)[21] is higher than the value of anisole ($N = -1.18$, $s_N = 1.20$).[20] This means that the reactivity of furan is 250 times higher than anisole. If we assume a similar effect of the additional methylol group

and a comparability of the –OMe with the –OH substituent, the reactivity of furfuryl moieties should be higher and thus homopolymers should be formed.

The presence of different reaction scenarios can be supported by DSC measurements (see Fig. 2) of monomer **1** solely and together with potential catalysts. The catalysts 1,8-diazabicycloundec-7-ene (DBU) and trifluoroacetic (TFA) acid are used for the polymerization in bulk, as they are suitable catalysts for the twin polymerization of **Spiro**.[8] During the annealing of monomer **1** (black line) up to 400 °C, an exothermic peak is visible at around 267 °C. When DBU is added as a catalyst, the temperature of this exothermic peak is reduced to 136 °C, indicating the catalytic activity of the base. The addition of TFA leads to a polymerization already starting at room temperature during the mixing of the monomer and the catalyst (see Fig. S2, ESI,† for **1** + TFA). To delay this reaction the room temperature solid trichloroacetic acid (TCA) was used as a catalyst in the DSC investigations. When the integrals of the exothermic peaks are compared, it is obvious that the acid catalyzed polymerization is more exothermic than the base catalyzed polymerization. Exact values cannot be obtained, as the endothermic melting of TCA and the beginning of the evaporation of DBU occur in the same temperature range as the exothermic reaction (see Fig. S1, ESI†). The curves are calculated per mol of monomer only, neglecting the effects from the catalyst. These first results were verified by reproducing these polymerizations on a multigram scale, and the subsequent analysis of the products. Monolithic hybrid materials were obtained by TFA (**A**), or DBU (**B**) catalyzed as well as thermal polymerization (**T**) of **1**. **BA** describes the hybrid material from DBU catalyzed polymerization after post-treatment with methanesulfonic acid (MSA) (see Table 1).

A first indication, if the furfuryloxy-fragment has been polymerized or not, is the color of the hybrid material. During the formation of poly(furfuryl alcohol) some conjugated structures are always formed, which explain its dark green almost black color.[22] Only the hybrid material from the DBU catalyzed

Table 1 Summary of the synthesis conditions of the hybrid materials and the composition as measured by quantitative elemental analysis and thermogravimetric analysis (TGA)

Sample	Catalyst (conc./mol%)	Temp./°C	Residue mass TGA/%		Carbon content/%	Picture
			Air	He		
A	TFA (10)	50	21.3	50.1	57.0	
B	DBU (10)	140	13.4	39.2	65.0	
T	—	250	25.0	44.7	60.4	
BA	1. DBU (10) 2. MSA (10)	140 25	23.2	59.5	55.2	

Paper

polymerization is orange and transparent, which indicates that the polymerization of the furfuryloxy-fragment did not take place.

Fig. 3 shows the $^{13}C\text{-}\{^1H\}$-CP-MAS-NMR spectra of hybrid materials obtained from the polymerization of monomer **1** in the melt with different catalysts compared to the ^{13}C-NMR of compound **1** in CDCl$_3$ with the related chemical structures. All solid-state NMR spectra prove the formation of phenolic resin (signals a–e in Fig. 3). Only traces of unreacted CH$_2$O– R-Groups can be found, which indicates a high conversion of the salicyl alcohol fragments. When the polymerization was carried out with DBU as the catalyst, the sharp signals at 57 ppm and 142 ppm indicate unbroken CH$_2$–O–Si units, and the unsubstituted carbon in position 5 of the furan ring, respectively (see Fig. 3). This can be explained by the formation of a twin prepolymer and phenolic resin as suggested in Scheme 2. In the hybrid materials from acid catalyzed or thermally induced polymerization the isolated signals 4 and 13 of typical side products as well as the broad signals 5 and 6 show the formation of poly(furfuryl alcohol). The other signals overlap with the phenolic resin signals.[23] The absence of a signal at 57 ppm and the very low intensity of the signal at 142 ppm indicate that the furfuryl alcohol fragment showed a high conversion during the polymerization, as well. Salabarria *et al.* describe a reaction between furfuryl alcohol and phenol occurring mainly in the *para* position of the phenol.[24] Signals b and c represent unsubstituted *ortho* and *para* carbon atoms
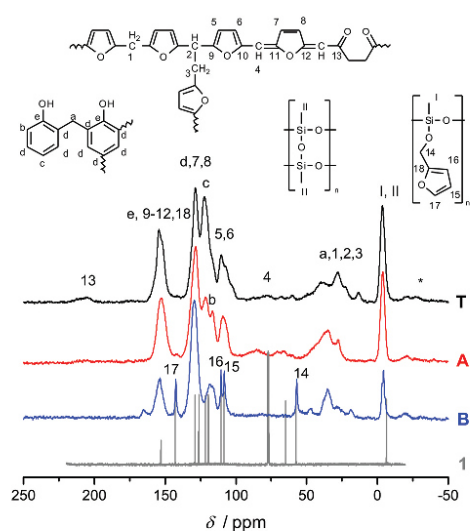
of the phenolic ring,[23,25] which shows that a reaction of furfuryl alcohol with the phenolic resin is of minor importance. In the solid state $^{29}Si\text{-}\{^1H\}$-CP-MAS-NMR spectra of the hybrid materials different T signals can be distinguished.[26,27] They result from structural units shown in Fig. 4, which further supports the described polymerization reactions. When DBU is used as a base catalyst for a polymerization in bulk, two relatively sharp, separated peaks, indicating the presence of T$_2$ and T$_3$ structures, and one peak of minor intensity, indicating T$_1$ units, are found. T$_3$ signals in the hybrid material from the base catalyzed polymerization might result from already occurring condensation reactions. Structural units of the suggested twin prepolymer can explain T$_2$ and T$_1$ signals. For the thermal and acid catalyzed polymerization in bulk still T$_2$ but mainly T$_3$ units are found. The peaks are broader and less separated, which indicates a higher condensed network. When the polymerization was carried out with MSA as precipitation polymerization, almost only the T$_3$ signal is found (see Fig. S4 ESI†). This shows that for the polymerization in bulk there might be a diffusion limitation leading to an incomplete polymerization of the inorganic fragment. It should be noted that, due to the cross polarization NMR experiments, the signal intensity of silicon atoms with hydrogen in the proximity is higher. Thus, the T$_1$ and T$_2$ structures give stronger signals than T$_3$ structures.

To investigate the accessibility of the furfuryloxy moieties for further reactions, the hybrid material from the DBU catalyzed twin polymerization of monomer **1** was ground and examined in the DSC. When solely the hybrid material is measured, no heat flow is observed. The same measurement, after addition of TCA, clearly shows an exothermal signal that
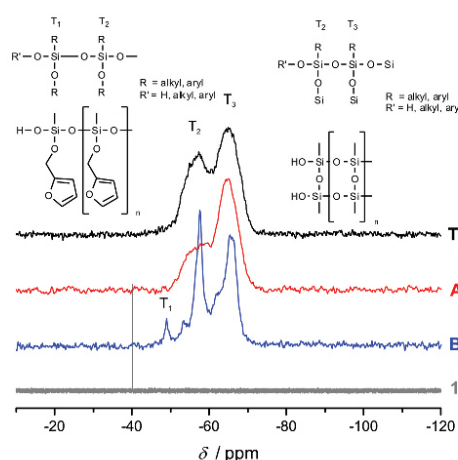

Fig. 3 ^{13}C-NMR spectrum of compound **1** in CDCl$_3$ compared with the solid state $^{13}C\text{-}\{^1H\}$-CP-MAS-NMR spectra of hybrid materials, obtained from the polymerization of monomer **1** thermally induced (black line) or catalyzed with **DBU** (blue line) and **TCA** (red line), together with the attributed chemical structures.

Fig. 4 ^{29}Si-NMR of compound **1** in CDCl$_3$ compared with the solid state $^{29}Si\text{-}\{^1H\}$-CP-MAS-NMR spectra of hybrid materials, obtained from the polymerization of monomer **1** with different catalysts, together with the attributed chemical structures.
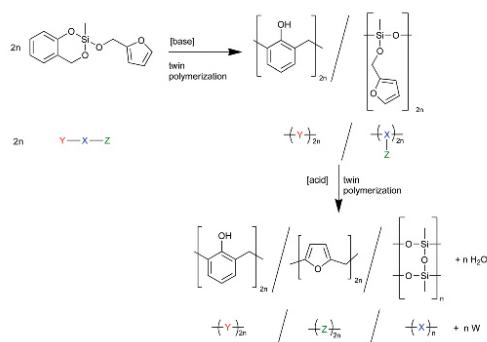
Scheme 3 Schematic description and reaction equation of the twin polymerization of monomer **1** yielding a twin prepolymer which can then undergo further twin polymerization to the final hybrid material.

Fig. 6 ^{29}Si-$\{^1H\}$-CP-MAS-NMR spectra of hybrid materials, obtained from the polymerization of monomer **1** with **DBU** as a catalyst compared with the acid post treated material, together with the attributed chemical structures.

indicates a polymerization (see Fig. S5, ESI†). Thus, the ground hybrid material **B** was suspended in CH_2Cl_2, and MSA was added as an acid catalyst, which should trigger a further polymerization as shown in Scheme 3. MSA is chosen as it is a good catalyst for twin polymerization of **Spiro** in solution.[8] Immediately after the addition of the acid the color becomes darker, which indicates the polymerization of the furanic moieties. The final hybrid material was isolated by filtration and investigated with solid state NMR spectroscopy to prove the molecular structure. It should be emphasized that soluble components are washed off during this process and do not remain in the hybrid material. It was found that the signals for the monomeric furfuryloxy moieties (signals 17 and 14 in Fig. 5) are drastically reduced, and poly(furfuryl) alcohol is
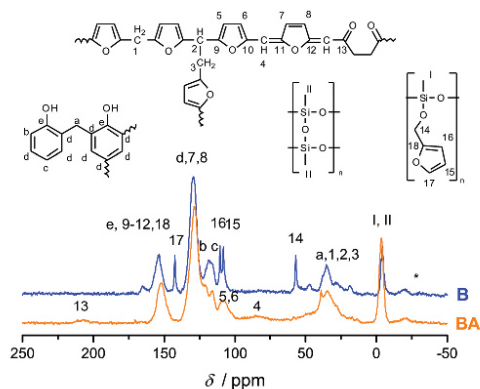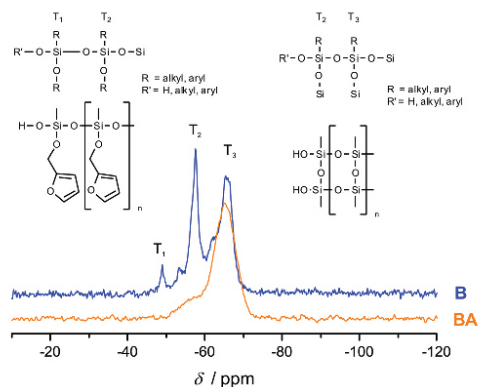
found in the final hybrid material as evidenced by the newly occurring peaks 4, 5, 6 and 13. Furthermore, after the treatment with an acid, the T_2 signal in the ^{29}Si-$\{^1H\}$-CP-MAS-NMR spectra (see Fig. 6) is reduced compared to the T_3 signal, which indicates the formation of a fully condensed poly-methylsilsesquioxane network. This shows that the hybrid material is still flexible enough to allow the polymerization
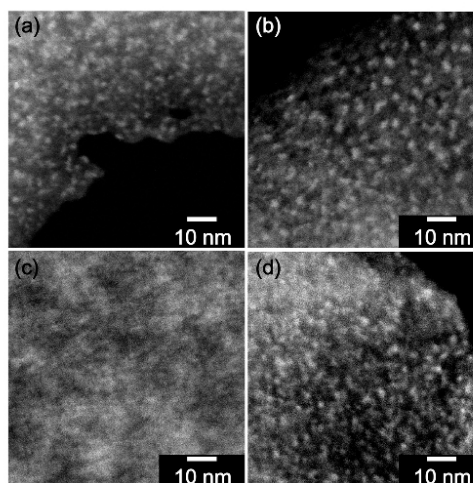

Fig. 5 ^{13}C-$\{^1H\}$-CP-MAS-NMR spectra of hybrid materials, obtained from the polymerization of monomer **1** with **DBU** as a catalyst compared with the acid post treated material, together with the attributed chemical structures.

Fig. 7 HAADF-STEM images from the hybrid material synthesized by acid catalyzed (a), thermally induced (b) and base catalyzed (c) multiple polymerization of monomer **1** compared with the hybrid material of the base catalyzed polymerization with additional treatment with methanesulfonic acid (d).

reactions of the furfuryloxy moieties and the inorganic network.

For information on the size of the phase domains high angle annular dark field scanning transmission electron microscopy (HAADF-STEM) investigations were carried out. This technique shows an elemental contrast besides the contrast attributed to sample thickness and density. With an increasing atomic number, higher signal intensity is observed.[28] Thus, silicon-rich domains of the hybrid material are shown brighter than the organic polymers. When the HAADF-STEM images of the different hybrid materials are compared (Fig. 7), it can be seen that the materials from the TFA catalyzed and thermally induced multiple polymerization show bright SiO_2 clusters with a rather similar size of 1–3 nm (see Fig. 7a and b). These SiO_2 clusters are very similar to the inorganic domains described for the phenolic resin/SiO_2 hybrid material obtained by twin polymerization of **Spiro**.[8] In contrast, the hybrid material derived from the DBU catalyzed twin polymerization of monomer **1** shows only a little contrast (Fig. 7c). This is attributed to the fact that the furfuryloxy unit is still connected to the silicon of the inorganic polymer and

thus the elemental contrast is reduced. Remarkably, after the post treatment with MSA, the silicon rich domains can clearly be seen. They show a similar size to the hybrid materials from acid catalyzed and thermally induced multiple polymerization of monomer **1** (Fig. 7d). This leads to the conclusion that the hybrid material **B** also consists of co-continuous nanodomains. By treating this hybrid material with MSA, the Si–O–CH_2 bond is cleaved and poly(furfuryl) alcohol is formed, leading to polymethylsilsesquioxane as an inorganic phase with a lower content of carbon, hydrogen, and oxygen.

The synthesized hybrid materials can be converted into porous carbon by annealing in an inert atmosphere and the removal of the inorganic network. To obtain porous SiO_2 the organic parts can be removed by annealing in an air atmosphere. During the oxidation the polymethylsilsesquioxane is oxidized to SiO_2.[29] As the organic and inorganic networks are interpenetrating, the occurring pores give an indication of the domain size of their respective counterparts in the hybrid materials.

The annealing in air leads to porous SiO_2, which shows specific surface areas between 423 and 621 m^2 g^{-1}. After
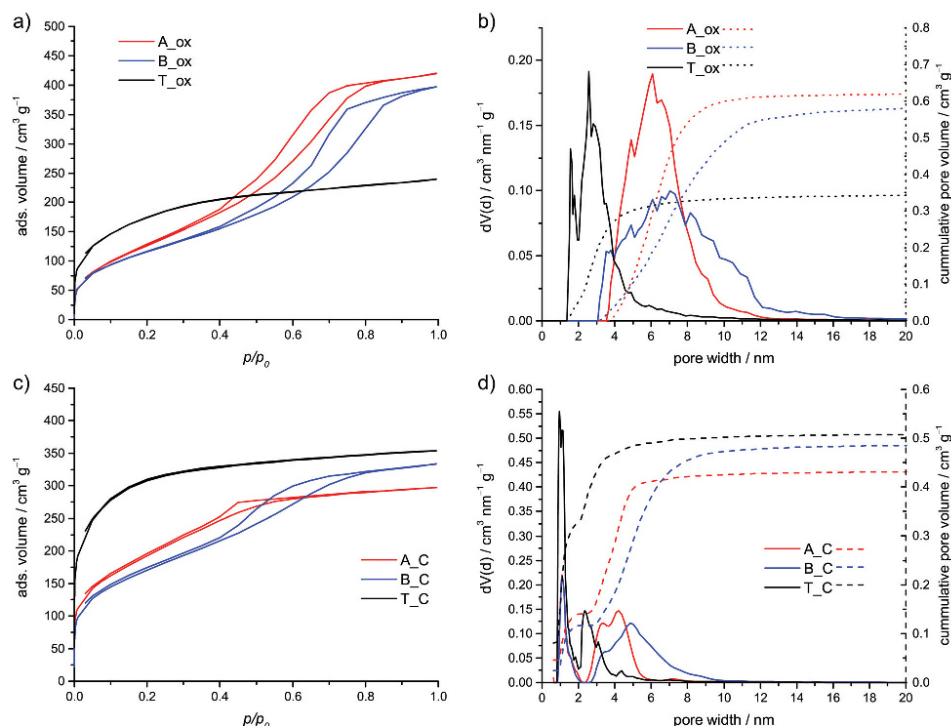

Fig. 8 Nitrogen sorption isotherms measured at 77 K and pore size distribution (NLDFT, adsorption branch, cylindrical pores) of the oxidized hybrid materials (a, b) and nitrogen sorption isotherms and pore size distribution (QSDFT, adsorption branch, slit pores + cylindrical pores) of the carbon materials obtained by inert annealing and subsequent HF etching of the hybrid materials (c, d).

Polymer Chemistry

Table 2 Summary of the results from nitrogen sorption analysis of the porous SiO_2 and carbon from the respective hybrid materials

Sample	BET surface area/m^2 g^{-1}	DFT surface area/m^2 g^{-1} (method)	Pore volume/cm^3 g^{-1}	Micropore volume/cm^3 g^{-1}
A_ox	473	406 (NLDFT)	0.627	0
B_ox	423	346 (NLDFT)	0.595	0
T_ox	621	481 (NLDFT)	0.349	0.053
A_C	638	688 (QSDFT)	0.433	0.140
B_C	603	547(QSDFT)	0.489	0.116
T_C	1114	1038(QSDFT)	0.510	0.329

oxidation, the theoretic amount of the residue is 22.9 wt% if the furfuryloxy moieties are polymerized, and 23.7 wt% if they remain unpolymerized. In contrast to the other hybrid materials **B** shows a residue of only 13.4 wt% (see Table 1, Fig. S7, ESI†). This is explained by a partial removal of the inorganic polymer and is known for polydimethylsiloxanes,[30–32] especially in the presence of base catalysts.[33] This result further proves the lower extend of condensation of the inorganic polymer.

The obtained SiO_2 materials **A_ox**, **B_ox** and **T_ox** show different adsorption properties (see Fig. 8a and b; Table 2). The isotherms of the SiO_2, obtained from the hybrid material of acid or base catalyzed polymerization, can be classified as type IV isotherms according to IUPAC.[34] In contrast, the isotherm of the SiO_2 from thermal polymerization is similar to type I. This behavior is reflected in the calculated pore size distribution. The type I isotherm is caused by smaller pores including some amount of micropores. In contrast, the hybrid materials **A_ox** and **B_ox** show only mesopores mainly between 3.5 and 10 nm and 3 and 12 nm for TFA and DBU catalyzed polymerization, respectively.

A similar trend is observed for the carbon materials obtained by carbonization of the hybrid material and the removal of the inorganic component. The inert annealing of polymethylsilsesquioxane leads to a mixture of SiO_2, carbon and silicon oxycarbide[35–37] with SiO_2 as the main component.[36] Thus, it can be removed with hydrofluoric acid solution. During inert annealing the hybrid material **B** shows the lowest amount of residue (see Fig. S8, ESI†). Furthermore, material **B**, after carbonization, shows the highest mass loss in an air atmosphere. Thus, it has the lowest inorganic content (see Fig. S9, ESI†) compared to the other carbonized materials due to a partial decomposition of the inorganic network. The final carbon materials were investigated in TGA and show mass losses of 98.8 wt% and more in an air atmosphere, proving the almost complete removal of the inorganic network (see Fig. S6, ESI†). The isotherm of the porous carbon **T_C** can be classified as type I isotherm, whereas the carbon materials **A_C** and **B_C** show a hysteresis (see Fig. 8c). While the latter shows a type IV isotherm, it is difficult to assign an isotherm type for the carbon **A_C**. The calculated pore size distributions can be seen in Fig. 8d. Though, in all cases, some micropores are present, the content of micropores is the highest for the carbon obtained from the hybrid material of the thermal polymerization. Both, the content and the size of the remaining mesopores are the highest for carbon from the DBU cata-

lyzed hybrid material. Together with the HAADF-STEM investigation, these results prove that in all cases nanostructured hybrid materials are obtained.

Conclusions

The heterotrifunctional monomer 2-(furfuryloxy)-2-methyl-4H-1,3,2-benzodioxasiline was synthesized and investigated for its polymerization behavior. It could be shown that, by the choice of the polymerization conditions, either two or three polymers are formed in one reaction step using, at the most, one catalyst. It is the first single-source monomer, which can be polymerized to three different polymers. The formation of the different networks occurs on the same time scale. Therefore, phase separation is very small and very similar to the already known hybrid materials from twin polymerization. This shows that regardless of whether two or three different polymers are formed, the underlying concept of the simultaneous formation of two or more polymers from only one monomer can lead to hybrid materials with very small nanodomains of its components. Future work will focus on the synthesis of other heteromultifunctional monomers for the multiple polymerization. Replacing furfuryl alcohol with 2-thiophenemethanol leads to a monomer, which might be polymerized in similar ways. Due to the additional sulfur, a more detailed investigation of the distribution of the individual polymers can be conducted.

Acknowledgements

Notes and references

1 M. Antonietti, *Nat. Mater.*, 2003, **2**, 9–10.
2 A. S. Aricò, P. Bruce, B. Scrosati, J.-M. Tarascon and W. van Schalkwijk, *Nat. Mater.*, 2005, **4**, 366–377.

3   A. Thomas, F. Goettmann and M. Antonietti, *Chem. Mater.*, 2008, **20**, 738–755.

4   H. S. Thiam, W. R. W. Daud, S. K. Kamarudin, A. B. Mohammad, A. A. H. Kadhum, K. S. Loh and E. H. Majlan, *Int. J. Hydrogen Energy*, 2011, **36**, 3187–3205.

5   G. Kickelbick, *Hybrid materials: synthesis, characterization, and applications*, Wiley-VCH, Weinheim, 2007.

6   S. Grund, P. Kempe, G. Baumann, A. Seifert and S. Spange, *Angew. Chem., Int. Ed.*, 2007, **46**, 628–632.

7   S. Spange and S. Grund, *Adv. Mater.*, 2009, **21**, 2111–2116.

8   S. Spange, P. Kempe, A. Seifert, A. A. Auer, P. Ecorchard, H. Lang, M. Falke, M. Hietschold, A. Pohlers, W. Hoyer, G. Cox, E. Kockrick and S. Kaskel, *Angew. Chem., Int. Ed.*, 2009, **48**, 8254–8258.

9   T. Ebert, A. Seifert and S. Spange, *Macromol. Rapid Commun.*, 2015, **36**, 1623–1639.

10 P. Kempe, T. Löschner, A. A. Auer, A. Seifert, G. Cox and S. Spange, *Chem. – Eur. J.*, 2014, **20**, 8040–8053.

11 T. Löschner, A. Mehner, S. Grund, A. Seifert, A. Pohlers, A. Lange, G. Cox, H.-J. Hähnle and S. Spange, *Angew. Chem., Int. Ed.*, 2012, **51**, 3258–3261.

12 T. Löschner, A. Seifert, R. Lungwitz, G. Cox, A. Lange, H.-J. Hähnle and S. Spange, *Macromol. Rapid Commun.*, 2011, **32**, F60–F61.

13 M. Göring, A. Seifert, K. Schreiter, P. Müller and S. Spange, *Chem. Commun.*, 2014, **50**, 9753–9756.

14 A. D. Jenkins, P. Kratochvíl, R. F. T. Stepto and U. W. Suter, *Pure Appl. Chem.*, 1996, **68**, 2287–2311.

15 J. V. Alemán, A. V. Chadwick, J. He, M. Hess, K. Horie, R. G. Jones, P. Kratochvíl, I. Meisel, I. Mita, G. Moad, S. Penczek and R. F. T. Stepto, *Pure Appl. Chem.*, 2007, **79**, 1801–1829.

16 T. Ebert, G. Cox, E. Sheremet, O. Gordan, D. R. T. Zahn, F. Simon and S. Spange, *Chem. Commun.*, 2012, **48**, 9867.

17 X. Zhang and D. H. Solomon, *Chem. Mater.*, 1998, **10**, 1833–1840.

18 A. Pizzi, G. Tondi, H. Pasch and A. Celzard, *J. Appl. Polym. Sci.*, 2008, **110**, 1451–1456.

19 S. Abdalla, A. Pizzi, F. Bahabri and A. Ganash, *Maderas: Cienc. Tecnol.*, 2015, 99–104.

20 H. Mayr, B. Kempf and A. R. Ofial, *Acc. Chem. Res.*, 2003, **36**, 66–77.

21 J. Ammer, C. Nolte and H. Mayr, *J. Am. Chem. Soc.*, 2012, **134**, 13902–13911.

22 M. Choura, N. M. Belgacem and A. Gandini, *Macromolecules*, 1996, **29**, 3839–3850.

23 G. A. Webb, *Annual reports on NMR spectroscopy*, Academic Press, San Diego, London, 1994, vol. 29.

24 I. R. Salabarría, P. A. Oyanguren, D. P. Fasce and R. J. J. Williams, *Polym. Int.*, 1995, **37**, 21–26.

25 R. Rego, P. J. Adriaensens, R. A. Carleer and J. M. Gelan, *Polymer*, 2004, **45**, 33–38.

26 R. Joseph, S. Zhang and W. T. Ford, *Macromolecules*, 1996, **29**, 1305–1312.

27 Z. L. Da, *eXPRESS Polym. Lett.*, 2007, **1**, 698–703.

28 S. Pennycook and D. Jesson, *Phys. Rev. Lett.*, 1990, **64**, 938–941.

29 V. V. Kireev, B. I. D'yachenko and V. P. Rybalko, *Polym. Sci., Ser. A*, 2008, **50**, 394–402.

30 C. W. Lewis, *J. Polym. Sci.*, 1958, **33**, 153–159.

31 T. H. Thomas and T. C. Kendrick, *J. Polym. Sci., Part B: Polym. Phys.*, 1969, **7**, 537–549.

32 T. H. Thomas and T. C. Kendrick, *J. Polym. Sci., Part B: Polym. Phys.*, 1970, **8**, 1823–1830.

33 M. Kučera, J. Láníková and M. Jelínek, *J. Polym. Sci.*, 1961, **53**, 301–310.

34 K. S. W. Sing, *Pure Appl. Chem.*, 1985, **57**, 603–619.

35 V. Belot, R. J. P. Corriu, D. Leclercq, P. H. Mutin and A. Vioux, *J. Mater. Sci. Lett.*, 1990, **9**, 1052–1054.

36 J. Ma, L. Shi, Y. Shi, S. Luo and J. Xu, *J. Appl. Polym. Sci.*, 2002, **85**, 1077–1086.

37 G. Trimmel, R. Badheka, F. Babonneau, J. Latournerie, P. Dempsey, D. Bahloul-Houlier, J. Parmentier and G. D. Soraru, *J. Sol–Gel Sci. Technol.*, 2003, **26**, 279–283.

3.1.5. A novel CAU-10-H MOF membrane for hydrogen separation under hydrothermal conditions

Authors: H. Jin, **A. Wollbrink**, R. Yao, Y. Li, J. Caro

A novel CAU-10-H MOF membrane for hydrogen separation under hydrothermal conditions

Hua Jin [a,b], Alexander Wollbrink [c], Rui Yao [a,b], Yanshuo Li [a,*], Juergen Caro [c], Weishen Yang [a,*]

[a] State Key Laboratory of Catalysis, Dalian Institute of Chemical Physics, Chinese Academy of Sciences, Dalian 116023, China
[b] University of Chinese Academy of Sciences, Beijing 100049, China
[c] Institute of Physical Chemistry and Electrochemistry, Leibniz University Hannover, Callinstr. 3, D-30167 Hannover, Germany

ARTICLE INFO

ABSTRACT

Hydrogen selective membranes with excellent hydrothermal stability are highly demanded in ethanol steam reforming. For this goal, a novel CAU-10-H MOF membrane has been prepared on α-Al_2O_3 disc for the first time by *in situ* solvothermal synthesis. The as-prepared CAU-10-H membrane shows high selectivity for H_2 with mixed gas separation factors of 10.5 and 74.7 for H_2/CO_2 and H_2/CH_4 binary mixtures, respectively, indicating the successful synthesis of CAU-10-H membrane with high-quality. The performance of the CAU-10-H membrane for hydrogen separation in the presence of steam was systematically investigated by variation of feed pressure (2–5 bar) and temperature (150–300 °C). The CAU-10-H membrane is selective for H_2, with separation factors of 11.1 and 5.67 for H_2 over CO_2 and H_2O, respectively. More importantly, the CAU-10-H membrane is still structure-preserving and hydrogen-selective after long-term test under hydrothermal conditions. These results demonstrate that the CAU-10-H membrane is an excellent candidate for hydrogen separation in steam reforming of ethanol in a membrane reactor.

© 2016 Elsevier B.V. All rights reserved.

1. Introduction

Hydrogen, a promising renewable fuel, has attracted tremendous attention as an ideal substitute for fossil fuels [1]. Recently, approximately 96% of the hydrogen has been produced from fossil-based processes [2], which are considered to be energy intensive and environment unfriendly. Reforming of biomass-derived ethanol is a type of promising low-carbon technology for hydrogen production, and has been studied extensively in recent years [3,4]. Except the main reaction pathway $C_2H_5OH + 3H_2O \rightleftarrows 2CO_2 + 6H_2$, numerous other competing side-reactions (*e.g.*, ethanol decomposition and methanation) can occur simultaneously [5], leading to the formation of undesirable by-products. An appealing method to effectively enhance the H_2 selectivity is adopting a membrane reactor for the continuous removal of H_2. Ethanol steam reforming is a strongly endothermic reaction, and therefore, high temperature (*i.e.*, higher than 350 °C) is required. More importantly, the product mixture contains a large amount of steam due to the necessity of a sufficient supply of steam to maximize hydrogen production in the process. Given all this, thermally and hydrothermally stable membranes with intrinsic high H_2/CO_2 and H_2/H_2O selectivity are highly demanded for *in situ* removing hydrogen from the ethanol steam reforming process.

Several types of inorganic membranes, such as Pd-based membranes, silica membranes and zeolite membranes, have been studied in hydrogen separation under steam and high temperature conditions. The Pd-based membranes have been widely used due to their full perm-selectivity to hydrogen. However, the high Pd cost and membrane degradation when contacting with hydrocarbon impurities or H_2S are major setbacks for their large-scale application [6]. Microporous silica membranes generally show excellent selectivity for H_2 over some larger gas molecules (*e.g.*, N_2 and CH_4), but they have proven to be unstable in humidified atmospheres [7]. To improve the hydrothermal stability, some research groups have synthesized the following two types of membranes: metal-doped silica membranes by metal doping to silica [8] and hybrid silica membranes fabricated from organic-inorganic hybrid alkoxides [9]. The modified silica membranes demonstrated good H_2 permeation with the H_2/H_2O selectivity around 30 under steam atmosphere at high temperature. Nevertheless, a decrease in H_2 permeance after exposure to steam was still observed after several hours [10]. Zeolite membranes can withstand harsh thermal and chemical conditions but show low H_2/CO_2 selectivity owing to the relatively large pores compared with small kinetic diameters of H_2 and CO_2 (0.289 and 0.330 nm,

* Corresponding authors.
E-mail addresses: leeys@dicp.ac.cn (Y. Li), yangws@dicp.ac.cn (W. Yang).

respectively) [11]. Besides, zeolite membranes are normally H_2O selective due to the adsorption of H_2O within the framework and the smaller kinetic diameter of H_2O (0.265 nm) compared with that of H_2 [12]. Until now, only a few zeolite membranes that exhibited good H_2 separation performance (H_2 permeance, H_2/CO_2 and H_2/H_2O selectivity) have been reported and the synthesis of these membranes is rather complicated [13].

Metal organic frameworks (MOFs), consisting of metal ions coordinated to organic linkers, are novel crystalline materials with potential applications in catalysis, gas storage and separation [14]. Compared with zeolites, MOFs possess extremely high surface areas and tuneable pore size and functionality which make them suitable materials for molecular sieve membranes [15]. More recently, MOF membranes, such as MIL-53 membrane [16], ZIF-7 membrane [17], $Zn_2(bim)_4$ nanosheets based membrane [18], ZIF-90 membrane [19] and CAU-1 membrane [20], have revealed excellent H_2/CO_2 separation performance. However, long-term hydrothermal stability of these MOF membranes has not been studied yet. CAU-10-H (CAU=Christian-Albrechts-University, Kiel, Germany), firstly reported by Stock et al. [21], is formed from aluminium ions and the V-shaped linker molecule 1,3-benzene dicarboxylic acid. Indexing of the powder pattern of CAU-10-H suggested a tetragonal cell with the space group $I4_1$. The structure of CAU-10-H is built up by cis corner-sharing AlO_6 polyhedra to form a helix, and then each helix is connected *via* isophthalic acid to four adjacent helices of alternating rotational orientation (Fig. 1). Thus, square-shaped channels with a maximum diameter of 7 Å are formed along c axis. The accessible diameter of the aperture formed by the aromatic rings of the linker is 4 Å according to the crystallographic data, which is around the kinetic diameter of light gases (CO_2, N_2, CH_4, etc.). CAU-10-H is stable in aqueous media at different pH-range from 2 to 8 and demonstrates good thermal stability at a temperature of around 430 °C. In addition, hydrothermal stability of CAU-10-H was confirmed by long-term *in situ* thermogravimetric cycling tests in a humid atmosphere [22]. Based on the fascinating properties above, the CAU-10-H MOF membrane is appropriate for H_2 purification from $H_2/CO_2/H_2O$ ternary mixture in bio-ethanol steam reforming process.

In the current work, a high-quality CAU-10-H membrane was fabricated for the first time by *in situ* solvothermal synthesis. The MOF membrane is highly efficient for H_2 separation with mixed gas separation factors of 10.5 and 74.7 for H_2/CO_2 and H_2/CH_4, respectively. The CAU-10-H membrane was also investigated for separation of H_2 from the ternary mixture 41 vol% H_2/41 vol% CO_2 /18 vol% H_2O at different feed pressures and temperatures.

2. Experimental

2.1. Chemicals

$Al_2(SO_4)_3 \cdot 18H_2O$ ($\geq 98\%$, Sigma-Aldrich), isophthalic acid (1,3-H_2BDC, 99%, Sigma-Aldrich), N,N-dimethylformamide (DMF, $\geq 99.5\%$, Tianjin Bodi Chemical Co., Ltd.), deionized water (H_2O, home-made), acetic acid ($\geq 99.5\%$, Sinopharm Chemical Reagent Co., Ltd.).

2.2. Membrane preparation

The CAU-10-H membrane was prepared by *in situ* solvothermal synthesis on porous alumina support. The membrane support purchased from Inocermic GmbH is a circular disc with a diameter of 18 mm and a thickness of 1 mm. The support has a double-layered structure consisting of a coarse α-Al_2O_3 layer coated with finer top layer of α-Al_2O_3 of average 70 nm pore size. In order to obtain a high-quality membrane, the CAU-10-H membrane was synthesized two times using the exactly same procedure. In a typical procedure, 800 mg of $Al_2(SO_4)_3 \cdot 18 H_2O$, 200 mg of 1,3-$H_2$BDC, 1 ml of DMF and 4 ml of H_2O was mixed together by sonication in an ultra-sonic bath for 15 min. Then the mixture was transferred into a Teflon autoclave in which the asymmetric α-alumina disc was placed horizontally. Afterwards the autoclave was heated in a microwave oven (Ethos 1, MLS) to 135 °C in 10 min, and kept at 135 °C in 45 min. After cooling, the membrane was washed with acetic acid and deionized water and dried at 60 °C for 2 h.

2.3. Characterization

The X-ray powder diffraction (XRD) measurements were carried out on Bruker D8 Advance diffractometer (Bruker AXS GmbH)
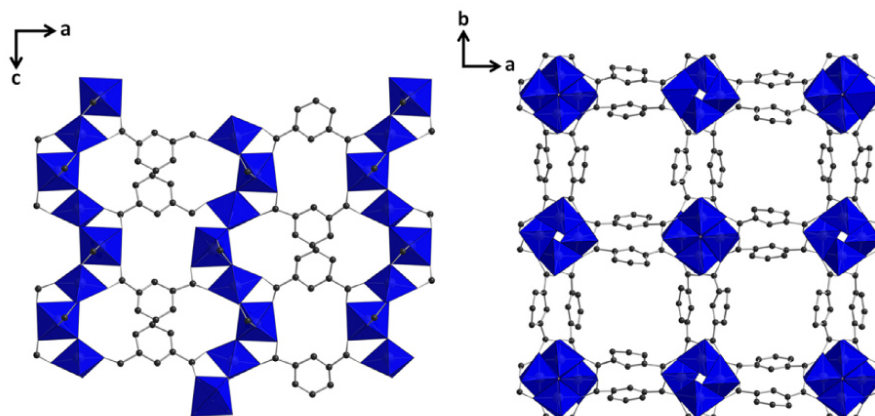

Fig. 1. The framework structure of CAU-10-H as seen along the b-axis and c-axis. AlO_6-polyhedra are shown in blue, and carbon atoms as dark spheres. (For interpretation of the references to color in this figure legend, the reader is referred to the web version of this article.)

with a Bragg-Brentano geometry using a CuKα radiation, secondary Ni-Filter and a 1-dimensional LynxEye detector with silicon strip. Data were collected in a step-scan mode in the range of 5–50° with step size of 0.01° and interval time of 0.15 s.

The scanning electron microscopy (SEM) images were taken in secondary electron contrast with a JEOL JSM-6700F instrument using a cold-field emission gun with an acceleration voltage of 2 kV and an emission current of 10 μA. The EDXS measurements were performed on the SEM at 5 kV, 10 mA for 1 h scanning.

2.4. Gas permeation experiments

The as-synthesized CAU-10-H membrane was sealed in a permeation module developed by TU Delft (F. Kapteijn, J. Gascon) with black O-rings (Perlast® G75B/FFKM 79) as seals on both ends. Before gas permeation tests, the membrane was activated to remove the occluded DMF and water molecules in its cavities. The activation method was as follows: keeping the membrane at 200 °C over night with H_2/CO_2 mixture (each gas of 50 ml min^{-1}) as feed gas and He (6 ml min^{-1}) as sweep gas.

For mixed gas separation, the feed flow rate was constant with a total volumetric flow rate of 100 ml min^{-1} with each gas of 50 ml min^{-1} (1:1 mixture). The feed temperature was fixed at 200 °C. No sweep gas was used in the permeate side and the driving force for permeation comes from pressure difference across the membrane. By doing this, the influence of sweeping gas on the measurement of separation properties of the membranes could be eliminated. The absolute feed pressure varied from 2 up to 5 bar while the permeate pressure was always at 1 bar. The composition of the permeate was analyzed by a calibrated gas chromatograph (Agilent 7890B). The permeate flow rate was measured by a bubble counter with a total volume of 4 ± 0.02 ml.

For the hydrogen separation under hydrothermal conditions, a controlled evaporator mixer system (type: W102A, Co. Bronkhorst-Nord GmbH) coupled with a digital mass flow meter/controller (mini-CORI-FLOW: M-12P) was used to saturate the H_2/CO_2 gas mixture (each gas of 50 ml min^{-1}) with steam. The steam content of the ternary gas mixture was limited to 18 vol% in order to prevent the feed pressure regulating system from undesired pressure jumps due to uncontrolled condensation. The separation performance for the $H_2/CO_2/H_2O$ ternary mixture was investigated at feed pressure range of 2–5 bar and temperature range of 150–300 °C. During the entire testing process, no sweep gas was used and the pressure in the permeate side was constant at 1 bar.

Permeance and selectivity are two important parameters generally used to characterize membrane performance. The permeance F_i for the permeating gas i is defined as:

$$F_i = \frac{N_i}{\Delta P_i A}$$

where N_i is the permeating rate of component i (mol s^{-1}), ΔP_i is the transmembrane pressure difference of component i (Pa), and A is the effective membrane area (m^2). The mixed gas separation factor $\alpha_{i,j}$ is defined as:

$$\alpha_{i,j} = \frac{y_i/y_j}{x_i/x_j}$$

where y_i (y_j) is the molar fraction of component i (j) in the permeate, x_i (x_j) is the molar fraction of component i (j) in the feed. The relation of gas permeance and temperature can be described by the Arrhenius equation:

$$F_i = F_i^0 \exp\left(-\frac{E_{act}}{RT}\right)$$

where F_i is the permeance of component i, F_i^0 the pre-exponential

factor, E_{act} the apparent activation energy of permeation, R the ideal gas constant, and T the temperature in Kelvin.

3. Results and discussion

3.1. Characterization of the as-synthesized CAU-10-H membrane

Fig. 2 presents the XRD patterns and SEM images of the as-synthesized CAU-10-H membrane. As can be seen from Fig. 2a, the membrane is composed of pure CAU-10-H phase. Furthermore, the CAU-10-H layer has no preferential orientation by comparing XRD patterns of the isotropic powder and the membrane. The SEM top-view (Fig. 2b) reveals that the CAU-10-H layer consists of randomly oriented crystals, which is in conformity with the XRD result. The SEM cross-section view (Fig. 2c) shows that the membrane is well intergrown with a thickness of about 6 μm. Energy-dispersive X-ray spectroscopy (EDXS) reveals that there is a sharp transition between the CAU-10-H layer and the alumina support.

3.2. Mixed gas separation performance of the CAU-10-H membrane

The performance of the CAU-10-H membrane was evaluated by mixed gas permeation tests using equimolar binary gas mixtures (H_2/CH_4 or H_2/CO_2) at a temperature of 200 °C and feed pressure of 2 bar. Fig. 3 depicts the gas permeance in function of molecular size. It can be found that there is a steep decrease in the permeance between H_2 and CO_2, which can be interpreted by the size-exclusive molecular sieving mechanism. Thus the corresponding mixed gas separation factors of H_2/CO_2 and H_2/CH_4 are 10.5 and 74.7, respectively, which are higher than the Knudsen separation factors (4.7 and 2.8, respectively). Owing to the hindering effects of strongly adsorbed CO_2, the H_2 permeance of H_2/CO_2 binary mixture is slightly lower than that of H_2/CH_4 binary mixture.

For the separation of H_2/CO_2 binary mixture at 200 °C, the effect of feed pressure on membrane performance was investigated. As illustrated in Fig. 4, both the H_2 and CO_2 permeances increased gradually with increasing feed pressure, while the H_2/CO_2 mixed gas separation factors decreased. The maximum H_2/CO_2 selectivity obtained at a feed pressure of 2 bar was 10.5 with the H_2 permeance of 3.8×10^{-9} mol m^{-2} s^{-1} Pa^{-1}. The H_2/CO_2 separation factor decreased from 10.5 at 2 bar to 7.9 at 3 bar, and then maintained constant at a value of around 7.5. The separation factor exceeded the Knudsen separation factor (4.7) at pressure up to 5 bar, indicating that the CAU-10-H membrane can still be used for H_2/CO_2 separation at high pressure. As the feed pressure increases, CO_2 adsorbs more preferentially than H_2 because of the stronger interaction between CO_2 and MOF pores [21,23]. Therefore, the suppression effect of CO_2 on H_2 permeation through the CAU-10-H membrane leads to the observed decrease of the H_2/CO_2 separation factor.

3.3. $H_2/CO_2/H_2O$ multicomponent selectivity of the CAU-10-H membrane

As to ethanol steam reforming, sufficient supply of steam is essential to maximize hydrogen production. Thus, the impact of H_2O on the H_2 separation performance of the CAU-10-H membrane is obliged to be considered. Effect of feed pressure and temperature on the membrane performance (H_2 permeance, H_2/CO_2 separation factor and H_2/H_2O separation factor) was investigated for the ternary mixture of 41 vol% H_2/41 vol% CO_2/18 vol% H_2O. Overall, the maximum H_2/CO_2 and H_2/H_2O mixed gas separation factors were 11.1 and 5.67, respectively, with a H_2 permeance of 1.53×10^{-8} mol m^{-2} s^{-1} Pa^{-1} obtained at a
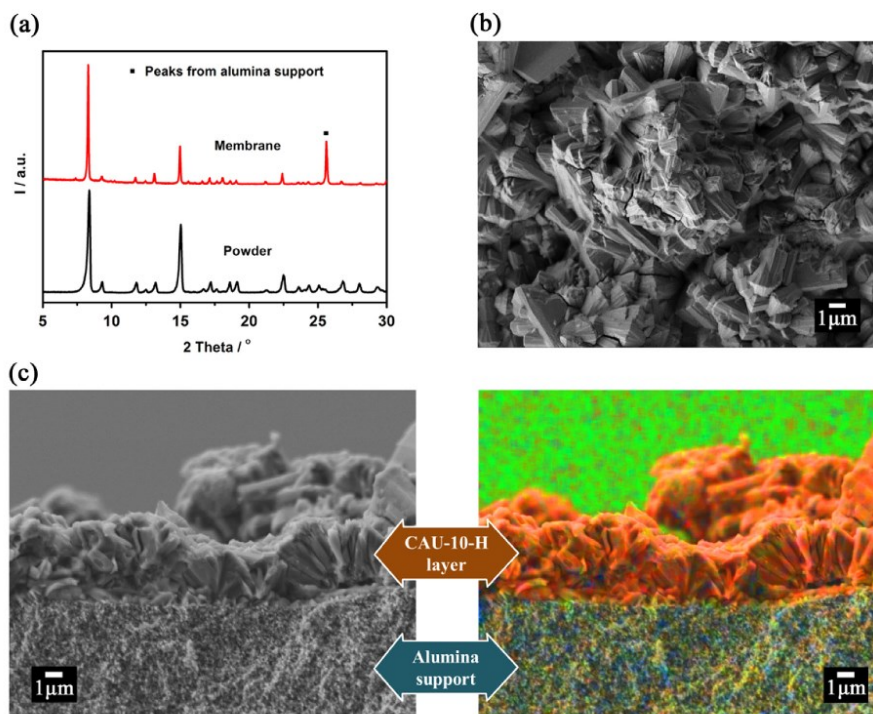
43

Fig. 2. (a) XRD patterns of the CAU-10-H powder (black line) and membrane (red line); (b) top view SEM image of the CAU-10-H membrane; (c) cross-sectional SEM image and the corresponding EDXS-mapping of the CAU-10-H membrane; orange-red C. (For interpretation of the references to color in this figure legend, the reader is referred to the web version of this article.)
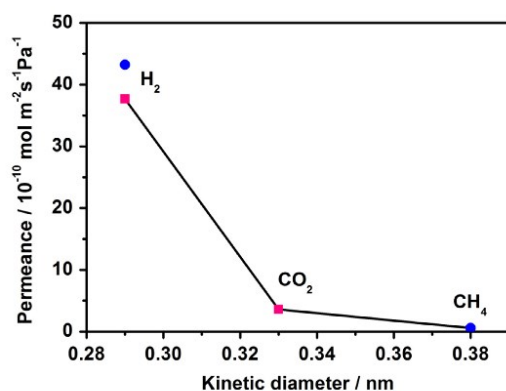

Fig. 3. H_2, CO_2 and CH_4 mixed gas permeances from equimolar binary mixtures (H_2/CH_4 or H_2/CO_2) of the CAU-10-H membrane as a function of the kinetic diameter (circles: H_2/CH_4 mixture, squares: H_2/CO_2 mixture).
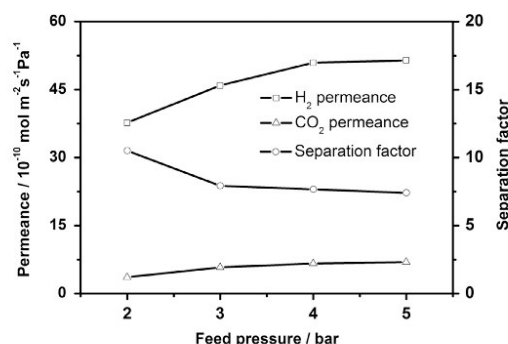

Fig. 4. H_2 and CO_2 permeances from equimolar binary mixtures and H_2/CO_2 mixed gas separation factor of the CAU-10-H membrane as a function of the feed pressure at 200 °C.

temperature of 150 °C and feed pressure of 2 bar. These results demonstrate that the CAU-10-H membrane is H_2 selective in the presence of steam at high temperature. Table 1 compares the performance of CAU-10-H membrane with the limited literature data on the separation of $H_2/CO_2/H_2O$ ternary mixture using microporous membranes. The CAU-10-H membrane showed good

H_2/CO_2 separation factor comparable with that of ZSM-5/Silicalite bilayer membrane [13], and a higher one than that of Silicalite I membrane [24], ZSM-5 membrane [24] and graphite membrane [25]. The CAU-10-H membrane showed higher H_2 permeance under similar testing conditions compared with the literature reported membranes. The H_2/H_2O selectivity of the CAU-10-H membrane is lower than that of pure Silicalite I membrane [24] and ZSM-5/Silicalite bilayer membrane [13]. The latter membrane

Table 1
Comparison of the H_2 separation performances of the CAU-10-H membrane in this work with other membranes in the literatures.

Membrane	Temperature (°C)	Partial pressure of H_2O (kPa)	H_2 permeances (mol m^{-2} s^{-1} Pa^{-1})	Selectivity		Ref.
				H_2-CO_2	H_2-H_2O	
Silicalite	550	76	5.8×10^{-7}	3.5	103	[24]
ZSM-5	550	76	5.2×10^{-7}	3.4	12	
ZSM-5/Silicalite bilayer	200	0	8.7×10^{-8}	17	–	[13]
	300	0	1.0×10^{-7}	22	–	
	500	154	1.0×10^{-7}	14	155	
Pressed graphite	200	50	9×10^{-9}	5	12	[25]
CAU-10-H	150	36	1.5×10^{-8}	11.1	5.7	This study
	200	36	8.0×10^{-8}	10.3	5.3	
	300	36	1.8×10^{-7}	8.9	3.6	

showed much higher H_2/H_2O selectivity than the H_2/CO_2 selectivity, although H_2O has a smaller kinetic diameter than CO_2. The authors attributed this phenomenon to two reasons, i) the hydrophobic Silicalite I layer may significantly limit the water vapour permeation through the membrane; ii) the low H_2O permeance of the membrane may also stem from the surface adsorption of H_2O molecules on ZSM-5, considering the stronger adsorption affinity between H_2O molecules and the top ZSM-5 zeolite. The second speculation might also be valid to explain the results of our CAU-10-H membrane, since CAU-10-H is relatively hydrophilic. As far as we know, the CAU-10-H membrane is the first MOF membrane reported for gas separation including steam at harsh conditions (*i.e.*, feed pressure up to 5 bar and temperature up to 300 °C).

Feed pressure dependence of the H_2, CO_2, H_2O permeances and the corresponding H_2/CO_2, H_2/H_2O separation factors at 200 °C are shown in Fig. 5. The H_2 permeance remained nearly unchanged with increasing feed pressure, while the CO_2 and H_2O permeances gradually increased and the corresponding H_2/CO_2 and H_2/H_2O selectivity exhibited a steady decrease. The selectivity-pressure relationship is consistent with that obtained in H_2/CO_2 binary mixture separation (see Fig. 4) owing to the strong interaction of CO_2 and H_2O with CAU-10-H framework [21]. An interesting phenomenon was found comparing Fig. 4 and 5: the H_2 and CO_2 permeances increased more than one order of magnitude after adding 18 vol% H_2O to the equimolar H_2/CO_2 mixture. Normally, the presence of steam has a suppression effect on H_2 and CO_2 permeation [24]. The reason is still unclear at present. The possibility of membrane degradation can be eliminated. CAU-10-H is hydrophilic, perfectly stable towards water and has not shown any
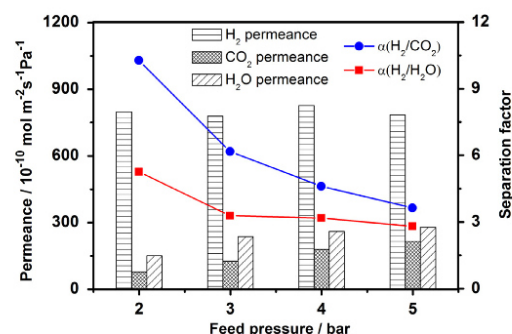
sign of degradation over 700 repeated adsorption/desorption cycles [22]. The stability is not compromised when this MOF is coated on a substrate for an adsorption driven heat pumps and chillers [26,27]. Besides, the H_2/CO_2 separation factors were basically unaffected after adding water. As can be seen from the adsorption isotherm, water is preferentially adsorbed by CAU-10-H [21]. Accordingly, we speculate that the stronger adsorption affinity between H_2O molecules and CAU-10-H might weaken the interactions between H_2 or CO_2 with the pore walls of CAU-10-H, resulting in a remarkably enhanced permeability of H_2 or CO_2 through the membrane.

Fig. 6 represents the effect of temperature on H_2, CO_2, H_2O permeances and the corresponding separation factors from their ternary mixture at a feed pressure of 2 bar. The permeances of H_2, CO_2 and H_2O increased quickly with increasing temperature and the corresponding H_2/CO_2 and H_2/H_2O separation factors displayed a slow decrease. The increase of the permeance with temperature indicates that the permeation through the CAU-10-H membrane follows an activated permeation mechanism. Fig. 7 shows Arrhenius-type plots of the permeances for H_2, CO_2 and H_2O on the CAU-10-H membrane. The correlation coefficients were 1.000, 0.9991 and 0.9997 for H_2, CO_2 and H_2O, respectively, indicating good fits to the Arrhenius expression. The apparent activation energy (E_{act}) for H_2 permeation calculated by fitting the available gas permeance data to the Arrhenius equation is 33.4 kJ mol^{-1}, which is at the upper limit of the scattering values 2–35 kJ mol^{-1} reported in the literatures [28]. As pointed out by Burggraaf and co-workers, high quality membranes should have activation energy of at least 10 kJ mol^{-1} for H_2 permeance [29]. The E_{act} of H_2 on our CAU-10-H membrane is much higher than 10 kJ mol^{-1},
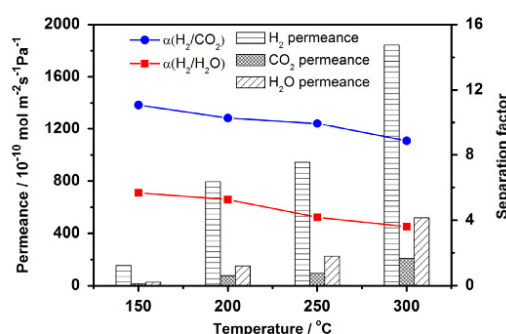

Fig. 5. H_2, CO_2 and H_2O permeances from ternary mixture (41 vol% H_2/41 vol% CO_2/18 vol% H_2O) and H_2/CO_2, H_2/H_2O separation factors of the CAU-10-H membrane as a function of the feed pressure at 200 °C.

Fig. 6. H_2, CO_2 and H_2O permeances from ternary mixture (41 vol% H_2/41 vol% CO_2/18 vol% H_2O) and H_2/CO_2, H_2/H_2O separation factors of the CAU-10-H membrane as a function of the temperature at a feed pressure of 2 bar.
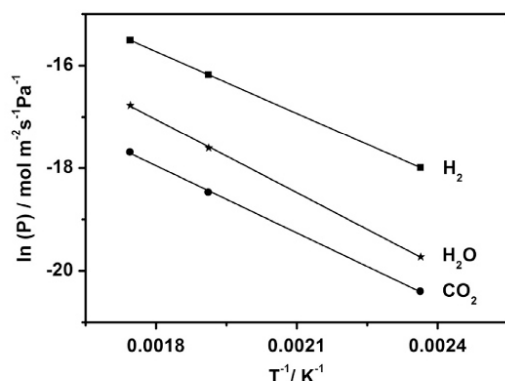
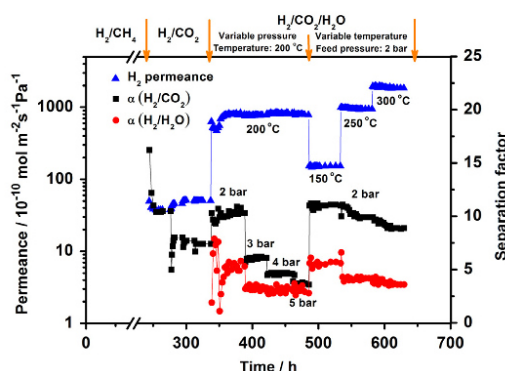**Fig. 7.** Arrhenius plots of the permeances for H_2, CO_2 and H_2O on the CAU-10-H membrane.

Fig. 8. A summary of the long term test of the CAU-10-H membrane.

H_2 with increasing temperature, leading to slightly decreasing H_2/CO_2 or H_2/H_2O separation factor. At 300 °C, the H_2/CO_2 and H_2/H_2O separation factors obtained were about 8.9 and 3.6, respectively, still exceeding the Knudsen separation factors (4.7 and 3, respectively). It is amazing that a MOF membrane exhibits good H_2 separation performance in the presence of steam at high temperature up to 300 °C. The exciting result reported here is important for expanding the application scope of MOF membranes.

Furthermore, it is worth noting that the permeance of H_2O was found to be lower than that of H_2 despite of the smaller kinetic diameter of H_2O in comparison with H_2. H_2O is a polar non-spherical molecule that is stronger adsorbed than H_2 due to the hydrophilic character of CAU-10-H, which may reduce its diffusivity through CAU-10-H membrane. Therefore, by the interplay of mixed gas adsorption and diffusion, H_2 separation from H_2/H_2O binary mixture is possible.

3.4. Long-term durability test

Fig. 8 is a summary of the long-term test of the CAU-10-H membrane. The membrane was firstly studied with equimolar binary mixtures H_2/CH_4 and H_2/CO_2 at 200 °C with variable feed pressure for half past a month. Then the hydrogen separation performance of the CAU-10-H membrane for the ternary mixture (41 vol% H_2/41 vol% CO_2/18 vol% H_2O) was investigated by varying the feed pressure and temperature. After nearly one month test, the CAU-10-H membrane was re-measured for $H_2/CO_2/H_2O$ ternary mixture separation at 200 °C and a feed pressure of 2 bar. The H_2/CO_2 and H_2/H_2O mixed gas separation factors are 7.50 and 4.39, respectively, and this finding is basically consistent with the starting measurements (10.3 and 5.26, respectively). The spent membrane was then characterized with XRD and SEM. As can be seen from the XRD pattern (Fig. 9a), the crystal structure of the CAU-10-H layer remained unchanged. The SEM image (Fig. 9b) indicates that the MOF crystals were less faceted but still in integrity. This might suggest some annealing of defects took place when operated at high temperature in the presence of steam. Generally, the CAU-10-H membrane was still hydrogen-selective after long-term gas separation test under hydrothermal conditions, which makes CAU-10-H membranes promising for high temperature hydrogen purification in bio-ethanol steam reforming process.
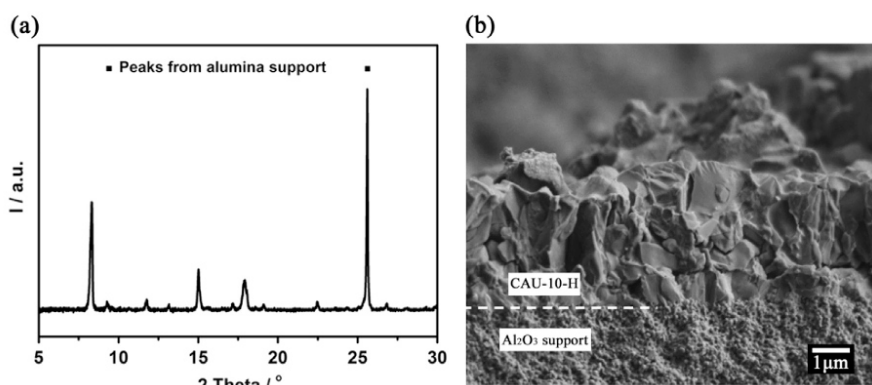
demonstrating that the high-performance CAU-10-H membrane for hydrogen separation was developed. The activation energies estimated for CO_2 and H_2O are 36.2 and 39.6 kJ mol^{-1}, respectively, both of which are slightly higher than that of H_2. Therefore, the permeance of CO_2 or H_2O increased at a faster rate than that of

Fig. 9. XRD pattern (a) and SEM image (b) of the spent CAU-10-H membrane.

Results and Discussion: Microporous carbon membranes

4. Conclusions

In summary, a novel CAU-10-H membrane with thickness of about 6 μm was prepared for the first time by a simple *in situ* solvothermal method. The as-prepared CAU-10-H membrane has H_2/CH_4 mixed gas selectivity as high as 74.7, demonstrating the successful synthesis of a continuous and crack-free membrane. The separation performance of the CAU-10-H membrane for $H_2/CO_2/H_2O$ ternary mixture was investigated at different feed pressures and temperatures. The membrane shows preferential permeation of H_2, and the maximum mixed gas separation factors for H_2/CO_2 and H_2/H_2O are 11.1 and 5.67, respectively, with a H_2 permeance of 1.53×10^{-8} mol m^{-2} s^{-1} Pa^{-1}. After the gas permeation test at high temperature for nearly one month, the crystal structure of the CAU-10-H membrane is preserved. To the best of our knowledge, the CAU-10-H membrane is the first reported MOF membrane exhibiting a comparative stability under hydrothermal conditions with good H_2/CO_2 and H_2/H_2O selectivities, demonstrating the potential of CAU-10-H membrane reactor for H_2 separation in bio-ethanol steam reforming.

Acknowledgment

References

[1] T. Bak, J. Nowotny, M. Rekas, C.C. Sorrell, Photo-electrochemical hydrogen generation from water using solar energy. Materials-related aspects, Int. J. Hydrogen Energy 27 (2002) 991–1022.
[2] M. Balat, Potential importance of hydrogen as a future solution to environmental and transportation problems, Int. J. Hydrogen Energy 33 (2008) 4013–4029.
[3] M. Ni, D.Y.C. Leung, M.K.H. Leung, A review on reforming bio-ethanol for hydrogen production, Int. J. Hydrogen Energy 32 (2007) 3238–3247.
[4] A. Haryanto, S. Fernando, N. Murali, S. Adhikari, Current status of hydrogen production techniques by steam reforming of ethanol: a review, Energy Fuels 19 (2005) 2098–2106.
[5] L.V. Mattos, G. Jacobs, B.H. Davis, F.B. Noronha, Production of hydrogen from ethanol: review of reaction mechanism and catalyst deactivation, Chem. Rev. 112 (2012) 4094–4123.
[6] A. Iulianelli, A. Basile, Hydrogen production from ethanol via inorganic membrane reactors technology: a review, Catal. Sci. Technol. 1 (2011) 366–379.
[7] Y.S. Lin, I. Kumakiri, B.N. Nair, H. Alsyouri, Microporous inorganic membranes, Sep. Purif. Methods 31 (2002) 229–379.
[8] R. Igi, T. Yoshioka, Y.H. Ikuhara, Y. Iwamoto, T. Tsuru, Characterization of Co-doped silica for improved hydrothermal stability and application to hydrogen separation membranes at high temperatures, J. Am. Ceram. Soc. 91 (2008) 2975–2981.
[9] M. Kanezashi, K. Yada, T. Yoshioka, T. Tsuru, Design of silica networks for development of highly permeable hydrogen separation membranes with hydrothermal stability, J. Am. Chem. Soc. 131 (2009) 414–415.
[10] T. Tsuru, R. Igi, M. Kanezashi, T. Yoshioka, Permeation properties of hydrogen and water vapor through porous silica membranes at high temperatures, AIChE J. 57 (2011) 618–629.
[11] B. Michalkiewicz, Z.C. Koren, Zeolite membranes for hydrogen production from natural gas: state of the art, J. Porous Mater. 22 (2015) 635–646.
[12] S.A.S. Rezai, J. Lindmark, C. Andersson, F. Jareman, K. Möller, J. Hedlund, Water/hydrogen/hexane multicomponent selectivity of thin MFI membranes with different Si/Al ratios, Microporous Mesoporous Mater. 108 (2008) 136–142.
[13] H.B. Wang, X.L. Dong, Y.S. Lin, Highly stable bilayer MFI zeolite membranes for high temperature hydrogen separation, J. Membr. Sci. 450 (2014) 425–432.
[14] H.C. Zhou, J.R. Long, O.M. Yaghi, Introduction to metal-organic frameworks, Chem. Rev. 112 (2012) 673–674.
[15] H. Furukawa, K.E. Cordova, M. O'Keeffe, O.M. Yaghi, The chemistry and applications of metal-organic frameworks, Science 341 (2013) 974–986.
[16] F. Zhang, X.Q. Zou, X. Gao, S.J. Fan, F.X. Sun, H. Ren, G.S. Zhu, Hydrogen selective NH₂–MIL-53(Al) MOF membranes with high permeability, Adv. Funct. Mater. 22 (2012) 3583–3590.
[17] Y.S. Li, F.Y. Liang, H. Bux, A. Feldhoff, W.S. Yang, J. Caro, Molecular sieve membrane: supported metal-organic framework with high hydrogen selectivity, Angew. Chem. Int. Ed. 49 (2010) 548–551.
[18] Y. Peng, Y.S. Li, Y.J. Ban, H. Jin, W.M. Jiao, X.L. Liu, W.S. Yang, Metal-organic framework nanosheets as building blocks for molecular sieving membranes, Science 346 (2014) 1356–1359.
[19] A.S. Huang, J. Caro, Covalent post-functionalization of zeolitic imidazolate framework ZIF-90 membrane for enhanced hydrogen selectivity, Angew. Chem. Int. Ed. 50 (2011) 4979–4982.
[20] S.Y. Zhou, X.Q. Zou, F.X. Sun, H. Ren, J. Liu, F. Zhang, N. Zhao, G.S. Zhu, Development of hydrogen-selective CAU-1 MOF membranes for hydrogen purification by 'dual-metal-source' approach, Int. J. Hydrogen Energy 38 (2013) 5338–5347.
[21] H. Reinsch, M.A. van der Veen, B. Gil, B. Marszalek, T. Verbiest, D. de Vos, N. Stock, Structures, sorption characteristics, and nonlinear optical properties of a new series of highly stable aluminum MOFs, Chem. Mater. 25 (2013) 17–26.
[22] D. Fröhlich, S.K. Henninger, C. Janiak, Multicycle water vapour stability of microporous breathing MOF aluminium isophthalate CAU-10-H, Dalton Trans. 43 (2014) 15300–15304.
[23] A.D. Wiersum, C. Giovannangeli, D. Vincent, E. Bloch, H. Reinsch, N. Stock, J.S. Lee, J.S. Chang, P.L. Llewellyn, Experimental screening of porous materials for high pressure gas adsorption and evaluation in gas separations: application to MOFs (MIL-100 and CAU-10), ACS Comb. Sci. 15 (2013) 111–119.
[24] H.B. Wang, Y.S. Lin, Effects of water vapor on gas permeation and separation properties of MFI zeolite membranes at high temperatures, AIChE J. 58 (2012) 153–162.
[25] A. Schulz, F. Steinbach, J. Caro, Pressed graphite crystals as gas separation membrane for steam reforming of ethanol, J. Membr. Sci. 469 (2014) 284–291.
[26] M.F. de Lange, C.P. Ottevanger, M. Wiegman, T.J.H. Vlugt, J. Gascon, F. Kapteijn, Crystals for sustainability-structuring Al-based MOFs for the allocation of heat and cold, CrystEngComm 17 (2015) 281–285.
[27] M.F. de Lange, T. Zeng, T.J.H. Vlugt, J. Gascon, F. Kapteijn, Manufacture of dense CAU-10-H coatings for application in adsorption driven heat pumps: optimization and characterization, CrystEngComm 17 (2015) 5911–5920.
[28] D. Koutsonikolas, S. Kaldis, G.P. Sakellaropoulos, A low-temperature CVI method for pore modification of sol-gel silica membranes, J. Membr. Sci. 342 (2009) 131–137.
[29] R.S.A. de Lange, J.H.A. Hekkink, K. Keizer, A.J. Burggraaf, Y.H. Ma, Gas transport on microporous sol-gel derived ceramic membranes. Part II. Sorption studies, J. Porous Mater. 2 (1995) 141–149.

3.2. Porous graphite membranes

The following chapter deals with permeation and separation behavior of a porous graphite membrane and five different kinds of porous surface modified graphite (SMG) membranes made of pressed graphite crystals in terms of their hydrogen-selectivity under dry and hydrothermal conditions. The membranes under study are described as "pristine" graphite and SMG membranes by the introduction of three functional groups of increasing hydrophobic and one of hydrophilic character. The investigations of the membranes summarized in this chapter are related with 2 accepted publications.

For the described application of CMR for bio-ethanol steam reforming (b-ESR), the graphite and SMG membranes are studied under i.) dry conditions, i.e. using an equimolar binary feed gas mixture of (H_2/CO_2), and ii) under hydrothermal conditions, i.e. using a ternary feed mixture of 41 vol.-% H_2/ 41 vol.-% CO_2/ 18 vol.-% H_2O. Here, the membranes under study are primarily investigated in the feed pressure range between 1×10^5 Pa (1 bar) and 6×10^5 Pa (6 bar) and in the temperature range of room temperature under dry conditions or 100°C (hydrothermal conditions) and 300°C. The permeate side of the membranes under study primarily remains at ambient pressure at 1×10^5 Pa (1bar).

Publications to "Porous graphite membranes"

3.2.1. Pressed graphite crystals as gas separation membrane for steam reforming of ethanol

Authors: **A. Schulz**, F. Steinbach, J. Caro

Pressed graphite crystals as gas separation membrane for steam reforming of ethanol

A. Schulz, F. Steinbach, J. Caro *

Institute of Physical Chemistry and Electrochemistry, Leibniz University Hannover, Callinstr. 3A, D-30167, Germany

ARTICLE INFO

ABSTRACT

Pressed graphite was evaluated as a potential membrane for steam reforming of ethanol in membrane reactors. In ethanol steam reforming, hydrogen has to be in situ removed selectively from a mixture with ethanol, CO_2, and H_2O. Commercial graphite flakes (single crystals) have been pressed into disc membranes of different thicknesses. Both single gas permeation and $H_2/CO_2/H_2O$ mixed gas permeation were studied. From single gas permeation, a relatively high ideal separation factor of 35,…,60 for the H_2/CO_2 mixture could be predicted. However, the study of the real separation factor of this mixture by gas-chromatographic analysis gave real mixture separation factors around 5. This experimental finding is explained by a Knudsen-type mechanism with permeation paths along the grain boundaries of the pressed graphite flakes. At temperatures between 100 and 250 °C, the pressed graphite membrane is indeed hydrogen-selective. Hydrogen is separated from a $H_2/CO_2/H_2O$ mixture with a separation factor of 5 relative to CO_2 and 12 relative to H_2O, but only 2.4 relative to ethanol. Pressing of the graphite crystals results in a self-orientation (brick layer structure) of the individual graphite crystals. Hydrogen permeation parallel to the aligned flake-shaped crystals is by the factor 25 faster than perpendicular to them. The hydrogen permeabilities through the pressed graphite membranes are about one to two orders of magnitude higher than those through molecular sieve membranes such as supported zeolite or MOF membranes.

© 2014 Elsevier B.V. All rights reserved.

1. Introduction

Using bioethanol as fuel, hydrogen can be produced by steam reforming according to $C_2H_5OH + 3\,H_2O \rightleftharpoons 2\,CO_2 + 6\,H_2$. However, the reaction suffers from poor selectivity since other undesired products such as CH_4 and CO are formed during steam reforming and by ethanol decomposition [1–4]. There are also numerous other competing reactions like the *water-gas shift* (WGS) reaction and methanation [5,6]. In the past few years, the low temperature ($T < 600$ °C) ethanol steam reforming have become increasingly attractive but here also the wide range of undesired products and low hydrogen selectivity are the main hurdles [7–11]. Most of these problems can be solved if a hydrogen-selective membrane is applied for the in situ removal of hydrogen from the products at reaction temperatures < 400 °C.

However, the removal of H_2 in the presence of CO_2 and H_2O is a challenging task. Pd alloy membranes show severe degradation problems in the presence of hydrocarbons. Simple molecular sieve membranes will not work since hydrogen as the molecule to be removed has a larger kinetic diameter than water and is only slightly smaller than carbon dioxide (H_2: 2.9 Å, H_2O: 2.6 Å, CO_2: 3.3 Å).

The application of graphite is very diverse and ranges from its use as grease till the protection of plasma-facing components in thermonuclear fusion devices or for rechargeable battery techniques. There are only a few papers on the use of graphite as hydrogen-permeable membrane [12–14], on the application of graphite materials for hydrogen isotope separation [15,16], and on the molecular understanding of hydrogen transport in graphite [17–19]. However, most of these papers study hydrogen permeation under extreme conditions such as very low hydrogen partial pressures and very high temperatures. Except for the study of Kiyoshi et al. [20], the membranes were cut from bulk graphite materials instead of pressing graphite flakes as done in this work. Since graphite can adsorb carbon dioxide with a capacity of several mmol/g in the area of 3–12 bar, graphite has also been proposed as a cheap material for CO_2 storage [21]. A few attempts have been made to evaluate graphene as a novel carbon-based membrane material. Since the C_6 rings of the graphene carpet are impermeable for any gas, graphene oxide has been chosen as the material of choice [22–27].

The aim of this work is to investigate the separation behavior of pressed graphite discs as membranes for the ternary system $H_2/CO_2/H_2O$ as the key molecules of ethanol steam reforming with the aim to separate in situ hydrogen. Taking as a rough estimate, that the membrane selectivity can be approximated as diffusion selectivity multiplied by adsorption selectivity, it will be interesting to see which effect influences the permeation behavior: H_2 has the higher

Results and Discussion: Porous graphite membranes

Table 1
Sizes of the 4 charges of the commercial flake-shaped graphite crystals purchased from GK Kropfmühl and pressed into membranes.

Sample	Crystal length (μm)	Crystal width (μm)	Crystal height (μm)
1	400	250	13.0
2	290	190	9.4
3	28/36[a]	21/26	0.0/1.2
4	5	2.8	0.2

[a] Bimodal distribution.

diffusivity compared with CO_2, but CO_2 is better adsorbed than H_2. On the other hand, H_2 as the molecule to be separated through the membrane has a slightly larger kinetic diameter than H_2O which is expected to remain in the retentate. To identify the separation mechanism, single and mixed gas separation under variation of the partial pressure differences over the membrane and using different permeation methods such as flow measurement by soap bubble counter or permeate analysis using gas chromatography have been performed.

2. Experimental

2.1. Graphite material and pressing of membranes

Four different charges of graphite flakes were purchased (Table 1). The graphite membranes were prepared by pressing (using 392 MPa) a certain amount of graphite flakes (RFL 99.5, Co. GK Kropfmühl: www.gk-graphite.com) as obtained (Fig. 1a) to 0.5/1.0 mm thick discs with a diameter of 18 mm. For the study of permeation anisotropy, a 25 mm high cylinder with the same diameter was pressed from sample 2 (see Table 1), drilled with a core drill and sliced and polished to a thickness of 1.0 mm (Fig. 6b).

2.2. Characterization

Scanning electron microscopy (SEM) pictures were taken with the Jeol JSM 6700F with a cold field emission gun using 2 kV excitation voltage. The transmission electron microscopy (TEM) pictures were measured with the Jeol JEM-2100F UHR with an acceleration voltage of 200 kV using a Schottky field-emitter (ZrO/W(100)) with a lattice resolution in STEM of 0.2 nm. For Small Area Electron Diffraction (SAED), a Gatan Imaging Filter (GIF 2001) using a 1k-CCD camera was used. The X-ray powder diffraction (XRPD) measurements were carried out on a Bruker D8 Advance diffractometer (Bruker AXS GmbH) with a Bragg–Brentano geometry using Cu ($K\alpha_{1,2}$) radiation, secondary Ni-filter and a 1-dimensional LynxEye detector (silicon strip). The XRD measurements of graphite membranes in Fig. 6 were performed between 10° and 85° (2θ), step size of 0.01°, time per step of 0.02 s for Fig. 6c and 0.6 s for Fig. 6d, a total number of 7133 steps, without rotation at room temperature. The shown XRD patterns are Cu ($K\alpha_2$) and background corrected. The indexing of reflexes related to graphite based on pattern data base (00-056-0159) with the space group of P 6_3/mmc (No. 194). The shown patterns are normalized to the intensity of the 002 reflex.

2.3. Evaluation of single gas permeation and mixture gas separation

For permeation studies the graphite membranes were stabilized by a porous α–Al_2O_3 support additionally.[1] The membranes

---

[1] Up to 2 bar difference pressure, the pressed graphite membranes turned out to be mechanically stable without support. To measure at 4 bar pressure difference over the membrane (5 bar feed pressure, 1 bar permeate pressure), this stabilization of the pressed graphite was necessary.
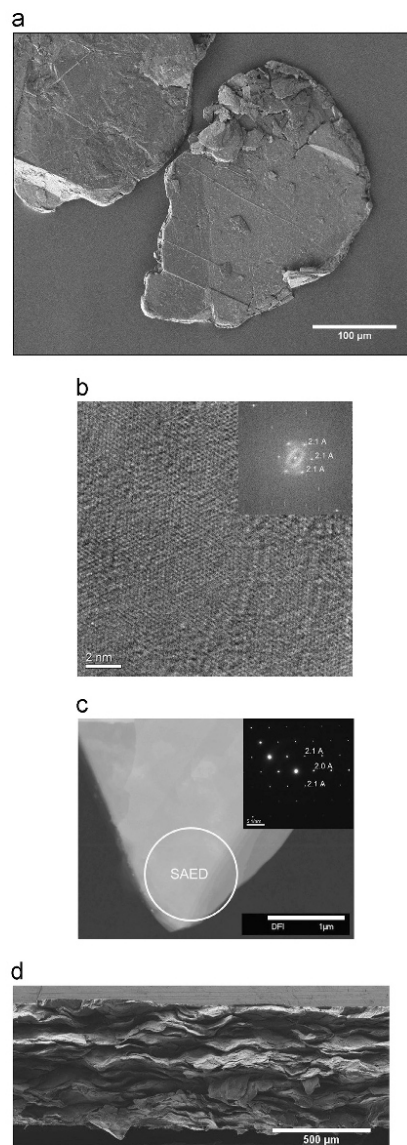

Fig. 1. (a) Graphite flakes as purchased from GK Kropfmühl before pressing into membrane discs (sample 1 of Table 1). (b) High-resolution TEM of a graphite flake. The inset shows Fast Fourier Transformation (FFT) of the shown area. (c) TEM of a graphite flake. The Small Area Electron Diffraction (SAED) shows the characteristic pattern of graphite (inset). (d) Cross section of the rough broken graphite membrane with self-arranged graphite crystals perpendicular to the direction of uniaxial pressing at $\approx$ 390 MPa (sample 1 of Table 1, see Fig. 1a).

were sealed in a permeation module using black O-rings (Vi370-FKM: www.cog.com) with an inner diameter of 14 mm and a cord diameter of 2 mm. For temperature-dependent measurements up to 250 °C, O-rings (Perlast G75B-FFKM) with a higher thermal

stability were used. The measurements were carried out in different ways: (i) For single gas permeation, bubble gas counting was applied. The feed pressure varied from 1 up to 5 bar. The permeate side was always at 1 bar and the permeate flew through the bubble counter. (ii) For mixed gas separation, the feed pressure was also varied from 1 up to 5 bar while the permeate side was either at 1 bar (permeate stream against atmospheric pressure) or the permeate side was evacuated by using a vacuum pump (Pfeiffer-MVP015-4). The permeate composition was analyzed by gas chromatography (Agilent 7890A). The feed and sweep gases were controlled by calibrated mass flow controllers (Bronkhorst-Mättig).

The separation factors α of a binary mixture of the components i and j have been calculated as the ratio of the component permeances as the pressure-normalized fluxes: The ideal separation factor $SF(i,j)$ has been formed as the ratio of the single component fluxes measured by a simple bubble counter, whereas the mixed gas separation factors $\alpha(i,j)$ have been formed as ratio of the permeances of the components i and j found in mixed gas permeation with gas chromatography analysis [28].

3. Results and discussion

Before pressing, the purchased graphite material (Table 1, Fig. 1a) was characterized by XRD and TEM. The XRD of the different graphite samples (not given here) show the typical powder patterns of graphite (space group: P 6_3/mmc, No. 194).

From high-resolution TEM studies (Fig. 1b,c) we can see the well-structured graphite layers in the known hexagonal arrangement with blurred sections depending on the overlay of multiple atomic sheets whereby each carbon atom is located in the center below or above a carbon six-ring. The Fast Fourier Transformation of the shown area in Fig. 1b has been directly reproduced in the Small Area Electron Diffraction (SAED) (Fig. 1c). Since the SAED at 10 different positions of the flake were identical, each flake represents a graphite single crystal and not a polycrystalline material. Lattice plane distances of around 3.35 Å could be assigned (cf. Fig. 1b,c).

By pressing of the graphite crystals into 0.5 and 1.0 mm thick discs, the individual graphite flakes (Fig. 1a) align to larger clusters of parallel crystals (Fig. 1d). It follows from the cross section of the pressed membrane that there is a preferential orientation of the grain boundaries perpendicular to the pressing direction, that is to say in the plane of the disc.

To identify the mass transport mechanism through pressed graphite discs, first the single component permeances of different gases have been measured for two different membrane thicknesses of 0.5 and 1 mm and various difference pressures over the membrane. As an example, a difference pressure of $\Delta P = 4$ bar over the membrane means that the feed side was at 5 bar whereas the permeate side of the membrane was at the constant pressure of 1 mm (bubble counter measurements). Fig. 2a shows that the permeances do not correlate with the kinetic diameters of the permeating gases under study, that is to say no molecular sieving mechanism takes place. However, a reasonable correlation of the permeance of the different gases is found for a Knudsen plot as shown in Fig. 2b. Further, as expected the permeances of the 0.5 mm thick graphite membrane are about double the data of the 1.0 mm thick membrane.

Before studying the permeation behavior of the binary system H_2/CO_2, we will first discuss the single component permeation behavior. Fig. 3a shows the single gas permeances as a function of the pressure differences ΔP over the membrane for 0.5 and 1.0 mm thick membranes measured by the bubble counter. Whereas the hydrogen permeance as the pressure-normalized
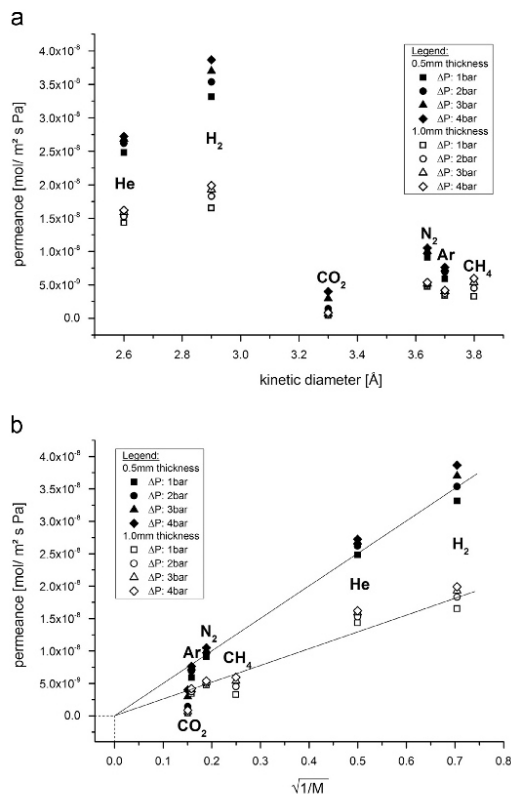

Fig. 2. (a) Single gas permeances of different probe gases at room temperature as a function of the gas kinetic diameter for two graphite membranes of different thicknesses (0.5, open symbols, and 1 mm, filled ones) (sample 1 of Table 1) for four partial pressure differences (ΔP) across the membrane. Measurements by bubble counter. (b) Single gas permeances as shown in panel (a) in a Knudsen plot as a function of the squared root of the reciprocal molecular mass of different probe molecules. Measurements by bubble counter.

flux is almost constant with increasing pressure difference ΔP over the membrane, which is an indication for a linear adsorption isotherm, the carbon dioxide permeance increases slightly with ΔP. This experimental finding can be understood if we assume that with increasing amounts of adsorbed CO_2 the influence of the surface heterogeneity of the carbon becomes less and – as a direct result – the surface diffusion of CO_2 increases.

As the ratio of the single component fluxes H_2 and CO_2, the ideal separation factors SF (H_2/CO_2) as a rough prediction to separate a system can be calculated (Fig. 3b). Since the CO_2 permeances increase with increasing pressure difference and those of H_2 remain almost constant, as a direct result, the ideal separation factors H_2/CO_2 decrease with increasing pressure difference ΔP from initially 40 to about 10,…,25. These ideal selectivities are surprisingly high since from Fig. 2b a Knudsen mechanism could be derived. In previous studies, the transport of hydrogen compared to argon through pressed graphite flakes is described as a molecular flow in the pressure area of 0.5–100 Pa at room temperature [20]. Therefore, the ratio of their permeances is the square root of the inverse ratio of their molecular weights,
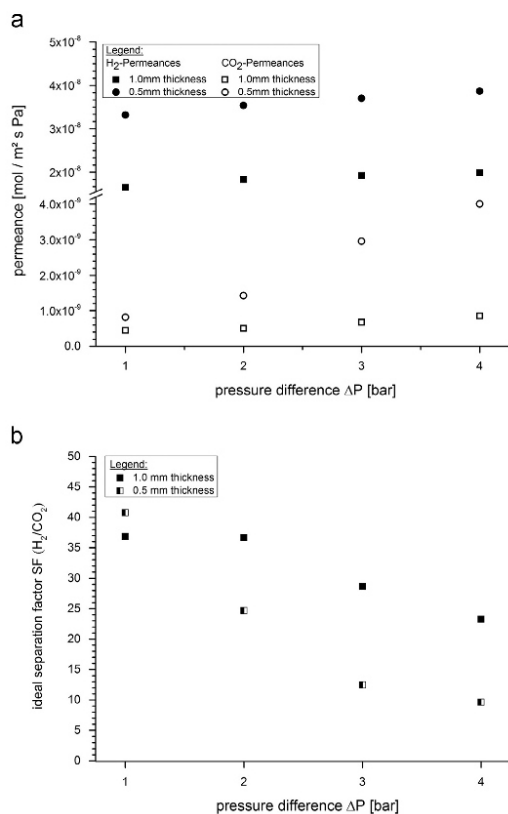
Results and Discussion: Porous graphite membranes

a

b

Fig. 3. (a) H_2 and CO_2 single gas permeances of two graphite membranes of 0.5 and 1.0 mm thickness (sample 1 of Table 1) as a function of the partial pressure differences (ΔP) at room temperature. Measurements by bubble counter. (b) Ideal separation factors for the binary system H_2/CO_2 calculated as the ratio of the single gas permeances given in panel (a) as a function of the partial pressure difference (ΔP) over the membranes. Measurements by bubble counter.

Fig. 4. H_2 and CO_2 mixed gas permeances and appropriate mixed gas separation factors $\alpha(H_2/CO_2)$ as measured by gas chromatography as a function of the partial pressure difference (ΔP) over the membrane. Pressed sample 1 of Table 1, thickness 1.0 mm, room temperature (sample 1).

indicating a molecular diffusion after Knudsen according to $J_{H_2}/J_{CO_2} = (M_{CO_2}/M_{H_2})^{0.5}$. This mechanism would imply a rather low Knudsen separation factor of 4.7 under low pressure conditions and at room temperature, respectively.

Fig. 4 presents the H_2/CO_2 mixed gas permeation and mixed gas separation factor α (see also Table 2 for the case $\perp$). Compared with the single gas permeation (Fig. 3a), the H_2 permeance remains constant in the binary mixture whereas the CO_2 permeance increases by almost one order of magnitude. The increase of the CO_2 permeance is due to the curved adsorption isotherm of CO_2 [29,30], in comparison with the linear isotherm for H_2 on carbon materials [31]. Assuming the validity of the 1st Fick Law, for the same pressure difference over the membrane, in the case of a curved isotherm the concentration gradient as driving force for permeation is higher in the low (partial) pressure region than at higher pressures. When permeating the single component CO_2, feed side is at 2 bar, permeate side at 1 bar (operating in high pressure regime). In the case of the binary 50%/50% mixture, feed side is at 2 bar (each partial pressure 1 bar), and the permeate side has a composition of 20% CO_2 and 80% H_2 for an $\alpha = 4$ (operation in low partial pressure regime).
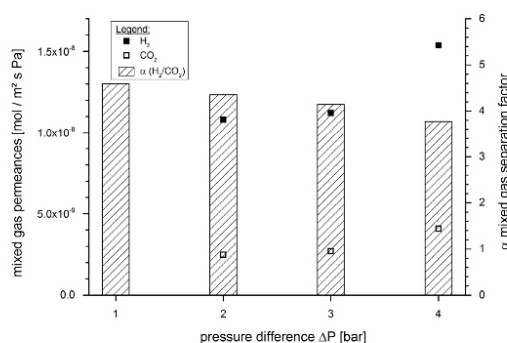
As a consequence, the real mixture separation factor $\alpha(H_2/CO_2)$ is at low pressure differences ΔP over the membrane of the order of 3–4 (Fig. 4) and much lower than the ideal separation factor of $SF \leq 40$ as derived from the single component behavior of the sample in Fig. 3b. For high data of ΔP the mixture separation factor drops to 3.8 which is even lower than the Knudsen value. This experimental finding can be explained by the assumption that at increased pressure the Knudsen separation mechanism changes into a fluid flow.

Fig. 5 shows the hydrogen permeances for membranes pressed from graphite crystals of 4 different sizes (cf. Table 1). The linear correlation of the hydrogen permeance with the reciprocal of the permeation path length L is a clear indication for a Knudsen-like transport along the grain boundaries. The real permeation length L through the stack of graphite crystals forming the membrane can be calculated from the geometrical data of the different crystals given in Table 1 and assuming a brick-layer structure as shown in Fig. 6a and found experimentally in the SEM of the cross section of a pressed membrane as shown in Fig. 1d. The tortuosity of the membranes S1–S4 has been calculated assuming the self-orientation of the graphite flake by pressing perpendicular to the uniaxial pressing direction as shown schematically in Fig. 6a. The extension of the permeation path in our pressed graphite flakes has been calculated according to the treatment of barrier films which consist of aligned impermeable flakes in polymer films [32].

We simply calculated the length of the permeation path of a molecule through the brick-layer structure shown in Fig. 6a. The parameters are: thickness of the pressed disc and geometry of the graphite platelets, i.e., averaged length and width of the platelet and height (as given in Table 1). Our foregone conclusion is very similar to Ref. [32].

As a proof of the model that the mass transport through the membrane made by pressing graphite crystals is controlled by grain boundary transport, two graphite discs have been prepared from a pressed graphite block as shown in Fig. 6b with grain boundaries perpendicular (this was the case discussed so far in this paper) and parallel to the permeation directions, indicated with $\perp$ and $\parallel$ (cf. Table 2).

Before the permeation studies, the orientation of the graphite crystals in the two membranes with different crystal orientations has been proved by XRD measurements (cf. Fig. 6c,d).

The XRD pattern of Fig. 6c shows the "texture effect" of the strongly anisotropic graphite crystals (cf. Fig. 1) which consists of only the two X-ray reflexes (Laue symbols) 002 and 004 of the set of net planes parallel to (001). Since other reflexes are suppressed,

Results and Discussion: Porous graphite membranes

Table 2

Single and mixed gas permeances of hydrogen and carbon dioxide as well as the ideal separation factors SF and the mixed gas separation factors α(50 vol% H$_2$/50 vol% CO$_2$) at room temperature for a graphite membrane pressed from sample 2 (see Table 1) for flake orientations perpendicular ($\perp$) and parallel ($\parallel$) with a thickness of 1 mm and the related anisotropic permeances (cf. Fig. 6a).

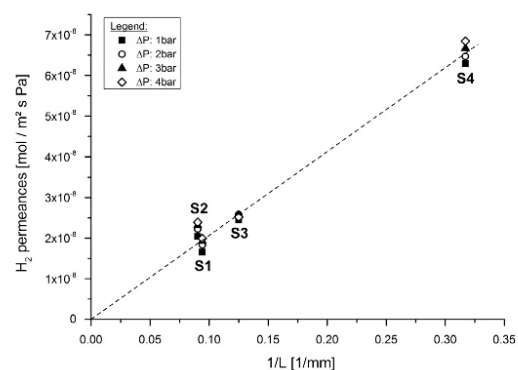|	H$_2$ (as single gas) mol/m² s Pa	CO$_2$ (as single gas) mol/m² s Pa	SF (H$_2$/CO$_2$)	H$_2$ (as mixture) mol/m² s Pa	CO$_2$ (as mixture) mol/m² s Pa	α(H$_2$/CO$_2$)
Permeance for flake orientation $\perp$	2.0×10^{-8}	3.4×10^{-10}	59.8	1.2×10^{-8}	2.8×10^{-9}	4.4
Permeance for flake orientation $\parallel$	4.5×10^{-7}	6.0×10^{-8}	7.4	3.0×10^{-7}	7.9×10^{-8}	3.7

Fig. 5. Hydrogen permeance for 4 different graphite specimens of different sizes (samples denoted as S1–S4, see Table 1) as function of the reciprocal permeation length L as calculated from the brick-layer structure shown in Fig. 6a with the geometry data from Table 1.

Fig. 6. (a) Permeation anisotropy of a pressed graphite block (sample 2 of Table 1) at room temperature: By uniaxial pressing at 390 MPa, the graphite flakes undergo a self-orientation perpendicular to the uniaxial pressure direction. As a result, the permeation lengths become different and the hydrogen permeances become direction-dependent. (b) The photo shows how to prepare pressed graphite discs of different orientations from the block. (c, d) The XRD patterns of two graphite membranes (pressed by sample 2) with their different orientated graphite crystals, described in Table 2: (c) graphite crystals $\parallel$ to the XRD beam but perpendicular to the permeation fluxes in the gas experiments, (d) graphite crystals $\perp$ to the XRD beam but parallel to the permeation fluxes in the gas experiments. (*: reflexes belonging to residual wax depending on preparation because of polishing)

a perfect parallel orientation of the graphite crystals relative to the membrane surface can be concluded.

The XRD pattern shown in Fig. 6d consists of more reflexes which were suppressed in Fig. 6c since now – for a perpendicular orientation of the graphite crystals relative to the membrane surface – more sets of parallel net planes can contribute to the XRD pattern. The 002 and 004 reflexes should not be found in this diffractogram. However, the remaining intensities of the 002 and 004 reflexes are not surprising because of some disoriented graphite crystals to the X-ray beam which give a strong signal. The intense 004 signal as shown in Fig. 6d can be simulated if less than 2% of the graphite crystals are disoriented parallel to the X-ray beam.

In complete accordance with our expectation, we find for the hydrogen single gas permeance that P(H$_2$) $\parallel$ is about 25 times larger than P(H$_2$)$\perp$ while the mixed gas selectivites α(H$_2$/CO$_2$) remain unchanged near the Knudsen value for both orientations (Fig. 6a). This permeation anisotropy is a result of the self-orientation of the graphite flakes by the uniaxial pressing.

It follows from Fig. 7a that the mixed gas permeances decrease with increasing temperature but the mixed gas separation factor α (H$_2$/CO$_2$) remained constant at 5 (cf. Fig. 7a). This finding can be explained by the influence of adsorption rather than diffusion on permeation. With increasing temperature, both H$_2$ and CO$_2$ become less adsorbed on the graphite surface of the grain boundaries, and the surface permeation flux decreases.

Fig. 7b shows, as we can expect, there is a tendency that with increasing pressure the gas permeances decrease since with increasing pressure in the intercrystalline transport space becomes smaller. Permeances are the filled and empty symbols. Interestingly, the mixture separation factor remains constant (columns). There is some scattering in the permeances (not in the separation factor) as a function of the pressing pressure. This effect is most
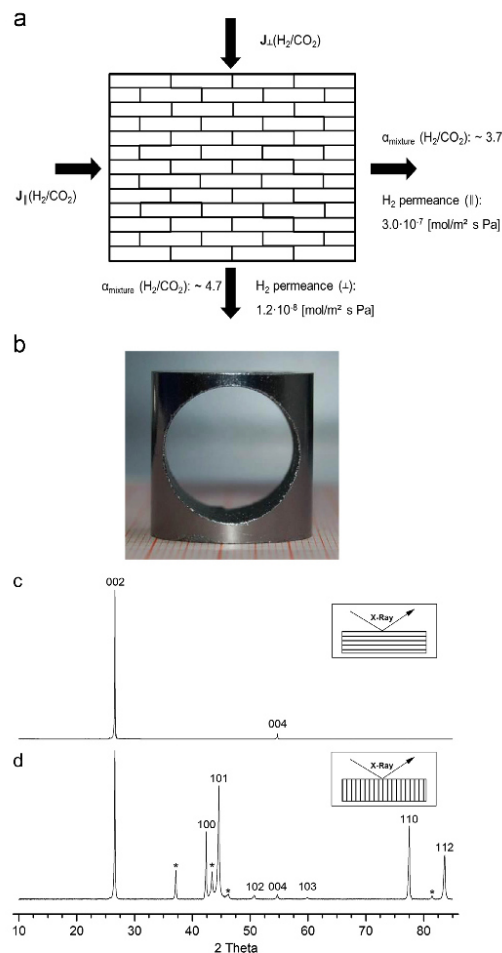
Results and Discussion: Porous graphite membranes

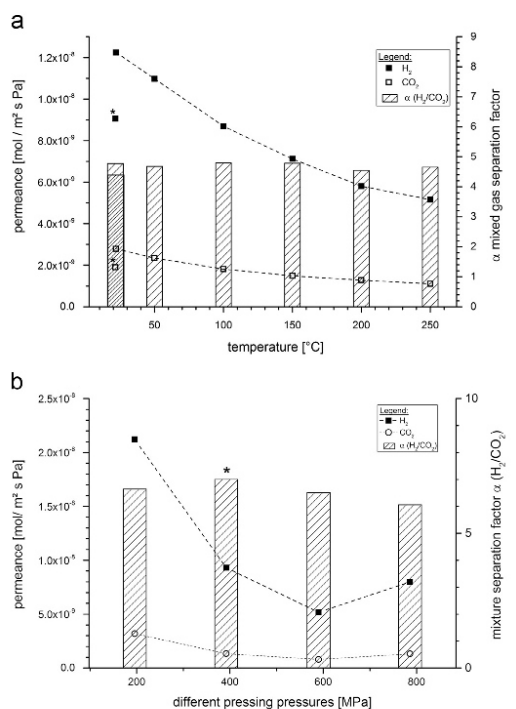**Fig. 7.** (a) Mixed gas permeances and appropriate mixed gas separation factors $\alpha(H_2/CO_2)$ of hydrogen and carbon dioxide (50 vol% H_2/50 vol% CO_2) on pressed graphite membrane (sample 2, "normal" orientation $\perp$) of 1.0 mm thickness as a function of temperature. The mixed gas separation factor α was constant and amounted to $\alpha(H_2/CO_2) \approx 4.5$–5.0. The asterisks denote the first measurement with the hydrated carbon membrane at room temperature without membrane activation using a vacuum pump. (b) Mixed gas permeances and corresponding mixed gas separation factors $\alpha(H_2/CO_2)$ of hydrogen and carbon dioxide (50 vol% H_2/50 vol% CO_2) on pressed graphite membranes (made from sample 2, "normal" orientation $\perp$) of 1.0 mm thickness as a function of different pressing pressures using a vacuum pump at room temperature (∗:pressure used in this work).
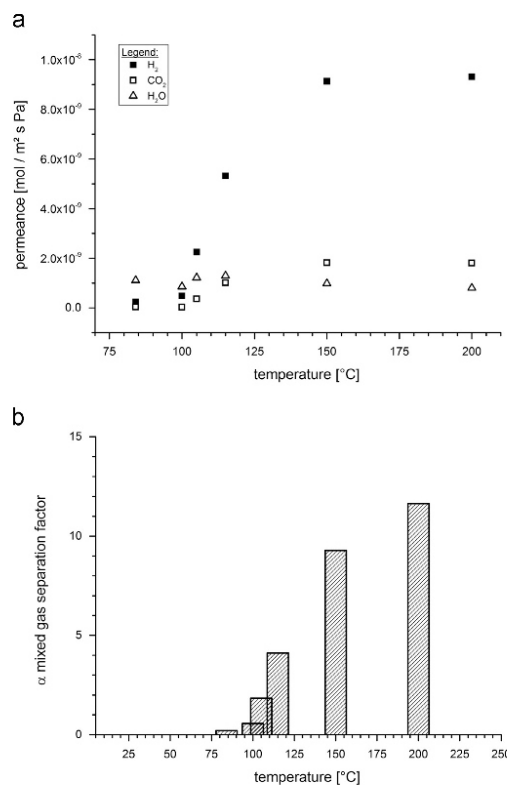

Fig. 8. (a) Permeances of a ternary steam/hydrogen/carbon dioxide mixture (50 vol% steam/25 vol% H_2/25 vol% CO_2) as a function of the permeation temperature of a 1.0 mm thick membrane using vacuum pump (sample 2, "normal" orientation $\perp$). (b) Mixed gas separation factors $\alpha(H_2/H_2O)$ for the practice-relevant ethanol steam reforming mixture of the composition 50 vol% steam/25 vol% H_2/25 vol% CO_2 obtained as ratio of the mixed gas permeances. Data from (a).

probably due to the difficult process of self-orientation of the graphite crystals during the pressing.

Fig. 8a shows the permeances for the practice-relevant ternary mixture of 50 vol% H_2O/25 vol% H_2/25 vol% CO_2 – as it is found in ethanol steam reforming – as a function of the permeation temperature. It follows from Fig. 8a that with increasing temperature, hydrogen permeates preferentially through the graphite membrane while the permeances of water and carbon dioxide show a much lower permeance. Fig. 8b shows that the mixed gas separation factor $\alpha(H_2/H_2O)$ of the ternary system 50 vol% H_2O/25 vol% H_2/25 vol% CO_2 increases with increasing temperature and amounts to > 10 for $T = 200\,°C$ while the value of $\alpha(H_2/CO_2)$ remained constant at 5. This behavior can be explained as follows. At low temperatures, water is enriched in the intercrystalline space between the graphite crystals since H_2O can undergo at low temperatures much more molecular interactions than CO_2 or H_2 with heterogeneous surface sites: H-bridging, dipolar interaction. Therefore, H_2O is enriched in the membrane at low temperatures, and water is dominant in the permeate since the gases CO_2 and H_2 cannot pass the membrane easily at 84 °C, the mixture separation factor $\alpha(H_2/H_2O) \approx 0.8$, that is to say the membrane is slightly water-selective. However, at high temperatures, the selectivity

becomes opposite. At 200 °C, less H_2O is adsorbed, and the mobile gases CO_2 and H_2 can pass the now empty membrane easily, which results in a mixture separation factor of $H_2/H_2O \approx 12$ (see Fig. 8b).

Further tests of the pressed graphite in the catalytic membrane reactor in the ethanol steam reforming will show if these selectivities are sufficient to increase the hydrogen yield. In numerous studies on alkane dehydrogenation in membrane reactors it was found that the membrane selectivity toward hydrogen must be much higher than Knudsen selectivity [33].

In Fig. 9, we have compared the permeability (thickness-normalized permeance, obtained as product of permeance multiplied by membrane thickness) of our pressed graphite membrane with previously published metal-organic framework and zeolite membranes. We can state that the hydrogen permeabilitiy of the "standard" graphite membrane ($\perp$ orientation of the crystals) is about one order of magnitude larger than that of a common ZIF-8 membrane [34] and two orders of magnitude larger than that of a zeolite SOD membrane [35].

In the steam reforming of ethanol following $C_2H_5OH + 3\,H_2O \rightleftarrows 2\,CO_2 + 6\,H_2$ steam is used in an over-stoichiometric ratio to shift the equilibrium from the left to the right hand side of the equation. This is a standard method in industrial reaction engineering to overcome equilibrium-controlled restrictions (e.g.,
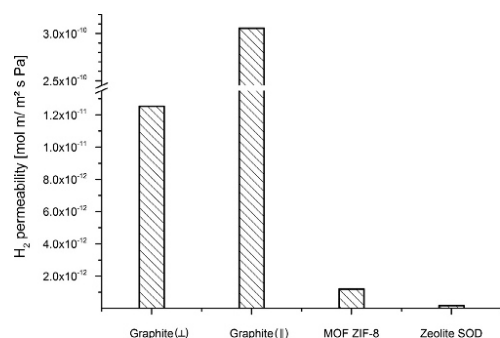
Fig. 9. Comparison of hydrogen mixed gas permabilities of different membranes: Pressed graphite with flake orientation (∥) and (⊥) (this work), and supported ZIF-8 [34] and zeolite SOD [35].

Table 3
Permeances and molar fluxes of H_2 and ethanol (EtOH) related to the equimolar mixture (50%/50%) at a reactor temperature of 150 °C using a vacuum pump. The membrane was prepared by sample 2 and pressed with 392 MPa (cf. Fig. 7b).

H_2 (mol/m² s Pa)	EtOH (mol/m² s Pa)	α(H_2/EtOH)
5.0×10^{-9}	2.1×10^{-9}	2.4

in esterifications, the cheapest educt, acid or alcohol, is given in a 10-fold excess). As Table 3 shows, the mixed gas separation factor H_2/ethanol is only 2.4. But – as stated – this is less dramatic since the equilibrium is shifted by steam excess from the left to right hand of the reaction equation.

In our case of gas permeation through pressed graphite membranes, we have two kinds of errors. One error originates from the sample preparation. We use different graphite powders from one and the same producer, but of different platelet sizes of the crystals. During the pressing, the crystals undergo a self-orientation into the brick-layer structure shown in Fig. 6a (see also Fig. 1d). This can be accompanied by an error of the factor of 2. Much smaller is the error of the permeation measurements which amounts to less than 10% (cf. Fig. 7b).

4. Conclusions

TEM proves that commercial graphite flakes can be regarded as single crystals. Pressed graphite crystals have been evaluated as a candidate for a membrane reactor for the steam reforming of ethanol. At temperatures > 200 °C, there is a hydrogen selectivity for the practice-relevant mixture of the composition 50 vol% H_2O/ 25 vol% H_2/25 vol% CO_2. For this mixture, α(H_2/CO_2) ≈ 5 and α(H_2/H_2O) ≈ 12 were found at 200 °C. The hydrogen permeabilities of the pressed graphite membranes are anisotropic with respect to the direction of uniaxial pressing as proved by XRD patterns. The anisotropy ratio of the permeances P(H_2)∥/P(H_2)⊥ is about 25 at room temperature.

For practical use, membranes made of graphite crystals can be easily prepared, are available and very cheap (about 3.0–0.3 cents per membrane depending on the changing market prizes) and offer high fluxes at medium or low selectivities. The scale-up process can be easily done by numbering up of modules in a series geometry. The low mechanical stability can be compensated by porous supports. The graphite membranes will be evaluated in future membrane-supported ethanol reforming studies.

References

[1] M. Ni, D.Y.C. Leung, M.K.H. Leung, A review on reforming bio-ethanol for hydrogen production, Int. J. Hydrogen Energy 32 (2007) 3238–3247.
[2] Y. Men, G. Kolb, R. Zapf, V. Hessel, H. Löwe, Ethanol steam reforming in a microchannel reactor, IChemE 85 (2007) 413–418.
[3] A. Therdthianwong, T. Sakulkoakiet, S. Therdthianwong, Hydrogen production by catalytic ethanol steam reforming, ScienceAsia 27 (2001) 193–198.
[4] S. Cavallaro, Ethanol steam reforming on Rh/Al₂O₃ catalysts, Energy Fuels 14 (2000) 1195–1199.
[5] M.D. Lazar, M. Dan, M. Mihet, G. Borodi, V. Almasan, Hydrogen production by ethanol steam reforming on Ni/oxide catalysts, AIP Conf. Proc. 1425 (2012) 131–134.
[6] V.V. Galvita, G.L. Semin, V.D. Belyaev, V.A. Semikolenov, P. Tsiakaras, V.A. Sobyanin, Synthesis gas production by steam reforming of ethanol, Appl. Catal. A: Gen. 220 (2001) 123–127.
[7] H.-S. Roh, A. Platon, Y. Wang, D.L. King, Catalyst deactivation and regeneration in low temperature ethanol steam reforming with Rh/CeO₂–ZrO₂ catalysts, Catal. Lett. 110 (2006) 1–6.
[8] H.-S. Roh, Y. Wang, D.L. King, A. Platon, Y.-H. Chin, Low temperature and H₂ selective catalysts for ethanol steam reforming, Catal. Lett. 108 (2006) 15–19.
[9] P. Ciambelli, V. Palma, A. Ruggiero, Low temperature catalytic steam reforming of ethanol. 1. The effect of the support on the activity and stability of Pt catalysts, Appl. Catal. B: Environ. 96 (2010) 18–27.
[10] P. Ciambelli, V. Palma, A. Ruggiero, Low temperature catalytic steam reforming of ethanol. 2. Preliminary kinetic investigation of Pt/CeO₂ catalysts, Appl. Catal. B: Environ. 96 (2010) 190–197.
[11] V. Palma, E. Palo, F. Castaldo, P. Ciambelli, G. Iaquaniello, Catalytic activity of CeO₂ supported Pt–Ni and Pt–Co catalysts in the low temperature bio-ethanol steam reforming, Chem. Eng. Trans. 25 (2011) 947–952.
[12] A. Spitsyn, A. Pisarev, A. Skovoroda, V. Gureev, Y.u. Martynenko, Permeation of hydrogen through MPG-8 graphite, J. Nucl. Mater. 363-365 (2007) 833–838.
[13] H. Atsumi, K. Tauchi, Hydrogen adsorption and transport in graphite materials, J. Alloys Compd. 356–357 (2003) 705–709.
[14] R. Ash, R.T. Lowson, Transport of single gases and of binary gas mixtures in a microporous carbon membrane, J. Chem. Soc. Faraday Trans. 169 (1973) 2166–2178.
[15] A.V. Spitsyn, A.V. Golubeva, M. Mayer, A.A. Skovoroda, Gas-driven hydrogen isotopes permeation through different carbon materials, J. Nucl. Mater. 390-391 (2009) 701–704.
[16] R. Schneider, A. Rai, A. Mutzke, M. Warrier, E. Salonen, K. Nordlund, Dynamic Monte-Carlo modeling of hydrogen isotope reactive-diffusion transport in porous graphite, J. Nucl. Mater. 367–370 (2007) 1238–1242.
[17] O.-E. Haas, J.M. Simon, S. Kjelstrup, Surface self-diffusion and mean displacement of hydrogen on graphite and a PEM fuel cell catalyst support, J. Phys. Chem. C 113 (2009) 20281–20289.
[18] I.E. Gabis, Transport of hydrogen in films of graphite, amorphous silicon, and nickel oxide, Semiconductors 31 (1997) 110–114.
[19] M. Warrier, R. Schneider, E. Salonen, K. Nordlund, Multi-scale modeling of hydrogen isotope transport in porous graphite, J. Plasma Phys. 72 (2006) 799–804.
[20] T. Kiyoshi, T. Namba, M. Yamawaki, Hydrogen permeation through graphite, J. Nucl. Mater. 155–157 (1988) 230–233.
[21] A.K. Mishra, S. Ramaprabhu, Study of CO₂ adsorption in low cost graphite nanoplatelets, Int. J. Chem. Eng. Appl. 1 (2010) 266–269.
[22] R.K. Joshi, P. Carbone, F.C. Wang, V.G. Kravets, Y. Su, I.V. Grigorieva, H.A. Wu, A.K. Geim, R.R. Nair, Precise and ultrafast molecular sieving through graphene oxide membranes, Science 343 (2014) 752–754.
[23] H. Li, Z. Song, X. Zhang, Y. Huang, S. Li, Y. Mao, H.J. Ploehn, Y. Bao, M. Yu, Ultrathin, molecular sieving graphene oxide membranes for selective hydrogen separation, Science 342 (2013) 95–98.
[24] H. Huang, Z. Song, N. Wei, L. Shi, Y. Mao, Y. Ying, L. Sun, Z. Xu, X. Peng, Ultrafast viscous water flow through nanostrand-channelled graphene oxide membranes, Nature 4 (2013) 3979.
[25] B. Mi, Graphene oxide membranes for ionic and molecular sieving, Science 343 (2014) 740–742.
[26] K.S. Kim, Y. Zhao, H. Jang, S.Y. Lee, J.M. Kim, K.S. Kim, J.H. Ahn, P. Kim, J.Y. Choi, B.H. Hong, Large-scale pattern growth of graphene films for stretchable transparent electrodes, Nature 457 (2009) 706–710.

[27] K. Celebi, J. Buchheim, R.M. Wyss, A. Droudian, P. Gasser, I. Shorubalko, J.-l. Kye, C. Lee, H.G. Park, Ultimate permeation across atomically thin porous grapheme, Science 344 (2014) 289–292.

[28] W.J. Koros, Y.H. Ma, T. Shimidzu, Terminology for membranes and membrane processes, Pure Appl. Chem. 68 (1996) 1479–1489.

[29] L.E. Cascarini de Torre, E.S. Flores, J.L. Llanos, E.J. Bottani, Gas–solid potentials for N_2 O_2 and CO_2 adsorbed on graphite, amorphes carbon, Al_2O_3 and TiO_2, J. Am. Chem. Soc. 11 (1995) 4742–4747.

[30] C. Banciu, A. Băra, L. Leonat, D. Pătroi, Carbon monoliths for CO_2 adsorption, Optoelectron. Adv. Mater. Rapid Commun. 5 (12) (2011) 1341–1345.

[31] R.V. Siriwardane, M.-S. Shen, E.P. Fischer, J.A. Poston, Adsorption of CO_2 on molecular sieves and activated carbon, Energy Fuels 15 (2001) 279–284.

[32] N.K. Lape, E.E. Nuxoll, E.L. Cussler, Polydisperse flakes in barrier films, J. Membr. Sci. 236 (2004) 29–37.

[33] M.F. Kemmere, J.T.F. Keurentjes, in: S.P. Nunes, K.-V. Peinemann (Eds.), Membrane Technology, Wiley-VCH, 2001.

[34] H. Bux, A. Feldhoff, J. Cravillon, M. Wiebcke, Y.-S. Li, J. Caro, Oriented zeolitic imidazolate framework-8 membrane with sharp H_2/C_3H_8 molecular sieve separation, Chem. Mater. 23 (2011) 2262–2269.

[35] N. Wang, Y. Liu, A. Huang, J. Caro, Supported SOD membrane with steam selectivity by a two-step repeated hydrothermal synthesis, Micropor. Mesopor. Mater. 192 (2013) 8–13.

3.2.2. **Improved hydrogen selectivity of Surface Modified Graphite (SMG) membranes: Permeation experiments and characterisation by micro-Raman spectroscopy and XPS**

Authors: **A. Wollbrink**, C.H. Rüscher, K. Volgmann, J. Koch, A. Breuksch, C. Tegenkamp, J. Caro

Improved hydrogen selectivity of Surface Modified Graphite (SMG) membranes: Permeation experiments and characterisation by micro-Raman spectroscopy and XPS

A. Wollbrink[a,b,*], C.H. Rüscher[b,c], K. Volgmann[a,b], J. Koch[d], A. Breuksch[a], C. Tegenkamp[d], J. Caro[a,b]

[a] Institute of Physical Chemistry and Electrochemistry, Leibniz University Hannover, Callinstr. 3A, D-30167 Hannover, Germany
[b] ZFM – Center for Solid State Chemistry and New Materials, Leibniz University Hannover, Callinstr. 3, D-30167 Hannover, Germany
[c] Institute of Mineralogy, Leibniz University Hannover, Callinstr. 3, D-30167 Hannover, Germany
[d] Institute of Solid State Physics, Leibniz University Hannover, Appelstr. 2, D-30167 Hannover, Germany

ARTICLE INFO

ABSTRACT

Permeation experiments on Surface Modified Graphite (SMG) membranes showed an improved mixed gas separation factor α (H_2/CO_2) of 9.2 (+80%) and α (H_2/H_2O) of 10.2 (+70%) compared with the pristine graphite membranes with α (H_2/CO_2) of 5.1 and α (H_2/H_2O) of 6.0. The surface modification was obtained by the treatment with different silanes at 140 °C, for 2 h under reflux and continuous stirring in an argon atmosphere. The dried powders were pressed to discs and evaluated for the ternary feed mixture (41 vol.-% H_2/ 41 vol.-% CO_2/18 vol.-% H_2O). XPS analysis of the membrane surface revealed sp^2 and sp^3 hybridisation states, carbonyl, carboxyl groups and CF_x bonds for the pristine and SMG membranes. Spatially resolved micro-focused Raman spectroscopy showed that the improved separation performance correlates with a specific modification of the G and D1 modes of the pristine graphite surface for each functionalisation carried out. Therefore, the improved performances result from the specific chemical and physical interactions of H_2, CO_2 and H_2O with the applied defect modifications of the SMG membranes.

1. Introduction

The application of steam reforming in terms of bio-ethanol due to $C_2H_5OH+3H_2O{\rightarrow}2CO_2+6H_2$ is an important contribution to the production of renewable energies [1–5]. The use of hydrogen-selective carbon-based membranes for the application in a catalytic membrane reactor can be one tool to push the reaction to full conversion below 400 °C. To reach this goal, we tested Surface Modified Graphite (SMG) as membrane which is easily pressed into discs, easy to scale up, to handle and has low production costs.

The dominating separation mechanism for membranes made of pressed graphite flakes is based on Knudsen diffusion [6,7], i.e. the separation mechanism sensitively depends on the mean free path length $λ(p,T)$, which in turn is given by the kinetic diameter of gas molecules, the applied feed pressure, temperature, and the mean distance of the extra-crystalline voids between neighbouring graphite flakes. This transport mechanism was verified for pressed graphite membranes by permeation experiments under certain conditions [8]. The results showed that the dominating separation mechanism is in the Knudsen regime but could be pushed into an unselective viscous flow regime with rising feed pressure. Furthermore, temperature-dependent permeation experiments revealed that the molar flux of the pressed graphite membrane is still affected by mixed gas viscosity since the mean free path length λ is in the dimension of the mean distance of the extra-crystalline voids [9]. The extra-crystalline voids between the pressed graphite flakes were deduced to be in the range of 10 to 50 nm. Thus, these membranes are classified as mesoporous bodies or divided bodies, in accordance with the IUPAC classification [10], and their separation mechanism is better described by the randomly reflected molecules for molecule-wall collisions than by the interplay of adsorption and diffusion phenomena in microporous materials [11–13].

In this study, we evaluate Surface Modified Graphite (SMG) membranes for their potential application in a hydrogen-selective catalytic membrane reactor for steam reforming below 400 °C. The membranes were comprehensively characterised by X-ray photoelectron spectroscopy (XPS) and micro-Raman spectroscopy. As model feed mixture for steam reforming, a ternary gas mixture with the composition of 41 vol.-% H_2/41 vol.-% CO_2/18 vol.-% H_2O was

Results and Discussion: Porous graphite membranes

selected [8]. We will show that the functionalisation of the graphite surface with different silanes occurs very localised, shown by micro-focused Raman spectroscopy, and selectively affects the permeation behaviour of H_2, CO_2 and H_2O by physico-chemical interactions, given by permeation experiments.

2. Experimental

2.1. Surface modification and membrane preparation

0.6 g pristine graphite crystals (GK Kropfmühl, KFL-flakes) were treated with 10 mL toluene (Roth, 7346.2) and 6 mMol silane: Chloro(3,3,3-Trifluoropropyl)dimethylsilane (CFDMS: AB111469), Methoxydimethylphenylsilane (MDMPS: AB206289); Ethoxytrimethyl-lsilane (ETMS: AB111497), Tetraethoxysilane (TEOS: AB111385) from Co. ABCR. The surface modification was carried out in a laboratory glass-bottle (Duran) at about 140 °C, for 2 h under reflux and continuous stirring (350 rpm) in an argon atmosphere. Afterwards, the modified graphite crystals were washed and dried overnight at 80 °C. The resulting graphite crystals were pressed into a disc as described in ref. [7].

2.2. Methods

Regarding the permeation experiments, the SMG membranes were measured at a feed pressure of 2×10^5 Pa. The permeate pressure was always kept at 1×10^5 Pa (atmospheric pressure). For the evaluation of mixed gas permeation and mixed gas separation a ternary feed mixture of 41 vol.-% H_2/41 vol.-% CO_2/18 vol.-% H_2O was used. The mixed gas separation factors α (H_2/CO_2) and α (H_2/H_2O) were determined as the ratio of the individual mixed gas permeances P (pressure-normalised fluxes) analysed by an online coupled gas chromatograph. Further details about the permeation experiments are reported in ref. [8]. The XPS experiments were performed with a non-monochromatic X-ray source using an Al-K_α emission (SPECS XR-50, 100 W, 54° incident angle, excited area of about 1 cm^2). The kinetic energies of the photoelectrons were measured with a hemispherical analyser (SPECS-PHOIBOS 100, Detector: MCD-5) with 30 scans and a pass energy of 20 eV. All XPS spectra are shown as a function of binding energy with respect to the Fermi level. The photoelectron peak areas were calculated after background corrections using the Shirley algorithm described in ref. [14]. Raman spectra were taken with a Bruker Senterra for confocal micro-focused Raman spectroscopy with a spatial-resolution of about 1 µm^2 using a green laser (λ: 532 nm, depolarised beam) and a 50×1000 µm objective lens. A laser power of 20 mW, 10 co-additions and an integration time of 2 s was used. The spectra were fitted with the software OPUS 7.5 after background correction (rubber-band method) using local least squares algorithm until fit-curves converged.

3. Results and discussion

3.1. Mixed gas permeation and separation

The mixed gas permeances of H_2, CO_2 and H_2O (steam) for the surface modified graphite (SMG) membrane with Ethoxytrimethylsilane, named SMG (ETMS), are compared with the data of the pristine graphite membrane in Figs. 1a–c. The corresponding mixed gas separation factors α (H_2/CO_2) and α (H_2/H_2O), as deduced from Fig. 1, of the pristine graphite and SMG (ETMS) membrane are summarised in Figs. 2a–b. Furthermore, we describe the influence of the used solvent (toluene) as proof of concept, named SMG (toluene). The permeation studies were carried out with a ternary feed mixture (41 vol.-% H_2/41 vol.-% CO_2/18 vol.-% H_2O) from 100 °C to 250 °C, described in detail in Ref. [9].

For the pristine graphite membrane, the mixed gas permeances decrease with increasing temperature for H_2 (−43%), CO_2 (−49%) and

H_2O (−52%) from 100 °C to 250 °C see Fig. 1a–c. The corresponding mixed gas separation factor of α (H_2/CO_2) slightly increases from 4.5 to 5.1 (+12%), which is also observed for α (H_2/H_2O) from 4.5 to 5.5 (+22%), see Figs. 2a–b. As a proof of concept, we treated the same amount of graphite under identical conditions with pure toluene only, see Section 2.1. In comparison with the pristine graphite membrane, the mixed gas permeances of the SMG (toluene) membrane show for H_2 a slightly increased mixed gas permeances of +29% at 100 °C and of +21% at 150 °C and decreased values of about 50% above 150 °C, see Fig. 1a. The mixed gas permeance of CO_2 is decreased for all temperatures whereas that of H_2O (steam) is increased of +28% at 100 °C and becomes almost comparable with rising temperature to the steam permeance measured for the pristine graphite membrane, see Figs. 1b–c. Consequently, the mixed gas separation factor α (H_2/CO_2) increases to the value of 7.0 (+46%) whereas α (H_2/H_2O) remains comparable to the pristine graphite membrane below 150 °C and decreases with increasing temperature to 3.2 (−42%), see Figs. 2a–b.

For the SMG (ETMS) membrane, the mixed gas permeances also decrease with increasing temperature, see Figs. 1a–c. The comparison of the mixed gas permeances of the SMG (ETMS) membrane with the values of the pristine graphite membrane show for H_2 an almost unchanged permeance, for CO_2 a systematically reduction of about 30% and also for H_2O a reduced permeance of −52% at 150 °C and −20% at 250 °C. Therefore, the resulting mixed gas separation factor α (H_2/CO_2) of 8.1 (averaged) displays an improved hydrogen selectivity of +69% between 100 °C and 250 °C (see Fig. 2a). The mixed gas separation factor α (H_2/H_2O) varies between 4.7 (+4%) at 100 °C, reaches a maximum of 10.2 (+100%) at 150 °C and decreases with increasing temperature to 6.7 (+24%) at 250 °C (see Fig. 2b).

The defect modification on the graphite surface by different silanes may result in varying mixed gas separation factors α (H_2/CO_2) and α (H_2/H_2O) due to the different terminal groups. Therefore, different SMG (silane) membranes were prepared by using different silanes: with three terminal methyl groups (ETMS), one methyl group was substituted by a phenyl ring (MDMPS) or a CF_3 group (CFDMS) and also a complete substitution by ethoxy groups (TEOS) was tested, see Figs. 2c–d. Independent from the different used hydrophobic terminal groups, all of the different SMG (silane) membranes showed an overall improved mixed gas separation factor α (H_2/CO_2) of about 8.0 (+70%) compared with the separation performance of the pristine graphite membrane, see Fig. 2c. The SMG membrane using Methoxydimethylphenylsilane (MDMPS) showed the highest selectivity for α (H_2/CO_2) of 9.2 (+80%) which decreases with increasing temperature to 7.6 (+62%). The mixed gas separation factor α (H_2/H_2O) shows for all applied silane modifications a strong tempera-ture-dependency and decreases with increasing temperature. Here, the SMG (ETMS) displays the highest selectivity for α (H_2/H_2O) of 10.2 at 150 °C in comparison with the other silanes. For the SMG (TEOS) membrane, a mixed gas separation factor α (H_2/H_2O) of 7.4 at 150 °C could be observed which also decreased with increasing temperature to α (H_2/H_2O) of 3.8 at 250 °C (see Fig. 2d).

The dominating separation mechanism for the pristine graphite membrane is described by the Knudsen mechanism [6–9]. In this regime, the number of molecule-wall collisions becomes higher than the number of intermolecular collisions. The molecules hitting the pore walls are randomly reflected and the separation of different molecules only appear due to their molecular weight ratio, as it is the case for an ideal Knudsen separation mechanism, see Scheme 1. For gas mixtures, containing two or more molecular species, effects by intermolecular collisions cannot be completely excluded [11]. Furthermore, the molecular species, which are passing the membrane, can be affected by physical (steric hindrance) or by chemical interactions (molecule-surface). Here, the hydrogen selectivity can differ from the ideal Knudsen-selectivity which can result in a positive or negative separa-tion performance. Consequently, we named this behaviour a modified Knudsen separation mechanism, see Scheme 1.
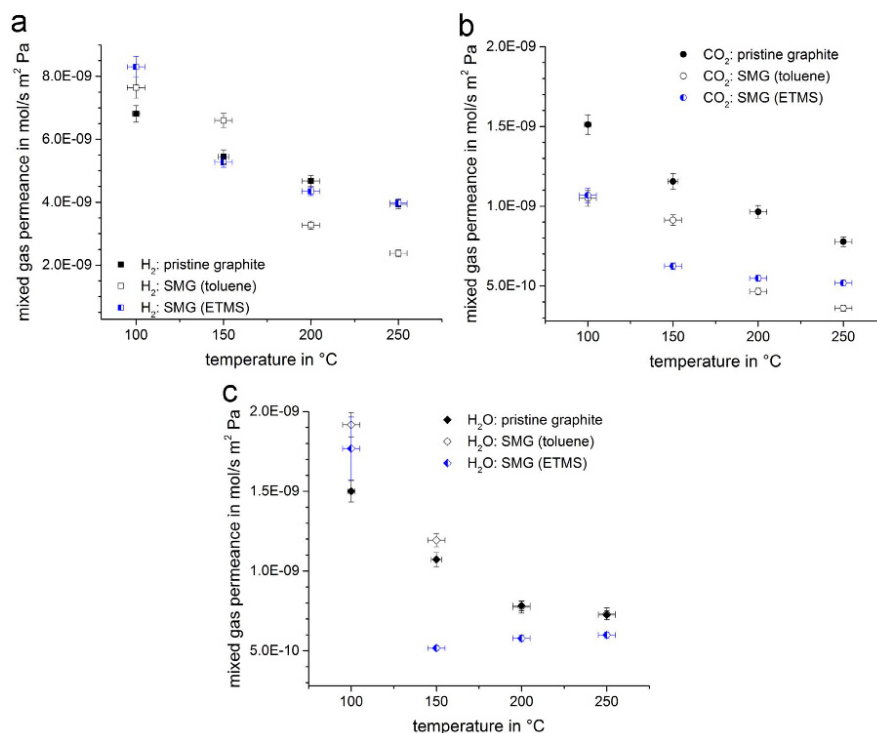
Fig. 1. Temperature-dependent mixed gas permeances of H_2 (a), CO_2 (b) and H_2O (steam) (c) for the pristine graphite, SMG (toluene) and SMG (ETMS) membrane for the ternary feed mixture (41 vol.-% H_2/41 vol.-% CO_2/18 vol.-% H_2O). The corresponding mixed gas separation factors are given in Fig. 2.

For all membranes under study, the mixed gas permeances of H_2, CO_2 and H_2O mainly decrease with increasing temperature, which is in accordance with the literature due to the increase of the mixed gas viscosity [8]. However, the mixed gas permeances and corresponding mixed gas separation factors strongly depend on the corresponding type of membrane as the pristine graphite, the different SMG (silane) membranes using hydrophobic or hydrophilic terminal groups and also the SMG (toluene) membrane. Furthermore, the mixed gas separation factor α (H_2/H_2O) shows a much more complex and strong temperature-dependence compared with α (H_2/CO_2), see Figs. 2a–b.

For the pristine graphite membrane, the mixed gas separation factor α (H_2/CO_2) is about 4.8 (averaged) from 100 °C to 250 °C, which is in good agreement with the ideal Knudsen separation factor of 4.7, calculated by the root of the molecular weight ratio of CO_2 and H_2, see Figs. 2a [6–8]. The pristine graphite membrane differs from such ideal separation behaviour for α (H_2/H_2O) of 5.4 at 250 °C, which is remarkably higher than the ideal Knudsen separation factor α (H_2/H_2O) of 3.0 (see Fig. 2b). Therefore, the separation performance of H_2/H_2O is also described as a modified Knudsen separation mechanism due to the already present hydrophobic fluorine groups on the pristine graphite membrane, given by XPS analysis (see Section 3.2.). The slight increase of α (H_2/CO_2) and also α (H_2/H_2O) by about 12% with increasing temperature is also in accordance with the rise of molecule-wall collisions, as discussed before (see Figs. 1a–c).

The SMG (toluene) membrane surprisingly shows an improved mixed gas separation factor α (H_2/CO_2) compared with the pristine graphite membrane of 7.0 (+46%) and a decreased α (H_2/H_2O) to 3.2 (−42%) above 150 °C, see Figs. 2a–b. The observed effect can be described by the localised surface modification by π-π interactions of the aromatic C_6-ring of toluene with the graphite surface, which is given by Raman analysis, see section 3.3 [15–19]. The permeation results show that the SMG (toluene) affects rather the mixed gas permeances of CO_2 and H_2 above 150 °C than of H_2O, see Figs. 1a–c. Therefore, the lower hydrogen selectivity of (H_2/H_2O), which is in the range of an ideal Knudsen separation mechanism, can only be explained by steric hindrance of H_2 due to the toluene on the graphite surface and the rise of the mixed gas viscosity. In this case, the almost unaffected H_2O permeance above 150 °C indicates that the kinetic diameter is the deciding parameter here, which is for the H_2O (2.6 Å), H_2 (2.9 Å) and CO_2 (3.3 Å).

Improved mixed gas separation factors of α (H_2/CO_2) and α (H_2/H_2O) are observed for the SMG (ETMS) membrane, compared with the pristine graphite membrane (see Figs. 2a–b). The increased selectivity of α (H_2/CO_2) can be explained by the presence of ETMS molecules on the graphite surface, which narrowed sterically the extra-crystalline voids and also increase the number of diffusively scattered molecules, see Fig. 2a and Scheme 1. In this case, CO_2 is systematically reduced in its permeance for all temperatures, see Fig. 1. Furthermore, the improved hydrogen selectivity α (H_2/H_2O) based on the hydrophobic nature of the terminal group of the ETMS molecule. The methyl groups slightly hinders the water molecule to path the extra-crystalline voids due to steric hindrance as well as chemical interactions, additionally. In the comparison of all SMG membranes with different kinds of hydrophobic terminal groups, it is interesting to note that the SMG (MDMPS) membrane show the most improved hydrogen selectivity for α (H_2/CO_2). On the other hand, the SMG (CFDMS) membrane is
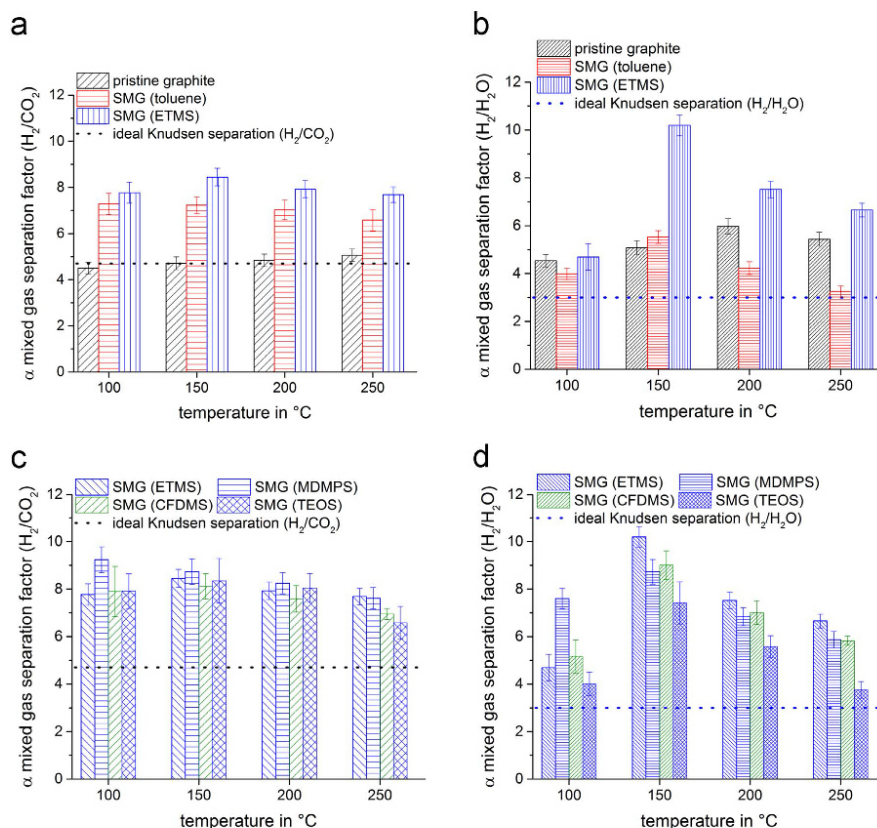
318

A. Wollbrink et al.

Fig. 2. Temperature-dependent mixed gas separation factors α (H₂/CO₂) (a) and α (H₂/H₂O) (b) for the pristine graphite, SMG (toluene) and SMG (ETMS) membranes calculated from corresponding mixed gas permeances, given in Fig. 1. The dashed line shows the ideal selectivity for an ideal Knudsen separation mechanism. An overview of all SMG (silane) membranes is shown for α (H₂/CO₂) (c) and α (H₂/H₂O) (d).
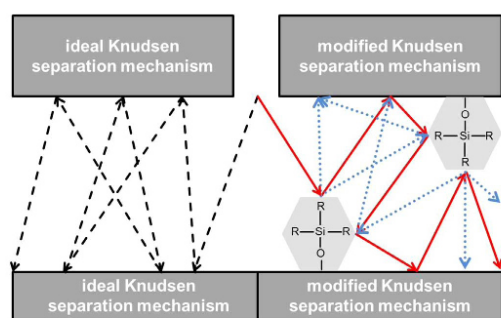
Scheme 1. Schematic illustration of molecule pathways through the extra-crystalline voids for an ideal Knudsen mechanism (i), shown by dashed arrows (black), a modified Knudsen separation mechanism (ii) by surface modifications between two neighbouring graphite flakes, shown by solid arrows (red). The dotted arrows (blue) illustrate the possible process of diffuse reflected molecules.

slightly weaker in its separation performance for α (H₂/H₂O) in comparison with the other SMG (silane) membranes although it contains terminal fluorine groups. The slight decrease of the hydrogen selectivity of about −10% for the shown SMG (silane) membranes can result from: i) degradation effects of the different surface modifications with rising temperature or ii) the temperature-dependent increase of the mixed gas viscosity, which counteracts the effects introduced by the applied defect functionalisation. However, the effect of surface-linked molecules on the separation performance for membranes using extra-crystalline voids is still quite complex and has been not reported in literature so far, by the best of our knowledge.

For the SMG (TEOS) membrane, we analyse the effect if all terminal groups are replaced by hydroxyl (polar) groups, which is the case for the hydrolysed TEOS molecule. In comparison with the different SMG membranes with hydrophobic (nonpolar) terminal groups, the SMG (TEOS) membrane reveals a comparable hydrogen selectivity for α (H₂/CO₂) whereas α (H₂/H₂O) lies in between the values of the pristine graphite, with lower separability, and the different SMG (silane) membranes, with the highest separability. Consequently, the hydrogen selectivity is not only temperature-dependent but also a function of the chemical interactions (hydrophobic, hydrophilic etc.) between terminal groups and single molecule species. Furthermore, it is also
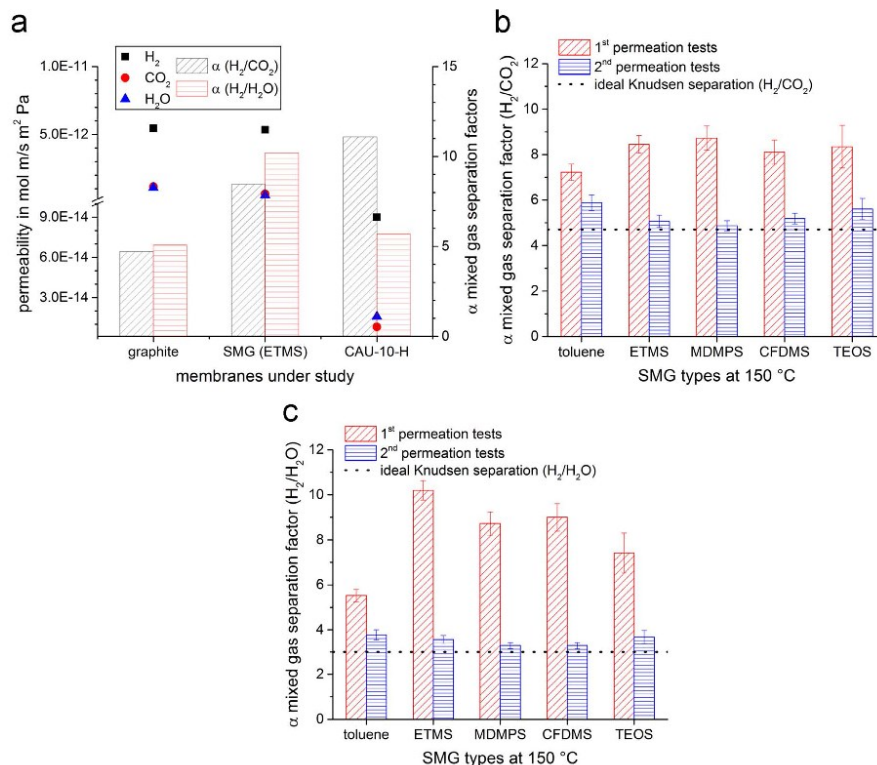
Fig. 3. Mixed gas permeabilities (thickness-normalised permeances) of H_2, CO_2, H_2O (steam) and corresponding mixed gas separation factors α (H_2/CO_2) and α (H_2/H_2O) for pristine graphite (graphite), SMG (ETMS) and CAU-10-H (MOF) membranes (a). Mixed gas separation factors of SMG (toluene) and SMG (silane) membranes for the 1st and 2nd permeation tests for α (H_2/CO_2) (b) and for α (H_2/H_2O) (c). All shown data are tested with a ternary feed mixture (41 vol.-% H_2/41 vol.-% CO_2/18 vol.-% H_2O) using a feed pressure of 2×10^5 Pa at 150 °C.

affected steric by the used defect or surface modification.

In Fig. 3a, we summarise the mixed gas permeabilities, which are the thickness-normalised permeances, of H_2, CO_2 and H_2O and the corresponding mixed gas separation factors for the investigated pristine graphite and SMG (ETMS) membrane with the metal-organic framework (MOF) membrane CAU-10-H for the ternary feed mixture

at 150 °C. The comparison reveals for the SMG (ETMS) membrane a similar separation performance as observed for the CAU-10-H membrane [20]. In this case, the SMG (ETMS) membrane shows similar or higher mixed gas separation factor α (H_2/CO_2) of 8.5 (−23%) and α (H_2/H_2O) of 10.2 (+79%) compared with the CAU-10-H membrane. Simultaneously, the SMG (ETMS) membrane reveals a 59 times higher
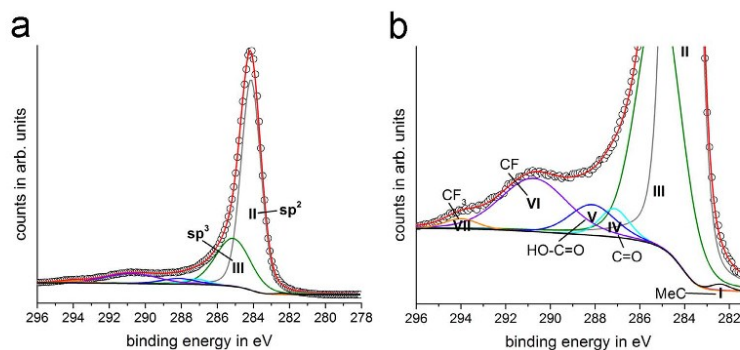

Fig. 4. C 1s spectrum of the pristine graphite membrane (a) from surface analysis by XPS and a magnification of the small signals (b), see Table 1.

320

Table 1

Surface analysis by XPS of the pristine graphite, SMG (toluene) and SMG (CFDMS), see Fig. 4. With E_B: binding energy, FWHM: full width at half maximum and signal area: related areas of the C 1s spectra for the respective membrane under study.

Signals	C 1s					Chemical information After Refs. [21–25]
	Pristine graphite			SMG (toluene)	SMG (CFDMS)	
	E_B in eV	FWHM in eV	Signal areas in %	Signal areas in %	Signal areas in %	
I	282.4	1.0	0.3	0.4	0.3	MeC
II	284.1	1.3	61.4	62.8	62.6	sp^2
III	285.1	2.3	24.8	25.3	24.2	sp^3
IV	287.1	1.5	1.8	1.1	0.9	C=O
V	288.1	2.4	3.1	2.4	2.5	O=C-OH
VI	290.7	3.5	7.9	7.2	8.5	CF
VII	294.0	1.7	0.8	0.7	0.9	CF_3

hydrogen permeability compared with the CAU-10-H (MOF) membrane. According to this, the SMG membranes are quite competitive with the thin CAU-10-H (MOF) membrane which is synthesised by complex growth conditions and need to be supported.

All membranes shown in this work were tested from 100 to 250 ºC, every 50 ºC for at least 48 h until the dynamic equilibrium between feed and permeate concentration was reached. After the SMG membranes were analysed at 250 ºC, additional permeation tests (2nd) revealed a complete decline of the mixed gas separation factors α (H_2/CO_2) and α (H_2/H_2O) to the values observed for the pristine graphite membrane or lower, as given in Figs. 3b–c. These dramatic changes are further discussed, see Section 3.3. Raman analysis.

3.2. Surface composition of pristine graphite and SMG membranes by XPS analysis

A typical XPS spectrum together with a detailed profile analysis of the pristine graphite membrane is given in Fig. 4. The main peaks are related to the presence of sp^2, at 284.1 eV, as well as sp^3, at 285.1 eV, hybridised carbon, see Fig. 4a [21]. The sp^2 hybridised carbon is attributed to graphite whereas the sp^3 hybridised species indicate some amorphous carbon on the membranes surface [8]. Further peaks are assigned as denoted in the magnified spectrum, see Fig. 4b. The results from the fits are collected in Table 1. First of all, the intensity ratio of the sp^2 and sp^3 hybridised species is 61.4/24.8≈2.5. This ratio remains stable within the limit of error for all analysed SMG membranes. Moreover, for the pristine graphite membrane some percentages of carbonyl (1.8%), carboxyl groups (3.1%), CF_x groups (8.7%) and traces of MeC (0.3%) could be identified, which is in agreement with similar samples [22–25]. The presence of CF_x groups on the membrane surface can explain the higher mixed gas separation factor of α (H_2/H_2O)=5.4 at 250 ºC of the pristine graphite membrane compared with the ideal Knudsen separation factor of 3.0, see Section 3.1. The observed carboxyl groups represent chemical active sites (functional groups) for a possible functionalisation with silanes whereas the observed carbonyl groups should be inactive for functionalisation processes. Additionally, traces of silica, fluorine and other compounds were also detected as expected for the pristine graphite flakes made from natural ore, see Section 2.1. Comparative analyses of the SMG membranes reveal a slightly increased Si 2s and Si 2p emissions but their detailed quantification was not possible caused by the background intensity and silica residuals. Additionally, the spectra of the C 1s and F 1s emissions revealed similar peak positions and intensities with no significant changes for a quantitative analysis between the pristine graphite and SMG (toluene, CFDMS) membranes, see Table 1. Therefore, the character of the available functional groups for the surface modification of graphite remains undetermined, here [26,27].

3.3. Micro-focused Raman spectroscopy

The membranes were systematically investigated using confocal micro-focused Raman spectroscopy. The excitation area was about $1 \mu m^2$ for all measured spots. A linescan of 12 spots along a total distance of 220 µm with an increment of 20 µm were carried out starting at a randomly chosen point. Examples of spectra obtained along such a linescan on the pristine graphite, SMG (toluene) and the SMG (toluene) annealed membrane surfaces are shown in Fig. 5. All spectra show between 50 and 2000 cm^{-1} (first order spectral region) two main peaks assigned to the G peak at about 1581 cm^{-1} and D1 peak at about 1350 cm^{-1} [28]. In the case of a strong D1 peak, also the D2 peak at about 1620 cm^{-1} seen as a shoulder at the G peak becomes separated.

The G peak is the only symmetry allowed Raman-active vibration mode for an ideal graphite crystal with the space group of P6$_3$/mmm (D_{6h}) [29]. It is related to an in-plane angle deformation related to bond-stretching vibrations of opposite sp^2 hybridised carbon atoms in the C_6-ring with an E_{2g} lattice symmetry [30]. According to the literature, the D1 mode corresponds with a carbon-carbon stretching vibration related to a C_6-breathing mode obeying an A_{1g} lattice symmetry. The D1 band is only observed by in-plane symmetry breaches and corresponds with a disordered or distorted graphite lattice. The D2 peak is also related to a disordered graphite lattice but corresponds to an E_{2g} symmetry in the irreducible representation. Therefore, both vibration modes (D1 and D2) become allowed in the Raman spectrum by the presence of "defects" which could be due to growth conditions as well as physico-chemcial treatment of the used graphite flakes [31–33]. It is observed that the D1/D2 peaks become much more intensified in the Raman spectra of the SMG (toluene) membrane compared with the pristine graphite membrane, see Figs. 5a–b. Annealing of the SMG (toluene) membrane up to 250 ºC reverses this trend again (see Fig. 5c).

A Lorentzian peak-fitting analysis with the parameters peak position, FWHM and intensity revealed the following systematics. Plotting the FWHM of the G peak versus the relative intensity of the D1 peaks show a general trend of an increasing FWHM related to an increased relative intensity of D1 (see Fig. 6a). A significant distribution of this dependency is already observed for the pristine graphite membrane as shown by the marked area in the figure. The measured point outside of the marked area may also be noted, indicating that such type of defect is present here, too. The SMG (toluene) shifts the distribution markedly to still higher D1 peak intensities and G peak FWHMs. This trend becomes reversed with thermal treatment resembling almost the distribution of the pristine graphite membrane. A systematic change in the distribution of the peak position for the D1 mode could also be observed (see Fig. 6b). The peak position of the G mode showed similar to the D1 mode slight shifts to lower wavenumbers by approx. 1–2 cm^{-1}, what also provides a low
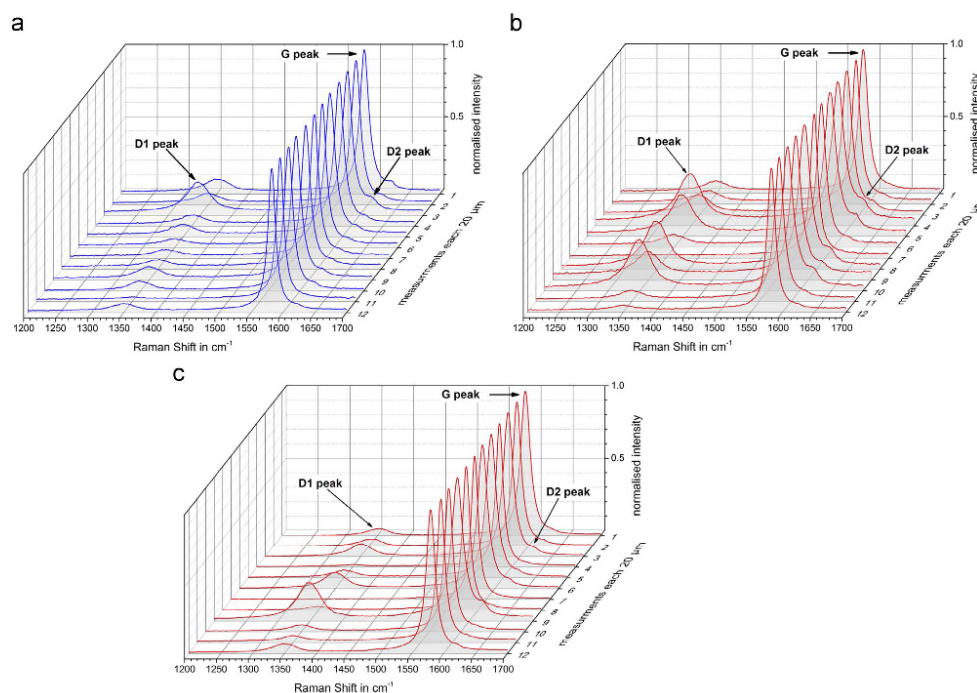
A. Wollbrink et al.

Fig. 5. Linescans of micro-focused Raman spectra along a distance of 220 μm with an increment of 20 μm on the pristine graphite (a), the SMG (toluene) (b) and the SMG (toluene) annealed membrane surface (c), observed in the spectral region between 50 and 2000 cm^{-1}.

number of defect modification, whereas a clear trend of the D1 mode to somewhat smaller wavenumbers with increasing intensity could be observed. This trend also becomes reversed for the SMG (toluene) membrane annealed up to 250 °C. In detail, for the pristine graphite membrane, the FWHM of the G peak varies typically between 14 and 19 cm^{-1} corresponding with a relative intensity distribution between 2–9%. The increase of the D1 intensity may be related to lattice distortions which immediately lead to a broadening of the G mode lattice vibration due to strain effects [34]. Simultaneously, the observed Raman shift for the D1 mode slightly moves to lower wavenumbers from about 1351 cm^{-1} to 1349 cm^{-1} with increasing relative intensity which shows the character

of the defects. Following these arguments, the Raman spectra of the SMG (toluene) membrane show an additional broadening of the G peak FWHM up to 24 cm^{-1} related to a variation of the Raman shift of the D1 mode up to 26%. Contrary to the commercial graphite membrane, the Raman shift of the D1 mode nearly stagnates for the SMG (toluene) at 1348 cm^{-1} while its relative intensity still increases. If graphite is described as an almost chemical stable material under these conditions, it can be assumed that the number of defects at the graphite surface is not increased by the thermo-chemical treatment of SMG (toluene) at about 140 °C. Therefore, the observed effects correspond with a stronger strain effect induced by the modification of the distinctive oscillator strength due to the addition of
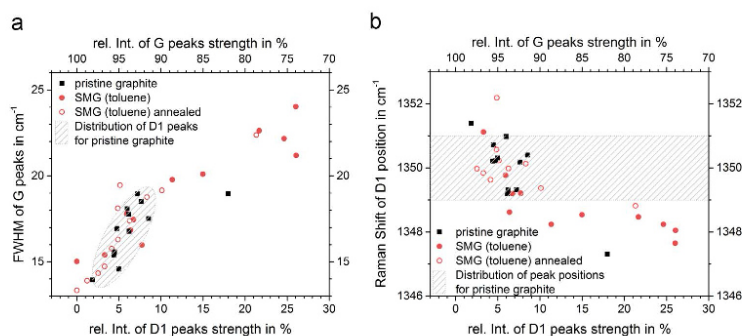
Fig. 6. Analysed micro-focused Raman spectra shown in Fig. 5 are given for the G mode "Full Width at Half Maximum" (FWHM) (a) and also for the D1 mode position (b) as a function of the relative intensity of D1 peaks strength in % for the pristine graphite, the SMG (toluene) and the SMG (toluene) annealed membrane.

Fig. 7. Analysed Raman spectra for the G peaks FWHM (left column) and for the D1 peaks position (right column) as a function of the relative intensity of D1 peaks strength in % for the SMG (CFDMS), (ETMS), (MDMPS) and (TEOS) membrane.

323

other compounds at the defect locations (see Fig. 6b).

The Raman spectra of all the other SMG (silane) membranes were measured in the same way as described for the pristine graphite and SMG (toluene) membrane. Here, the observed G and D peaks could be also analysed by a Lorentzian peak-fitting, collected in Fig. 7.
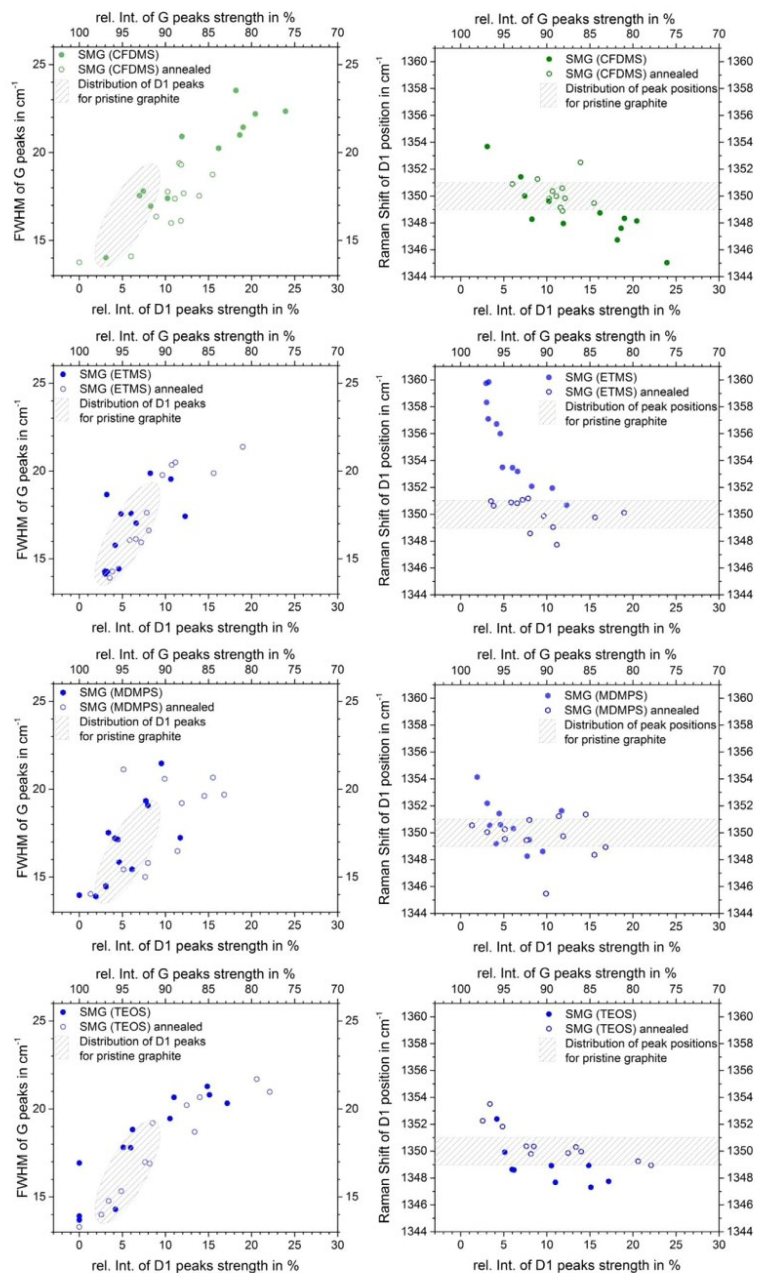
In the case of the SMG (CFDMS) membrane, a broadening of the G peak FWHMs up to 23 cm^{-1} related to an increased intensity of D1 mode up to 25% could be found, similar to the SMG (toluene) membrane. The Raman shift of the D1 mode shows a much broader dispersion between 1354 and 1345 cm^{-1}, which totally corresponds with a three wavenumbers lower Raman shift than observed for the SMG (toluene) membrane. For the SMG (ETMS) membrane, the G mode FWHMs and the intensity of the D1 mode nearly varies in the area known for the pristine graphite membrane. In contrast to that, the Raman shift of the D1- mode shows here the highest variation between 1360 cm^{-1} and 1351 cm^{-1} observed for the low intensities of the D1 mode. The SMG (MDMPS) membrane shows comparable G mode FWHMs with in the area of the pristine graphite membrane but the position of the D1 mode is located at wavenumbers between 1354 cm^{-1} and 1348 cm^{-1}. The SMG (TEOS) membrane, shows in accordance with the other silane modified membranes also characteristically affects. The G mode FWHMs are also related to increased intensities of the D1 mode between 0% and 17% which results in a wide scattering of the shown data, whereas the Raman shift of the D1 mode between 1352 cm^{-1} and 1347 cm^{-1} is in accordance with the observed effects, as discussed before.

In general, the Raman peak positions depend on the chemical potential of the graphite surface which is changed due to the defects and their modification. The fact that the G shift is comparably small indicates that the concentration of modified surface defects is rather low, which is in accordance with the conclusions drawn from the XPS analysis, see Section 3.2. From these data it follows, that the D1 peaks in the Raman spectra of the pristine graphite membrane showed the existence of defects which should correspond to the different oxygen or fluorine groups observed by XPS analysis (see Fig. 4, Table 1). From these groups, only a small fraction can be expected to be chemically active for the defect modifications on the graphite surface, mainly hydroxyl or carboxyl groups. The relative intensity of the D1 mode is a function of the character and quantity of the chemically modified defects which already exist on the pristine graphite surface. This is concluded from the variation of the G mode FWHMs and D1 mode peak positions. These variations are specific for the different silanes as well as for toluene modified defects due to the molecular weights, kind of terminal groups and chemical reactivity, see Figs. 6 and 7.

For the SMG (toluene) membrane, the Raman spectra revealed changes of the G and D1 modes which are comparable with the effects observed for the different SMG (silane) membranes. Therefore, these results provide the discussion of toluene molecules on the graphite surface, which we described as localised surface modification by π-π interactions, see Section 3.1. For the SMG (CFDMS, ETMS and MDMPS) membranes distinctive defect modifications could be observed although all of them have only one functional group to bond at the defect sites on the graphite surface. Therefore, the dissociation of the chlorine group is expected to be more active compared with the ethoxy or methoxy groups, which explains their different effects on the G and D1 modes. The molecular weights differ as follows: M(CFDMS) =190.67 g/mol > M(MDMPS)=166.30 g/mol > M(ETMS)=118.28 > M(toluene)=92.14 g/mol. This also distinguishes the used silane among themselves which results from different effects observed for the G and D modes.

For all SMG annealed membranes, which were heated to 250 ℃ for at least 48 h, dramatic changes in their G mode FWHMs and Raman Shift of the D1 mode could be observed (see Figs. 6 and 7). For the annealed SMG (toluene) membrane the FWHMs of the G band, the Raman Shift of D1 and its relative intensity resemble the values of the pristine graphite membrane (see Fig. 6). Such changes of the G and D1 modes in the Raman spectra for the SMG (toluene) membrane show a

completely reversible behaviour which is in accordance with our discussion of toluene molecules on the graphite surface by π-π interactions, see Section 3.1. For the SMG (silane) membranes, the G mode FWHMs, the Raman shift and the intensity of the D1 mode are reduced but do not reach the values observed for the pristine graphite membrane. These effects indicate that some groups remain at the defect sites in contrast to the SMG (toluene) annealed membrane. The thermal stability of surface linked silanes on silica can be found in literature up to 450 ℃ under oxidising conditions whereas the terminal groups (methyl groups) start to decompose by oxidation but do not desorb from the silica surface [35]. In the case of functional groups in organic polymers, the thermal stability is described in literature as below 300 ℃ and is closely dependent on the used silane, its connectivity, surface properties and experimental conditions, as we could observe by permeation experiments (see Fig. 2) or Raman spectra (see Figs. 6 and 7) [36].

4. Conclusion

Surface modified graphite (SMG) membranes showed improved hydrogen selectivities compared with the pristine graphite membrane which makes them interesting for steam reforming in catalytic membrane reactors below 400 ℃. The membranes, prepared by pressing pristine or modified graphite flakes, were investigated for the ternary feed mixture (41 vol.-% H_2/41 vol.-% CO_2/18 vol.-% H_2O) from 100 ℃ to 250 ℃. Compared with the pristine graphite membrane, the mixed gas separation factors α (H_2/CO_2) and α (H_2/H_2O) for the SMG membranes are improved by 80% and 70%, respectively. It could be shown, that the increased hydrogen selectivities are closely related to the functionalisation of the graphite surface using various silanes with hydrophobic terminal groups (ETMS, MDMPS, CFDMS), hydrophilic terminal groups (TEOS hydrolysed). However, the concentration of functional groups on the graphite membrane surface by the modification carried out at 140 ℃ was very low and was only indirectly determined by confocal micro-focused Raman spectroscopy and the affected membrane performances by gas chromatographic analysis.

This work demonstrates that further functionalisation of the defect sites for the pristine graphite surface is possible and has a huge impact on the separation performance of pressed graphite membranes. Surface modification alters the character of the extra-crystalline voids within these membranes which affects the separation mechanism by physical and/or chemical interactions. Here, the number of elastic or inelastic molecule-wall collisions rise which are diffusively reflected from the graphite surface. Consequently, molecules with a smaller kinetic diameter are less affected than bigger ones and also light molecules are less influenced.

The concentration of defect sites, e.g. hydroxyl or carboxyl groups, on the pristine graphite membrane could be determined by XPS but with no details about the concentrations of chemical modifications. In this study, the confocal micro-focused Raman spectroscopy was the main method to reveal the following important aspects: functional groups (structural defects) are already existing on the pristine graphite surface (i) and the chemical modification by toluene (ii) and also different silanes (iii) of the defect sites differently affect the relative intensity and position of the defect mode D1 and the FWHMs of the G mode by modified lattice distortions. In addition, the low shift of the G mode position also provides a low number of defect modifications. Therefore, the results of XPS and Raman cannot quantify the number of defect modifications but support themselves.

Furthermore, the results show that the thermal stability of SMG membranes suffers at temperatures equal or higher than 250 ℃. To increase the hydrogen selectivity even more, further investigations could be tried to increase the concentration of defect sites on the graphite surface by physical or chemical treatments. In addition, the thermal stability of the surface modifications should be generated by a higher connectivity between the functionalisations on the graphite surface.

Results and Discussion: Porous graphite membranes

Acknowledgements

References

[1] M. Ni, D.Y.C. Leung, M.K.H. Leung, A review on reforming bio-ethanol for hydrogen production, Int. J. Hydrog. Energy 32 (2007) 3238–3247.

[2] V. Palma, E. Palo, F. Castaldo, P. Ciambelli, G. Iaquaniello, Catalytic activity of CeO$_2$ supported Pt-Ni and Pt-Co catalysts in the low temperature bio-ethanol steam reforming, Chem. Engin. Trans. 25 (2011) 947–952.

[3] V. Palma, E. Palo, F. Castaldo, P. Ciambelli, G. Iaquaniello, Catalytic activity of CeO$_2$ supported Pt-Ni and Pt-Co catalysts in the low temperature bio-ethanol steam reforming, Chem. Engin. Trans. 25 (2011) 947–952.

[4] S. Tosti, Overview of Pd-based membranes for producing pure hydrogen and state of art at ENEA laboratories, Int. J. Hydrog. Energy 35 (2010) 12650–12659.

[5] S. Tosti, Overview of Pd-based membranes for producing pure hydrogen and state of art at ENEA laboratories, Int. J. Hydrog. Energy 35 (2010) 12650–12659.

[6] T. Kiyoshi, T. Namba, M. Yamawaki, Hydrogen permeation through graphite, J. Nucl. Mater. 155 (1988) 230–233.

[7] A. Schulz, F. Steinbach, J. Caro, Pressed graphite crystals as gas separation membrane for steam reforming of ethanol, J. Membr. Sci. 469 (2014) 284–291.

[8] A. Wollbrink, K. Volgmann, J. Koch, K. Kanthasamy, C. Tegenkamp, Y. Li, H. Richter, S. Kämnitz, F. Steinbach, A. Feldhoff, J. Caro, Amorphous, turbostratic and crystalline carbon membranes with hydrogen selectivity, Carbon 106 (2016) 93–105.

[9] D.S. Scott, F.A.L. Dullien, Diffusion in ideal gases in capillaries and porous solids, AlChE J. 8 (1962) 113–117.

[10] J. Rouquerol, D. Avnir, D.H. Everett, C. Fairbridge, M. Haynes, N. Pernicone, J.D.F. Ramsay, K.S.W. Sing, K.K. Unger, Guidelines for the characterization of porous solids, Stud. Surf. Sci. Catal. 87 (1994) 1–9.

[11] J. Kärger, D.M. Ruthven, D.N. Theodorou, Diffusion in Nanoporous Materials 1, Wiley-VCH, 2012, pp. 85–109.

[12] R. Krishna, J.M. van Baten, Investigating the relative influences of molecular dimensions and binding energies on diffusivities of guest species inside nanoporous crystalline materials, J. Phys. Chem. 116 (2012) 23556–23568.

[13] R. Krishna, Describing the diffusion of guest molecules inside porous structures, J. Phys. Chem. C 113 (2009) 19756–19781.

[14] D.A. Shirley, High-resolution x-ray photoemission spectrum of the valence bands of gold, Phys. Rev. B 5 (1972) 4709–4714.

[15] G.-Y. Oh, Y.-W. Ju, M.-Y. Kim, H.-R. Jung, H.J. Kim, W.-J. Lee, Adsorption of toluene on carbon nanofibers prepared by electrospinning, Sci. Total Environ. 393 (2008) 341–347.

[16] S. Gotovac, H. Honda, Y. Hattori, K. Takahashi, H. Kanoh, K. Kaneko, Effect of nanoscale curvature of single-walled carbon nanotubes on adsorption of polycyclic aromatic hydrocarbons, Nano Lett. 7 (2007) 583–587.

[17] J.L. Achtyl, A.M. Buchbinder, F.M. Geiger, Hydrocarbon on carbon: coherent vibrational spectroscopy of toluene on graphite, J. Phys. Chem. Lett. 3 (2012) 280–282.

[18] C.A. Hunter, J.K.M. Sanders, The Nature of π-π Interactions, J. Am. Chem. Soc. 112 (1990) 5525–5534.

[19] C.R. Martinez, B.L. Iverson, Rethinking the term "pi-stacking", Chem. Sci. 3 (2012) 2191–2201.

[20] H. Jin, A. Wollbrink, R. Yao, Y. Li, J. Caro, W. Yang, A novel CAU-10-H MOF membrane for hydrogen separation under hydrothermal conditions, J. Membr. Sci. 513 (2016) 40–46.

[21] P. Mérel, M. Tabbal, M. Chaker, S. Moisa, J. Margot, Direct evaluation of sp^3 content in diamond-like-carbon films by XPS, Appl. Surf. Sci. 136 (1998) 105–110.

[22] G. Nguila Inari, M. Petrissans, J. Lambert, J.J. Ehrhardt, P. Gérardin, XPS characterization of wood chemical composition after heat-treatment, Surf. Interface Anal. 38 (2006) 1336–1342.

[23] Z. Wang, B. Huang, Y. Dai, Y. Liu, X. Zhang, X. Qin, J. Wang, Z. Zheng, H. Cheng, Crystal facets controlled synthesis of graphene@TiO$_2$ nanocomposites by a one-pot hydrothermal process, Cryst. Eng. Comm. 14 (2012) 1687–1692.

[24] I.P. Asanov, V.M. Paasonen, L.N. Mazalov, A.S. Nazarov, X-Ray photoelectron study of fluorinated graphite intercalation compounds, J. Struct. Chem. 39 (1998) 928–932.

[25] W.-K. Lee, I. Losito, J.A. Gardella Jr, W.L. Hicks Jr., Synthesis and surface properties of fluorocarbon end-capped biodegradable polyesters, Macromolecules 34 (2001) 3000–3006.

[26] A. Lerf, H. He, M. Forster, J. Klinowski, Structure of graphite oxide revisited, J. Phys. Chem. B 102 (1998) 4477–4482.

[27] H.P. Boehm, Surface oxides on carbon and their analysis: a critical assessment, Carbon 40 (2002) 145–149.

[28] A. Sadezky, H. Muckenhuber, H. Grothe, R. Niessner, U. Pöschl, Raman micro-scopy of soot and related carbonaceous materials: spectral analysis and structural information, Carbon 43 (2005) 1731–1742.

[29] F. Tuinstra, J.L. Koenig, Raman spectrum of graphite, J. Chem. Phys. 53 (3) (1969) 1126–1130.

[30] A.C. Ferrari, J. Robertson, Interpretation of Raman spectra of disordered and amorphous carbon, Phys. Rev. B 61 (2000) 14095–14107.

[31] O. Beyssac, D. Ruble, Graphitic carbon: a ubiquitous, diverse, and useful geomaterial, Elements 10 (6) (2014) 415–420.

[32] P.R. Buseck, O. Beyssac, From organic matter to graphite: graphitization, Elements 10 (6) (2014) 421–426.

[33] Y. Wang, D.C. Alsmeyer, R.L. McCreery, Raman spectroscopy of carbon materials: structural basis of observed spectra, Chem. Mater. 2 (1990) 557–563.

[34] E.K.H. Salje, Chemical mixing and structural phase transitions: the plateau effect and oszillatory zoning near surfaces and interfaces, Eur. J. Miner. 7 (1995) 791–806.

[35] A. Hilonga, J.-K. Kim, P.B. Sarawade, H.T. Kim, Low-density TEOS-based silica aerogels prepared at ambient pressure using isopropanol as the preparative solvent, J. Alloy. Compd. 487 (2009) 744–750.

[36] P.G. Pape, E.P. Plueddemann, Methods for improving the performance of silane coupling agents, J. Adhes. Sci. Technol. 5 (1991) 831–842.

4. Conclusion

To the present day, the global production of pure hydrogen still originates primarily from fossil fuels and is dominated by industry, i.e. mainly by petroleum refining and ammonia production [106,107]. Nevertheless, the huge advantage of the classic CESR process ("state of the art" technique) for the commercial production of hydrogen from hydrocarbons is related to its high hydrogen-selectivity and full conversion of ethanol. Nevertheless, numerous disadvantages are described by the energy-intensive process for a full ethanol conversion (endothermic reaction) at temperatures up to 1000°C; the use of non-renewable (fossil) hydrocarbons as hydrogen source; the release of high amounts of CO, beside several other side-reactions; the presence of high amounts of water steam (necessary for the reaction), and therefore the requirement of additional purification steps. The removal of the undesired gases through additionally required processes, e.g. CO removal by low temperature WGSR or pressure swing adsorption, and water steam removal by distillation and further dehydration using zeolites for adsorption, makes the classical technique in comparison with other methods (e.g. water splitting by electrolysis) very cost-intensive and unattractive. At low temperatures of smaller than 400°C, the classic CESR process suffers from low ethanol conversion related with low hydrogen selectivity whereas the formation of CO and other side-products is suppressed.

The hydrogen production from biomass, water, biomass-water mixture or renewable electricity (supplied by solar or wind generators) are currently almost negligible, i.e. for example the contribution of hydrogen produced from water electrolysis was less than 0.1% of the global hydrogen production in 2018. Currently, the hydrogen production is responsible for the emissions of about 830 million tons of CO_2. The crucial point here are the recent production costs of about 1-3 USD per kg of hydrogen from fossil fuels in contrast to 3-7.5 USD per kg of hydrogen from renewable production [107].

The current state in industrial production technique of hydrogen is from steam reforming of natural gas. Afterwards, the hydrogen separation from the generated reaction mixture is carried out by pressure swing adsorption (PSA) technique [108]. A further purification of the produced hydrogen is followed by the high energy consuming "Linde-Hampson process" [109,110]. Here, hydrogen and other impurities (e.g.: nitrogen or oxygen) are separated by its different liquefaction and boiling temperatures. These methods are time and highly energy consuming and require several steps of separation and purification. Therefore, the topic of the

development of a cleaner, more riskless and cheaper technical solution for the production of so-called "green hydrogen" as a sustainable energy carrier is from the project start (2012/2013) until today (2020) more than ever of strong interest, also reinforced in Germany by the national hydrogen-based strategy of the German Federal Government in 2020 [17]. Generally, the pseudonym of so-called "green hydrogen" is related with carbon-free technologies but here it is applicable due to the described closed carbon circle (carbon neutral resource) by the use of bio-ethanol and water. In addition to that, bio-ethanol can also serve as efficient "CO_2 storage" in terms of a global sustainable energy carrier and its necessary production in the hypothetical dimensions of a myriad of tones.

An alternative to these separation processes is the use of membranes for gas separation. Generally, the main advantages for the use of membrane technology for the separation of hydrogen with different purity are related to low capital costs (i.e. for acquisition and construction), low operation costs (i.e. ease of operation), energy efficiency, ease and flexibility in operation, modular arrangement (i.e. adaptable), and integrable to still established industrial processes [108,111,112]. Furthermore, the combination of a catalytic reaction and hydrogen separation for the continuous removal of hydrogen during the reaction is especially suited for thermodynamic limitation, i.e. the reaction is carried out at commonly to low temperatures to suppress disturbing side reactions [11,13,21–23]. Consequently, the use of a hydrogen-selective membrane with improved properties for the application in a catalytic membrane reactor (CMR) for bio-ethanol steam reforming (b-ESR) still belongs to the "state of the art" technique in present membrane technologies but is also associated with huge challenges due to the quite complex interaction of reaction mechanisms, long-term stability under hydrothermal conditions, and required membrane properties.

Today's state-of-the-art in hydrogen separation by means of classic membrane separation, i.e. only gas separation without a combined reaction takes place, is commonly described by the use of several membrane types that can be classified into dense and porous membranes in the focus of hydrogen-selective membranes [108,111,112]. Both types, i.e. dense and porous, of inorganic membranes are generally suited for gas separation. In general, dense inorganic membranes have the theoretical advantage of a complete hydrogen-selectivity at the expense of comparable low permeability whereas porous membranes have comparable high permeability but have rather low hydrogen-selectivity in comparison with dense membranes. For the required conditions of b-ESR in a CMR, the choice of a certain membrane type is

crucial and generally depends on the specific application. Consequently, not every membrane type is generally suited here, independent from its hydrogen-selectivity.

In Literature, the most common hydrogen-selective membranes are made from the group of dense materials, i.e. palladium and its alloys, proton-conducting ceramics, polymers, as well as porous materials, i.e. huge group of zeolites, silica molecular sieves or silica-alumina composites.

The group of dense membrane materials has the theoretical advantage of complete hydrogen selectivity. One of the disadvantages of such materials as hydrogen-selective membranes originates from their selective transport process related with a relative high thermal activation energy that also requires high process temperatures. The hydrogen permeance of a Pd-based as well as proton-conducting ceramic membrane is directly related with the working temperature and decrease or increase as the temperature is changed, respectively. For example, the required working temperature of a Pd-based membrane for a sufficient hydrogen permeance is mainly studied at about 400°C or above [113]. Below 300°C, Pd-based membranes start to embrittle due to the present phase transition of formed hydrides. Additionally, both membrane types used in the hydrogen separation process are accompanied by alteration effects due to the presence of reactive gases (e.g. CO, CO_2, H_2O) or undesired side-products (e.g. decomposition of ethanol to carbonaceous matter) in the reaction mixture. For example, the decrease in hydrogen permeance is related with i) complete blockage of hydrogen permeance by the presence of CO at the membrane surface of noble-metal membranes [113–118] or H_2S as well, even at low concentrations, ii) the surface passivation of densely sintered ceramic membranes by carbonate formation [119–121], or iii) the general passivation of the membrane surface by the formation of carbonaceous matter. The huge group of dense polymer membranes can have the advantage of moderate hydrogen-selectivity but have the general disadvantages of comparable low permeability, low operation temperature of about 100 °C, low chemical or hydrothermal stability [108,112]. Additionally, the performance of polymeric membranes is limited to the semi-empirical "upper bound line" of polymers, described by Robeson[122,123].

The group of porous membrane materials has the theoretical advantage of high hydrogen permeability whereas the hydrogen selectivity is comparable low. Generally, porous zeolite, silica molecular sieves, or silica-alumina composites have the advantages of general uniform pore size distribution with high temperature and chemical stability. Here, the huge disadvantages for such membranes is related to practical low hydrogen-selectivity due to the

difficult synthesis of the growth of an uniform and suitable membrane layer without intracrystalline voids, interstitial pores, or cracks [108,111]. Furthermore, silica molecular sieves, or silica-alumina composites can be damaged in the presence of steam due to hydrolysis of siloxanes and its mobilization into the pores [124].

Carbon-based membranes are discussed as promising material in gas separation applications [125–128]. Especially, the class of molecular-sieve carbon membranes (MSCMs) is carefully described to have the potential to technically compete with polymer membranes. The circumstance is due to their comparable high permeability and separation performance (related with their molecular sieving effect), superior thermal resistance and chemical stability in corrosive environments, and its relative ease of preparation from industrial polymers or polymer blends. MSCM are also discussed to be able to break the "upper bound" of polymer membranes [122,123]. MSCMs are generally synthesized by pyrolysis of organic precursor, e.g. Kapton, Matrimis, phenolic resins, polyimides etc. Extensive works on MSCMs to applications of recovery of air hydrogen (H_2/N_2), (H_2/CH_4), separation of oxygen (O_2/N_2), CO_2 capture (CO_2/N_2), natural gas purification (CO_2/CH_4) and (N_2/CH_4), propane/propene, or dehydration of fine chemical products are still present whereas only a small number of issues regarding the separation of (H_2/CO_2) are present. For the latter ones, pure gas data show selectivity of (H_2/CO_2) of less than 20. In addition to that, most references of MSCM studies are still designed for applications in laboratory scale. The challenge or disadvantage is the poor mechanical strength and brittleness after pyrolysis of the organic precursor that needs a careful handling with thin-layer samples and also makes reproducible separation properties difficult due to cracks, defects during pyrolysis.

Nevertheless, two companies "Carbon Membranes Ltd." and "Blue Membranes GmbH" (Germany) are known to produce large-scale MSCM modules. Carbon Membranes Ltd. was the first company which produced large-scale MSC modules based on pyrolysed cellulose fibres with about 10.000 fibers with 4 m² per module but it closed in 2001. Additionally, the company "Blue Membranes GmbH" (Germany) developed flat membranes in a "honeycomb" configuration, supported by ceramics, is still registered and active. It still deals with the production and sale of membrane filtration modules for water, waste water, and solid-liquid separation.

Recent references of Metal-organic framework (MOF) membranes are generally investigated in laboratory-scale applications for diverse separation fields, i.e. H_2 purification (H_2/N_2, H_2/CO, H_2/CO_2), air separation (N_2/O_2), CO_2 capture (CO_2/H_2), natural gas sweetening

Conclusion

(CO_2/CH_4) organic dehydration or extraction, hydrog etc [129–132]. Also applications in catalytic membrane reactors are discussed to persuit economics and sustainability in modern energy consumptions and chemical manufacturing. The huge interest of MOF applications is due to their versatile properties by synthesis of multifaceted networks of metal polyeder and highly functional organic linkers that includes various functionalities as well as tuneable properties to withstand harsh chemical environments and thermally challenging conditions in real industrial processes. Generally, the chemical and thermal stability of MOFs is very low and unsuitable for moisture and aggressive conditions. Nevertheless, some MOF-structures could be found to be stable up to 400 °C, under hydrothermal conditions, .e.g. ZIFs, MILs, UiOs as well as CAUs. Nevertheless, the practical use of MOF membranes also deals with the difficult synthesis of the growth of an uniform and suitable membrane layer without intracrystalline voids, interstitial pores, or cracks, as mentioned for MSCMs as well as zeolite membranes,

However, in industry the majority of hydrogen-selective membranes are made of polymers due to its low costs, ease of manufacturing, and processibility[112,125–128]. The said other membranes are generally discussed and experimental investigated only in the laboratory scale related with high capital cost by manufacturing problems as mentioned before. Only some membrane materials are applied in niches or commercially available, e.g. Pd-based membranes or molecular-sieve carbon membrane (MSCM).

Porous Carbon-based and MOF membranes can be suitable candidates for the challenging separation by their general hydrothermal stability (in the described temperature range), their adjustable microtexture and porosity (as the function of the used precursor and Carbonization steps), and diversity of functional groups due to e.g. oxygen-containing surface functional groups (still present after Carbonization or introduced).

In this context, a new concept of different hydrogen-selective porous Carbon-based Membranes were investigated as suitable candidates for the purpose of the production of so-called "green hydrogen" for the concept of a catalytic membrane reactor (CMR) for bio-ethanol steam reforming (b-ESR). The carbon-based membranes under study were investigated by means of classic gas separation experiments, without a catalytic reaction, in an effective temperature range between "room temperature" and 300 °C. Temperature- and pressure-dependent single and mixed-gas permeation experiments were mainly applied most closely to industrial conditions, i.e. only a pressure-gradient (up to 5 bar) between feed- and permeate-site (without sweep gas), binary (dry condition) and ternary (hydrothermal

Conclusion

condition) feed-mixtures, were preferably used for the characterization of membrane performances in laboratory scale. The systematic characterization of the carbon-based membranes revealed the dominating separation mechanisms due to the pore size distribution that result the classification into two groups: *i.*) Microporous Carbon Membranes, i.e. the separation mechanism of the: amorphous carbon membrane is adsorption-dominated, turbostratic carbon membrane occurs through selective surface diffusion, cCMS/SiO$_2$ occurs diffusion-dominated for H$_2$, CO$_2$ and adsorption-dominated for H$_2$O, CAU-10-H (MOF) membrane occurs by size-exclusive molecular sieving mechanism and *ii.*) Porous Graphite Membranes, i.e. the separation mechanism of the: pressed graphite membrane occurs through Knudsen diffusion, "surface modified graphite" (SMG) membranes occur through a modified Knudsen mechanism.

From the described membranes under study, it could be shown that two kinds of carbon-based membranes, i.e. the metal-organic framework (CAU-10-H) membrane and the group of SMG membranes, comparatively showed the most promising results in the hydrogen separation from a ternary gas mixture compared with the other ones. The mixed gas separation factors of the CAU-10-H and SMG graphite (e.g. ETMS-modified) membrane could reached for α (H$_2$/CO$_2$) of 11.1 or 8.0 and for α (H$_2$/H$_2$O) of 5.7 and 10.2, respectively. Both membrane types showed reasonably mixed gas separations factors in comparison with the other membranes under study independent from their different separation mechanisms whereas their hydrogen permeabilities greatly differ from each other. Here, the hydrogen permeability of the SMG graphite (e.g. ETMS modified) membrane is in the range of 44 to 15 times higher, the mixed gas separation factor α (H$_2$/H$_2$O) is approximately 80% higher whereas α (H$_2$/CO$_2$) is about 30% lower as compared with the CAU-10-H membrane.

Nevertheless, the group of SMG and the CAU-10-H membrane types may show beneficial separation performances of hydrogen in the presence of large quantities of steam (up to 18 vol.-% H$_2$O) in the required temperature range and a general hydrothermal stability in classic gas separation experiments in laboratory-scale for their possible application in a CMR for b-ESR at that point of study. Furthermore, the impact of the introduction of different functional groups with increasing hydrophobic and a hydrophilic character at the intrinsic oxygen-containing functional groups present in commercial graphite flakes could be investigated in this work.

Finally, no of the promising porous Carbon-based membranes of this work could be tested for the *in situ* removal of hydrogen in a catalytic membrane reactor (CMR) for bio-ethanol steam

reforming (b-ESR). Consequently, the observed hydrogen-selectivity seems not to be sufficient enough for the described application in a CMR. Nevertheless, an appropriate classification of the investigated membrane performances is difficult due to the required hydrogen-selectivity that also depends on the used catalyst, its kinetic parameters and the required purity for a specific application.

5. Outlook

Independent from the runtime of the project, a short outlook is given for the required investigations at the end of this work. In the case of the described CAU-10-H (MOF) membrane, additional investigation for the improve of its hydrogen-selectivity and hydrothermal stability could be applied related with i) the use of other functionalities (with terminal groups: $-CH_3$, $-OCH_3$, $-NO_2$, $-NH_2$, $-OH$) than hydrogen of the used organic linker 1,3-benzendicarboxylic acid (1,3-H_2BDC) [133,134] and ii) the reduction of two-dimensional defects (grain boundaries) during the growth of the still polycrystalline membrane due to heterogenic nucleation on the surface of the necessarily porous substrate.

In the case of the described "Surface modified Graphite" (SMG) membrane, further investigation could be applied in terms of the hydrothermal stability and hydrogen-selectivity by the kind (e.g. oxygen- vs. nitrogen-containing groups) and higher quantity of surface functional groups (hydrophobic as well as hydrophilic) by previous surface treatments.

6. Bibliography

[1]   Anonymous, Pariser Übereinkommen, Klimapolitik - Eur. Comm. (2016).
        https://ec.europa.eu/clima/policies/international/negotiations/paris_de (accessed March 5, 2017).

[2]   Bundesregierung | Artikel | Klimaabkommen von Paris wird Gesetz, (n.d.).
        https://www.bundesregierung.de/Content/DE/Artikel/2016/07/2016-07-06-ratifizierung-pariser-
        klimaabkommen.html (accessed March 5, 2017).

[3]   New York: Pariser Klimaabkommen wird Wirklichkeit, Zeit. (2016).
        http://www.zeit.de/politik/ausland/2016-10/klimaabkommen-paris-ratifizierung-deutschland-ban-ki-moon-
        barack-obama (accessed March 5, 2017).

[4]   I. des B.- BMUB, Kyoto-Protokoll, (n.d.). http://www.bmub.bund.de/P204/ (accessed March 5, 2017).

[5]   Systemadmin_Umwelt, Klimaverhandlungen, Umweltbundesamt, 2011.
        http://www.umweltbundesamt.de/publikationen/klimaverhandlungen (accessed March 5, 2017).

[6]   B.D. Solomon, K. Krishna, The coming sustainable energy transition: History, strategies, and outlook,
        Energy Policy. 39 (2011) 7422–7431. https://doi.org/10.1016/j.enpol.2011.09.009.

[7]   R.D. Misra, M.S. Murthy, Straight vegetable oils usage in a compression ignition engine—A review,
        Renew. Sustain. Energy Rev. 14 (2010) 3005–3013. https://doi.org/10.1016/j.rser.2010.06.010.

[8]   K. Rajashekara, History of electric vehicles in General Motors, IEEE Trans. Ind. Appl. 30 (1994) 897–
        904. https://doi.org/10.1109/28.297905.

[9]   Erneuerbare Energien in Europa - FaltblattErneuerbareEnergien0040003119001.pdf, (n.d.).
        https://www.destatis.de/DE/Publikationen/Thematisch/Internationales/FaltblattErneuerbareEnergien00400
        03119001.pdf?__blob=publicationFile (accessed February 25, 2017).

[10]   V.A. Goltsov, T.N. Veziroglu, L.F. Goltsova, Hydrogen civilization of the future—A new conception of
        the IAHE, Int. J. Hydrog. Energy. 31 (2006) 153–159. https://doi.org/10.1016/j.ijhydene.2005.04.045.

[11]   V. Palma, F. Castaldo, G. Iaquaniello, P. Ciambelli, Sustainable hydrogen production by catalytic bio-
        ethanol steam reforming, INTECH Open Access Publisher, 2012.
        http://cdn.intechopen.com/pdfs/30633/InTech-
        Sustainable_hydrogen_production_by_catalytic_bio_ethanol_steam_reforming.pdf (accessed February 22,
        2017).

[12]   P.L. Spath, M.K. Mann, Life cycle assessment of hydrogen production via natural gas steam reforming,
        National Renewable Energy Laboratory Golden, CO, 2000. http://www-
        pord.ucsd.edu/~sgille/mae124_s06/27637.pdf (accessed February 27, 2017).

[13]   J.D. Holladay, J. Hu, D.L. King, Y. Wang, An overview of hydrogen production technologies, Catal.
        Today. 139 (2009) 244–260. https://doi.org/10.1016/j.cattod.2008.08.039.

[14]   M. Ni, D.Y.C. Leung, M.K.H. Leung, K. Sumathy, An overview of hydrogen production from biomass,
        Fuel Process. Technol. 87 (2006) 461–472. https://doi.org/10.1016/j.fuproc.2005.11.003.

[15]   M. Ni, D.Y.C. Leung, M.K.H. Leung, A review on reforming bio-ethanol for hydrogen production, Int. J.
        Hydrog. Energy. 32 (2007) 3238–3247. https://doi.org/10.1016/j.ijhydene.2007.04.038.

[16]   V.V. Galvita, G.L. Semin, V.D. Belyaev, V.A. Semikolenov, P. Tsiakaras, V.A. Sobyanin, Synthesis gas
        production by steam reforming of ethanol, Appl. Catal. Gen. 220 (2001) 123–127.
        https://doi.org/10.1016/S0926-860X(01)00708-6.

[17]   BMBF-Internetredaktion, Nationale Wasserstoffstrategie - BMBF, Bundesminist. Für Bild. Forsch. -
        BMBF. (n.d.). https://www.bmbf.de/de/nationale-wasserstoffstrategie-9916.html (accessed July 12, 2020).

[18]   B.S. Dien, M.A. Cotta, T.W. Jeffries, Bacteria engineered for fuel ethanol production: current status, Appl.
        Microbiol. Biotechnol. 63 (2003) 258–266. https://doi.org/10.1007/s00253-003-1444-y.

[19]   M. Galbe, G. Zacchi, A review of the production of ethanol from softwood, Appl. Microbiol. Biotechnol.
        59 (2002) 618–628. https://doi.org/10.1007/s00253-002-1058-9.

[20]   B. Hahn-Hägerdal, M. Galbe, M.F. Gorwa-Grauslund, G. Lidén, G. Zacchi, Bio-ethanol – the fuel of
        tomorrow from the residues of today, Trends Biotechnol. 24 (2006) 549–556.
        https://doi.org/10.1016/j.tibtech.2006.10.004.

Bibliography

[21] H.-S. Roh, Y. Wang, D.L. King, A. Platon, Y.-H. Chin, Low temperature and H 2 selective catalysts for ethanol steam reforming, Catal. Lett. 108 (2006) 15–19.

[22] P. Ciambelli, V. Palma, A. Ruggiero, Low temperature catalytic steam reforming of ethanol. 1. The effect of the support on the activity and stability of Pt catalysts, Appl. Catal. B Environ. 96 (2010) 18–27.

[23] P. Ciambelli, V. Palma, A. Ruggiero, Low temperature catalytic steam reforming of ethanol. 2. Preliminary kinetic investigation of Pt/CeO 2 catalysts, Appl. Catal. B Environ. 96 (2010) 190–197.

[24] J. Rouquerol, D. Avnir, D.H. Everett, C. Fairbridge, M. Haynes, N. Pernicone, J.D.F. Ramsay, K.S.W. Sing, K.K. Unger, Guidelines for the Characterization of Porous Solids, in: F.R.-R. J. Rouquerol K.S.W. Sing and K.K. Unger (Ed.), Stud. Surf. Sci. Catal., Elsevier, 1994: pp. 1–9. https://doi.org/10.1016/S0167-2991(08)63059-1.

[25] J. Kärger, D.M. Ruthven, D.N. Theodorou, Elementary Principles of Diffusion, in: Diffus. Nanoporous Mater., Wiley-VCH Verlag GmbH & Co. KGaA, 2012: pp. 1–24. https://doi.org/10.1002/9783527651276.ch1.

[26] K.S.W. Sing, F. Schüth, Definitions, Terminology, and Classification of Pore Structures, in: F. Schüth, K.S.W. Sing, J. Weitkamp (Eds.), Handb. Porous Solids, Wiley-VCH Verlag GmbH, 2002: pp. 24–33. https://doi.org/10.1002/9783527618286.ch2.

[27] W.J. Koros, Y.H. Ma, T. Shimidzu, Terminology for membranes and membrane processes (IUPAC Recommendations 1996), Pure Appl. Chem. 68 (1996). https://doi.org/10.1351/pac199668071479.

[28] P.W. Atkins, J. de Paula, Physikalische Chemie, 4. vollständig überarbeitete Auflage, Wiley-VCH, Weinheim, 2006.

[29] H.W. Haynes Jr, L.L.L. GGG00S000S, A note on diffusive mass transport, Chem Eng Ed. 20 (1986) e27.

[30] J. Kärger, D.M. Ruthven, Diffusion in zeolites, Handb. Zeolite Sci. Technol. 341 (1992). http://aussiezeolite.com.au.p8.hostingprod.com/yahoo_site_admin/assets/docs/DK2772_ch10.158222922.pdf (accessed March 15, 2017).

[31] J. Kärger, D.M. Ruthven, D.N. Theodorou, Chromatographic and Permeation Methods of Measuring Intraparticle Diffusion, in: Diffus. Nanoporous Mater., Wiley-VCH Verlag GmbH & Co. KGaA, 2012: pp. 459–513. https://doi.org/10.1002/9783527651276.ch14.

[32] E. Wicke, R. Kallenbach, Die Oberflächendiffusion von Kohlendioxyd in aktiven Kohlen, Kolloid-Z. 97 (1941) 135–151. https://doi.org/10.1007/BF01502640.

[33] D.W. Breck, Zeolite molecular sieves: structure, chemistry, and use, Wiley, 1973.

[34] J. Kärger, D.M. Ruthven, D.N. Theodorou, Diffusion Mechanisms, in: Diffus. Nanoporous Mater., Wiley-VCH Verlag GmbH & Co. KGaA, 2012: pp. 85–110. https://doi.org/10.1002/9783527651276.ch4.

[35] G.L. Kington, A.C. Macleod, Heats of sorption of gases in chabazite, energetic heterogeneity and the role of quadrupoles in sorption, Trans. Faraday Soc. 55 (1959) 1799–1814.

[36] F.M. Mourits, F.H. Rummens, A critical evaluation of Lennard–Jones and Stockmayer potential parameters and of some correlation methods, Can. J. Chem. 55 (1977) 3007–3020.

[37] J. Caro, Fluid Flow, in: F. Schüth, K.S.W. Sing, J. Weitkamp (Eds.), Handb. Porous Solids, Wiley-VCH Verlag GmbH, 2002: pp. 352–370. https://doi.org/10.1002/9783527618286.ch10.

[38] M. Mulder, Basic Principles of Membrane Technology, Springer Netherlands, Dordrecht, 1996. https://doi.org/10.1007/978-94-009-1766-8.

[39] D.S. Scott, F.A.L. Dullien, Diffusion of ideal gases in capillaries and porous solids, AIChE J. 8 (1962) 113–117. https://doi.org/10.1002/aic.690080126.

[40] T. Kiyoshi, T. Namba, M. Yamawaki, Hydrogen permeation through graphite, J. Nucl. Mater. 155–157 (1988) 230–233. https://doi.org/10.1016/0022-3115(88)90245-0.

[41] O. Beyssac, D. Rumble, Graphitic Carbon: A Ubiquitous, Diverse, and Useful Geomaterial, Elements. 10 (2014) 415–420. https://doi.org/10.2113/gselements.10.6.415.

[42] M. Binnewies, M. Finze, M. Jäckel, P. Schmidt, H. Willner, G. Rayner-Canham, Allgemeine und Anorganische Chemie, Springer Berlin Heidelberg, Berlin, Heidelberg, 2016. https://doi.org/10.1007/978-3-662-45067-3.

[43] J.N. Rouzaud, A. Oberlin, Structure, microtexture, and optical properties of anthracene and saccharose-based carbons, Carbon. 27 (1989) 517–529. https://doi.org/10.1016/0008-6223(89)90002-X.

[44] A. Oberlin, S. Bonnamy, A Realistic Approach to Disordered Carbons, in: Chem. Phys. Carbon Ser. Chem. Phys. Carbon ISBN 978-1-4398-2094-0 CRC Press Ed. Ljubisa Rad. Pp 1-84, 2012: pp. 1–84. https://doi.org/10.1201/b12960-2.

[45] A. Oberlin, High-resolution TEM studies of carbonization and graphitization, Chem. Phys. Carbon. 22 (1989) 1–143.

[46] P.R. Buseck, O. Beyssac, From Organic Matter to Graphite: Graphitization, Elements. 10 (2014) 421–426. https://doi.org/10.2113/gselements.10.6.421.

[47] O. Beyssac, B. Goffé, C. Chopin, J.N. Rouzaud, Raman spectra of carbonaceous material in metasediments: a new geothermometer: RAMAN SPECTROSCOPY OF CARBONACEOUS MATERIAL, J. Metamorph. Geol. 20 (2002) 859–871. https://doi.org/10.1046/j.1525-1314.2002.00408.x.

[48] P.A. Pfendt, Comparison of the general chemical nature of various kerogens based on their reactivities towards bromine, Org. Geochem. 6 (1984) 383–390. https://doi.org/10.1016/0146-6380(84)90060-3.

[49] R.D. Heidenreich, W.M. Hess, L.L. Ban, A test object and criteria for high resolution electron microscopy, J. Appl. Crystallogr. 1 (1968) 1–19. https://doi.org/10.1107/S0021889868004930.

[50] J. Millet, J. Millet, A. Vivares, Composition chimique des cokes et graphitation, J. Chim. Phys. 60 (1963) 553–562. https://doi.org/10.1051/jcp/1963600553.

[51] X. Bourrat, A. Oberlin, J.C. Escalier, Microtexture and structure of semi-cokes and cokes, Fuel. 65 (1986) 1490–1500. https://doi.org/10.1016/0016-2361(86)90323-6.

[52] X. Bourrat, A. Oberlin, J. Escalier, Sulphur behaviour during asphalt heat-treatment, Fuel. 66 (1987) 542–550. https://doi.org/10.1016/0016-2361(87)90161-X.

[53] M. Guigon, A. Oberlin, Heat-treatment of high tensile strength PAN-based carbon fibres: Microtexture, structure and mechanical properties, Compos. Sci. Technol. 27 (1986) 1–23. https://doi.org/10.1016/0266-3538(86)90060-6.

[54] E.R. Vorpagel, J.G. Lavin, Most stable configurations of polynuclear aromatic hydrocarbon molecules in pitches via molecular modelling, Carbon. 30 (1992) 1033–1040. https://doi.org/10.1016/0008-6223(92)90133-H.

[55] J. Ravey, G. Ducouret, D. Espinat, Asphaltene macrostructure by small angle neutron scattering, Fuel. 67 (1988) 1560–1567. https://doi.org/10.1016/0016-2361(88)90076-2.

[56] J.C. Ravey, E. Espinat, Macrostructure of petroleum asphaltenes by small angle neutron scattering, in: M. Zulauf, P. Lindner, P. Terech (Eds.), Trends Colloid Interface Sci. IV, Steinkopff, Darmstadt, 1990: pp. 127–130. https://doi.org/10.1007/BFb0115538.

[57] A. Oberlin, M. Oberlin, M. Maubois, Study of thin amorphous and crystalline carbon films by electron microscopy, Philos. Mag. 32 (1975) 833–846. https://doi.org/10.1080/14786437508221623.

[58] Coal - 3rd Edition, (n.d.). https://www.elsevier.com/books/coal/van-krevelen/978-0-444-89586-8 (accessed June 4, 2020).

[59] B. Durand, Kerogen: Insoluble Organic Matter from Sedimentary Rocks, Editions TECHNIP, 1980.

[60] R. Diamond, X-ray diffraction data for large aromatic molecules, Acta Crystallogr. 10 (1957) 359–364. https://doi.org/10.1107/S0365110X5700105X.

[61] R. Diamond, A least-squares analysis of the diffuse X-ray scattering from carbons, Acta Crystallogr. 11 (1958) 129–138. https://doi.org/10.1107/S0365110X58000384.

[62] J. Zawadzki, Infrared-spectroscopy in surface-chemistry of carbons, Chem. Phys. Carbon. 21 (1989) 147–380.

[63] J. Zawadzki, IR spectroscopy studies of oxygen surface compounds on carbon, Carbon. 16 (1978) 491–497. https://doi.org/10.1016/0008-6223(78)90098-2.

[64] F. Rodriguez-Reinoso, Microporous structure of activated carbons as revealed adsorption methods, Chem. Phys. Carbon. 21 (1989) 1.

[65] R. Schlögl, Surface Composition and Structure of Active Carbons, in: F. Schüth, K.S.W. Sing, J. Weitkamp (Eds.), Handb. Porous Solids, Wiley-VCH Verlag GmbH, 2002: pp. 1863–1900. https://doi.org/10.1002/9783527618286.ch24c.

Bibliography

[66] B. McEnaney, Properties of Activated Carbons, in: F. Schüth, K.S.W. Sing, J. Weitkamp (Eds.), Handb. Porous Solids, Wiley-VCH Verlag GmbH, 2002: pp. 1828–1863. https://doi.org/10.1002/9783527618286.ch24b.

[67] P. Brender, R. Gadiou, J.-C. Rietsch, P. Fioux, J. Dentzer, A. Ponche, C. Vix-Guterl, Characterization of Carbon Surface Chemistry by Combined Temperature Programmed Desorption with in Situ X-ray Photoelectron Spectrometry and Temperature Programmed Desorption with Mass Spectrometry Analysis, Anal. Chem. 84 (2012) 2147–2153. https://doi.org/10.1021/ac102244b.

[68] M.S. Shafeeyan, W.M.A.W. Daud, A. Houshmand, A. Shamiri, A review on surface modification of activated carbon for carbon dioxide adsorption, J. Anal. Appl. Pyrolysis. 89 (2010) 143–151. https://doi.org/10.1016/j.jaap.2010.07.006.

[69] B. Farbos, P. Weisbecker, H.E. Fischer, J.-P. Da Costa, M. Lalanne, G. Chollon, C. Germain, G.L. Vignoles, J.-M. Leyssale, Nanoscale structure and texture of highly anisotropic pyrocarbons revisited with transmission electron microscopy, image processing, neutron diffraction and atomistic modeling, Carbon. 80 (2014) 472–489. https://doi.org/10.1016/j.carbon.2014.08.087.

[70] T. Ishii, T. Kyotani, Chapter 14 - Temperature Programmed Desorption, in: M. Inagaki, F. Kang (Eds.), Mater. Sci. Eng. Carbon, Butterworth-Heinemann, 2016: pp. 287–305. https://doi.org/10.1016/B978-0-12-805256-3.00014-3.

[71] R. Pietrzak, XPS study and physico-chemical properties of nitrogen-enriched microporous activated carbon from high volatile bituminous coal, Fuel. 88 (2009) 1871–1877. https://doi.org/10.1016/j.fuel.2009.04.017.

[72] R. Pietrzak, H. Wachowska, P. Nowicki, Preparation of Nitrogen-Enriched Activated Carbons from Brown Coal, Energy Fuels. 20 (2006) 1275–1280. https://doi.org/10.1021/ef0504164.

[73] A. Manceau, K.L. Nagy, Quantitative analysis of sulfur functional groups in natural organic matter by XANES spectroscopy, Geochim. Cosmochim. Acta. 99 (2012) 206–223. https://doi.org/10.1016/j.gca.2012.09.033.

[74] A. Attar, F. Dupuis, Data on the Distribution of Organic Sulfur Functional Groups in Coals, in: M.L. Gorbaty, K. Ouchi (Eds.), Coal Struct., AMERICAN CHEMICAL SOCIETY, WASHINGTON, D. C., 1981: pp. 239–256. https://doi.org/10.1021/ba-1981-0192.ch016.

[75] J. Kakinoki, K. Katada, T. Hanawa, Heat treatment of evaporated carbon films, Acta Crystallogr. 13 (1960) 448–449. https://doi.org/10.1107/S0365110X60001060.

[76] S. Bonnamy, Carbonization of various precursors. Effect of heating rate, Carbon. 37 (1999) 1707–1724. https://doi.org/10.1016/S0008-6223(99)00044-5.

[77] S. Bonnamy, T. d'Etat, Caracterisation des produits pétroliers lors de la pyrolyse de leur fraction lourde, Etude Géochimique Stucturale. (1987) 149.

[78] J. Kakinoki, Y. Komura, T. Ino, Electron diffraction study of evaporated carbon films, Acta Crystallogr. 13 (1960) 171–179. https://doi.org/10.1107/S0365110X60000418.

[79] I. Ogawa, M. Sakai, M. Inagaki, Texture and graphitizability of carbons made from pitch and phenolic resin mixtures, J. Mater. Sci. 20 (1985) 17–22. https://doi.org/10.1007/BF00555893.

[80] J.D. Brooks, G.H. Taylor, The formation of graphitizing carbons from the liquid phase, Carbon. 3 (1965) 185–193. https://doi.org/10.1016/0008-6223(65)90047-3.

[81] A. Oberlin, Carbonization and graphitization, Carbon. 22 (1984) 521–541. https://doi.org/10.1016/0008-6223(84)90086-1.

[82] S. Bonnamy, Carbonization of various precursors. Effect of heating rate, Carbon. 37 (1999) 1691–1705. https://doi.org/10.1016/S0008-6223(99)00043-3.

[83] J.L. White, G.L. Guthrie, J.O. Gardner, Mesophase microstructures in carbonized coal-tar pitch, Carbon. 5 (1967) 517-IN8. https://doi.org/10.1016/0008-6223(67)90028-0.

[84] J.L. white, J.E. Zimmer, Twist disclinations in the carbonaceous mesophase, Carbon. 16 (1978) 469–475. https://doi.org/10.1016/0008-6223(78)90094-5.

[85] J.F. Sadoc, Use of regular polytopes for the mathematical description of the order in amorphous structures, J. Non-Cryst. Solids. 44 (1981) 1–16. https://doi.org/10.1016/0022-3093(81)90128-9.

Bibliography

[86] J.F. Sadoc, R. Mosseri, Order and disorder in amorphous, tetrahedrally coordinated semiconductors A curved-space description, Philos. Mag. B. 45 (1982) 467–483. https://doi.org/10.1080/13642818208246413.

[87] M. Villey, V. M, SIMULATION THERMIQUE DE L'EVOLUTION DES KEROGENES, (1980). http://pascal-francis.inist.fr/vibad/index.php?action=getRecordDetail&idt=PASCALGEODEBRGM8020410856 (accessed July 3, 2020).

[88] M. Inagaki, Carbon materials science and engineering: from fundamentals to applications, 清华大学出版社有限公司, 2006.

[89] I. Rannou, V. Bayot, M. Lelaurain, Structural characterization of graphitization process in pyrocarbons, Carbon. 32 (1994) 833–843. https://doi.org/10.1016/0008-6223(94)90040-X.

[90] H. Takahashi, H. Kuroda, H. Akamatu, Correlation between stacking order and crystallite dimensions in carbons, Carbon. 2 (1965) 432–433.

[91] J.W. Patrick, S. Hanson, Pore Structure of Graphite, Coke and Composites, in: F. Schüth, K.S.W. Sing, J. Weitkamp (Eds.), Handb. Porous Solids, Wiley-VCH Verlag GmbH, 2002: pp. 1900–1922. https://doi.org/10.1002/9783527618286.ch24d.

[92] J.R. Fryer, The micropore structure of disordered carbons determined by high resolution electron microscopy, Carbon. 19 (1981) 431–439. https://doi.org/10.1016/0008-6223(81)90026-9.

[93] R.E. Franklin, Crystallite Growth in Graphitizing and Non-Graphitizing Carbons, Proc. R. Soc. Math. Phys. Eng. Sci. 209 (1951) 196–218. https://doi.org/10.1098/rspa.1951.0197.

[94] R.E. Franklin, The structure of graphitic carbons, Acta Crystallogr. 4 (1951) 253–261. https://doi.org/10.1107/S0365110X51000842.

[95] J. Biscoe, B.E. Warren, An X-Ray Study of Carbon Black, J. Appl. Phys. 13 (1942) 364–371. https://doi.org/10.1063/1.1714879.

[96] J. Maire, J. Mering, Graphitization of soft carbons, Chem. Phys. Carbon. 6 (1970) 125–190.

[97] J. Maire, Recherche sur le phénomène de la graphitation, Schiffer, 1967.

[98] D. Joseph, A. Oberlin, Oxidation of carbonaceous matter—I, Carbon. 21 (1983) 559–564. https://doi.org/10.1016/0008-6223(83)90239-7.

[99] D. Joseph, A. Oberlin, Oxidation of carbonaceous matter—II, Carbon. 21 (1983) 565–571. https://doi.org/10.1016/0008-6223(83)90240-3.

[100] P. Burg, D. Cagniant, Characterization of carbon surface chemistry, Chem. Phys. Carbon. 30 (2008) 129.

[101] X. Bourrat, F. Langlais, G. Chollon, G.L. Vignoles, Low temperature pyrocarbons: a review, J. Braz. Chem. Soc. 17 (2006) 1090–1095. https://doi.org/10.1590/S0103-50532006000600005.

[102] J.-M. Vallerot, X. Bourrat, A. Mouchon, G. Chollon, Quantitative structural and textural assessment of laminar pyrocarbons through Raman spectroscopy, electron diffraction and few other techniques, Carbon. 44 (2006) 1833–1844. https://doi.org/10.1016/j.carbon.2005.12.029.

[103] A. Schoedel, O.M. Yaghi, Reticular Chemistry of Metal-Organic Frameworks Composed of Copper and Zinc Metal Oxide Secondary Building Units as Nodes, in: S. Kaskel (Ed.), Chem. Met.-Org. Framew. Synth. Charact. Appl., Wiley-VCH Verlag GmbH & Co. KGaA, Weinheim, Germany, 2016: pp. 41–72. https://doi.org/10.1002/9783527693078.ch3.

[104] S. Kaskel, ed., The Chemistry of Metal-Organic Frameworks: Synthesis, Characterization, and Applications: Synthesis, Characterization, and Applications, Wiley-VCH Verlag GmbH & Co. KGaA, Weinheim, Germany, 2016. https://doi.org/10.1002/9783527693078.

[105] F. Hoffmann, M. Fröba, Network Topology, in: S. Kaskel (Ed.), Chem. Met.-Org. Framew. Synth. Charact. Appl., Wiley-VCH Verlag GmbH & Co. KGaA, Weinheim, Germany, 2016: pp. 5–40. https://doi.org/10.1002/9783527693078.ch2.

[106] Hydrogen - Fuels & Technologies, IEA. (n.d.). https://www.iea.org/fuels-and-technologies/hydrogen (accessed December 12, 2020).

[107] The Future of Hydrogen – Analysis, IEA. (n.d.). https://www.iea.org/reports/the-future-of-hydrogen (accessed December 12, 2020).

Bibliography

[108] Y.H. Ma, Hydrogen Separation Membranes, in: N.N.L. senior scientist Director, A.G.F. Ph.D, W.S.W.H.B.S. vice-president M.S.,. Ph D. essor of Chemical senior, T. tsuura B.S. M.Sc (Eds.), Adv. Membr. Technol. Appl., John Wiley & Sons, Inc., 2008: pp. 671–684. https://doi.org/10.1002/9780470276280.ch25.

[109] D.J. Adolf, D.M. Fischedick, Nachhaltige Mobilität durch Brennstoffzelle und H2, (2017) 37.

[110] Shell Wasserstoffstudie, (n.d.). https://www.shell.de/medien/shell-publikationen/shell-hydrogen-study.html (accessed December 13, 2020).

[111] N. Pal, M. Agarwal, K. Maheshwari, Y.S. Solanki, A review on types, fabrication and support material of hydrogen separation membrane, Mater. Today Proc. 28 (2020) 1386–1391. https://doi.org/10.1016/j.matpr.2020.04.806.

[112] N. Sazali, M.A. Mohamed, W.N.W. Salleh, Membranes for hydrogen separation: a significant review, Int. J. Adv. Manuf. Technol. 107 (2020) 1859–1881. https://doi.org/10.1007/s00170-020-05141-z.

[113] S. Yun, H. Lim, S. Ted Oyama, Experimental and kinetic studies of the ethanol steam reforming reaction equipped with ultrathin Pd and Pd–Cu membranes for improved conversion and hydrogen yield, J. Membr. Sci. 409–410 (2012) 222–231. https://doi.org/10.1016/j.memsci.2012.03.059.

[114] A. Kleinert, G. Grubert, X. Pan, C. Hamel, A. Seidel-Morgenstern, J. Caro, Compatibility of hydrogen transfer via Pd-membranes with the rates of heterogeneously catalysed steam reforming, Catal. Today. 104 (2005) 267–273.

[115] H. Amandusson, L.-G. Ekedahl, H. Dannetun, The effect of CO and O2 on hydrogen permeation through a palladium membrane, Appl. Surf. Sci. 153 (2000) 259–267. https://doi.org/10.1016/S0169-4332(99)00357-8.

[116] S.H. Jung, K. Kusakabe, S. Morooka, S.-D. Kim, Effects of co-existing hydrocarbons on hydrogen permeation through a palladium membrane, J. Membr. Sci. 170 (2000) 53–60. https://doi.org/10.1016/S0376-7388(99)00357-9.

[117] J. Shu, B.P.A. Grandjean, A.V. Neste, S. Kaliaguine, Catalytic palladium-based membrane reactors: A review, Can. J. Chem. Eng. 69 (1991) 1036–1060. https://doi.org/10.1002/cjce.5450690503.

[118] P.J. Berlowitz, C.H.F. Peden, D.W. Goodman, Kinetics of carbon monoxide oxidation on single-crystal palladium, platinum, and iridium, J. Phys. Chem. 92 (1988) 5213–5221. https://doi.org/10.1021/j100329a030.

[119] K. Partovi Amarloei, Development of CO2-stable oxygen-transporting membranes for oxyfuel carbon capture process, (2015). https://doi.org/10.15488/8547.

[120] K. Partovi, B. Geppert, F. Liang, C.H. Rüscher, J. Caro, Effect of the B-Site Composition on the Oxygen Permeability and the CO_2 Stability of $Pr_{0.6} Sr_{0.4} Co_x Fe_{1-x} O_{3-\delta}$ $(0.0 \leq x \leq 1.0)$ Membranes, Chem. Mater. 27 (2015) 2911–2919. https://doi.org/10.1021/acs.chemmater.5b00166.

[121] C. Zuo, S.E. Dorris, U. Balachandran, M. Liu, Effect of Zr-Doping on the Chemical Stability and Hydrogen Permeation of the $Ni−BaCe_{0.8} Y_{0.2} O_{3-\alpha}$ Mixed Protonic−Electronic Conductor, Chem. Mater. 18 (2006) 4647–4650. https://doi.org/10.1021/cm0518224.

[122] L.M. Robeson, The upper bound revisited, J. Membr. Sci. 320 (2008) 390–400. https://doi.org/10.1016/j.memsci.2008.04.030.

[123] L.M. Robeson, Polymer membranes for gas separation, Curr. Opin. Solid State Mater. Sci. 4 (1999) 549–552. https://doi.org/10.1016/S1359-0286(00)00014-0.

[124] M.C. Duke, J.C.D. da Costa, D.D. Do, P.G. Gray, G.Q. Lu, Hydrothermally Robust Molecular Sieve Silica for Wet Gas Separation, Adv. Funct. Mater. 16 (2006) 1215–1220. https://doi.org/10.1002/adfm.200500456.

[125] N. Sazali, A review of the application of carbon-based membranes to hydrogen separation, J. Mater. Sci. 55 (2020) 11052–11070. https://doi.org/10.1007/s10853-020-04829-7.

[126] J.B.S. Hamm, A. Ambrosi, J.G. Griebeler, N.R. Marcilio, I.C. Tessaro, L.D. Pollo, Recent advances in the development of supported carbon membranes for gas separation, Int. J. Hydrog. Energy. 42 (2017) 24830–24845. https://doi.org/10.1016/j.ijhydene.2017.08.071.

[127] W.N.W. Salleh, A.F. Ismail, Carbon membranes for gas separation processes: Recent progress and future perspective, J. Membr. Sci. Res. 1 (2015). https://doi.org/10.22079/jmsr.2015.12301.

Bibliography

[128] P.J. Williams, W.J. Koros, Gas Separation by Carbon Membranes, in: N.N. Li, A.G. Fane, W.S.W. Ho, T. Matsuura (Eds.), Adv. Membr. Technol. Appl., John Wiley & Sons, Inc., Hoboken, NJ, USA, 2008: pp. 599–631. https://doi.org/10.1002/9780470276280.ch23.

[129] Y. Ban, N. Cao, W. Yang, Metal-Organic Framework Membranes and Membrane Reactors: Versatile Separations and Intensified Processes, Research. 2020 (2020). https://doi.org/10.34133/2020/1583451.

[130] Z. Kang, L. Fan, D. Sun, Recent advances and challenges of metal–organic framework membranes for gas separation, J. Mater. Chem. A. 5 (2017) 10073–10091. https://doi.org/10.1039/C7TA01142C.

[131] E. Adatoz, A.K. Avci, S. Keskin, Opportunities and challenges of MOF-based membranes in gas separations, Sep. Purif. Technol. 152 (2015) 207–237. https://doi.org/10.1016/j.seppur.2015.08.020.

[132] S. Qiu, M. Xue, G. Zhu, Metal–organic framework membranes: from synthesis to separation application, Chem Soc Rev. 43 (2014) 6116–6140. https://doi.org/10.1039/C4CS00159A.

[133] H. Reinsch, M.A. van der Veen, B. Gil, B. Marszalek, T. Verbiest, D. de Vos, N. Stock, Structures, Sorption Characteristics, and Nonlinear Optical Properties of a New Series of Highly Stable Aluminum MOFs, Chem. Mater. 25 (2013) 17–26. https://doi.org/10.1021/cm3025445.

[134] L.-H. Schilling, H. Reinsch, N. Stock, Synthesis, Structure, and Selected Properties of Aluminum-, Gallium-, and Indium-Based Metal-Organic Frameworks, in: S. Kaskel (Ed.), Chem. Met.-Org. Framew. Synth. Charact. Appl., Wiley-VCH Verlag GmbH & Co. KGaA, Weinheim, Germany, 2016: pp. 105–135. https://doi.org/10.1002/9783527693078.ch5.

7. Appendix

List of publications included in the Dissertation

1. **A. Schulz**, F. Steinbach, J. Caro, Pressed graphite crystals as gas separation membrane for steam reforming of ethanol, J. Membr. Sc. 469 (2014) 284-291.

2. **A. Wollbrink**, K. Volgmann, J. Koch, K. Kanthasamy, C. Tegenkamp, Y. Li, H. Richter, S. Kämnitz, F. Steinbach, A. Feldhoff, J. Caro, Amorphous, turbostratic and crystalline carbon membranes with hydrogen selectivity, Carbon 106 (2016) 93-105.

3. H. Jin, **A. Wollbrink**, R. Yao, Y. Li, J. Caro, W. Yang, A novel CAU-10-H MOF membrane for hydrogen separation under hydrothermal conditions, J. Membr. Sc. 513 (2016) 40-46.

4. T. Ebert, **A. Wollbrink**, A. Seifert, R. John and S. Spange, Multiple polymerization – formation of hybrid materials consisting of two or more polymers from one monomer, Polym. Chem. 7 (2016) 6826-6833.

5. **A. Wollbrink**, K. Volgmann, A. Breuksch, J. Koch, C. Tegenkamp, J. Caro, Improved hydrogen selectivity of Surface Modified Graphite (SMG) membranes: Permeation experiments and characterisation by micro-Raman spectroscopy and XPS, J. Membr, Sc. 528 (2017) 316-325.

List of not published Results included in the Dissertation

1. **A. Wollbrink**, K. Volgmann, J. Koch, K. Kanthasamy, C. Tegenkamp, Y. Li, H. Richter, S. Kämnitz, F. Steinbach, A. Feldhoff, J. Caro, Effects of steam containing gas mixtures on the separation performance of amorphous, turbostratic and crystalline carbon membranes. *(in progress)*

2. **A. Wollbrink**, T. Ebert, J. Koch, C. Tegenkamp, J. Caro, S. Spange, Separation performance of a composite Carbon Molecular Sieve ($cCMS/SiO_2$) membrane obtained from a hybrid material synthesised by twin polymerization. *(in progress)*

List of publications not included in the Dissertation

1. H. Richter, H. Voss, N. Kaltenborn, S. Kämnitz, **A. Wollbrink**, A. Feldhoff, J. Caro, S. Roitsch, I. Voigt, High-flux carbon molecular sieve membranes for gas separation, Angew. Chem. Int. Ed. 56 (2017) 7760-7763.

2. S. Friebe, L. Diestel, A. Knebel, **A. Wollbrink**, and J. Caro, MOF-based mixed Matrix Membranes in gas separation – Mystery and Reality, Chem. Ing. Tech. 11 (2016) 1788-1797.

3. C. H. Rüscher, F. Kiesel, **A. Wollbrink**, L. Schomborg, J.-Ch. Buhl, Dehydration diffusion of $B(OH)_4$-sodalite investigated by micro-Raman spectroscopy on single crystals and combined TG/IR on powders. diffusion-fundamentals.org 25 (2016) 3, pp 1-13.

4. J. Xue; **A. Schulz**; H. Wang; A. Feldhoff, Phase stability of the Ruddlesden-Popper type oxide $(Pr_{0.9}La_{0.1})_{2.0}Ni_{0.74}Cu_{0.21}Ga_{0.05}O_{4+\delta}$ in oxidizing environment, Journal of Membrane Science, 497 (2015) 357-364.

5. K. Volgmann, **A. Schulz**, A.-M. Welsch, T. Bredow, S. Nakhal, M. Lerch, and P. Heitjans, Lattice Vibrations to Identify the Li/Na ratio in $Li_xNa_{2-x}Ti_6O_{13}$ (x = 0 … 2), Zeitschrift für Physikalische Chemie, 229(9) (2015) 1351-1362.

6. S. Friebe, N. Wang, L. Diestel, Y. Liu, **A. Schulz**, A. Mundstock, J. Caro Deuterium/hydrogen permeation through different molecular sieve membranes: ZIF, LDH, zeolite, Microporous and Mesoporous Materials 216 (2015) 127-132.

7. L. Diestel, N.Wang, **A. Schulz**, F. Steinbach, and J. Caro, Matrimid-Based Mixed Matrix Membranes: Interpretation and Correlation of Experimental Findings for Zeolitic Imidazolate Frameworks as Fillers in H_2/CO_2 Separation, Ind. Eng. Chem. Res. 54, (2015) 1103−1112.

8. C. H. Rüscher, L. Schomborg, **A. Schulz**, J. C. Buhl, Basic Research on Geopolymer Gels for Production of Green Binders and Hydrogen Storage." Developments in Strategic Materials and Computational Design IV (2013) 97-114.

9. C. H. Rüscher, **A. Schulz**, M. H. Gougazeh, A. Ritzmann, Mechanical Strength Development of Geopolymer Binder and the Effect of Quartz Content." Developments in Strategic Materials and Computational Design IV (2013)13-23.

Appendix

List of conference contributions:

1. **A. Schulz**, Y. Li, J. Caro, Evaluation of amorphous, turbostratic and crystalline carbon membranes in the focus of bio-ethanol steam reforming, Z. Krist. Supplement Issue 35 (2015) 79-80.

2. **A. Schulz**, F. Steinbach, J. Caro, Hydrogen selective Graphite based Membranes, Z. Krist. Supplement Issue 34 (2014) 110.

3. **A. Schulz**, C. H. Rüscher, J.-Chr. Buhl: On the dehydration mechanism of $NaB(OH)_4$-sodalites investigated by micro-Raman spectroscopy. Z. Krist. Supplement Issue 33 (2013) 100.

4. **A. Schulz**, C. H. Rüscher, J.-Chr. Buhl: Single crystal dehydration of $NaB(OH)_4$-sodalites investigated by Raman depth profiling. Z. Krist. Supplement Issue 32 (2012) 81-82.

5. **A. Schulz**, C. H. Rüscher, J.-Chr. Buhl: Synthesis and characterisation of nano- and micro-sized $NaB(OH)_4$- sodalites. Z. Krist. Supplement Issue 31 (2011) 93.

8. Curriculum Vitae

Personal Data Sheet:

Name:	Wollbrink
Birth Name:	Schulz
First Name:	Alexander
Date of birth:	22.04.1987
Place of birth:	Stralsund
Personal status:	married

Professional Experience

Since 12.10.2020	Limited Partner at the Company of "MIB & ZMK GmbH and Co. KG", Hannover
04.2020-09.2020	Employee at the Company of "MIB & ZMK GmbH and Co. KG", Hannover
03.2017-03.2020	Research Assistant at Institute of Energy Research and Physical Technologies, TU Clausthal, <u>group:</u> Prof. Dr. Holger Fritze, topic: "In-situ methods for the determination of high oxygen deficits in ceria-zirconia solid solutions for the use in exhaust gas aftertreatment"

Higher Education:

04.2013-03.2017	Ph.D. student at Institute of physical Chemistry und Electrochemistry, group Prof. Dr. Jürgen Caro, topic: "Hydrogen production by bio-methane and bio-ethanol in catalytic membrane reactors".
10.2012-03.2013	Exposé-Stipendium (Grant) of the Graduierten Akademie at the Leibniz University of Hannover in the Institute of Mineralogy, group: Prof. Dr. J.-Ch. Buhl, topic: „Manner of reaction of hydrides of the light elements (NaH, MgH_2, $NaBH_4$) in amorphous and crystalline host materials".
10.2012-03.2013	Exercise Instructor: „Practice in Crystallography" for the lecture „Crystallography" at the Institute of Mineralogy, Leibniz University Hannover.

01.2011-09.2012	Research assistant in the group of Prof. Dr. J.-Ch. Buhl (Crystallography) at the Institute of Mineralogy, Leibniz University Hannover.
10.2010-09.2012	**Master of Science** in Mineralogy and Geochemistry at the Institute of Mineralogy, topic: Investigations for the thermal dehydration of $NaB(OH)_4$-Sodalite, Leibniz University Hannover.
10.2007-09.2010	**Bachelor of Science** in Geosciences Geochemistry at the Institute of Mineralogy, topic: Synthesis and Characterisation of nano-sized Tetrahydroxoborate Sodalite $Na_8[AlSiO_4]_6 [B(OH)_4]_2$, Leibniz University Hannover.

Personal training:

06.10.2020	Software training course on the principle use of "Metigo MAP 4.0"
21.11-24.11.2017	Participation to radiation protection course at the Institute of Radioökologie and Strahlenschutz (IRS) Hannover.
09-12.03.2015	DMG/DGK Ph.D. student course: Basic principles and applications for Rietveld refinements (TOPAS V. 4.2) at Max-Planck Institute Stuttgart.
21.-25.07.2014	International School on Ab initio Modelling of Solids, Universität Regensburg und Turin 2014 für "CRYSTAL14" calculations.
23.-25.06.2014	Bronkhorst High-Tech Product Training (MFC-Technique).